34th conference with international participation

COMPUTATIONAL MECHANICS 2018

BOOK OF EXTENDED ABSTRACTS

October 31 - November 2, 2018

HOTEL SRNÍ AND ŠUMAVA, SRNÍ
CZECH REPUBLIC

Central European Association
for Computational Mechanics

BOOK OF EXTENDED ABSTRACTS
34^{th} conference with international participation **Computational Mechanics 2018**

ISBN 978-80-261-0819-1

Published by
University of West Bohemia, Univerzitní 8, 301 00 Plzeň, Czech Republic, IC 49777513

Edited by
Vítězslav Adámek
Alena Jonášová
Stanislav Plánička
Martin Zajíček

Conference secretariat
Monika Grätschová
Department of Mechanics
Faculty of Applied Sciences
University of West Bohemia
Univerzitní 8
301 00 Plzeň
Czech Republic

phone: +420 377 632 301
e-mail: vm@kme.zcu.cz

PREFACE

The Book of Extended Abstracts contains 72 two-page abstracts presented at the 34th conference **Computational Mechanics 2018**, which was held at the Hotel Srní and Šumava in Srní, Czech Republic, on October 31 – November 2, 2018. This annual conference, which was attended by almost one hundred participants from the Czech Republic, Slovakia and from abroad, was organised by the Department of Mechanics, Faculty of Applied Sciences of the University of West Bohemia under the auspices of

- Vlasta Radová, the Dean of the Faculty of Applied Sciences,
- Ivana Bartošová, the Vice-President of the Pilsen Region for Education and Tourism,
- Czech Society for Mechanics,
- Czech National Committee of IFToMM,
- Central European Association for Computational Mechanics.

The main objective of this traditional conference is to bring together academicians, researchers and industrial partners interested in relevant disciplines of mechanics including

- solid mechanics,
- dynamics of mechanical systems,
- mechatronics and vibrations,
- reliability and durability of structures,
- fracture mechanics,
- mechanics in civil engineering,
- fluid mechanics and fluid-structure interaction,
- thermodynamics,
- biomechanics,
- heterogeneous media and multiscale problems,
- experimental methods in mechanics,

to create an opportunity for meeting, discussion and collaboration among the participants. As in the previous years, the three best papers presented at this conference were awarded the Czech Society for Mechanics Award for young researchers under 35 years of age.

To all conference participants, we offer the possibility to publish their peer-reviewed full papers in the international journal **Applied and Computational Mechanics** indexed by Scopus. This journal has been published by the University of West Bohemia since 2007 (see https://www.kme.zcu.cz/acm/).

We would like to express our gratitude to all the invited speakers for their significant contribution to the conference and the time and effort they put. Considerable acknowledgement belongs also to the members of the Organising Committee for their important work.

We strongly believe that all participants of the CM2018 enjoyed their stay in the beautiful nature of the Šumava region in a meaningful way. Finally, we would like to invite you all to come to the next conference CM2019.

Jan Vimmr
University of West Bohemia
Chairman of the Scientific Committee

Vítězslav Adámek
University of West Bohemia
Chairman of the Organising Committee

SCIENTIFIC COMMITTEE

Chairman:

Jan Vimmr
University of West Bohemia, Faculty of Applied Sciences, Czech Republic

Members:

Miroslav Balda
Research and Testing Institute Plzeň, Czech Republic

Jiří Burša
Brno University of Technology, Faculty of Mechanical Engineering, Czech Republic

Jan Dupal
University of West Bohemia, Faculty of Applied Sciences, Czech Republic

Václav Dvořák
Technical University of Liberec, Faculty of Mechanical Engineering, Czech Republic

Jiří Fürst
Czech Technical University in Prague, Faculty of Mechanical Engineering, Czech Republic

Miroslav Holeček
University of West Bohemia, Czech Republic

Jaromír Horáček
Institute of Thermomechanics, Czech Academy of Sciences, Czech Republic

Michal Kotoul
Brno University of Technology, Faculty of Mechanical Engineering, Czech Republic

Jiří Křen
University of West Bohemia, Faculty of Applied Sciences, Czech Republic

Vladislav Laš
University of West Bohemia, Faculty of Applied Sciences, Czech Republic

Justín Murín
Slovak University of Technology in Bratislava, Faculty of Mechanical Engineering, Slovak Republic

Milan Naď
Slovak University of Technology in Bratislava, Faculty of Materials Science and Technology in Trnava, Slovak Republic

Jiří Náprstek
Institute of Theoretical and Applied Mechanics, Czech Academy of Sciences, Czech Republic

Miloslav Okrouhlík
Institute of Thermomechanics, Czech Academy of Sciences, Czech Republic

Luděk Pešek
Institute of Thermomechanics, Czech Academy of Sciences, Czech Republic

Jindřich Petruška
Brno University of Technology, Faculty of Mechanical Engineering, Czech Republic

Jiří Plešek
Institute of Thermomechanics, Czech Academy of Sciences, Czech Republic

František Pochylý
Brno University of Technology, Faculty of Mechanical Engineering, Czech Republic

Pavel Polach
Research and Testing Institute Plzeň, Czech Republic

Eduard Rohan
University of West Bohemia, Faculty of Applied Sciences, Czech Republic
Josef Rosenberg
University of West Bohemia, Faculty of Applied Sciences, Czech Republic
Milan Růžička
Czech Technical University in Prague, Faculty of Mechanical Engineering, Czech Republic
Milan Sága
University of Žilina, Faculty of Mechanical Engineering, Slovak Republic
Petr Sváček
Czech Technical University in Prague, Faculty of Mechanical Engineering, Czech Republic
Zbyněk Šika
Czech Technical University in Prague, Faculty of Mechanical Engineering, Czech Republic
Michael Valášek
Czech Technical University in Prague, Faculty of Mechanical Engineering, Czech Republic
Jaroslav Zapoměl
VŠB – Technical University of Ostrava, Faculty of Mechanical Engineering, Czech Republic
Vladimír Zeman
University of West Bohemia, Faculty of Applied Sciences, Czech Republic

Table of Contents

COMPUTATIONAL MECHANICS 2018
34th conference with international participation
Srní
October 31 - November 2, 2018

Analysis of metal built-up members

I. Baláž [a], Y. Koleková [b], L. Moroczová [b]

[a] *Department of Metal and Timber Structures, Faculty of Civil Engineering, Slovak University of Technology in Bratislava, Radlinského 11, 810 05 Bratislava, Slovak Republic*
[b] *Department of Structural Mechanics, Faculty of Civil Engineering, Slovak University of Technology in Bratislava, Radlinského 11, 810 05 Bratislava, Slovak Republic*

Battened built-up member. The analysis of the 2nd order with imperfection is used in calculations. The geometrical equivalent global initial sway imperfection is taken according to EN 1993-1-1. The column is made of steel S355. The yield strength f_y = 355 MPa, the safety factors γ_{M0} = 1.0, γ_{M1} = 1.0. The member cross-section is given in Fig. 1.

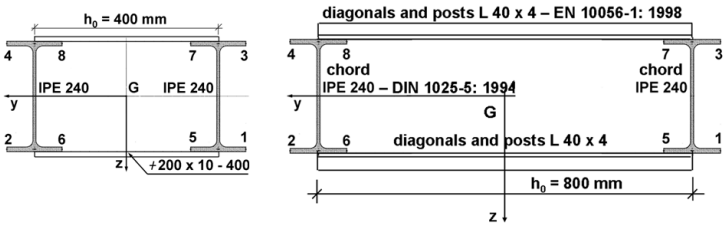

a) battened built-up member b) laced built-up member

Fig. 1. Cross-section of the built-up columns 2 IPE 240 – DIN 1025-5: 1994

The design values of the external actions applied at the column top with the length L = 7.2 m are given in Fig. 2 together with the obtained results of the analytical analysis. The horizontal force $H_{Ed,tot}$ consists of two parts: the external force H_{Ed} = 22 kN and the replacement of the global initial sway imperfection by equivalent horizontal force $N_{Ed}\Phi$ = 850 kN / 268.328 = 3.205 kN.

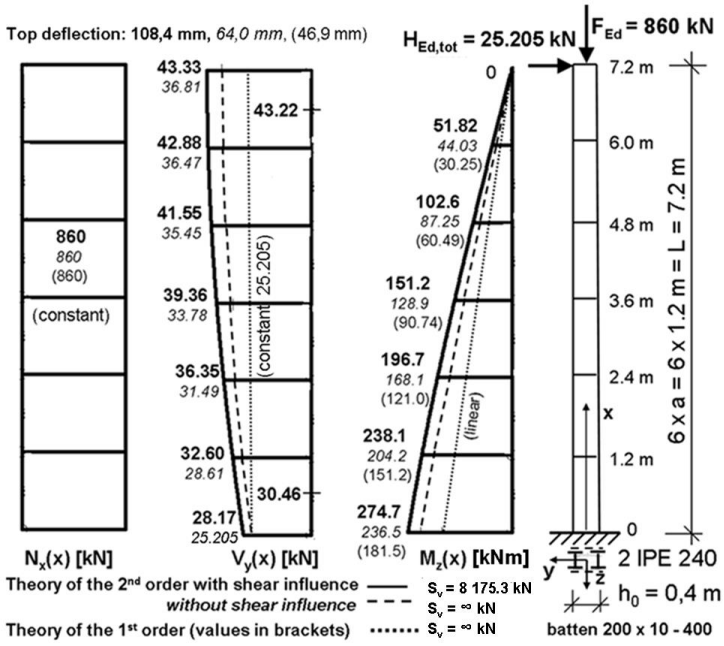

Fig. 2. Column geometry, actions and distributions of the internal forces $N_x(x)$, $V_y(x)$, $M_z(x)$

Laced built-up member. The cross-section is in Fig. 1 b). The design values of the external actions applied at the column top with the length L = 7.2 m are given in Fig. 3 together with the obtained results of the analytical analysis.

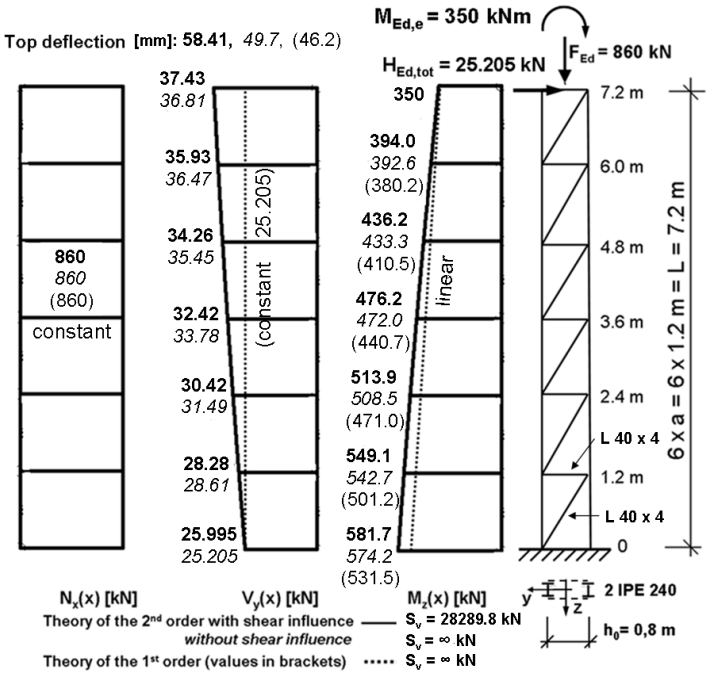

Fig. 3. Column geometry, actions and distributions of the internal forces $N_x(x)$, $V_y(x)$, $M_z(x)$

Conclusions. The most important parameters of the member are: the shear parameter γ, the member parameter ε, the parameter α_{cr} and amplification factor k_{II} ($M_{II} = k_{II} M_I$), see Table 1.

Table 1. Shear parameter γ, member parameter ε, α_c and amplification factor k_{II}. Index V indicates shear effects

Member parameters	Battened built-up member	Laced built-up member
$\gamma = \left[1/\left(1 - N_{Ed}/S_V\right)\right]^{0.5}$	1.118 (1.0 without shear influence)	1.031 (1.0 without shear influence)
$\varepsilon = L\left[\gamma N_{Ed}/\left(EI_{eff}\right)\right]^{0.5}$	0.863	0.418
$\alpha_{cr,V} = N_{cr,V}/N_{Ed}$	3.702 (for $N_{cr,V}$); 2.664 (for $N_{.cr}$)	14.542 (for $N_{cr,V}$); 10.084 (for $N_{.cr}$)
$k_{II,V} \approx \alpha_{cr,V}/\left(\alpha_{cr,V} - 1\right)$	1.370 (for $N_{cr,V}$); 1.601 (for $N_{.cr}$)	1.074 (for $N_{cr,V}$); 1.110 (for $N_{.cr}$)
by calculation: $k_{II,V} = M_{II,V}/M_I$	274.7 / 181.5 = 1.513	581.7 / 531.5 = 1.094

Notes: These parameters give to the designer information about built-up members without doing calculations similar to those in Figs. 2 and 3. More details including analytical solutions and Eurocode EN 1993-1-1 verification conditions may be found in [2, 3]. The comparisons of the results of the analytical solutions given in Figs. 2 and 3 with the results of the computer program IQ 100 [4] shown zero differences. The calculations according to the former Czechoslovak standard STN 73 1401: 1968 are in [1].

Acknowledgements

Project No. 1/0603/17 was supported by the Slovak Grant Agency VEGA.

References

[1] Balaz, I., Agocs, Z., Metal Structures, Part I., ES STU Bratislav, Bratislav, 1994. (in Slovak).
[2] Balaz, I., Kolekova, Y., Moroczova, L., Battened built-up member under compression and bending with one end fixed and the other end free, Proceedings of the 3rd International Conference on ESaT, Tatranské Matliare, 2018, pp. 12-14.
[3] Balaz, I., Kolekova, Y., Moroczova, L., Behaviour of steel laced built-up column, ESaT, Ibidem, 2018.
[4] Rubin, H., Aminbaghai, M., Weier, H., IQ 100, Vollversion Feb. 2010, TU Wien.

COMPUTATIONAL MECHANICS 2018
34th conference with international participation
Srní
October 31 - November 2, 2018

Life of composite bridges

P. Brož [a], D. Dobiáš [b]

[a] *Faculty of Applied Sciences, University of West Bohemia in Pilsen, Univerzitní 8, 306 14 Plzeň, Czech Republic*
[b] *CTU Klokner Institute, Šolínova 7, 166 08 Praha, Czech Republic*

Fatigue life assessment of said bridges can be based on fully probabilistic philosophy. The loading just as response history should be taken into account and a fatigue criterion based on the amplitude interpretation should be used. Design of structures issues from the requirements that a structural system has to fulfill. The part of great importance of this process is reliability assessment of the structure in question. Reliability means the ability of a structure to maintain qualities required in the course of the life-time appointed.

Up to now, the talking points have been solved e.g. in [3], [4] and [1], regarding the computational equipment in [2]. Failure represents a required property loss. It is possible to divide the reliability assessment into two parts. According to the limit state philosophy both loading effects and resistance of structures are investigated. And further we analyze an interaction of these two quantities.

The structure is reliable, if probability is very small, that load effects are greater than resistance of the structure. For reliability assessment it is necessary to consider rheological material properties, geometrical and material imperfections, and degradation factors et cetera. In the subjects of civil and mechanical engineering, fatigue is one of the most important limit state. In the reliability condition, it is possible to compare the state quantity with the limit value, namely by two methods.

The principle of reliability assessment concepts for a structure is indicated in Fig. 1, [2], in version (i) deterministic approaches – allowable stress design; (ii) partial factors design; (iii) fully probabilistic SBRA method.

These reliability evaluations are demonstrated in 2D (*R*, *S*) where *R* means resistance of a structure, *S* load effect, *NB* design point.

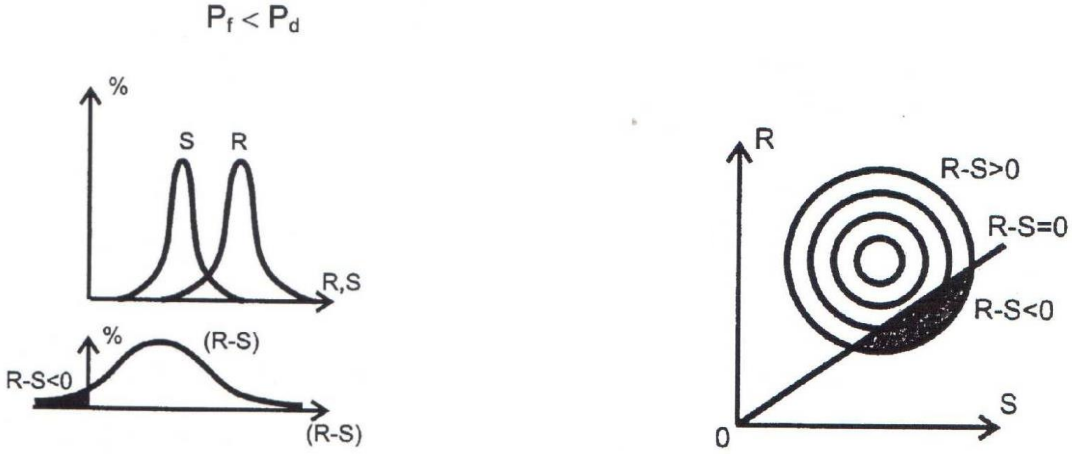

Fig. 1. Reliability assessment outline according to SBRA

Fatigue assessment of a welded detail is involved, embracing the stress spectrum in seven classes. It is considered:

- stress amplitudes in the particular classes with uniform distribution,
- cycle quantities with both normal distribution and coefficient of variation $v\,[n] = 0.05$,
- trilinear life curve with the constant exponents 3 and 5; its variability is determined by standard deviation $s\,[\log N] = 0.18$,
- limiting damage with log – normal distribution, median equal to 1, and coefficient of variation $v\,[D_M] = 0.3$.

Reliability margin is expressed in the form

$$G = D_M - Z = D_M - b_1 D_b$$

and D_M is limiting damage, Z is accumulated damage

$$Z = b_1 D_b ,$$

where b_1 is number of operation weeks, D_b is accumulated fatigue damage / per one week.

In the reliability condition being due to the fatigue limit state, in the treatise, the advantages of simulation methods, above all are analyzed and pointed in an exemplary fashion to, it is possible to apply the empirical distributions – histograms even the truncated random quantities distributions. For the purpose of bridge construction assessment methodology factors of both loading effects and resistance are analyzed in detail.

Acknowledgements

The authors gratefully acknowledge the financial support of the presented research by the University of West Bohemia in Pilsen. This article was prepared with support of the Project SGS – 2016 – 038.

References

[1] Brož, P., Prediction of fatigue life and its probability distribution for structural elements with a notch, Proceedings of the 12nd conference "Spolehlivost konstrukcí", Ostrava, 2011, pp. 47-48. (in Czech)
[2] Marek P., at al., Probabilistic assessment of structures using Monte Carlo simulation, background, exercises, software, ITAM Academy of Sciences of Czech Republic, Prague, Czech Republic.
[3] Rigueiro, C., at al., Life cycle assessment of steel-concrete bridges, ČVUT, Praha, 2018. (in Czech)
[4] Vlk, M., Assessment of fatigue life using the partial coefficient method and the SBRA method, Proceedings of the 6th conference "Spolehlivost konstrukcí", Ostrava, 2005, pp. 194-200. (in Czech)

COMPUTATIONAL MECHANICS 2018
34th conference with international participation
Srní
October 31 - November 2, 2018

Simple flight controller based on FlowPro-Matlab coupling

O. Bublík[a], A. Pecka[b], J. Vimmr[b]

[a] NTIS – New Technologies for the Information Society, Faculty of Applied Sciences, University of West Bohemia, Univerzitní 8, 306 14 Plzeň, Czech Republic

[b] Faculty of Applied Sciences, University of West Bohemia, Univerzitní 8, 306 14 Plzeň, Czech Republic

The aim of this work is the development of an interface between CFD software FlowPro and computing environment Matlab. FlowPro and Matlab coupled with the aid of the interface can be used to simulate complex problems such as fluid-structure interaction (FSI) problems. The fluid dynamics is managed by FlowPro and the structure dynamics is implemented in Matlab. FlowPro is an open-source CFD software based on the discontinuous Galerkin method [1, 2], which has been and is being developed by the authors of this study. FlowPro is capable of simulating complex fluid flow problems including turbulent fluid flow in oscillating blade cascade [3], FSI problems, shape optimalisation problems, etc. The main idea behind FlowPro-Matlab interface is to provide FlowPro, a very powerful CFD software, to Matlab users. In case of FSI simulations, the problem is split into two parts. The calculation of the fluid flow field, mesh deformation and forces acting on the bodies is performed by FlowPro. The solution of rigid body movement equations is left for the user of Matlab. The interface presented in this work manages the data transfer between FlowPro and Matlab.

Java sockets were found to be the most viable solution for the data transfer. The server is implemented in Matlab and the client is integrated in FlowPro. The simulation starts when the user executes the given Matlab script. The script launches the fluid flow simulation in FlowPro automatically. FlowPro performs one time step, computes forces acting on the bodies and sends them back to Matlab. Using these forces, new position of the bodies are established in Matlab. The new position are sent back into FlowPro, where the mesh deformation is computed. This process repeats until the computation is terminated. This type of fluid-structure interaction is known as weak coupling algorithm.

The usage of the developed interface is illustrated on the example of a flight controller of a simple 2D plane model, see Fig.1. The plane model consists of two NACA0012 airfoils of different sizes. The rotation of the smaller airfoil (angle β) is controlled by the PID regulator,

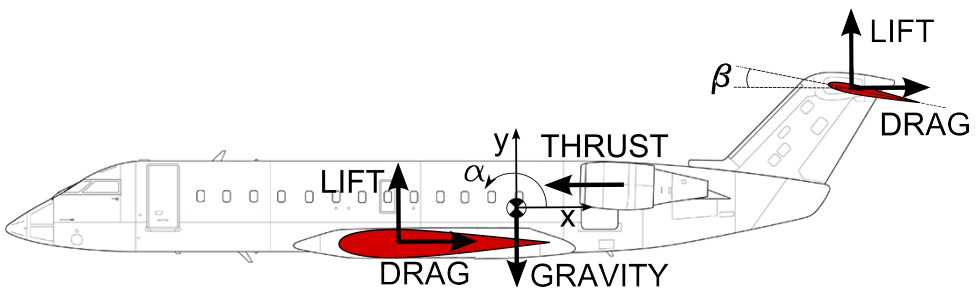

Fig. 1. Simple plane model with highlighted external forces

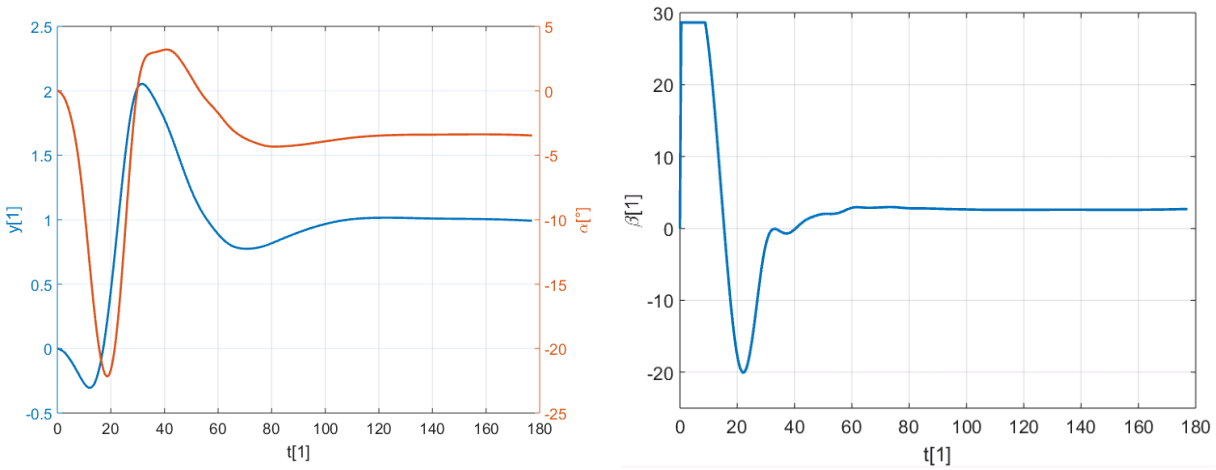

Fig. 2. Altitude y and pitch α of the plane vs. time (*left*); controlled angle β vs. time (*right*)

whose parameters were set empirically. The initial position of plane's gravity center is $x = 0$, $y = 0$ and $\alpha = 0$. The aim of the simulation is to reach the target altitude $y = 1$. The altitude y and pitch α of the plane with respect to dimensionless time are shown on the left-hand side of Fig. 2. The target altitude $y = 1$ is reached at time $t = 100$. The angle β, which is controlled by PID regulator, is shown on the right-hand side of Fig. 2.

The presented example shows that it is possible to use the developed interface for a variety of FSI problems. The advantage of this approach is that it provides a very accurate evaluation of non-linear forces acting on the bodies as opposed to simplified linear expressions, which are typically used.

Acknowledgement

The authors appreciate the kind support by the grant GA 16-04546S "Aero- elastic couplings and dynamic behaviour of rotational periodic bodies" of the Czech Science Foundation.

References

[1] Prausová, H., Bublík, O., Vimmr, J., Luxa, M., Hála, J., Clearance gap flow: Simulations by discontinuous Galerkin method and experiments, EPJ Web of Conferences 92 (2015) 02073, doi: 10.1051/epjconf/20159202073.

[2] Vimmr, J., Bublík, O., Pecka, A., A parallel implementation of an implicit discontinuous Galerkin finite element scheme for fluid flow problems, Advances in Engineering Software 113 (2017) 108-119.

[3] Vimmr, J., Bublík, O., Pecka, A., Pešek, L., Procházka, P., Numerical and experimental study of fluid flow in simplified blade cascade with prescribed harmonic motion, EPJ Web of Conferences 180 (2018) 02116, doi: 10.1051/epjconf/201817002116.

COMPUTATIONAL MECHANICS 2018
34th conference with international participation
Srní
October 31 - November 2, 2018

Aeroelastic analysis of turboprop commuter aircraft with tip-tanks

J. Čečrdle [a], O. Vích [a]

[a] *VZLU – Czech Aerospace Research Centre, Beranových 130, 199 05 Praha - Letňany, Czech Republic*

This paper deals with aeroelastic (flutter) analysis of an aircraft with unconventional wing structure, which is specific by the installation of wing-tip tanks. The subjected aircraft is twin wing-mounted tractor turboprop commuter aircraft for 19 passengers, with a wingspan of 9.6 m and a maximal take-off weight of 7000 kg. The paper is focused on the assessment of specific flutter issue, originating from the unconventional wing configuration. Further, another flutter issues related to elevator flutter and rudder flutter are described.

Aircraft are required to have a reliability certificate including the flutter stability. Flutter analysis must include all mass configurations in terms of fuel or payload, which are applicable at an aircraft operation. These configurations are given from the typical flight profiles. Installation of tip-tanks significantly increases the number of applicable mass configurations. During the flight, the fuel is transmitted from the tip-tanks to the main tank, when enough space becomes available. The amount of fuel in the tip-tanks decreases while the fuel in the main tank increases; however, it must also take into account the fuel consumption because the fuel pumping process takes some time, during which the aircraft is burning fuel. Installation of tip-tanks causes significant variability in characteristics of the wing bending and torsional modes. Fuel load in the tip-tank represent large moment of inertia, even placed at the wing-tip, and therefore, frequencies of wing torsional modes rapidly increase as the wing-tip fuel load decrease. At the same time, frequencies of the wing bending modes are increasing as well; however, the rate of change is considerably lower. As a consequence, the crossing of frequencies of some bending and torsional modes inherently appears with the negative outcome to the wing bending - torsional flutter. This flutter is very sensitive to the wing modal characteristics.

Wing bending – torsional flutter: For the subjected aircraft, the major contributing modes of the mentioned bending - torsional flutter type were 1st symmetric wing torsion and 2nd symmetric wing bending. In addition, Symmetric engine pitch vibration mode was also contributing to this flutter. Considering the maximal flight distance flight profile, frequency of the 1st symmetric wing torsion rapidly increased as long as the tip-tank fuel was decreasing (i.e., during fuel transmission) and remained at the same level for the zero tip-tank fuel. Contrary to that, frequency of the 2nd symmetric wing bending mode increased as long as the wing fuel was decreasing, and remain roughly at the same level during the fuel transmission process. Considering the early-stage computational model, based on the structural parameters, which were set according to the virtual model, there was the frequency crossing of 1st symmetric wing torsion and 2nd symmetric wing bending modes with the consequence in the significant drop in the flutter speed. The lowest flutter speed values were under the certification velocity ($1.2*V_D$) for some mass configurations and for some flight altitudes. Such a case would not be acceptable with respect to the certification rules. After the ground vibration test (GVT) of the aircraft prototype, computational model was updated according to the results of GVT. Such a model, with the relation to the real prototype structure is

considered as more reliable. Considering the updated model, the frequency crossing was eliminated as the frequency of the 1st symmetric wing torsion mode significantly increased. Consequently, flutter speeds got higher and well above the certification threshold. Also, flutter frequencies increased. The certification problem of bending - torsional flutter was therefore eliminated.

Elevator flutter: Elevator of the subjected aircraft was specific due to its large static unbalance (centre of gravity aft a hinge axis). In general, static unbalance makes a structure vulnerable to control surface flutter. In addition, static unbalance has usually negative effect on a dynamic balance with respect to common modes of a surface. Therefore, static unbalance is not generally recommended, but it is acceptable, provided no flutter appearance within the certification envelope is properly justified. Elevator unbalance was adopted from the previous specification of the subjected aircraft. Although, the unbalanced elevator has been already in operation, flutter study was required anyway, at least due to the increase in certification speed of the subjected aircraft compare to the previous specification. Several types of elevator flutter or elevator tab flutter (both symmetric and antisymmetric) were found; each of them was caused by a specific combination of elevator and tailplane modes. Finally, flutter study evidenced no flutter inside the envelope of required stability considering the nominal state and considering the reasonable variation of structural parameters. Thus, unbalanced elevator might have been applied on the subjected aircraft.

Rudder flutter: Vertical tail and rudder of the subjected aircraft was, compare to the previous specification of the aircraft, modified. Modification included increase in span, and increase in rudder horn balance surface in terms of both span and chord. Consequently, rudder mass-balance weights were modified as well. Removable weights to adjust the rudder balance were placed at the leading edge of the horn balance. There was found rudder flutter instability with the combination of rudder flapping and rudder torsional mode. Also, rudder tab flapping mode was contributing to this flutter issue. The key factor was increase in the mass moment of inertia of the upper rudder part due to the increase in mass-balance weight arm. Considering the nominal (statically balanced) rudder, flutter speed was very close to the margin of the required stability, but still above the certification threshold. However, any unbalance of rudder would push the flutter speed below the threshold. Moreover, rudder over-balance by increasing the removable weight placed at the horn balance leading edge had almost no effect on the flutter speed. Therefore, the study of rudder dynamic balance with respect to node lines of appropriate modes was performed. The study evidenced small dynamic effect of the horn balance weight with respect to the flutter major mode. After that, optional placement for the mass-balance weight, which was dynamically effective, was determined. The removable mass-balance weight was moved to this new, rudder bottom-part, position. Over-balance using the new weight placement had significantly stabilising effect. Therefore, the problem of rudder flutter was eliminated.

References

[1] Čečrdle, J., Hlavatý, V., Aeroelastic analysis of light sport aircraft using ground vibration test data, Journal of Aerospace Engineering 229 (12) (2015) 2282-2296.

[2] Čečrdle, J., Maleček, J., Černý, O. Aeroelastic Analysis of Twin Turboprop Utility Aircraft, Proceedings of the Institution of Mechanical Engineers, Part G: Journal of Aerospace Engineering, 225 (5) (2011), 585-594.

[3] Tempelton, H., Massbalancing of Aircraft Control Surfaces, Chapman & Hall Ltd., London, 1954.

COMPUTATIONAL MECHANICS 2018
34th conference with international participation
Srní
October 31 - November 2, 2018

Hydroxyapatite coating influence on performance of bone-implant contact in cranioplasty: Finite element study

J. Chamrad [a], D. Kalasová [b], P. Marcián [a], T. Zikmund [b] and J. Kaiser [b]

[a]*Department of Solid Mechanics, Mechatronics and Biomechanics, Brno University of Technology, Technická 2896/2, 616 69, Brno, Czech Republic*
[b]*CEITEC – Central European Institute of Technology, Brno University of Technology, Purkyňova 123, 612 00 Brno, Czech Republic*

Reliable connection of bone-implant-fixation system, see Fig. 1, is necessary for patients with cranial defects. In case of implant or mini-plate failure, the re-operation is worse than the first operation. It leads to focus on finding the best way of fixation either current procedures or using favourable properties of materials for example using of Hydroxyapatite (HA) coating.

Coating is used in case of improving unsatisfactory properties or performance of a technical material. HA coating increases osseointegration between bone tissue and implant material with coating due to its bioactivity and porosity [2]. It is sprayed by plasma on implant surface, which is in contact with bone. Implant has to be manufactured from material, which can be 3D printed and which can withstand high temperatures (e. g. Titanium alloy – Ti-6Al-4V).

The aim of this study is to analyse mechanical performance of cranial Titanium implant with and HA coating and to compare it with ordinary used implant materials (PMMA, PEEK and Titanium alloy without coating) using computational modelling.

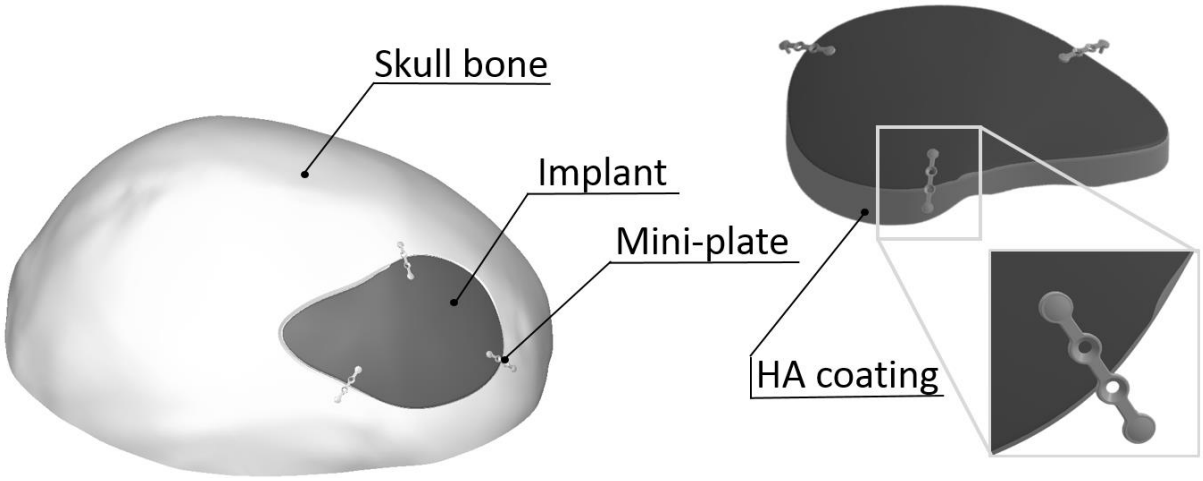

Fig. 1. Cranial bone with implant and fixation mini-plates including HA coating on bone-implant contact (BIC)

Cranial geometry was based on computed tomography (CT) dataset of undamaged skull. The defect was added artificially. Material properties of all components were modelled as homogeneous linear isotropic materials. The only load, applied to the skull and implant, was physiological intracranial pressure (ICP) of value 15 mmHg (2 kPa) [1]. The skull was fixed with fixed support sufficiently far from the implant location. Gradual process of osseointegration was modelled using two different types of contact, bonded and frictional. From the beginning, the BIC was modelled as frictional (friction coefficient was 0.05). Then,

gradually 13 calculations were performed and small parts of coating in the locations of lowest implant displacements changed to contact type bonded (due to HA bioactivity). Number of elements and nodes were approximately 510 000 and 1 530 000 respectively.

Maximum values of total displacements of implant and mini-plates for all analysed implant materials were between 0.055 and 0.070 mm. However, implant with coating did progress due to its bioactivity. In case of 30 % osseointegration BIC, the displacements for implant decreased to 0.010 mm and for the most stressed mini-plate to 0.007 mm.

Similar situation occurred in case of von Mises stress. The maximum values of stresses decreased when the osseointegration ratio on BIC increases, as shown in Fig. 2.

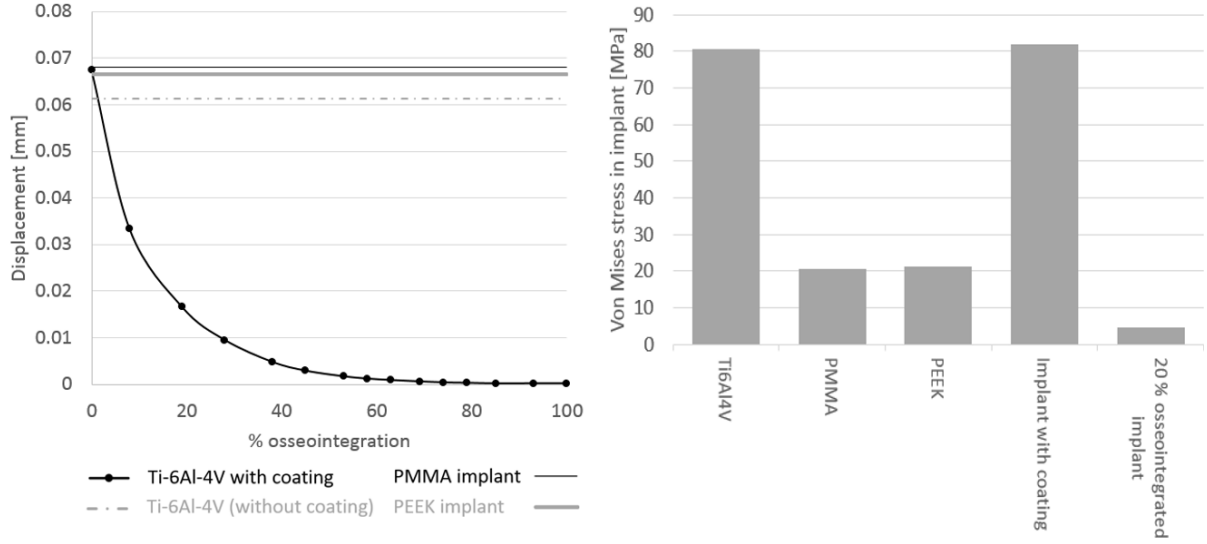

Fig. 2. Comparison of HA coating influence on maximum values of total displacement (left) and von Mises stress of implant to ordinary used biomaterials

In this study, influence of HA coating on cranial implants was investigated. Due to HA bioactivity and based on results from FE analyses, using coating appeared to be beneficial. However, the description of bioactivity has to be investigated more.

Acknowledgement

The work has been supported by the research project FSI/STI-J-18-5337.

References

[1] Czosnyka, M., Pickard, J.D., Onitoring and interpretation of intracranial pressure, Journal of Neurology, Neurosurgery and Psychiatry 75 (6) (2004) 813-821.

[2] Dorozhkin, S.V., Calcium orthophosphate bioceramics, Journal of Biomimetics, Biomaterials and Tissue Engineering 5 (2010) 57-100.

COMPUTATIONAL MECHANICS 2018
34th conference with international participation
Srní
October 31 - November 2, 2018

The study of possibilities towards to extending the hybrid electric vehicle mathematical model by predictive control algorithm

P. Denk [a], Z. Šika [a], P. Steinbauer [a], J. Macek [b], J. Morkus [b]

[a] *Czech Technical University in Prague, Faculty of Mechanical Engineering, Department of Mechanics, Biomechanics and Mechatronics, Technická 4, Praha 6, Czech Republic*
[b] *Czech Technical University in Prague, Faculty of Mechanical Engineering, Department of Automotive, Combustion Engine and Railway Engineering, Technická 4, Praha 6, Czech Republic*

The term of "Hybrid Electric Vehicle (HEV)" represents the vehicle as a general mechanical system which cannot be structurally modified (for example by a different type of engine), but the modification from point of view the driving processes can be done by using a suitable control strategy. The control strategy is a very broad term which consist many control possibilities, many control strategies etc. but it is possible to divide it unequivocally into many different control levels. The introduced control levels can be further subdivided in the two groups with respect to the type of controlled processes. The first mentioned group represents control processes that may be fixed only on the past and present vehicle states (for example the level of electric voltage is controlled by rectifier regulator with respect to the current state of charge). The second group is represented by processes that can be controlled based on the past, present and with look into the future – control with prediction horizon (for example the heating can be switched on before a significant outdoor temperature change, because the vehicle bodywork has some thermal capacity). The special cases of these controlled processes are processes with discrete control strategy, typically for example gear switching, which can be done before the following slope and not in the slope. The other similarly control processes in the group of the same control levels may be considered the problems with vehicle physical bounds, for example maximal engine power, maximal value of the friction forces between tire and road surfaces etc. that may be represented as an bang-bang control problem.

Some of these introduced control problems can be sufficiently implemented directly into the vehicle mathematical model (not into the upper control levels), because the mathematical model at the same time generates a feedback for implemented individual controllers. However the implementation the predictive control processes into common simulation software with directly time flow direction (in-time numerical integration, for example MATLAB-Simulink) is very complicated, because it is not possible to go forward in the time direction and from the physical point of view the vehicle is a general dynamic system. In this meaning, the special cases for mathematical model implementation are also the group of physical bounds, because they can be reached at a define integration time and subsequently the simulation has to be stopped.

The presented problem creates very diverse space for answer the question "How to make it in in-time numerical integration systems?" and with respect to very sundry controls problems. One of the possible answer may be inspired by basic thoughts of the Adaptive Cruise control (ACC) and extended concept named Cooperative Adaptive Cruise Control (CACC) [1, 2]. The basic different between ACC and CACC is the inputs information to the second (controlled) vehicle that is also the main advantage of this concept. The first vehicle in traffic

flow cannot be controlled with some predictive control horizon, because it has not the information about the situation ahead, but with compare to the second (next) vehicle, it has these information previously (in time direction). From the point of view of the second vehicle, the presented information contain many interesting facts, which may be used for its control and provided a predictive view to the future. The second vehicle has at the one moment (integration time) information about the past, current and future route and traffic properties (for example the current set of the traffic light in the next crossroad).

This is the first and most important knowledge for the extending an ordinary in-time mathematical model, but in general, the first and the second vehicle should be the same. The difference between mathematical model the first and the second vehicle can caused transmitting the wrong information. For example if the first vehicle has the automatically gearbox and the second (controlled) vehicle has a manual gearbox, the information about the setting suitable gear ratio is unusable. However, this contradictory concept property may be successfully used for control the specific control problem that is shown above like group of the physical bounds problems. This mentioned control problem group in general strictly restricted possible control interventions and it may caused inappropriately stopping the simulation, but in the same time it finds a location of the potential simulation stop points. The simulation stop is not desirable, so the request for the first vehicle mathematical model for this time is that the vehicle has to be without physical bounds and it may be used for finding the potential simulation stop points. This presented property is the second and the most important knowledge for the extending an ordinary in-time mathematical model.

Both of the possibilities how to extending the HEV mathematical model can be used separately, but the best extending of the HEV mathematical model can be achieved only by a suitable combination of presented approaches. Some of the required vehicle properties may be contradictory so the best solution of this problem is creating more than one “the first vehicle” and create the set of the simplest “the first vehicles” which each of those vehicles will be designed only for specific feature. The set of the simplest first vehicles can be implemented in the original mathematical model with the same integration time. The real simulation start is also the simulation start for set of the first simplest vehicles and with the reasonable time delay starts the second vehicle. The second vehicle has at each time point a big set of information from own future and on the basis of which it can manage its own internal processes. The design of the first vehicles, the value of the reasonable time delay and other mentioned parameters presented in this abstract will be investigated and the introduced extending HEV mathematical model will be developed with respect to this concept.

Acknowledgements

The work has been supported by the grant EU project “ADVICE” (ADvancing user acceptance of general purpose hybridized Vehicles by Improved Cost and Efficiency) number 724095 and the word of thanks bellows also to support program for young researchers and Ph.D. students named Mechatronika a adaptronika 2016 SGS16/208/OHK2/3T/12.

References

[1] Wikipedia, Cooperative Adaptive Cruise Control, https://en.wikipedia.org/wiki/Cooperative_Adaptive_Cruise_Control.

[2] Wikipedia, Autonomous cruise control system, https://en.wikipedia.org/wiki/Autonomous_cruise_control_system.

COMPUTATIONAL MECHANICS 2018
34th conference with international participation
Srní
October 31 - November 2, 2018

Analysis of crack growth in 3D printed plastic wrench

P. Dlhý [a,b], L. Náhlík [a], F. Arbeiter [c], A. Gosch [c], P. Hutař [a]

[a] *Institute of Physics of Materials, Academy of Sciences of Czech Republic, Žižkova 22, 616 62 Brno, Czech Republic*
[b] *European Institute of Technology, Brno University of Technology, Technická 10, 616 00 Brno, Czech Republic*
[c] *Material Science and Testing of Polymers, Montanuniversitaet Leoben, Otto Gloeckel-Straße 2, 8700 Leoben, Austria*

Fused filament fabrication (FFF) is a type of extrusion-based additive manufacturing technique also known as fused deposition modeling (FDM) or 3D-printing. It is possible to use the process of additive manufacturing for manufacturing of prototypes and also the final products [2]. It is widely believed that parts produced by this method have the disadvantage of slightly worse mechanical properties because of consisting of many weld-lines in layers [4]. However, newer studies confirm that this negative effect can be significantly reduced by appropriate choice of welding conditions of the printing process [3]. Mechanical properties like ultimate tensile strength, modulus, etc. of printed parts can then be similar to properties of injection molded [2] or compressed parts [3].

Fracture properties and crack growth kinetics of the 3D-printing material (polylactic acid, PLA) were determined in a series of measurements on CT and SENB specimens (manufactured by FFF) carried out by Arbeiter [1]. Material constants A and m determining the crack kinetics in the Paris-Erdogan region were established: $A = 10^{-3.78}$ and $m = 2.87$. These parameters are necessary for estimating lifetime of the part. In order to verify the validity of the obtained material constants, a study of crack growth in a real mechanical part made of PLA is now in progress. This contribution deals with a simulation of crack growth in a mechanical part (a wrench) manufactured by FFF, as a part of this study. The results of the simulation are compared to an actual experiment and the numerical model is modified to match the behavior of the real part.

The wrench was modelled by FEM. The model is schematically pictured in Fig. 1. The wrench was fitted on a fixed nut via contact elements and a force load was applied by a small cylinder near the free end of the wrench (also via contact elements).

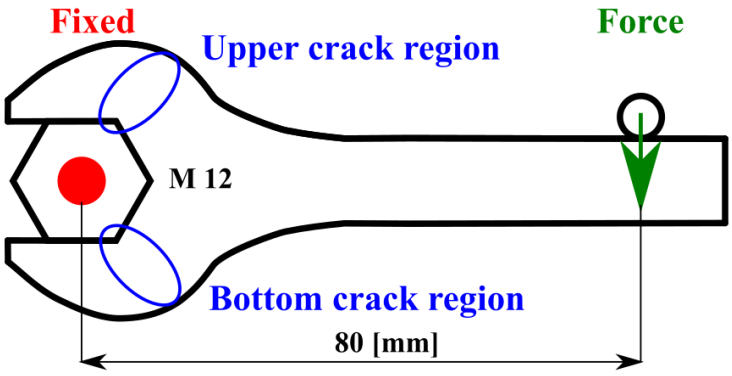

Fig. 1. Schematic figure of simulated wrench model

A 2D contact analysis using plane elements in plane strain condition was carried out. The material model used for the wrench as well as for nut and small cylinder was linear elastic and isotropic. Young's modulus of 3.4 GPa and Poisson's ratio of 0.37 were used for the wrench. Young's modulus of 210 GPa and Poisson's ratio of 0.33 were considered for the nut and the loading cylinder.

First results showed that crack should appear in the area marked as bottom crack region in Fig. 1. However, first experiments showed crack in the upper crack region. It was concluded that this might be happening due to friction between the wrench and the nut. Therefore, study of coefficient of friction between the wrench and the nut was done (the basic Coulomb friction model has been used in the model). It was found that there is a strong dependence of the SIF on the coefficient of friction, as showed in Fig. 2. SIF has been monitored over simulations with different coefficient of friction. SIF at bottom crack tip decreases with raising of coefficient of friction. On the other hand, SIF at upper crack tip has almost the same value over the whole range of studied coefficients of friction. There is only a small decrease between coefficients 0 and 0.2.

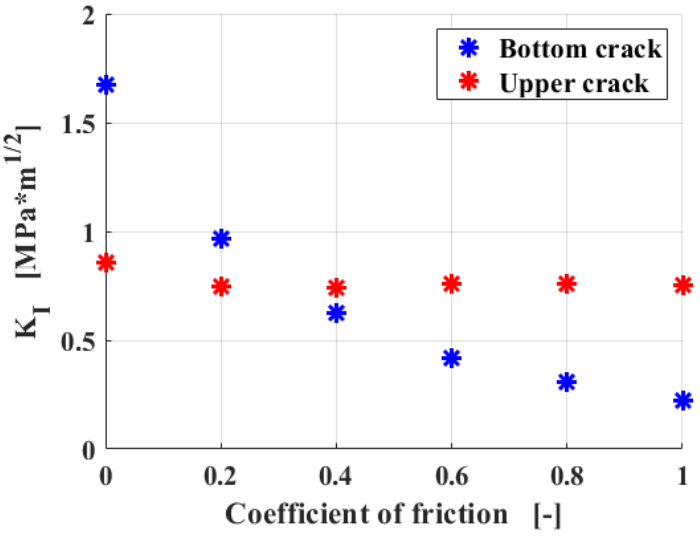

Fig. 2. Stress intensity factor dependence on coefficient of friction, crack length 0.1 [mm], force 7 [N]

This contribution deals with modelling of crack propagation in a wrench manufactured by FFF. First results from simulation and experiments was different. Therefore, there was a study of coefficient of friction to determine the cause of the difference. Results showed strong dependency of SIF on coefficient of friction. In order to validate material constants obtained from test specimens and obtain lifetime for real component, further work is needed to achieve equivalence of the numerical and experimental results.

Acknowledgements

This research has been supported by Polymer Competence Center Leoben GmbH (PCCL, Austria) and the Ministry of Education, Youth and Sports of the Czech Republic under the project m- IPMinfra (CZ.02.1.01/0.0/0.0/16_013/0001823) and the equipment and the base of research infrastructure IPMinfra were used during the research activities.

References

[1] Arbeiter, F., Spoerk, M., Wiener, J., Gosch, A., Pinter, G., Fracture mechanical characterization and lifetime estimation of near-homogeneous components produced by fused filament fabrication, Polymer Testing, 2018, pp. 105-113.

[2] Gibson, I., Rosen, D., Stucker, B., Additive manufacturing technologies, Springer New York, New York, 2015.

[3] Spoerk, M., Arbeiter, F., Cajner, H., Sapkota, J., Holzer, C., Parametric optimization of intra- and inter-layer strengths in parts produced by extrusion-based additive manufacturing of poly (lactic acid), Journal of Applied Polymer Science (2017) 1-15

[4] Ziemian, S., Okwara, M., Ziemian, C.W., Tensile and fatigue behavior of layered acrylonitrile butadiene styrene, Rapid Prototyping Journal (2015) 270-278.

COMPUTATIONAL MECHANICS 2018
34th conference with international participation
Srní
October 31 - November 2, 2018

Modelling of the turbine blade by new finite element

J. Dupal [a], M. Zajíček[a], V. Lukeš [a]

[a] *Faculty of Applied Sciences, University of West Bohemia in Pilsen, Univerzitní 8, 306 14 Plzeň, Czech Republic*

The paper deals with 1D finite element modelling of a turbine blade. The proposed finite element has only 16 degrees of freedom (DOF) and enables to achieve a complex model of turbo-machine with a relatively small DOF number, more details will be described in the article [1]. It is a great advantage but the pre-processing for the blade cross section parameters of the individual blades is a little bit more complicated. This approach means to solve a warping function in chosen cross sections of the blade and simultaneously calculate the geometrical parameters of those cross sections. The second step represents an approximation of the obtained parameters along the axis coordinate ξ by means of spline functions. The next step is gradual computation of local finite element matrices and assemblage of the global blade matrices.

The velocity of infinitesimal mass point is taken into account as a sum of cross section shear stress center *S* velocity corresponding to the translation motion and the secondary velocity from spherical motion with center in point *S*. Moreover, the axial motion of arbitrary point is affected by warping of the cross section caused by torsion deformation.

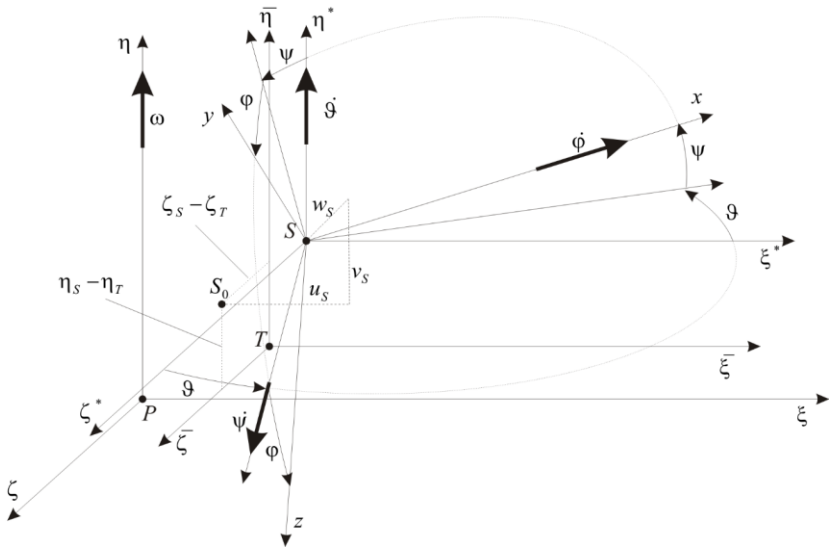

Fig. 1. Used coordinate systems

Having determined the displacements and velocities of the arbitrary cross section point according to Fig. 1 we can come to the relations for kinetic and potential energy of the blade finite element. Using e.g. Lagrange's equations it is possible to determine matrices of blade finite element. After assembly of all elements the whole blade equation of motion can be written in form

$$\mathbf{M}\,\ddot{\mathbf{q}}(t) + \omega\,\mathbf{G}\,\dot{\mathbf{q}}(t) + \left(\mathbf{K} - \omega^2\mathbf{M}_D - \omega^2\mathbf{M}_M\right)\mathbf{q}(t) = \mathbf{f}_Z(t) + \mathbf{f}_D\,., \tag{1}$$

where **M** is mass matrix, **G** is matrix of gyroscopic forces, **K** is stiffness matrix, $\omega^2 \mathbf{M}_M$ is membrane forces matrix, $\omega^2 \mathbf{M}_D$ is circulation matrix, $\mathbf{f}_Z(t)$ is vector of external forces and $\mathbf{f}_D$ is constant vector of centrifugal forces. The presented methodology was validated on one blade modelled by 3D elements and by the presented finite 1D blade elements. Comparison of the first two mode shapes obtained by the use of both approaches is shown in Fig. 2.

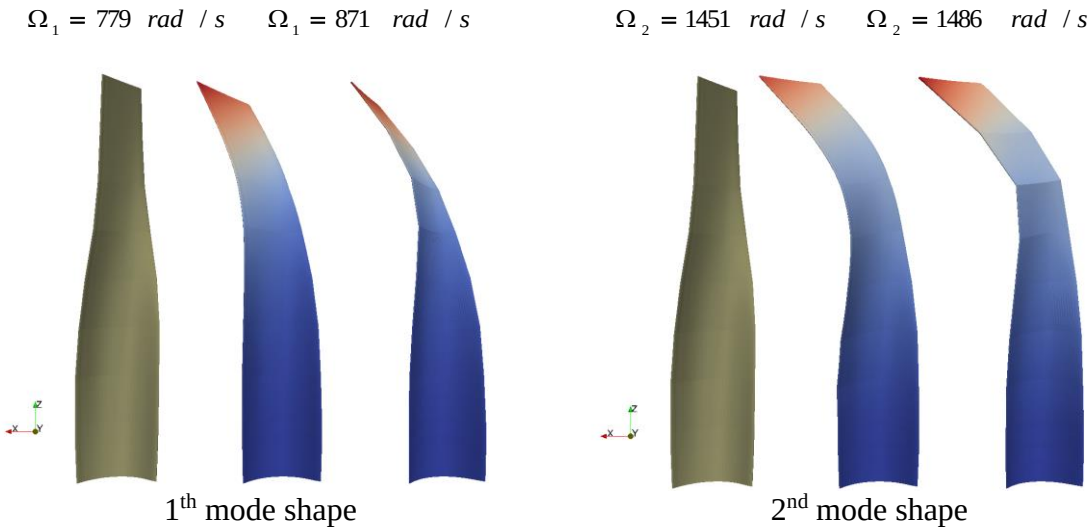

Fig. 2. Comparison of the mode shapes calculated using 3D and 1D approach

The model using presented finite element is described only by 154 DOF and 19 finite 1D blade elements. From the other side the model consisting of 3D elements has about 4.10^5 DOF. The modal analysis was performed for $\omega = 0\ rad/s$. As we can see the presented methodology means the great save of time and the capacity of computer for blade system analysis.

Acknowledgements

This publication was supported by the project TE 01020068 of the Technology Agency of the Czech Republic and by the project GA16-04546S.

References

[1] Dupal, J., Zajicek, M., Lukes, V., 1D finite element for modelling of turbine blade vibration in the field of centrifugal forces, Applied and Computational Mechanics (2018) 1-17. (under review)

COMPUTATIONAL MECHANICS 2018
34th conference with international participation
Srní
October 31 - November 2, 2018

Influence of friction force description on fretting wear considering stick-slip phenomenon

Š. Dyk[a]

[a] *NTIS – New Technologies for the Information Society, Faculty of Applied Sciences, University of West Bohemia, Technická 8, 301 00 Pilsen, Czech Republic*

Various friction models were formulated [3, 4] to describe such a complex and naturally non-smooth phenomenon. Generally, there are two categories of these models – *static* and *dynamic*. Static models describe friction phenomenon via friction characteristics governing the dependence of friction force on the relative velocity in the contact point. The basic Coulomb model is commonly implemented using its approximations by smooth functions (arctan, tanh) and a modified version of the model incorporating Stribeck effect is also widely used to describe different values of static and dynamic friction. The dynamic models are usually based on the bristle-analogy. In the contact surface, fictive deformable bristles are considered. From the mathematical point of view, dynamic models add one or more extra ordinary differential equation describing an average deflection of the bristles in the contact surface. These additional differential equations are solved together with the equations of motion. One of the basic dynamic models are Dahl [3] or LuGre [2] models, nevertheless there are even more sophisticated models such as elasto-plastic model, stick-slip model, Gonthier model etc [4]. The choice of friction force plays important role during the simulations of various mechanical problems.

Fretting wear is a phenomenon that occurs during the relative vibration (in tangential direction) of two surfaces which are at the same time under the load (in normal direction). Due to the presence of friction, undesirable loss of the mass in contact sufrace occurs. In the field of numerical simulations of such a phenomena, a choice of the model of friction force is of crucial importance.

The presented research is motivated by the numerical simulations of fuel rods vibration in the nuclar power plants. The fuel rods are grouped together in fuel assemblies and they are linked by spacer grids with radial prestress. During the vibration of flexible fuel rods and their bending in the prestressed spacer grid cells, fretting wear can be experienced. It can possibly lead to undesirable leakage of fission product to coolant of primary circuit. In all of the former models [1, 5], complex models of fuel rods have been developed and one of the most general static models of friction was implemented. However, in this models the stick-slip phenomenon is described only in the first approximation. The aim of this contribution is the analysis of the description of stick-slip transitions and their influence on fretting wear in the contact surface.

Simple single DoF benchmark model [4] (see Fig. 1) was used to reach stick-slip vibration. The body of mass m is attached to the frame by the spring with stiffness k. The mass lays on the belt which moves with constant velocity v_b. The mathematical model can be written in the compact form for both static and dynamic models of friction forces F_f

$$m\ddot{x}(t) + kx(t) = \begin{cases} F_f(v_{rel}(t)) & \text{for static models,} \\ F_f(v_{rel}(t), z(t), \dot{z}(t)) & \text{for single-state-variable dynamic models,} \end{cases}$$

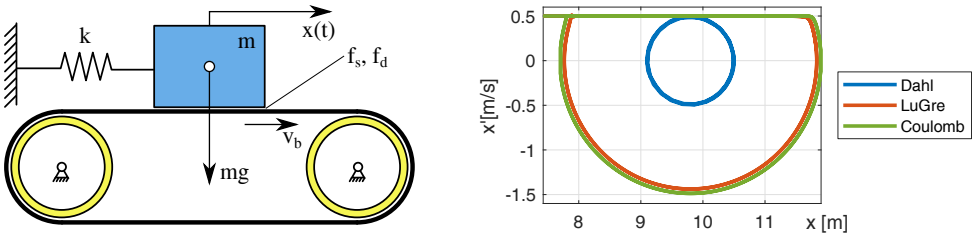

Fig. 1. Scheme of the considered system and an example of phase trajectories

where the static models depend only on the relative velocity in the contact surface $v_{rel} = v_b - \dot{x}$ and dynamic models have an additional dependency on state variable z and $\dot{z}$. In all of the analyses, smoothed Coulomb model with Striebeck effect is considered as a representative of static friction models and Dahl and LuGre models are used as a representatives of dynamic friction models. To estimate the fretting wear in contact surfaces, approach based on the work of the friction forces is used [1, 5]. For the illustration, examples of resulting friction forces are shown in Fig. 2. The comparison of resulting fretting wear values is provided considering variation of the key parameters of the system. The effect of an accurate description of stick-slip transitions is evaluated with respect to the hourly fretting wear introduced in [5].

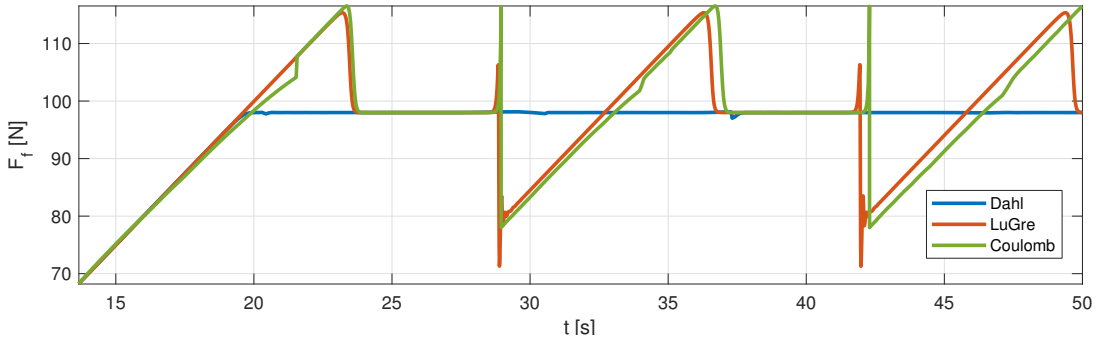

Fig. 2. Comparison of the friction forces in the contact surface

Acknowledgements

This publication was supported by the project LO1506 of the Czech Ministry of Education, Youth and Sports under the program NPU I and by the Motivation system of the University of West Bohemia – Part POSTDOC.

References

[1] Dyk, Š., Zeman, V., Evolution of grid-to-rod fretting of nuclear fuel rods during burnup, Progress in Nuclear Energy 108 (2018) 160-168.

[2] de Wit, C.C., Olsson, H., Astrom, K.J., Lischinsky, P., A new model for control of systems with friction, IEEE Transactions on Automatic Control 40(3) (1995) 419-425.

[3] Marques, F., Flores, P., Pimenta Claro, J.C., Lankarani, H.M., A survey and comparison of several friction force models for dynamic analysis of multibody mechanical systems, Nonlinear dynamics 86 (2016) 1407-1443.

[4] Pennestri, E., Rossi, V., Salvini, P., Valentini, P.P., Review and comparison of dry friction force models, Nonlinear dynamics 83 (2016) 1785-1801.

[5] Zeman, V., Dyk, Š., Hlaváč, Z., Mathematical modelling of nonlinear vibration and fretting wear of the nuclear fuel rods, Archive of Applied Mechanics 86(4) (2016) 657-668.

COMPUTATIONAL MECHANICS 2018
34th conference with international participation
Srní
October 31 - November 2, 2018

Coordinate-free formulation of the cutting process

J. Falta[a], M. Sulitka[a]

[a] RCMT, Faculty of Mechanical Engineering, CTU in Prague, Horská 3, 128 00 Prague 2, Czech Republic

Machining processes are invaluable in many industrial branches. Calculation of the cutting forces is important for quality prediction of the machined surface. The cutting forces are usually expressed and manipulated in a certain coordinate system. So long the geometry of the cutting process is simple, the approach works well, however dynamics of more general operations like 5-axis milling are often difficult to describe without some additional simplifications.

The total cutting force is a result of the pressure/friction fields acting on the tool-workpiece contact. For practical purposes, empirical expressions for the specific cutting force acting on an 1-D element of cutting edge are used—specific force $\mathbf{f}$ per unit chip width is introduced. It depends on local cutting process parameters like for instance the undeformed chip width h, the inclination angle λ or the rake angle α. The basis for the specific force is bound to the cutting edge geometry and its motion - tangential direction given by the cutting velocity $\boldsymbol{t}$, the normal direction by a normal $\boldsymbol{n}$ to the surface created by the cutting edge in space. The third basis vector $\boldsymbol{b}$ is perpendicular to both $\boldsymbol{t}$ and $\boldsymbol{n}$, see Fig. 1a.

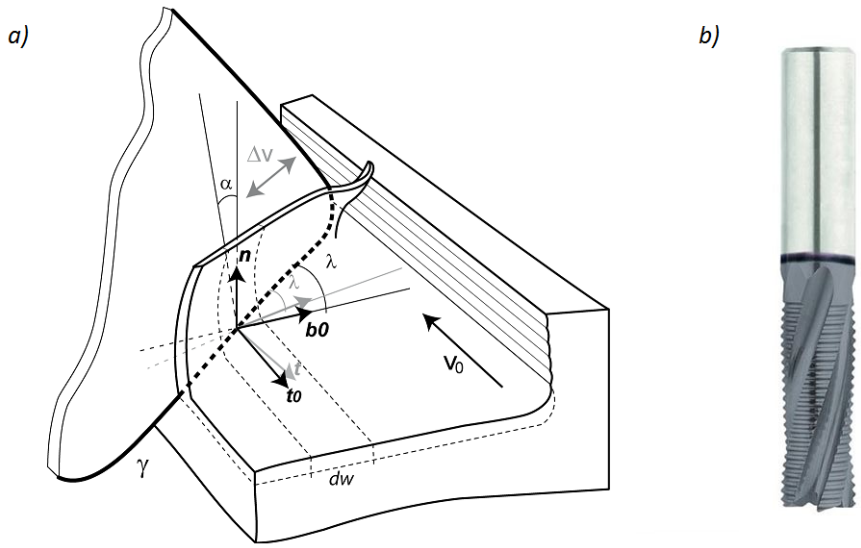

Fig. 1. a) Local force basis on the cutting edge element, b) serrated milling tool

The total cutting force is calculated as an integral over the cutting edges in contact with the workpiece

$$\boldsymbol{F} = \int_{\gamma} \mathbf{1}_S \, [\boldsymbol{t}\ \boldsymbol{n}\ \boldsymbol{b}] \, \mathbf{f}(h, \lambda, \alpha) dw \,,$$

where $\mathbf{1}_S$ is a characteristic function which is 1 if the element is in the engagement area S and 0 otherwise.

Probably the most important property of the tool-workpiece dynamic is its stability. Its calculation requires knowledge of the systems reaction to a small variation of the system's kinematics due to small vibrations. The first step of the coordinate free approach are definitions of all necessary cutting process parameters and basis vectors with respect to a chosen set of vector functions describing the unperturbed kinematics of the system and the geometry of the tool, e.g. axis of spindle rotation, feed direction, curves describing cutting edges. The characteristic function needs to be defined through coordinate free scalar constraints, e.g. non-negative chip thickness. In the second step variation of the total force with respect to a small perturbation of the kinematics is calculated. Virtually all the functions in the integrand may be affected by the perturbation.

The contribution of the characteristic function $\mathbf{1}_S$ to the cutting force differential requires application of Leibniz integral rule and implicit function theorem. A special case of this effect was studied by Eynian as an influence of tool tip radius on stability [3].

The transformation matrix $[\boldsymbol{t}\ \boldsymbol{n}\ \boldsymbol{b}]$ and the technological angles are affected by perturbation of tool/workpiece relative velocity direction. These effects were studied on 2-D tool geometries by Das and Tobias in 1967 [1]. They are rarely taken into account in the models of machining dynamics (recent exception being Molnar's article about process damping [4]).

The specific force is affected by the perturbation via the technological angles and the undeformed chip thickness h, which depends not only on perturbation of the actual position but on a past perturbation that deformed the new surface in the previous cut. This so called regenerative effect was discovered by Tlustý and Poláček in the early 1950s [5].

The resulting formula for the perturbed cutting force is too long to be presented here. The advantage of the coordinate free approach is that it allows formulation of the machining stability generally without limitation on the type of the cutting process or direction of the perturbation.

Another application of the coordinate free approach is calculation of more general undeformed chip thickness formula. It can be shown that the commonly used formula based on tool envelope normal and tool-workpiece displacement does not hold for serrated milling tools, see Fig. 1b. It means that the current analyses of machining stability for various serration are based on an incorrect model, e.g., Dombovari [2].

Acknowledgement

This work was supported by the Grant Agency of the Czech Technical University in Prague, grant No. SGS16/220/OHK2/3T/12.

References

[1] Das, M.K., Tobias, S.A., The relation between the static and the dynamic cutting of metals, International Journal of Machine Tool Design and Research 7 (2) (1967) 63-89.

[2] Dombovari, Z., Munoa, J., Stepan, G.,General milling stability model for cylindrical tools, Procedia CIRP 4 (2012) 90-97.

[3] Eynian, M., Altintas, Y., Chatter stability of turning and milling with process damping, Journal of Manufacturing Science and Engineering 131 (4) (2009) 041005, doi: 10.1115/1.3159047.

[4] Molnár, T.G., Insperger, T., Bachrathy, D. et al., Extension of process damping to milling with low radial immersion, The International Journal of Advanced Manufacturing Technology 89 (9-12) (2017) 2545-2556.

[5] Tlustý, J., Špaček L., Self-excited vibrations in machine tools, Nakladatelství CSAV, Prague, 1954. (in Czech)

COMPUTATIONAL MECHANICS 2018
34th conference with international participation
Srní
October 31 - November 2, 2018

Estimation of Lyapunov exponents of discrete data series

C. Fischer[a], J. Náprstek[a]

[a] *Institute of Theoretical and Applied Mechanics, CAS v.v.i., Prosecká 76, CZ-190 00 Praha, Czech Republic*

The dynamical systems describing general non-linear structures represent an interesting and demanding topic in various branches of engineering. This regards the both cases of mathematical and experimental models or an analysis of results from measurements in situ. In case of a complex behaviour of a structure or a non-linear mathematical model, the measured response or computed data series can exhibit wide range of response types, from stationary and periodic to diverging or chaotic behaviour. The stability in the sense of sensitivity to small perturbations, however, is the key property of each type of the system response.

The concept of Lyapunov exponents (LE) is the most usable and most robust stability measure, despite of numerous new methods and modifications. However, practical estimation of LE for both continuous systems and discrete data is still a demanding task. Even if the topic was addressed by numerous papers in the past it seems that the practical usage of recommended methods usually raise additional questions. It is natural because the theoretical results are mostly substantiated by an limiting relation, assumptions of which are hardly fulfilled in the practice.

The case of continuous systems is often dealt in the literature. As an interestin review can serve, e.g., paper [4]. A very promising approach for continuous systems is presented by Dieci et al. in [1]. On the other hand, the literature is meagre when it regards the case of discrete data set. The present contribution extends the previous work of the authors [2] and aims at presenting, comparison and analysis of two approaches derived specifically for the case when the dynamical system is represented only as a discrete data series (procedures due to Wolf et al. [6] and Rosenstein et al. [5]) and a possible extension of the mentioned algorithm due Dieci et al. [1] to certain discrete cases.

Let us consider the continuous dynamical system

$$\dot{x}(t) = f(x,t)\,, \qquad x(0) = x_0\,. \tag{1}$$

Stability of its solution $\tilde{x}_{x0}$ can be deduced from increasing separation of two nearby orbits, initial distance of which is δ_0 in $t = 0$:

$$\delta(t) = \tilde{x}_{x0}(t) - \tilde{x}_{x0+\delta_0}(t).$$

The commonly used estimates of LE fall into two main categories. The first uses a heuristic approach based on the relation

$$||\delta(t)|| = \mathrm{e}^{\lambda_1 t}||\delta(0)||. \tag{2}$$

Although usage this approach is not limited to the cases where only the discrete data are available, this methods are used mostly in such case. The second group, on the other hand, is based on so called variational equation

$$\mathbf{P}'(t) = A(x,t)\mathbf{P}(t)\,, \qquad \mathbf{P}(0) = \mathbf{I}\,, \tag{3}$$

where $\mathbf{P}(t)$ is the derivative of $\tilde{x}_{x0}$ with respect to initial condition x_0. Since this approach is based on the explicit knowledge of Jacobian $A(\tilde{x}, t)$, it is naturally aimed at analysis of continuous systems.

The popular algorithm belonging to the first group is the implementation which accompanies paper due to Wolf et al. [6]. The algorithm follows the nature of the problem: It is based on identification of close points on the orbit. Such points are considered as close or perturbed initial conditions and separation of corresponding orbital sections is measured. The largest LE λ_1 is computed from the growth of distance of both orbits. When the separation becomes large, a new trajectory is chosen near the reference trajectory considering close distance and direction.

The more recent procedure described by Rosenstein et al. [5] is similarly based on identifying different yet similar sections in the data series, which are used subsequently to simulate separation of close orbits. Result of the procedure is returned as dependence of the averaged distance of two orbits on the increasing time lag to initial "close" point. The distance should increase linearly in the logarithmic scale up to size of the attractor. The slope of the linear ramp then represents an estimate of the largest LE.

The weak point of the Rosenstein's approach is identification of the determinative part of the resulting dependence which is used for estimation of the average slope, see description in [2]. The authors successfully used a simple detection of the "corner sample" based on the horizontal direction of the upper plateau. A number of alternative approaches could be proposed, however, they mostly require some ad hoc intervention.

The main problem in algorithms based on the variational equation and belonging to the second group is that the auxiliary matrix $\mathbf{P}(t)$ has to be kept orthogonal. This requirement implies necessity of reorthogonalization in every iteration step. The work presented by Dieci et al. [1] is based on keeping the system $\mathbf{P}(t)$ in triangular form using the time-dependent orthogonal discrete or continuous QR transformation. Usage of this procedure claims certain prerequisites to the discrete data representing the dynamical system. Namely, the data set has to be capable of continuous interpolation.

Numerical experiments with the mentioned algorithms show that in the case of discrete data, namely those obtained experimentally, the functionality of all available approaches is limited and closely reflects quality of the data.

Acknowledgement

The kind support of the Czech Science Foundation project No. 17-26353J and of the RVO 68378297 institutional support are gratefully acknowledged.

References

[1] Dieci, L., Jolly, M.S., Van Vleck, E. S., Numerical techniques for approximating Lyapunov exponents and their implementation, Journal of Computational and Nonlinear Dynamics 6 (2011) 011003, doi: 10.1115/1.4002088.

[2] Fischer, C., Náprstek, J., Lyapunov exponents — practical computation, Proceedings of the conference Engineering Mechanics 2017, Svratka, 2017, pp. 310-313.

[3] Fischer, C., Náprstek, J., Numerical assessment of stability of the ball vibration absorber, Proceedings of the conference Computatinal Mechanics 2017, Špičák, 2017, pp. 23-24.

[4] Ramasubramanian, K., Sriram, M.S., A comparative study of computation of Lyapunov spectra with different algorithms, Physica D: Nonlinear Phenomena 139 (1) (2000) 72-86.

[5] Rosenstein, M.T., Collins, J.J., De Luca, C.J., A practical method for calculating largest Lyapunov exponents from small data sets, Physica D: Nonlinear Phenomena 65 (1-2) (1993) 117-134.

[6] Wolf, A., Swift, J.B., Swinney, H.L., Vastano, J.A., Determining Lyapunov exponents from a time series, Physica D: Nonlinear Phenomena 16 (3) (1985) 285-317.

COMPUTATIONAL MECHANICS 2018
34th conference with international participation
Srní
October 31 - November 2, 2018

Numerical simulation of non-stationary flows in water jet cutting nozzles

J. Fürst[a], T. Krátký[b], Z. Říha[c]

[a] Faculty of Mechanical Engineering, Czech Technical University in Prague, Karlovo nám. 13, 121 35 Praha, Czech Republic
[b] Hydraulic Research Centre, Ltd., Jan Sigmunda 313, 783 49 Lutín, Czech Republic
[c] Institute of Geonics of the CAS, Drobného 28, 602 00 Brno, Czech Republic

The use of a high-speed water jet is one of the modern technologies for cutting and machining the material. High efficiency can be achieved by either by increasing the operating pressure or by using a non-stationary mode created by an ultrasonic generator. The use of ultra-high pressures in continuous mode induces extreme loading to high pressure parts of the cutting machine. The alternative approach using pulsating jets from an ultrasonic generator can increase the efficiency of the cutting without the need of such high water pressures. The impact of droplets of the pulsating jet generates much higher impact pressure than the stagnation pressure generated by the action of continuous jet. The efficiency of the cutting is further increased by cyclic loading of the target as well as by large shear stresses generated by the jet, see [1].

The efficiency of the pulsating jet cutting is highly influenced by the amplification of the pressure oscillations created by the ultrasonic generator in the properly shaped domain. The higher amplification is obtained in the case of resonance in the high-pressure system. The propagation and amplification of these pulsations were previously studied using analytical and numerical models for the case of single nozzle systems (see, e.g., [1] or [2]).

The current article deals with the numerical simulation of the pulsating flows in the high pressure part of a cutting system with five nozzles. The final aim of the work is the shape optimization of the system in order to achieve high amplification of the pressure waves and hence the high amplitudes of jet velocities. First of all two numerical models are cross compared for the case of reference geometry (see Fig. 1).

The first model assumes compressible liquid with the water density and sound speed given by

$$\rho = C - \frac{1}{k^2\Delta p + kq}, \tag{1}$$

$$a = k\Delta p + q, \tag{2}$$

where $C = 1402.4\,\mathrm{kg/m^3}$, $k = 1.669 \times 10^{-6}\,\mathrm{m^2s/kg}$, $q = 1481.98\,\mathrm{m/s}$ and $\Delta p = p - 101\,325\,\mathrm{Pa}$. The model is based on the solution of Reynolds-averaged Navier-Stokes equations with an additional two-equation RNG $k-\epsilon$ turbulence model with non-equilibrium wall functions. The ultrasonic generator is modeled using moving mesh strategy as an oscillating wall with the frequency $f = 20\,\mathrm{kHz}$ and amplitude $A = 6 \times 10^{-6}\,\mathrm{m}$. The spatial discretization is achieved with the finite volume approach with a second order interpolations and the temporal derivatives are discretized by a first or second order implicit scheme. The model is the ANSYS Fluent package.

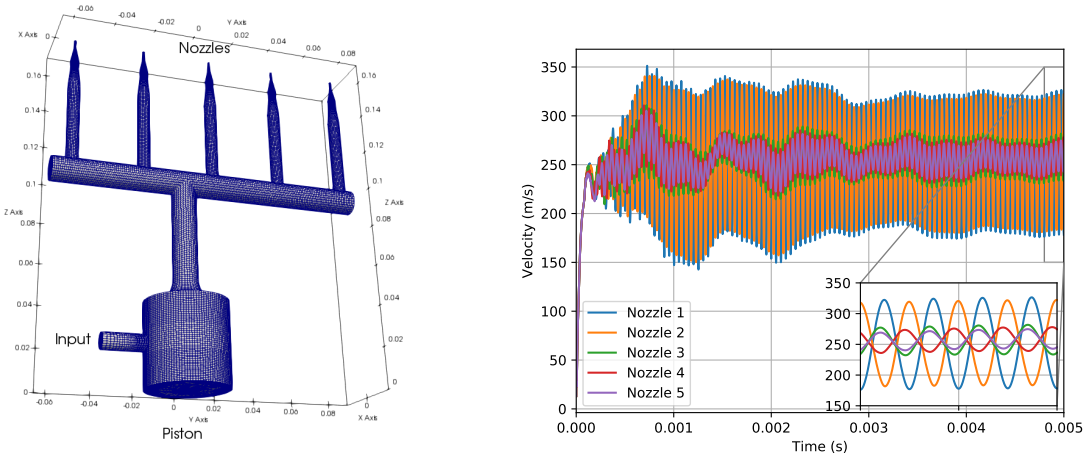

Fig. 1. Geometry of the cutting nozzle system and the maximal velocities in the nozzle throats

The second model uses simplified approach without turbulence model and modeling the ultrasonic generator with fixed grid prescribing the fluid velocity at the piston head as $v(t) = 2\pi f A \cos(2\pi f t)$. The density is given by linearized equation of state

$$\rho = \frac{p}{a^2} + \rho_0 \tag{3}$$

with $\rho_0 = 997.95\,\text{kg/m3}$ and $a = 1484.8\,\text{m/s}$. The relative difference of the density (3) and (1) is less than 1×10^{-6} for pressures in the range $0\,\text{MPa}$ to $35\,\text{MPa}$.

Both models predicts similar amplitudes of the velocity in the nozzles, however the second one requires less computational time than the first one.

An optimization was carried out with the first model using the objective function $J = \sum_{i=1}^{5}(\max w_i - \min w_i)/5$ (here w_i is the z-component of the velocity in the nozzle, maximum and minimum is taken over last few pulses). The achieved amplitudes are in the order of $120\,\text{m/s}$, whis is roughly $50\,\%$ of the average speed in the nozzles. Similar results were obtained also with the second model using objective function based on the amplitudes of pulses in the mass flux rate.

Acknowledgement

This work was supported by The Ministry of Education, Youth and Sports from the Large Infrastructures for Research, Experimental Development and Innovations project "IT4Innovations National Supercomputing Center - LM2015070".

References

[1] Foldyna, J., Use of acoustic waves for pulsating water jet generation. In: M.G. Beghi (ed.), Acoustic waves – From microdevices to helioseismology, InTech Europe, 2011.

[2] Říha, Z., Foldyna, J., Ultrasonic pulsation of pressure in a water jet cutting tool, Tehnički vjesnik 19 (3) (2012) 487-491. Available from: https://hrcak.srce.hr/86719

COMPUTATIONAL MECHANICS 2018
34th conference with international participation
Srní
October 31 - November 2, 2018

On the FE modelling of vocal folds pathologies

P. Hájek[a], P. Švancara[a,b], J. Horáček[b], J. G. Švec[c]

[a] *Institute of Solid Mechanics, Mechatronics and Biomechanics, Brno University of Technology, Technická 2896/2, 616 69 Brno, Czech Republic*
[b] *Institute of Thermomechanics of the Czech Academy of Sciences, Dolejškova 1402/5, 182 00 Prague, Czech Republic*
[c] *Department of Biophysics, Palacky University Olomouc, 17. listopadu 12, 771 46 Olomouc, Czech Republic*

Numerical modelling of some vocal folds (VF) pathologies can be realized by varying properties of VF layers. The aim of this paper is to show how damping of superficial lamina propria (SLP) affects vowel production in the finite element (FE) model of the VF self-sustained oscillation with fluid-structure-acoustic interaction.

Fluid flow and structure domain was solved separately in program system ANSYS. The 2D FE model features several phenomena present during human phonation: compressible unsteady viscous flow modelled by Navier-Stokes equations, setting to a pre-phonatory position, large deformations of the VF, their closure and excitation by lung pressure. The fluid mesh was deformed according to the VF motion using Arbitrary Lagrangian-Eulerian algorithm.

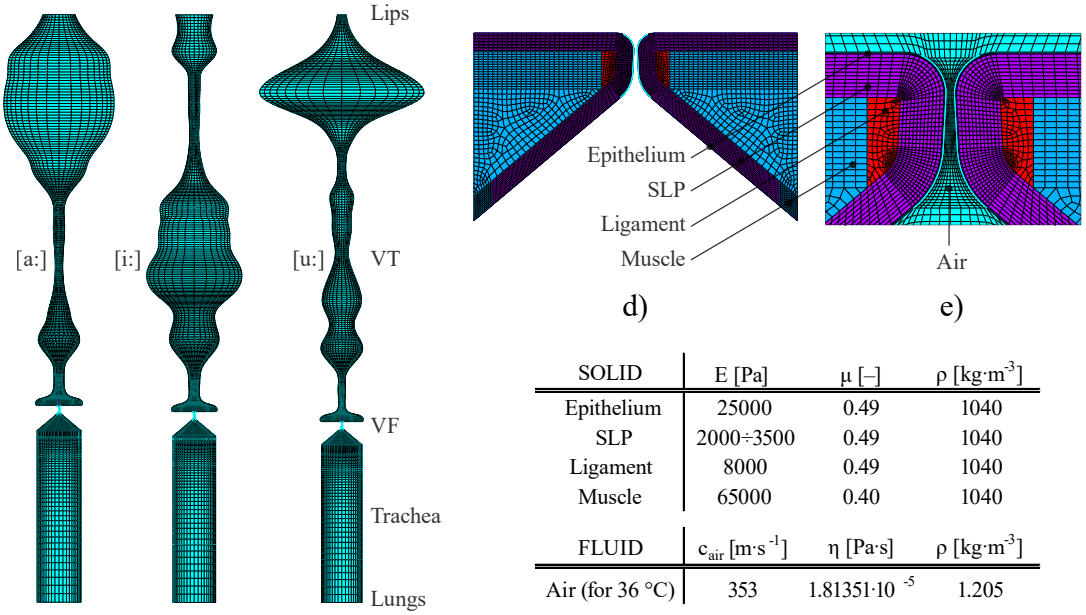

SOLID	E [Pa]	μ [–]	ρ [kg·m^{-3}]
Epithelium	25000	0.49	1040
SLP	2000÷3500	0.49	1040
Ligament	8000	0.49	1040
Muscle	65000	0.40	1040

FLUID	c_{air} [m·s^{-1}]	η [Pa·s]	ρ [kg·m^{-3}]
Air (for 36 °C)	353	$1.81351 \cdot 10^{-5}$	1.205

f)

Fig. 1. a) Fluid FE model of the acoustic spaces of the trachea and the vocal tract (VT) for the Czech vowel [a:], b) vowel [i:], c) vowel [u:], d) solid FE model of the four-layered tissue of the VF with e) detail of glottal gap, f) material properties [1]

The FE model was adjusted for using vocal tracts (VT) shaped for three Czech vowels [a:], [i:] and [u:] the geometry of which was obtained from magnetic resonance imaging (MRI) [2]. The VF model used M5 geometry [3] and was composed of four layers. The material properties are given in Fig. 1, for details see [1].

Several variants for four pairs of proportional damping coefficients and four Youngs moduli E_{SLP} of the SLP layer were computed, see Table 1. Using the following equation

$$\beta = \frac{b_{p2} - \frac{f_1}{f_2} b_{p1}}{\pi \cdot \left(f_2 - \frac{f_1^2}{f_2} \right)}, \qquad \alpha = 4\pi^2 f_1 \cdot \left(\frac{b_{p1}}{\pi} - f_1 \cdot \beta \right), \tag{1}$$

where f_1 and f_2 are natural frequencies of the VF, we obtain proportional damping coefficients α and β for arranged pairs of damping ratios b_{p1} and b_{p2}: $(0.05; 0.1)$, $(0.1; 0.2)$, $(0.2; 0.3)$ and $(0.3; 0.4)$.

Table 1 shows how the different elasticity, damping values and vocal tract shapes influence the frequency f of the self-oscillations, maximal width of glottis WG_{max} and open quotient OQ.

Table 1. Computed vocal fold vibration characteristics

E_{SLP} [Pa]	First two natural frequencies of VF		α [s^{-1}]	β [s]	[a:]			[i:]			[u:]		
	f_1 [Hz]	f_2 [Hz]			f [Hz]	WG_{max} [mm]	OQ [–]	f [Hz]	WG_{max} [mm]	OQ [–]	f [Hz]	WG_{max} [mm]	OQ [–]
2000	70.653	142.537	0.5083	0.0002	Computation crashed			Computation crashed			Computation crashed		
			1.0165	0.0004	130	0.54	0.36	143	0.65	0.49	133	0.63	0.39
			60.3776	0.0006	130	0.49	0.38	139	0.55	0.51	135	0.57	0.41
			119.7386	0.0007	132	0.47	0.38	141	0.54	0.55	133	0.51	0.41
2500	71.919	148.337	1.7917	0.0002	128	0.48	0.35	141	0.56	0.41	127	0.50	0.37
			3.5834	0.0004	123	0.44	0.35	130	0.49	0.43	130	0.49	0.38
			64.4495	0.0006	127	0.38	0.38	135	0.48	0.49	130	0.43	0.40
			125.3155	0.0007	122	0.37	0.37	132	0.46	0.49	123	0.41	0.40
3000	72.946	153.013	2.7622	0.0002	122	0.40	0.34	139	0.50	0.40	125	0.44	0.35
			5.5243	0.0004	110	0.36	0.33	133	0.45	0.43	116	0.39	0.40
			67.5990	0.0006	108	0.35	0.35	118	0.38	0.39	109	0.35	0.33
			129.6737	0.0007	111	0.35	0.40	99	0.34	0.35	98	0.36	0.33
3500	73.827	156.96	3.5315	0.0002	114	0.35	0.39	94	0.33	0.36	123	0.33	0.37
			7.0631	0.0004	98	0.32	0.32	86	0.28	0.30	108	0.33	0.35
			70.1592	0.0005	VF did not open			VF did not open			VF did not open		
			133.2553	0.0007									

From the results we can observe that damping values do not affect oscillation frequency and open quotient much. Maximal width of glottis decreases a little bit with increasing value of damping. The oscillation frequency and the maximal width of glottis decreases with increasing Young's modulus of SLP layer while the opening coefficient remains almost unchanged.

Acknowledgements

This research is supported by Grant Agency of the Czech Republic by the project No. 16-01246S.

References

[1] Hájek, P., Švancara P., Horáček J., Švec J.G., Numerical simulation of the effect of stiffness of lamina propria on the self-sustained oscillation of the vocal folds, Proceedings of the conference Engineering Mechanics 2016, Svratka, 2016, pp. 182-185.

[2] Radolf, V., Direct and inverse task in acoustics of the human vocal tract, Ph.D. thesis, Czech Technical University in Prague, Prague, 2010.

[3] Scherer, R.C., Shinwari, D., De Witt, K.J., Zhang, C., Kucinschi, B.R., Afjeh, A.A., Intraglottal pressure profiles for a symmetric and oblique glottis with a divergence angle of 10 degrees, Journal of the Acoustical Society of America 109 (4) (2011) 1616-1630.

COMPUTATIONAL MECHANICS 2018
34th conference with international participation
Srní
October 31 - November 2, 2018

Analysis of stretch and stress distribution in pelvic floor structures during vaginal delivery using computer modeling

L. Havelková [a], M. Jansová [a], V. Kališ [b], Z. Rušavý [b], L. Krofta [c]

[a] *New Technologies – Research Centre, University of West Bohemia, Univerzitní 8, 306 14 Plzeň, Czech Republic*
[b] *Biomedical Center, Faculty of Medicine in Pilsen, Charles Univerzity, Alej Svobody 1655/76, 323 00 Plzeň, Czech Republic*
[c] *Institute for the Care of Mother and Child, Podolské nábřeží 157, 147 00 Praha, Czech Republic*

Female pelvic floor dysfunction, such as urinary incontinence, fecal urgency or pelvic organ prolapse, is very often associated with injuries of pelvic floor structures during childbirth. This trauma usually causes lifelong complications leading to poorer social or/and sexual life. The paper from Great Britain published that only 9.6 % of primipara and 31.2 % of sekundipara deliver with intact perineum [5]. In addition, the older study showed that 85 % women are suffering from injury of perineum during vaginal delivery [4]. Therefore, it is essential to understand the anatomy and physiology of these structures to avoid or at least to decrease the trauma of vaginal delivery. The computer modeling is a sophisticated tool how to achieve that.

The main objective of this study was to improve already existing finite element model of the female pelvic floor [2]. The model consists of the female pelvis; pelvic floor muscles – the levator ani muscle (iliococcygeus, pubovisceral, puborectal) and the internal obturator muscle; perineal structures – the external and internal anal sphincter, the perinal body, the superficial transverse perineal muscle, the bulbospongiosus muscle, the ischiocavernosus muscle, the anococcygeal body; and the fetal head. All supporting structures were replaced by boundary conditions. The model geometry was based on live-subjects MRI data – women: 25-years-old, Caucasian, no previous vaginal delivery, normal POP-Q points, absence of PFD symptoms, no pathological changes, healthy in general; neonate: 1-day-old, after uncomplicated vaginal delivery at term, neurological indications for a MRI brain scan. The volunteers as well as the imaging protocol are described in more details in author's publication. The asked volunteer/legal representative gave written consent. The study was approved by the local ethics committee from the institution of authors. The considered simulations and analyses focused on the muscle pelvic and perinal muscle structures only. Thus, other surrounding organs and tissues were neglected. It was assumed that these organs (bladder, urethra, rectum, etc.) are pushed during the vaginal delivery without any significant reaction forces.

The bony segments were modelled by rigid bodies without any possibility of deformation, the soft tissues were modelled by hyperelastic Ogden material model to enable such a huge deformation [3]. The model constants were fitted using the stress-strain characteristic published in literature sources and least-square method in MATLAB (lsqcurvefit, optimization toolbox; R2013a; The MathWorks, Inc. Natick, Massachusetts, USA).

The initial model geometry was reconstructed from in-vivo scanned MRI using a free semi-automatic software 3D Slicer (3.0; BWH, Boston, MA, USA). The resulting geometry and mesh were created in commercial software HyperMesh (11.0; Altair, MI, USA). Rigid parts, such as female pelvis and fetal head, were constructed with 2D triangular mesh

including more than 100 000 elements in summary. Deformable parts, such as muscles, were modeled by 3D tetrahedral mesh consisting of almost 700 000 elements. The accuracy and efficiency of the finite element simulations considered in presented work is highly predisposed to the quality of the finite element mesh [1]. And thus, the process of element quality control was not neglected.

Vaginal delivery scaled in seconds was simulated for the optimal fetal head position - left occipitoanterior positon. The distribution of stretch and stress von Mises generated in pelvic floor structures during vaginal delivery was analysed using the finite element method and the commercial software Virtual Performance Solution (VPS 9.0; ESI Group, Paris, France). The final model is depicted in Fig. 1.

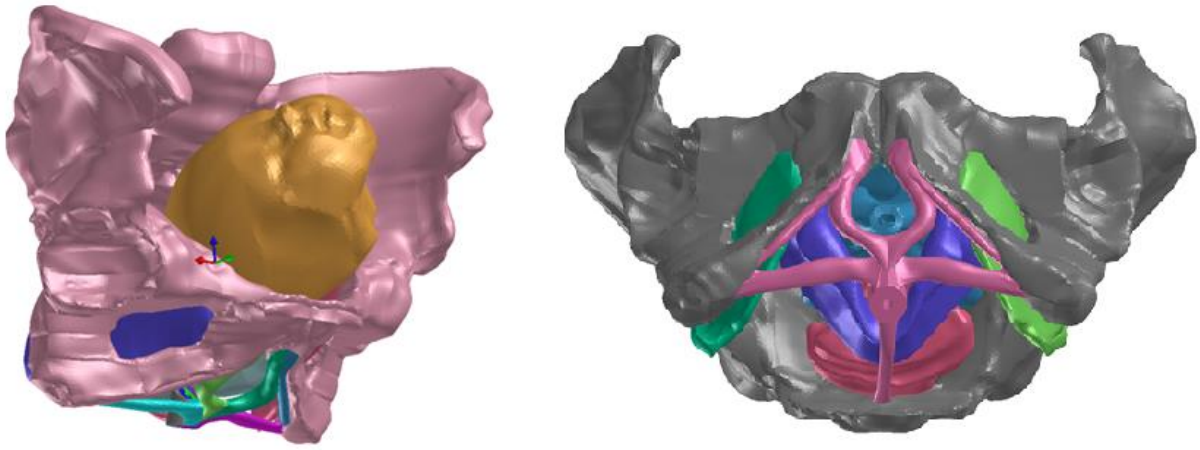

Fig. 1. The FE model of female pelvic floor; simulation of vaginal delivery considering the rigid fetal head in optimal initial position

Acknowledgements

This work was supported by the project n. 182 ‘Obstetrics 2.0 – Virtual models for the prevention of injuries during childbirth” realised within the frame of the Program INTERREG V-A: Cross-border cooperation between the Czech Republic and the Federal State of Germany Bavaria, Aim European Cross-border cooperation 2014-2020. The realisation is supported by financial means of the European Regional Development Fund (85 % of the costs) and the state budget of the Czech Republic (5 %).

References

[1] Burkhart, T.A., Andrews, D.M., Dunning, C.E., Finite element modeling mesh quality, energy balance and validation methods: a review with recommendations associated with the modeling of bone tissue, Journal of Biomechanics 46 (2013) 1477-1488.

[2] Krofta, L., Havelkova, L., Urbankova, I., Krcmar, M., Hyncik, L., Feyereisl, J., Finite element model focused on stress distribution in the levator ani muscle during vaginal delivery, International urogynecology journal 28 (2) (2017) 275-284.

[3] Ogden, R.W., Saxxomandi, G., Sgura, I., Fitting hyperelastic models to experimental data, Computational Mechanics 34 (2004) 484-502.

[4] Sleep, J., Grant, A., Garcia, J., Elbourne, D., Spencer, J., Chalmers, I., West Berkshire perineal management trial, British medicinal journal (Clinical research ed.) 289 (1984) 587-590.

[5] Smith, L.A., Price, N., Simonite, V., Burns, E.E., Incidence of and risk factors for perineal trauma: a prospective observational study, BMC pregnancy and childbirth 13 (1) (2013) 59.

COMPUTATIONAL MECHANICS 2018
34th conference with international participation
Srní
October 31 - November 2, 2018

Free surface flows modelling based on lattice Boltzmann method

V. Heidler[a], O. Bublík[a], L. Lobovský[a], J. Vimmr[b]

[a] *NTIS – New Technologies for the Information Society, Faculty of Applied Sciences, University of West Bohemia, Univerzitní 8, 301 00 Pilsen, Czech Republic*

[b] *Department Of Mechanics, Faculty of Applied Sciences, University of West Bohemia, Univerzitní 8, 301 00 Pilsen, Czech Republic*

Free surface flow is an important physical phenomenon involved in many manufacturing processes, e.g. material transport, machining, casting [2] etc. This work deals with the numerical simulation of free surface flows using the lattice Boltzmann method (LBM) [3–5], famous for its simplicity to algorithmize, fastness and its efficiency in parallel computing.

Basically free surface flows are two-phase flows. In this work the flow behaviour is dominated by the denser phase and therefore the air flow is neglected and represented by appropriate boundary conditions at the interface. To capture the free surface in the simulations, we adopt the algorithm based on the volume of fluid method (VOF) [6].

In the VOF method the interface is captured via the fill level of a cell, which qualifies the amount of a cell which is filled with fluid. Value 0 indicates an inactive gas cell and 1 corresponds to a filled cell inside the fluid. Fluid and gas cells are separated by a closed interface layer with a fill level between 0 and 1.

The aim of this work is to improve the accuracy of the algorithm by incorporating the surface tension and wetting angle effects [1]. The developed computational algorithm is tested on three benchmarks. In the first case, we solved the Poiseuille flow inside the channel formed by two infinite plates. The comparison with the analytical solution is shown in Fig. 1 (right).

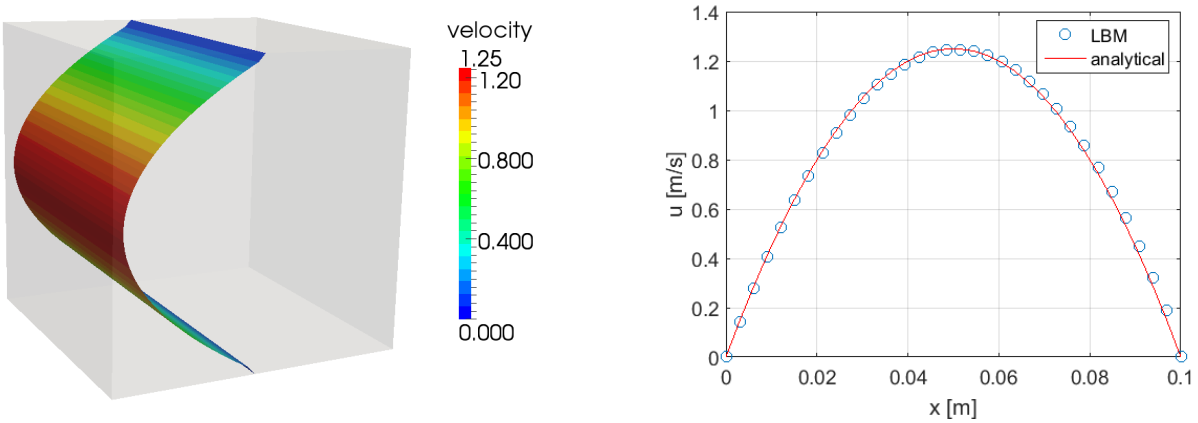

Fig. 1. Poiseuille flow between two infinite plates

The second case is focused on a validation of surface tension effect. We study the value of Laplace pressure, which is the pressure difference between the inside and the outside of a spherical water drop surface that forms the boundary between a gas and a liquid region. The error of the pressure inside the drop obtained by the numerical simulation on a relatively coarse mesh is 3.1 percent.

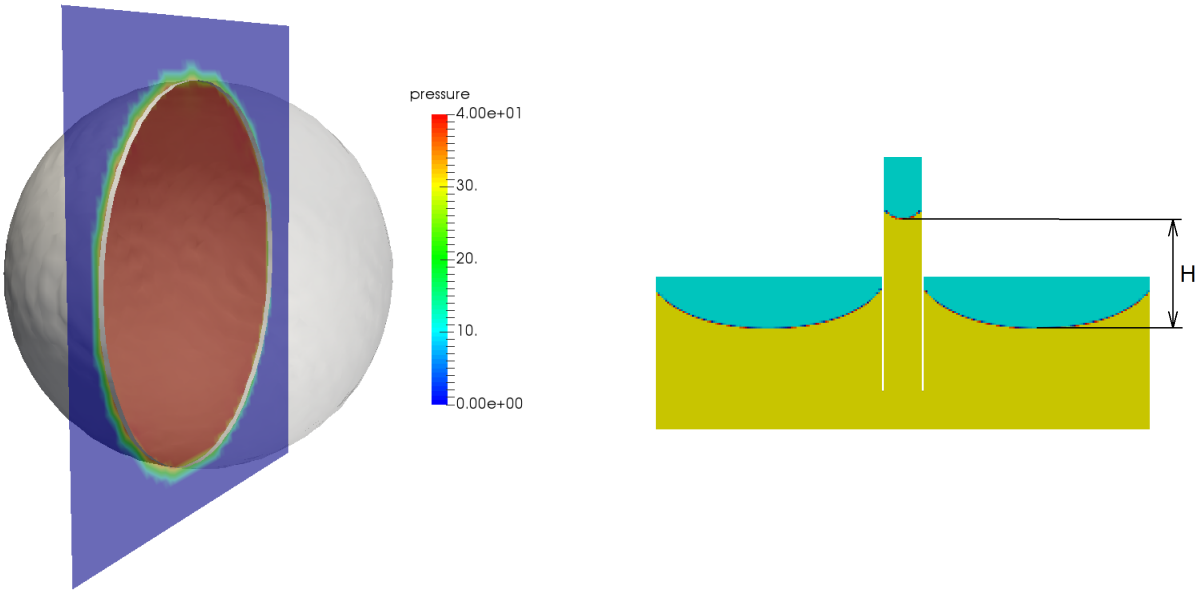

Fig. 2. Laplace pressure in a drop (*left*), capillary rise (*right*)

The third case deals with capillary action of a water between two infinite plates and serves for testing our implementation of wetting angle. The Fig. 2 (right) shows obtained increase of free surface H caused by the wetting angle and the surface tension. The error with respect to the analytical solution is below 5 percent.

The presented test cases are in a good agreement with the analytical data and show correctness of developed numerical algorithm for this kind of problems.

Acknowledgement

The authors appreciate the kind support by the grant GA 18-25734S "Experimental and computational modelling of free surface flow of non-Newtonian fluids with dispersed particles" of the Czech Science Foundation.

References

[1] Bogner, S., Rüde, U., Harting, J., Curvature estimation from a volume of fluid indicator function for the simulation of surface tension and wetting with a free surface lattice Boltzmann method, Physical Review E (93) (2016) 45-53.

[2] Ginzburg, I., Steiner, K., Lattice Boltzmann model for free-surface flow and its application to filling process in casting, Journal of Computational Physics (185) (2003) 61-99.

[3] He, X., Luo, L-S., Theory of the lattice Boltzmann method: From the Boltzmann equation to the lattice Boltzmann equation, Physical Review E (56) (1997) 6811-6817.

[4] Succi, S., The lattice Boltzmann equation for fluid dynamics and beyond, Oxford University Press, 2001.

[5] Sukop, M., Thorne, C., Daniel Jr., T., Lattice Boltzmann modeling: An introduction for geoscientists and engineers, Springer-Verlag Berlin Heidelberg, 2007.

[6] Thürey, N., Physically based animation of free surface flows with the lattice Boltzmann method, Ph.D. Thesis, Friedrich-Alexander University Erlangen-Nürnberg, 2007.

COMPUTATIONAL MECHANICS 2018
34th conference with international participation
Srní
October 31 - November 2, 2018

An efficient approach to model dynamics of a small engine crankshaft

V. Houdek[a], L. Smolík[a]

[a] *Faculty of Applied Sciences, University of West Bohemia, Univerzitní 8, 306 14 Plzeň, Czech Republic*

This paper deals with the computational modelling of a crankshaft. The main aim is to provide the overview of an efficient approach to model dynamics of a small engine crankshaft. The introduced computational model includes flexibility of bodies and employs a non-linear model of hydrodynamic forces in journal bearings. The whole model is assembled and analysed in MSC Adams software for multibody system dynamics.

The presented approach is based on the division of the crankshaft into a system of rigid bodies shown in Fig. 1 which are coupled with massless beam elements in accordance with Fig. 2. Properties of these elements, such as the second moment and polar moment of the cut area, are tuned in accordance with the results of a structural analysis with 3D finite elements.

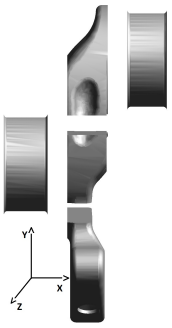

Fig. 1. Crankshaft division

Fig. 2. Beam elements

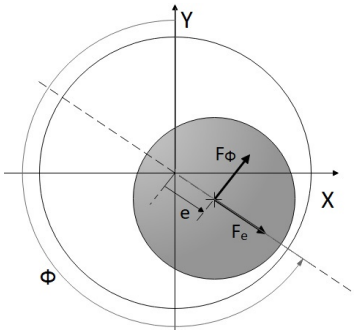

Fig. 3. Hydrodynamic forces

The beam properties has been tuned only in one part of the crankshaft. The tuned beams are depicted in Fig. 2 as red lines. Three types of static loads were defined for the system: a main bearing journal was fixed and forces in the main directions were applied in the centre of mass of a rod bearing journal. Resulting displacements of the center of the rod bearing journal are shown in Table 1.

Table 1. Displacement of the rod pin after tuning of the model parameters

force direction	**displacement – Ansys [μm]**	**displacement – MSC Adams [μm]**
X	2.265	2.275
Y	2.324	2.337
Z	2.018	2.040

The hydrodynamic forces (HD) acting in journal bearings of the engine are set as forces in the infinitely short bearing. The analytical solution of these forces is considered in the form of

$$F_e(\epsilon, \dot{\epsilon}, \dot{\Phi}, \omega) = -\mu R L \frac{L}{c}^2 \cdot \left[|\omega - 2\dot{\Phi}| \frac{\epsilon^2}{(1-\epsilon^2)^2} + \frac{\pi(1+2\epsilon^2)\dot{\epsilon}}{2(1-\epsilon^2)^{2.5}} \right], \quad (1)$$

$$F_\Phi(\epsilon, \dot{\epsilon}, \dot{\Phi}, \omega) = \mu R L \frac{L}{c}^2 \cdot \left[(\omega - 2\dot{\Phi}) \frac{\pi\epsilon}{4(1-\epsilon^2)^{1.5}} + \frac{2\epsilon\dot{\epsilon}}{(1-\epsilon^2)^2} \right], \quad (2)$$

where F_e and F_Φ are forces acting on the journal in radial and tangential directions respectively (Fig. 3), μ is the oil dynamic viscosity, R is the rotor radius, L is the bearing length, c is the radial clearance, ω is the rotor speed, ϵ is the rotor eccentricity and Φ is the angle to the eccentricity [1]. Validation of the forces was performed using a simplified model which only consists of a rotor pin supported on a journal bearing. The motion of the pin was compared with the motion of the Jeffcott rotor which is given in [2] and that has been simulated for the considered HD forces in journal bearings and for rotational speeds $\omega = \pi\, n/30$ rad/s, where $n = 2000 - 2900$ RPM.

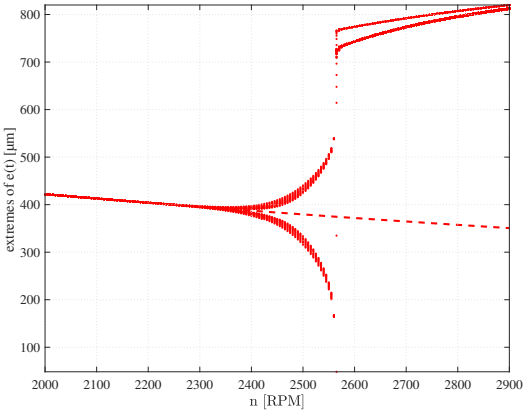

Fig. 4. Local extremes of displacement of the rotor pin [2]

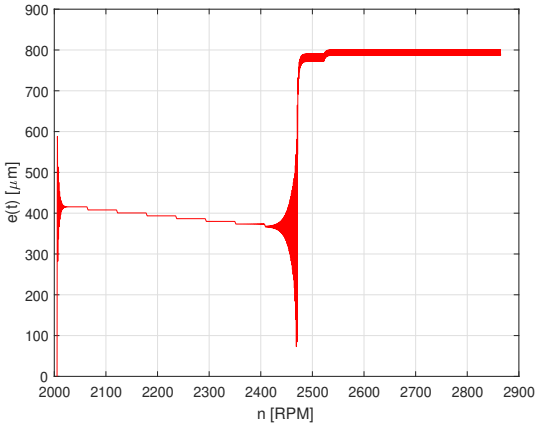

Fig. 5. Displacement of the rotor pin (MSC Adams)

The introduced computational model presents a powerful tool for a powertrain vibrations analysis. It is capable of incorporating not only linear but also non-linear behaviour of powertrain components and subsystems. The complex computational model should be verified by suitable experimental methods.

Acknowledgement

The work presented in this paper was supported by the project no. SGS-2016-038 of University of West Bohemia in Pilsen.

References

[1] Bastani, Y., De Queiroz, M., A new analytic approximation for the hydrodynamic forces in finite-length journal bearings, Journal of Tribology 132 (1) (2010) 014502, doi: 10.1115/1.4000389.

[2] Dyk, Š., Byrtus, M., Smolík, L., Steady-state behaviour of the rigid Jeffcott rotor comparing various analytical approaches to the solution of the Reynolds equation for plain journal bearing, DSTA 2017: Dynamical Systems in Applications. Cham, Springer, 2018, pp. 95-103.

COMPUTATIONAL MECHANICS 2018
34th conference with international participation
Srní
October 31 - November 2, 2018

A comparative analysis of treatment of a supracondylar periprosthetic femoral fracture under axial load and torque

M. Jansová[a], T. Malotín[b], J. Křen[a], P. Votápek[c], L. Lobovský[a], L. Hynčík[d]

[a]*NTIS - New Technologies for the Information Society, University of West Bohemia, Technická 8, 306 14 Plzeň, Czech Republic*
[b]*Department of Orthopaedics and Traumatology, Faculty of Medicine of Charles University and Faculty Hospital in Plzeň, Alej Svobody 80, 304 60 Plzeň, Czech Republic*
[c]*Department of Machine Design, Faculty of Mechanical Engineering, UWB, Univerzitní 22, 306 14 Plzeň, Czech Republic*
[d]*New Technologies – Research Centre, University of West Bohemia, Univerzitní 8, 306 14 Plzeň, Czech Republic*

A total knee arthroplasty (TKA) is in rare cases followed by an extra-articular fracture of distal femur. One type of fracture is a simple extra-articular fracture (A1 according to Schewring and Meggitt [3]). It can be stabilized only by surgical treatment. Several implant types are used by orthopedic surgeons for its management. In this study we compare a response to axial load and torque for Distal Femoral Nail (DFN) and Locking Compression Plate (LCP).

The model of bone with fracture, TKA and DFN is the same one as in the previous study [2]. Both compact and spongy bone are modelled by 3D elements. The gap of partially healed fracture with a callus is 2 mm wide. LCP geometry is based on a laser scan. The finite element models with the placement of DFN and LCP are shown in Fig. 1.

The material parameters of bone were obtained from available literature, the callus which forms several weeks after the fracture has material properties of a cartilage [4]. The screws, the spiral blade, DFN and LCP are made of titanium alloy.

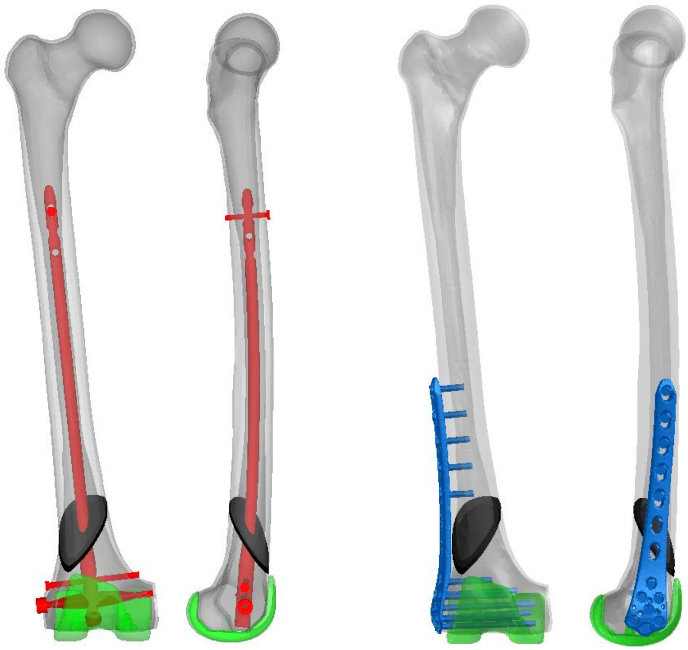

Fig. 1. The frontal (left) and lateral (right) view of model of femur with TKA (green), callus in the area of A1 fracture (black) and implants: DFN (red) and LCP (blue)

Two types of load were used – uniaxial load on the femoral head and torque. The loading conditions correspond to those of Brinkman et al. [1]. For both loads, a rigid body was formed at the surface of the femoral head and the greater trochanter and all degrees of freedom of the distal part of the femoral component were fixed. In case of the uniaxial load, a force corresponding to the body mass of 80 kg was applied on the center of femoral in the direction of mechanical axis and all other degrees of freedom were fixed. For torque, a moment of 5 Nm was applied on the center of femoral head about the mechanical axis and all other degrees of freedom were fixed.

The von Mises stress distribution in the implants and the displacement of femur in all three main directions were analyzed for all cases.

The results of uniaxial load show that in case of DFN there is an increased stress in the middle of the spiral blade in the area in contact with the nail and in the nail in the area around and above the fracture location. The femoral mid-shaft bends laterally and ventrally. Von Mises stress in LCP implant reaches high values also in the area around the fraction location and the screws are loaded mainly in the area of their intersection with compact bone. The femoral mid-shaft and LCP bend medially and ventrally. For both DFN and LCP the whole femur above the fracture moves distally, compressing the callus.

With torque about mechanical axis, the greater trochanter rotates dorsally for both implants. The femoral mid-shaft undergoes larger extension along the mechanical axis in case of LCP. The stress reaches significantly higher values in LCP implant, especially below the level of the screws in the diaphysis and through its whole width at the level of upper three screws on the condyle.

The most significant difference between the model with DFN and the one with LCP is in the displacement in the coronal plane under uniaxial load and markedly higher stress in LPC under torque.

Acknowledgements

The work was supported from European Regional Development Fund-Project “Application of Modern Technologies in Medicine and Industry” (No. CZ.02.1.01/0.0/0.0/17_048/0007280) and by projects SGS-2016-012 and SGS-2016-059 of the University of West Bohemia.

References

[1] Brinkman, J.M., et al., Biomechanical testing of distal femur osteotomy plate fixation techniques: the role of simulated physiological loading, Journal of Experimental Orthopaedics (1) (2014).

[2] Jansová, M., Malotín, T., Křen, J., Votápek, P., Lobovský, L., Hynčík, L., Finite element analysis of supracondylar periprosthetic femoral fracture treatment. Proceedings of the 32nd conference Computational Mechanics, Špičák, 2016, pp. 45-46.

[3] Schewring, D.J., Meggitt, B.F., Fracture of the distal femur treated with the AO dynamic condylar screw, The Journal of bone and joint surgery 74 (1) (1992) 122-125.

[4] Wehner, T., Steiner, M., Ignatius, A., Claes, L., Prediction of the time course of callus stiffness as a function of mechanical parameters in experimental rat fracture healing studies-a numerical study, PLoS One, 2014.

COMPUTATIONAL MECHANICS 2018
34th conference with international participation
Srní
October 31 - November 2, 2018

Probabilistic approach to prediction of fatigue life

M. Kepka Jr. [a], M. Kepka [a]

[a] *Regional Technological Institute, University of West Bohemia, Univerzitní 8, 306 14 Plzeň, Czech Republic*

In recent years, Kliman [4] presented a calculation of the fatigue life distribution function (FLDF). Under laboratory conditions, he considered the scatter of material properties of smooth material samples as well as the various random load processes, see Fig. 1.

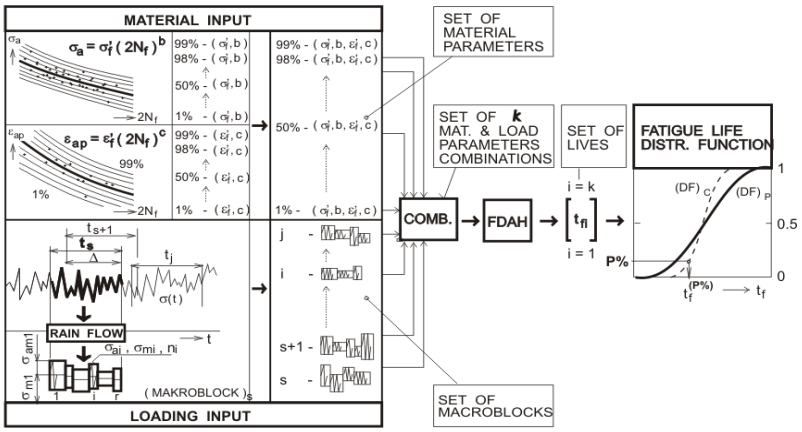

Fig. 1. Schematic procedure for calculating the FLDF by Kliman, [4]

We focused on the scatter of fatigue properties of specific components, see Fig. 2. It can be determined by evaluation of a sufficient number of fatigue tests of an investigated component. Alternatively, e.g. the BS 7608 [1] defines S-N curves of typical structural and technological details for different probabilities of survival. We applied this probabilistic approach and we calculated the FLDFs for several components exposed to real loading.

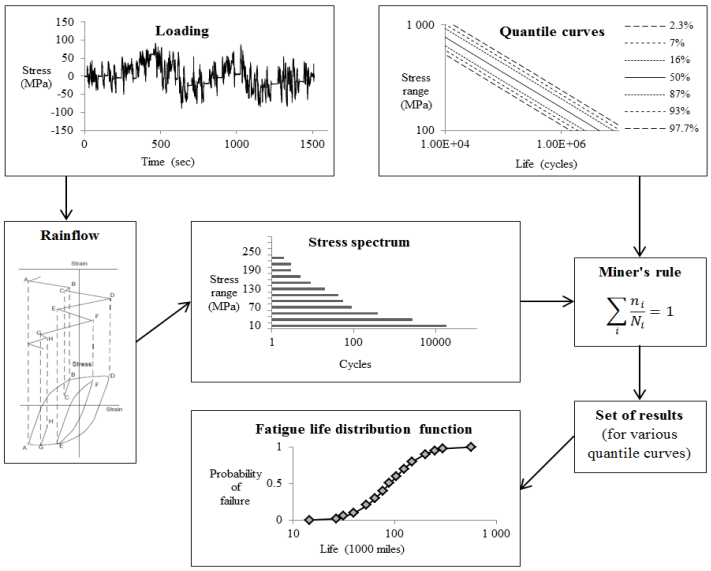

Fig. 2. Schematic procedure for calculating the FLDF of a real component with a scatter of fatigue properties

Fig. 3 shows two case studies. The first example shows the FLDFs that were calculated for a component with occurrence of fatigue cracks. It can be seen that service failures lie between the FLDFs calculated for two "extreme" operating modes, such as driving an empty vehicle (without passengers) and driving a fully occupied vehicle [2]. The second example shows the predicted FLDFs for a bus bodywork node made of different steels. One of the considered material solutions does not meet the required service life [3].

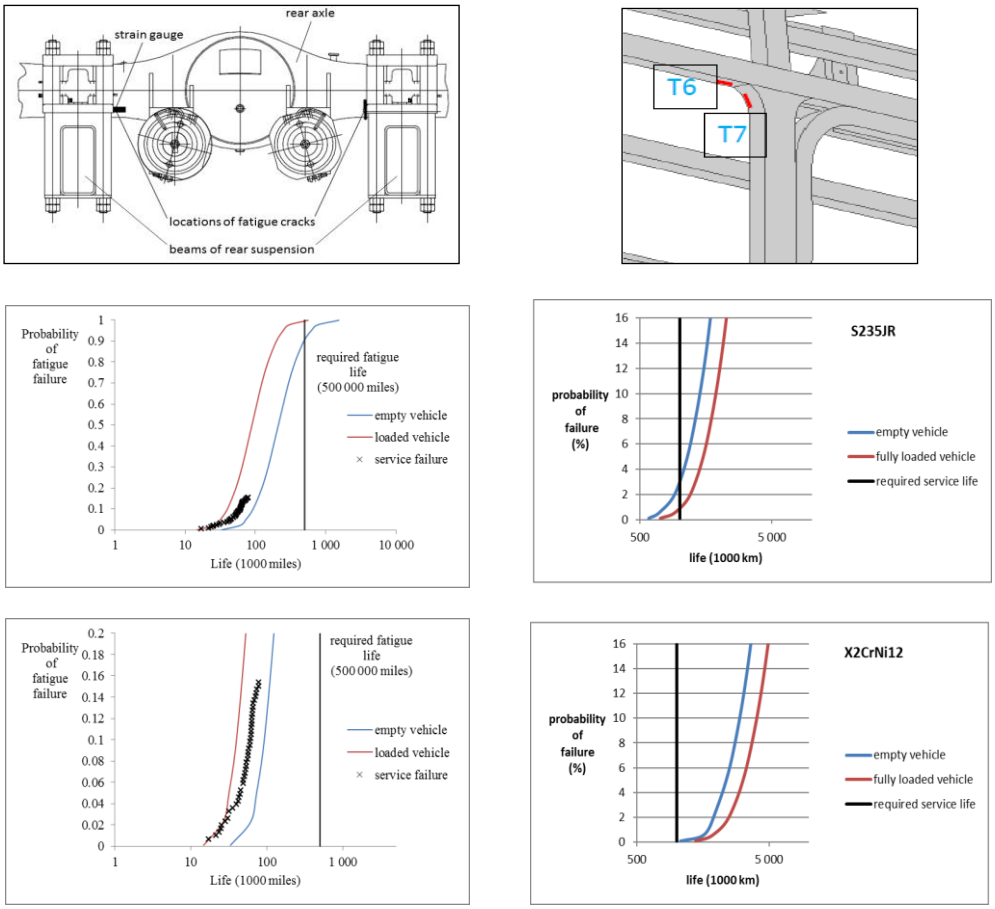

Fig. 3. Comparison of calculated FLDFs of a welded joint of a rear axle with service failures (left); Predicted FLDFs of a bus bodywork node made of different steels (right)

The probabilistic approach to prediction of fatigue life is appropriate for other practical situations. Some case studies will be presented in detail at the conference and in full paper.

Acknowledgements

The work has been supported by the research project LO1502 "Development of the Regional Technological Institute", under the auspices of the National Sustainability Programme I.

References

[1] The British Standards Institution, Fatigue design and assessment of steel structures, BS 7608, 1993.

[2] Kepka, M., Kepka Jr., M., Deterministic and probabilistic fatigue life calculations of a damaged welded joint in the construction of the trolleybus rear axle, Engineering Failure Analysis 93 (2018) 257–267.

[3] Kepka, M., Kepka Jr., M., Design, service and testing grounds stress spectra and their using to fatigue life assessment of bus bodyworks, Proceedings of the 12th International Fatigue Congress, Poitiers, 2018.

[4] Kliman, V., Jelemenska, J., Operational fatigue life evaluation using probabilistic approach, Engineering mechanics 2 (1995) 367-380.

COMPUTATIONAL MECHANICS 2018
34th conference with international participation
Srní
October 31 - November 2, 2018

Influence of the cooling bypass on the aircraft nozzle outflow

J. Klesa[a], J. Hejna[a], V. LeNours[b], T. Čenský[a]

[a] *Faculty of Mechanical Engineering, Czech Technical University, Karlovo náměstí 13, 121 35 Praha 2, Czech Republic*
[b] *SIGMA Clermont, Campus des Cézeaux, 63178 Aubière, France*

UL-39 ultralight aircraft has been developed at the Department of Aerospace Engineering, Czech Technical University in Prague [3]. This aircraft is powered by unique propulsion system, which consists of a fan driven by piston engine. Various concepts of the cooling system with various radiator positions were studied [2]. Radiator in the bypass channel behind fan is used at the flying prototype of UL-39.

Test bed with the model fan was build in order to conduct test and experiments for the development of this propulsion system [1]. Model of the UL-39 outlet duct is placed behind the fan, see Fig. 1. Radiator pressure loss is simulated by various inserts including clear frame (i.e., without pressure loss), honeycomb and screen. Bypass channel is is on the upper side of the outlet duct, i.e., on the opposite side than at the real UL-39 aircraft. Flow field behind the nozzle in the plane of symmetry is measured for each case by PIV (Particle Image Velocimetry) method for each case. Measurements were done in the wind tunnel at the Department of Aerospace Engineering. Fan RPM between 20,000 and 35,000 were used.

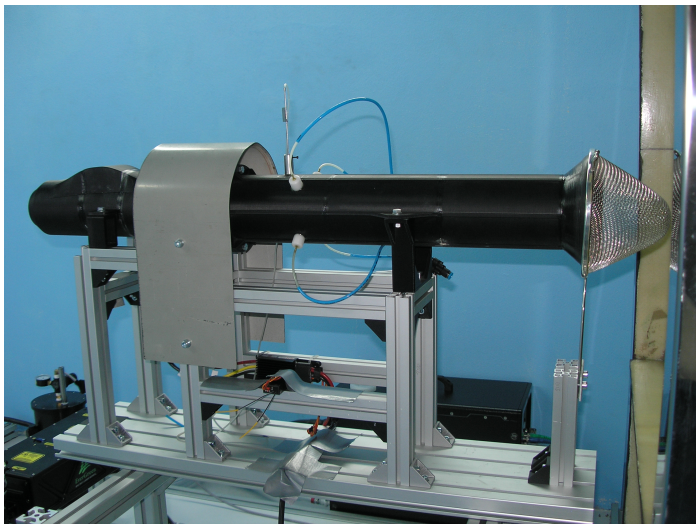

Fig. 1. Model fan test bed in the wind tunnel at the Department of Aerospace Engineering

Sample results of PIV measurements for 35,000 RPM are presented in Figs. 2 and 3. Fig. 2 shows asymmetrical velocity field behind the nozzle. Fig. 3 displays turbulence intensity. Difference in wake is clearly visible. Bypass duct with radiator influences both velocity magnitude (i.e., pressure losses causes decrease of outflow velocity) and turbulence characteristics. Bypass

causes more intensive grow of the shear layer between the of the flow from the nozzle and surrounding air. Model measurements will be compared with the flow field on full scale test bed of the UL-39 propulsion system.

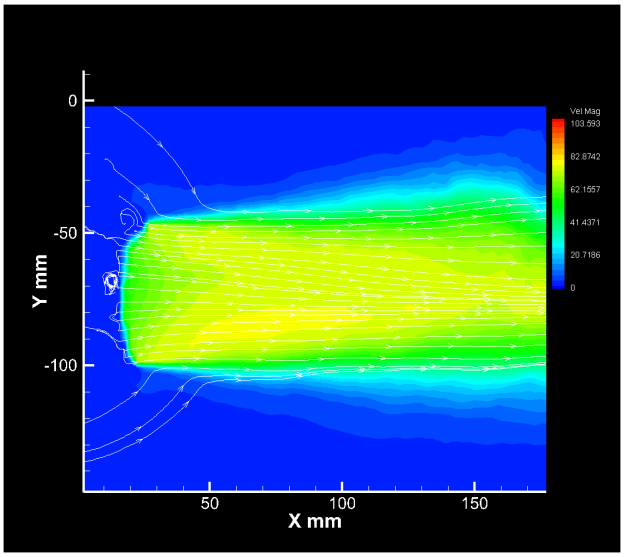

Fig. 2. Field of velocity magnitude with streamlines behind the nozzle for 35,000 RPM

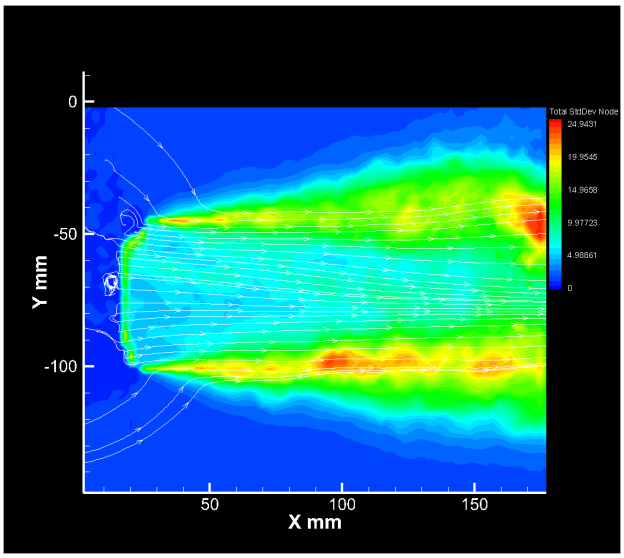

Fig. 3. Field of turbulence intensity with streamlines behind the nozzle for 35,000 RPM

References

[1] Hejna, M., Measurement of model fan characteristics, Bc. thesis, Czech Technical University in Prague, Prague, 2018.

[2] Klesa, J., Helmich, M., Sommer, T., Comparison of various fan conceptions for light sport aircraft, Proceedings of the 7th EASN Conference, Warszawa, Poland, 2017.

[3] Theiner, R., Brabec, J., Experience with the design of ultralight airplane with unconventional powerplant, Proceedings of the Institution of Mechanical Engineers, Part G: Journal of Aerospace Engineering (2018), doi: doi.org/10.1177/0954410018774117. (article in press)

COMPUTATIONAL MECHANICS 2018
34th conference with international participation
Srní
October 31 - November 2, 2018

Wave propagation in graded bars

R. Kolman[a], S.S. Cho[b], K.C. Park[c], A. González[d], A. Berezovski[e], P. Hora[f], V. Adámek[g]

[a] Institute of Thermomechanics, The Czech Academy of Sciences, v.v.i., Prague, Czech Republic
[b] Korea Atomic Energy Research Institute, Daejeon, Korea;
[c] University of Colorado at Boulder, Boulder, Co, USA
[d] Universidad de Sevilla, Sevilla, Spain
[e] Tallinn University of Technology, Tallinn, Estonia
[f] Institute of Thermomechanics, The Czech Academy of Sciences, v.v.i., Pilsen, Czech Republic
[g] NTIS - New Technologies for the Information Society, Faculty of Applied Sciences, University of West Bohemia, Pilsen, Czech Republic

Nowadays, additive technology is modern and high technology for manufacturing of complex bodies with advanced properties and various and complicated shapes, where conventional technologies are not possible to use. Applications of 3D printing technologies of metals can be found in mechanical, biomechanical or aerospace engineering. For that reason, understanding to wave processes in heterogeneous, layered and functionally graded materials is important issue for this time [5]. In this contribution, an explicit local time stepping scheme for modelling of discontinuous wave propagation problems in heterogeneous bars by the finite element method is used based on work [7]. In this method, the local stepping algorithm with respect to local wave speed and local stability condition at each material point is employed. The accurate modelling of discontinuous wave propagation in elastic heterogeneous bodies is still an open problem in numerical methods. Wave propagation problems in graded elastic bars has been studied in [4]. Numerical methods currently used comprise the finite volume method [2], higher order discontinuous Galerkin formulation, the graded finite element method [6] and etc.

We study discontinuous wave propagation in a graded bar with the linear distribution of elastic modulus and constant mass density. The analytical solution of the problem can be found in [3]. The length of the bar is $L = 1$ m. In this test, the mass density is chosen as $\rho = 1$ kg/m^3. The elastic modulus on the left side of the bar is $E_1 = 1$ Pa and on the right side it is set as $E_2 = 2.25$ Pa. The bar is loaded on the left side by the Heaviside pulse with the stress amplitude as $\sigma_0 = 1$ Pa. Results of numerical solution of the elastic wave propagation problem in the graded elastic bar are presented in Fig. 1 for time $T = 0.75$ s obtained by the analytical solution [3], semi-analytical solution with the numerical inverse Laplace transform [1], the finite volume method [2], the finite element method with explicit time integration by the central difference method, the finite element method with/without the local time stepping. For FEM and FVM, the time step size was set as a minimum value of local stable time steps over all elements/cells. Based on the test, the nominated scheme is suitable for accurate modelling of wave propagation in graded media.

Acknowledgements

The work of was supported by the Centre of Excellence for Nonlinear Dynamic Behaviour of Advanced Materials in Engineering CZ.02.1.01/0.0/0.0/15_003/0000493 (Excellent Research Teams) in the framework of Operational Programme Research, Development and Education,

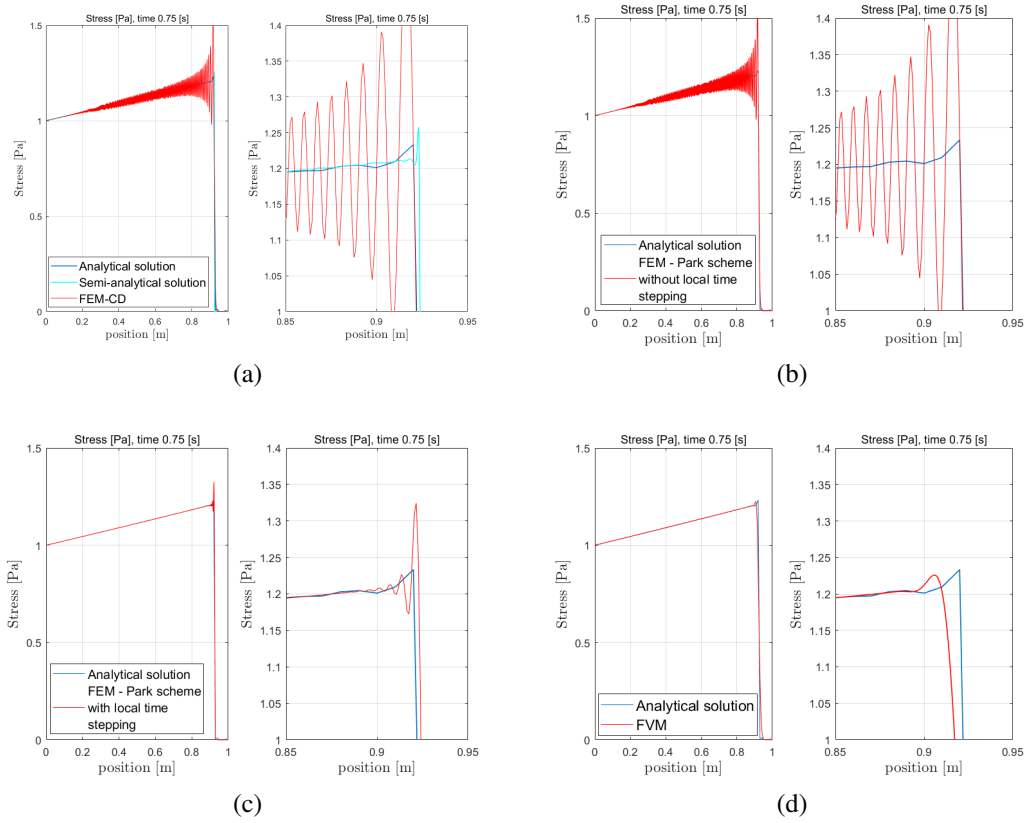

Fig. 1. Stress distributions in a graded bar obtained by a) FEM with the central difference method (CD), b) FEM with the Park method without local time stepping, c) FEM with the Park method with local time stepping, and d) FVM

within institutional support RVO: 61388998. The work of V. Adámek was supported by the project LO1506 of the Czech Ministry of Education, Youth and Sports.

References

[1] Adámek, V., Valeš, F., Červ, J., Numerical Laplace inversion in problems of elastodynamics: Comparison of four algorithms, Advances in Engineering Software 113 (2017) 120-129.

[2] Berezovski, A., Engelbrecht, J., Maugin G.A., Numerical simulation of waves and fronts in inhomogeneous solids, World Scientific Pub Co Inc., 2008.

[3] Brepta, R., Huněk, I., Impulse propagation in a thin bar with variable Young modulus, Technical Report Z1032/87, Institute of Thermomechanics CAS, 1987.(in Czech)

[4] Chiu, T.-C., Erdogan, F., One-dimensional wave propagation in a functionally graded elastic medium, Journal of Sound and Vibration 222 (1999) 453-487.

[5] Ebrahimi, R., Advances in functionally graded materials and structures, InTech, 2016.

[6] Kim, J.-H., Paulino G.H., Isoparametric graded finite elements for nonhomogeneous isotropic and orthotropic materials, Journal of Applied Mechanics 69 (2002) 502-514.

[7] Park, K.C., Lim, S.J., Huh, H., A method for computation of discontinuous wave propagation in heterogeneous solids: Basic algorithm description and application to one-dimensional problems, International Journal of Numerical Methods and Engineering 91 (6) (2012) 622-643.

COMPUTATIONAL MECHANICS 2018
34th conference with international participation
Srní
October 31 - November 2, 2018

Active multidimensional vibration absorbers for light structures

K. Kraus [a], Z. Šika [a], P. Beneš [a], T. Vyhlídal [a], M. Valášek [a]

[a] *Faculty of Mechanical Engineering, CTU in Prague, Technická 4,160 00 Praha 6, Czech Republic*

There has been high effort to increase production efficiency of production machines and robots last decades, including the usage of new types of kinematics [3], special control algorithms for non-traditional usage of machines [1], etc. The accurate motion control of the end-effector can be achieved through accurate measurement of the end-effector position and including such an information into the main control algorithm using base or additional actuators, but not all cases are suitable for such a design due to lack of space, bad work environment or many obstacles in the workspace. The counterpart of external end-point accurate measurement is the strategy of controlled vibration suppression [2], which can be realized through damping, vibro-isolation, vibro-compensation or vibro-absorption principles. Further differentiation distinguishes between active and semi-active approaches. Vibration suppression applications span from aircraft wings through towers and telescopes to cable bridges stabilization.

Well known passive vibration absorbing using mass connected to the primary structures works well in single DoF cases or even in multi DoF structures using more single DoF absorbers, but the frequency band is quite narrow and non-tunable while in operation. Using active or semiactive elements, better results in frequency band and response can be achieved. In this paper, single-mass multi-DoF active absorber is considered in order to reduce weight and spatial demands, so that added single body can reduce vibrations in many directions concurrently.

The concept of multi-level mechanisms consisting of main structure and additional single-mass multi-DoF absorber brings potential to improve dynamical properties of diverse lightweight robots with large workspace, since relatively small and light additional mass can be attached. This solution, along with well calibrated robot, presents an alternative idea of robot's end-point accuracy around its equilibrium, with less demanding and more robust local sensing, e.g. by accelerometers or geophones.

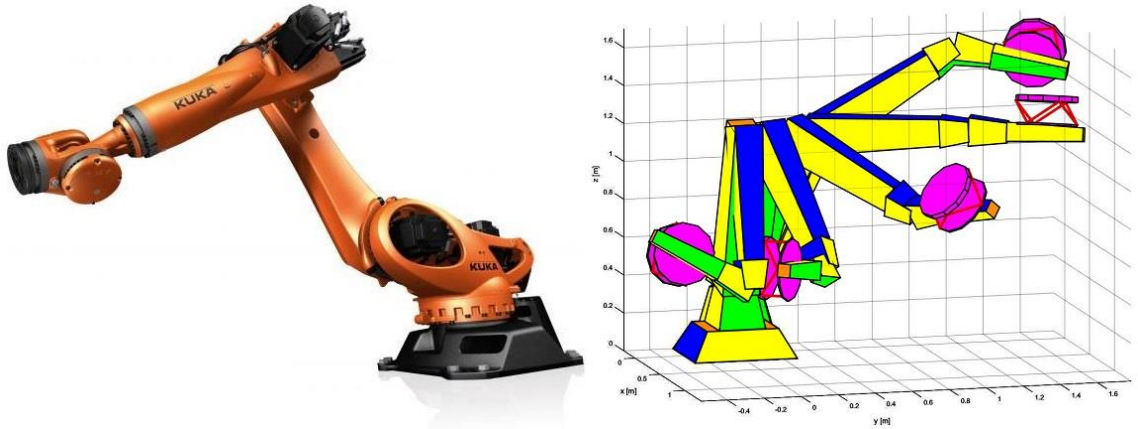

Fig. 1. Industiral light robot (left); simulation model of the robot with absorber in 5 different positions (right)

Fig. 1 (left) shows an example of 6-DoF light industrial robot, which can operate in large workspaces and concurrently suffers from end-point dynamical accuracy due to low stiffness. Fig. 1 (right) shows simulation mathematical model of such a light robot in five diverse positions through workspace already with vibration absorber attached. The absorber design is based on cubic structure, so that 6 active elements are formed along 6 edges of virtual cube, providing symmetrical neutrality of the additional mechanical structure.

Active elements of the absorbers consist of spring and voice-coil actuator. Dynamical properties of the absorber were optimized such that the vibrations in all directions and in all of the five robot's positions are as small as possible. Both, the robot and the absorber, are equipped with accelerometers providing feedback information.

Feedback control of mechanical parallel structure leads most likely to some type of centralized control algorithm, such as PID regulators, H-inf, LQR or Delayed resonator [4]. In this paper, LQR approach is considered as initial control design. There is a need of creating of multiple sets of ABCD matrices of local linearized state space models of the multi-level structure. Time-dependant ABCD matrices generations remains an opened question.

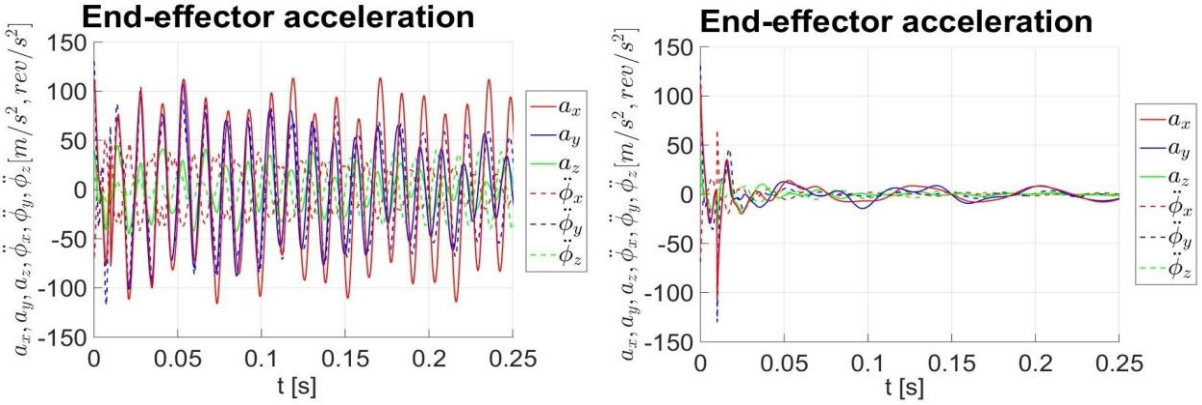

Fig. 2. End-effector acceleration in all directions without (left) and with (right) attached active absorber

Fig. 2 shows acceleration of the end-effector of the robot without (left) and with (right) attached active absorber based on LQR control. Absorbers are not designed to reach accurate positions, but to damp vibrations around equilibrium of the robot. The research of whole problematics is still in the process, so, many questions remain opened. For example, what sensors and what location of them to choose, how to adapt ABCD matrices through workspace, etc.

Acknowledgements

The work has been supported by the Czech Science Foundation project GA17-20943S "Active multidimensional vibration absorbers for complex mechanical structures based on delayed resonator method".

References

[1] Olsson, T., et al., Cost-efficient drilling using industrial robots with high-bandwidth force feedback, Robotics and Computer-Integrating Manufacturing 26 (2010) 24-38.
[2] Preumont, A., Vibration control of active structures - an introduction, Kluwer Academic Publishers, Dordrecht, 2002.
[3] Tesar, D., Butler, M.S., Generalized modular architecture for robot structures, Manufacturing Review 2 (2) (1989) 91-118.
[4] Vyhlídal, T., Olgac, N., Kučera, V., Delayed resonator with acceleration feedback - complete stability analysis by spectral methods and vibration absorber design, Journal of Sound and Vibration 333 (25) (2014) 6781-6795.

COMPUTATIONAL MECHANICS 2018
34th conference with international participation
Srní
October 31 - November 2, 2018

Myosin, numerical position determination and mechanical properties

M. Krejčová[a], M. Holeček[b]

[a] NTIS – New Technologies for the Information Society, Faculty of Applied Sciences, University of West Bohemia, Univerzitní 8, 301 00 Plzeň, Czech Republic
[b] Faculty of Applied Sciences, University of West Bohemia, Univerzitní 8, 301 00 Plzeň, Czech Republic

Myosin is a superfamily of molecular motor [3]. Especially, myosin II is able to generate force for a muscle contraction by sliding on an actin filament. To extract energy, the myosin motor has to hydrolyze adenosine triphosphate (ATP) to adenosine diphosphate (ADP). The energy is used for the power stroke.

We use three state mathematical model based on three connected Fokker-Planck equations [1]

$$\frac{\partial \rho_i}{\partial t} = D\frac{\partial}{\partial x}\left[\frac{1}{k_B T}\left(V_i'(x) + F_{Load}\right)\rho_i\right] + D\frac{\partial^2 \rho_i}{\partial x^2} + \sum_{j=1}^{N} k_{ij}\rho_j - \sum_{j=1}^{N} k_{ji}\rho_i, \tag{1}$$

where ρ is probability density function of a presence of a single myosin head at actin filament x in a time t. D is a diffusion coefficient, which describes Brownian motion in an aqueous solution (the myosin characteristic size is in nanometers—thus, myosin is also a kind of Brownian particle). k_B denotes the Boltzmann constant and T thermodynamic temperature. Their product is a characteristic value of thermal fluctuations. V is the active potential energy produced by the chemical reaction in a given state. The parameter F_{Load} is the external load force on myosin motor. The index i is used as a marker for a single state [1]. Equation (1) is solved by the WPE algorithm [5] for space variables x and by the MATLAB function ode15s for the time variable t.

The three states are known as unbound, weakly-bound and post-power-stroke [2]. None of these states does include the power stroke itself. The key step for obtaining mechanical properties of such system is the determination of the generation of the force. The force generated by a single myosin F has to be calculated based on the probability density distribution as

$$F = \int_0^L x\rho \mathrm{d}x, \tag{2}$$

where $L = 36\,\mathrm{nm}$, which is characteristic myosin II step. Other mechanical properties, like work W, can be obtained by its definition, for example,

$$W = \int F \mathrm{d}x. \tag{3}$$

In case of determination myosin head state and position, it is still possible to calculate these classical mechanical properties. In our model, the determination is simulated by a pseudorandom number generator provided by MATLAB. The generated number provides both the state

and position. We presume the procedure is not error-less [4]. The error has a Gaussian form

$$\rho_e = \frac{1}{\sqrt{2\pi\sigma^2}} \exp -\frac{(x-y)^2}{2\sigma^2}, \tag{4}$$

where the variance $\sigma^2 = 5\,\mathrm{m}^2$.

The next system evolution is started after determination myosin position with a new initial condition. The condition is created via Bayes' theorem.

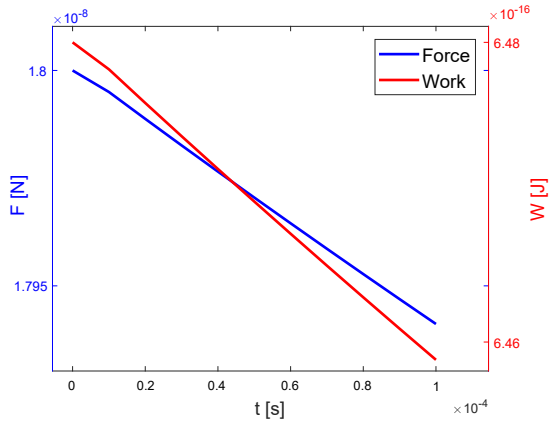

Fig. 1. Generated force and work before myosin state and position determination. The initial condition is the canonical one

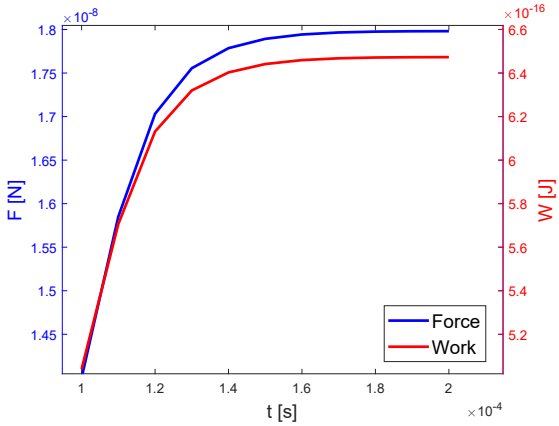

Fig. 2. Force and work after myosin state and position determination. The determined state is the unbound one

In Fig. 1 is visible the biggest value of force F and work W is in the equilibrium state. In the time of position and state determination is the system very disturbed. Its next values of mechanical properties are given of the myosin position mostly. For the unbound state we obtained an increase of the mechanical properties, see Fig. 2. For other states, we obtained different characteristics. For the weakly-bound state, there are almost constant and for post-power-stroke are decreasing, respectively.

Acknowledgements

M. Krejčová was supported by projects SGS-2016-038, SGS-2016-059 and LO1506 of the Czech Ministry of Education, Youth and Sports under the program NPU I. She also wishes to express her big thanks to Mr Rosenberg for his valuable advice.

References

[1] Chen, J., Zhang, X. Lin, S., Wan, H., Gu, L., Multiscale modeling of skeletal muscle active contraction in relation to mechanochemical coupling of molecular motors, Micromachines 6 (7) (2015) 902-914.

[2] Erdmann, T., Schwarz, U.S., Stochastic force generation by small ensembles of myosin II motors, Physical Review Letters 108 (18) (2012) 188101, doi: 10.1103/PhysRevLett.108.188101.

[3] Heissler S.M., Sellers, J.R., Various themes of myosin regulation, Journal of Molecular Biology 428 (2016) 1927-1946.

[4] Krejčová, M., Holeček, M., Chełminiak, P., The measurement of single myosin head in Fokker-Planck framework and information gain, Proceedings of the 20th international conference Applied Mechanics 2018, Myslovice, University of West Bohemia, 2018, pp. 63-68.

[5] Wang, H., Peskin, C.S., Elston, T.C., A robust numerical algorithm for studying biomolecular transport processes, Journal of Theoretical Biology 221 (4) (2003) 491-511.

COMPUTATIONAL MECHANICS 2018
34th conference with international participation
Srní
October 31 - November 2, 2018

Design of structure and control of planar robots with rigid and cable components

J. Krivošej [a], Z. Šika [a], K. Kraus [a]

[a] Faculty of Mechanical Engineering, CTU in Prague, Technická 4, 166 07 Praha 6, Czech Republic

This paper deals with designing and controlling a robot with rigid and cable elements. This work is the first step which leads to the idea of the 3D serial robot structure driven by cables and joints actuators. A planar robot structure is chosen, see Fig. 1. The structure is formed by

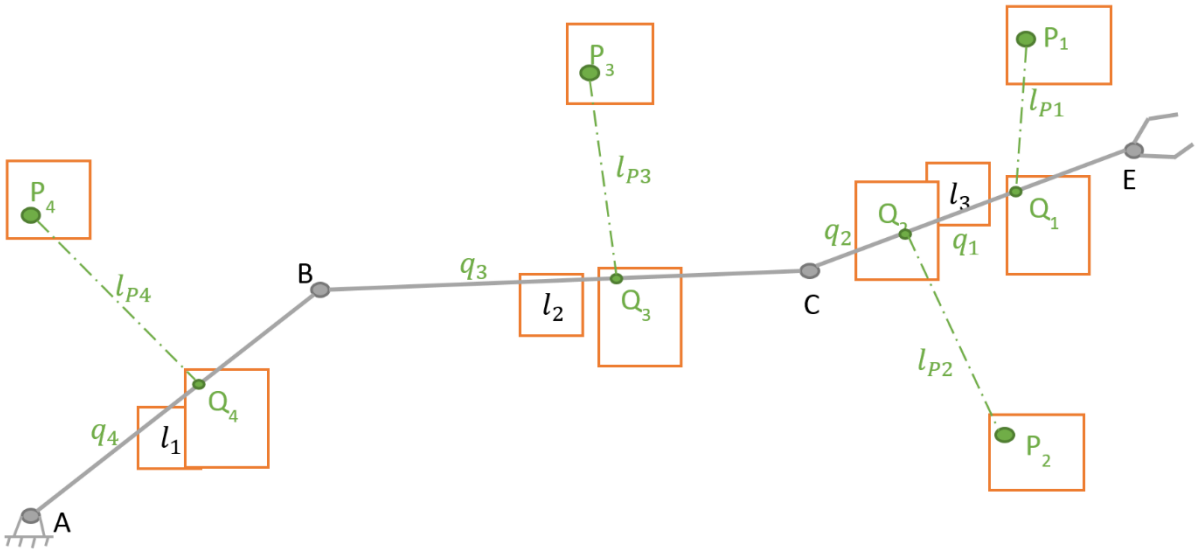

Fig. 1. Planar cable driven serial arm with marked parameters for optimization

a serial part (three beams connected by joint actuators) and a parallel part (four cables attached on serial structure and driven by actuators with pulley [3]).

Consequently, the further step has been optimization. Two different approaches were chosen. The first one is based on the local optimization algorithm method – simplex and the second one is based on the global algorithm method – genetic algorithm. In both methods the cable forces were treated to be only positive [5]. The main aim of this part was to develop, analyze and verify two models of the structure optimization.

The next step was to create the dynamic model of the chosen structure. One can easily see that this model is nonlinear thus the linearization method is needed. In the field of the Flatness theory was derived for this purpose (linearization of the robotic structure) theory "Computed Torque". By this theory one can transform the nonlinear model to a new linear one which can be written in Brunowski (canonical) form [4]. Once one obtains the linear model the linear control strategy could be used.

The control regulator was divided into two parts, see Fig. 2. The purpose of the first part has been controlling of the robotic structure without cables. And the second part of the regulator has controlled the force distribution of each cable [1]. For the first part of the control regulator

were chosen two different regulators – PID cascade with feedforward [2] and Flatness regulator (Fig. 3). It is necessary to note that the control regulator could control the robotic structure without cables and uses only actuators in joints A, B, C. For this case the cables are preloaded and help to hold the robot in desired or actual position. Besides, the preloaded cables help to increase the stiffness of the mechanism.

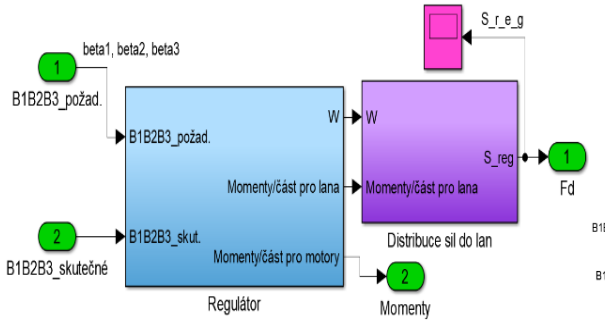

Fig. 2. Schemes of control implementation, distribution of the regulator

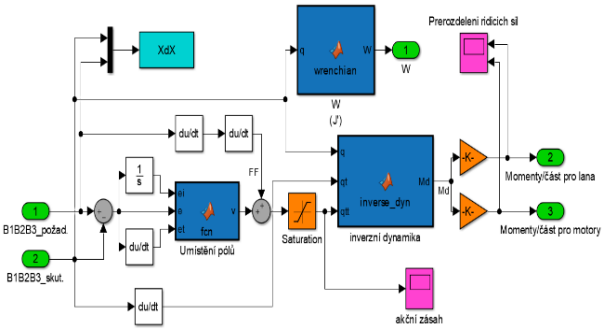

Fig. 3. Schemes of control implementation, flatness regulator

For the simulation were chosen three different trajectories (which tracked the end-effector – the point E) in the workspace determined by the optimization. Trajectories were S-curve (point to point trajectory), circle and rectangle.

The results of simulations showed that the regulation has been stable for all trajectories. Tracking of the desired trajectory was very accurate for the S-curve. For the simulation were used different parameters for the model and the control regulator.

Acknowledgements

The work has been supported by the project SGS16/208/OHK2/3T/12 “Mechatronics and adaptronics 2016” and Czech Science Foundation project GA17-20943S “Active multidimensional vibration absorbers for complex mechanical structures based on delayed resonator method” of CTU in Prague.

References

[1] Gouttefarde, M, et al., A versatile tension distribution algorithm for n-DOF parallel robots driven by n+2 cables, Transactions on Robotics 31 (6) (2015) 1444-1457.
[2] Kraus, K., Redundant parallel manipulator, Diploma thesis, CTU in Prague, Praha, 2016.
[3] Merlet, J.P., On the redundancy of cable-driven parallel robots, Proceedings of the 5th European Conference on Mechanisms Science, Guimarães, Springer International Publishing, 2014.
[4] Rigatos, G.G., Differential flatness theory and flatness-based control, Nonlinear Control and Filtering Using Differential Flatness Approaches (2015) 47-101.
[5] Svatoš, P., Optimization and control movement of fibre driven parallel mechanisms, Ph.D. thesis, CTU in Prague, Praha, 2016.

COMPUTATIONAL MECHANICS 2018
34th conference with international participation
Srní
October 31 - November 2, 2018

Numerical simulation of chloride transport in concrete

J. Kruis[a], J. Němeček[a]

[a]Department of Mechanics, Faculty of Civil Engineering, Czech Technical University in Prague, Thákurova 7, 166 29 Prague, Czech Republic

Penetration of chlorides into concrete causes various types of degradation and it affects durability of concrete. Extraction of chlorides from concrete can be significantly accelerated with the help of electric field. Such extraction is nondestructive and it is relatively very fast.

It is assumed in this work that concrete pores are fully filled with water which is a common case of many structures in wet or sea areas. In saturated pores, the ionic transport is driven by two main driving forces, the concentration gradient and the electromotive force acting on charged ions. The two forces can be considered in the ionic flux which then composes of the diffusion term (Fick's law) and the electrical migration term (Nernst-Planck equation) as

$$\boldsymbol{j} = -D\varrho\nabla c \; - \frac{DFz\varrho c}{RT}\nabla\phi, \tag{1}$$

where D [m^2/s] is the diffusion coefficient, $F = 96,487$ C/mol is the Faraday constant, z is the valence of ions, ϱ [kg/m^3] is the total density of concrete, $R = 8.314$ J/K/mol is the molar gas constant, T [K] is the temperature, ϕ [V] is the electric potential. The diffusion coefficient, D, is a function of many variables (concrete type, age, porosity, aggregate size, temperature, humidity and chloride concentration). However, it is assumed to be constant in this work for simplicity. On the other hand, an effect of chloride binding is taken into account. The amount of chlorides in concrete can be decomposed to two parts, the free chlorides (with concentration c_f) that can be transported and bound chlorides (with concentration c_b) that are chemically or physically bound to the concrete pore walls [1, 3]. The two concentrations must satisfy the condition $c = c_b + c_f$. The ratio between the free and bound chlorides is described by a binding isotherm [1–3]. The Freundlich binding isotherm is assumed in this work in the form $c_b = \alpha c_f^{\beta}$, where α and β are experimentally obtained constants. Then, the mass balance equation can be written for free chloride concentration in the form

$$\frac{\partial c_f}{\partial t}\left(1 + \frac{\mathrm{d}c_b}{\mathrm{d}c_f}\right) = \mathrm{div}\left(D\nabla c_f + \frac{DFzc_f}{RT}\nabla\phi - c_f\boldsymbol{v}\right). \tag{2}$$

The externally applied electric field during accelerated extraction of chloride is taken into account by using the Gauss law of electrostatics as

$$\mathrm{div}(\varepsilon_r\varepsilon_0\boldsymbol{E}) = -\Delta(\varepsilon_r\varepsilon_0\phi) = \sigma, \tag{3}$$

where $\boldsymbol{E}$ is the intensity of the electric field, ϕ [V] is the electric potential, σ [C/m^3] is the density of charge that is zero for our case, ε_r [–] is the relative permittivity and $\varepsilon_0 = 8.854 \times 10^{-12}$ F/m is the permittivity of the vacuum. The mass balance equation must be complemented

with a set of boundary conditions in the form of, e.g., Dirichlet conditions (prescribed concentrations at the boundary, $c_D(\boldsymbol{x}, t)$) or Neumann condition of the boundary flux, $j_N(\boldsymbol{x}, t)$, and initial condition (prescribed concentrations, $c_0(\boldsymbol{x}, t = 0)$). A finite element approximation using the Galerkin-Petrov approach was applied to Eq. (2), which leads to the assemblage of a non-symmetric system of ordinary differential equations in the form

$$\boldsymbol{C}\frac{\mathrm{d}\boldsymbol{c}}{\mathrm{d}t} + (\boldsymbol{K} - \boldsymbol{H})\boldsymbol{c} = \boldsymbol{f}, \tag{4}$$

where $\boldsymbol{C}$ is the capacity matrix, $\boldsymbol{K}$ is the diffusivity matrix, $\boldsymbol{H}$ is the conductivity matrix and $\boldsymbol{f}$ is the right hand side vector corresponding to the ion flux density normal to the boundary, $j_N(\boldsymbol{x}, t)$.

Fig. 1 shows typical graphs of chloride penetration into concrete due to diffusion and chloride extraction accelerated by an electric field. While the penetration lasts several years, the extraction takes usually only few days.

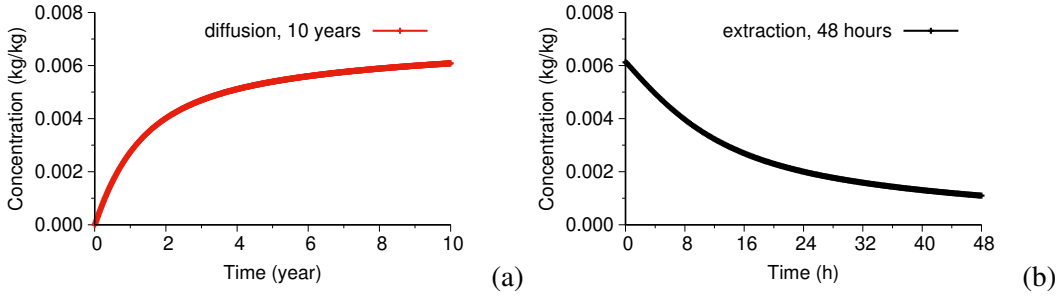

Fig. 1. (a) Concentration after 10 years of pure diffusion, (b) concentration after 2 days of extraction

Acknowledgment

Financial support of the Czech Science Foundation (project 16-11879S) is gratefully acknowledged.

References

[1] Florea, M.V.A., Brouwers, H.J.H., Chloride binding related to hydration products: Part I: Ordinary Portland Cement, Cement and Concrete Research 42 (2) (2012) 282-290.

[2] Tang, L., Nilsson, L.O., Chloride binding capacity and binding isotherms of OPC pastes and mortars, Cement and Concrete Research 23 (2) (1993) 247-253.

[3] Thomas, M.D.A., Hooton, R.D., Scott, A., Zibara, H., The effect of supplementary cementitious materials on chloride binding in hardened cement paste, Cement and Concrete Research 42 (1) (2012) 1-7.

COMPUTATIONAL MECHANICS 2018
34th conference with international participation
Srní
October 31 - November 2, 2018

Effective elastic properties of 3D printed auxetic metamaterials

A. Kruisová[a], R. Kolman[a], J. Trnka[a], J. Buchar[a], D. Mochar[a], J. Kober[a], J. Vtípil[b]

[a] *Institute of Thermomechanics, Czech Academy of Sciences, Dolejškova 5, 182 00 Praha 8, Czech Republic*
[b] *CARDAM s.r.o., Pražská 636, 252 41 Dolní Břežany, Czech Republic*

Mechanical metamaterials are artificially produced structures that derive their properties from their periodically repeated structure rather than from mechanical properties of their base material [3]. Often, these structures are manufactured by 3D printing. Nowadays the additive manufacturing technology can be used for producing complex bodies with complicated shapes and various properties which cannot be produced by conventional technologies. Such structures can posses superior properties such as e.g. the negative Poisson's ratio [2]. These materials exhibit a counter-intuitive behaviour when under the uniaxial tension, the structure expands transversely and vice versa. Applications of 3D printed bodies can be found in mechanical, biomechanical or aerospace engineering.

This contribution is focused on study of elastic properties of a structure made by the Selective laser melting (SLM). SLM is one of a 3D printing method enabling manufacturing of complex metallic metamaterials. The studied sample is based on bcc crystal structure and is shown in Fig. 1, detail of the structure is in Fig. 2. The diameter of the spheres is 1.25 mm, the diameter of connecting cylinders is 0.625 mm. The size of the elementary unit cell was set 2 mm.

The structure was produced from the stainless steel SS 316L-0407 powder for additive manufacturing. The material properties of the printed material are slightly anisotropic, according to the producer the Young modulus varies in the horizontal and vertical direction of printing, but this was not included in our computation of the effective elastic properties. Only two parameters of the base material was taken into account, Young modulus of bulk material 167 GPa and Poisson's ratio of bulk material equal to 0.33.

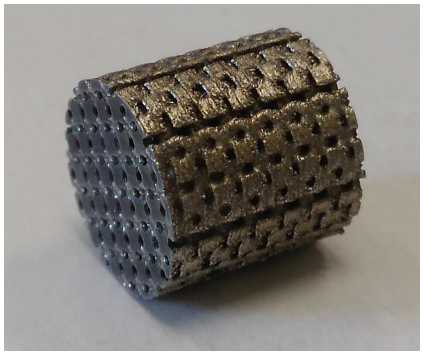

Fig. 1. Sample of metallic metamaterial

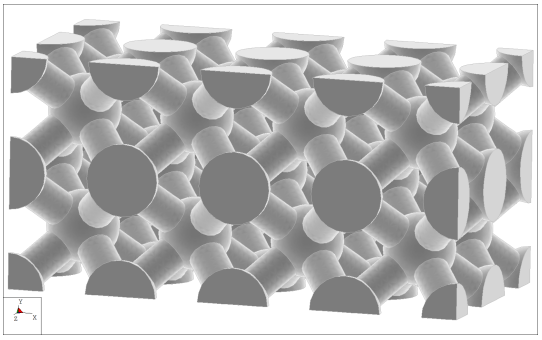

Fig. 2. Model of bcc structure

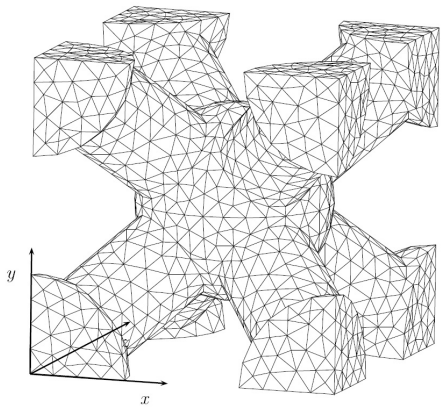

Fig. 3. FEM model used in REV for estimation of effective elasticity

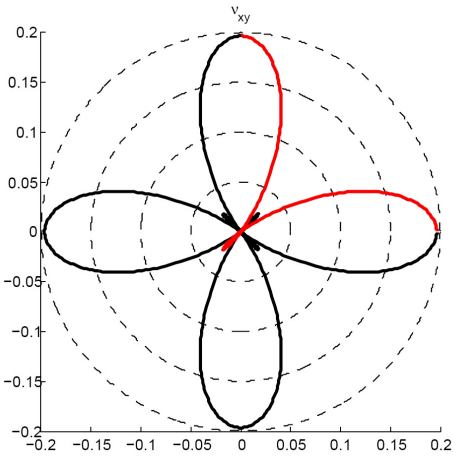

Fig. 4. Directional distribution of Poisson ratio in x, y plane

The effective elastic properties of the structure given by the elasticity tensor were obtained by the representative elementary volume (REV) homogenization method used in composites [1]. The FEM calculations were carried out on the model of the representative volume element, Fig. 3, in COMSOL Multiphysics computing software [4] by using the periodic boundary conditions to simulate the periodicity of the structure. Three simple deformation modes were used, plain strain mode, simple shear mode and pure shear mode. Three independent elastic constants $c_{11} = 17.5$ GPa, $c_{12} = 4.3$ GPa and $c_{44} = 10.3$ GPa were numerically determined.

The direction dependence of the Poisson ratio in $x - y$ plane is shown in Fig. 4. Its values for a quarter of plane are plotted in red line thus it can be clearly observed that the value of the Poisson's ratio in the direction of the axis x or y of the coordinate system given is 0.1966, in contrast with the value of the Poisson ratio in the diagonal direction, which is negative and its value is -0.0256. In future work, we plan to pay attention to the influence of effective elastic properties to the modelling of wave propagation in metallic metamaterials.

Acknowledgement

The work was supported by the grant project TK 01030108 - NEMENUS of the Technology Agency of the Czech Republic within the institutional support RVO: 61388998.

References

[1] Hill, R., Elastic properties of reinforced solids: Some theoretical principles, Journal of the Mechanics and Physics of Solids 11 (5) (1963) 357-372.

[2] Lakes, R., Advances in negative Poisson's ratio materials, Advanced Materials 5 (1993) 1038-1040.

[3] Ren, X., Das, R., Tran, P., Ngo, T.D., Xie, Y.M., Auxetic metamaterials and structures: A review, Smart materials and structures 27 (2018) 023001.

[4] COMSOL Multiphysics Reference Manual, version 5.3, COMSOL, Inc, www.comsol.com

COMPUTATIONAL MECHANICS 2018
34th conference with international participation
Srní
October 31 - November 2, 2018

Influence of material stiffness and damping on dynamic behaviour of production machines

V. Kulíšek [a], J. Smolík [b], M. Růžička [a], P. Kolář [b]

[a] *Department of Mechanics, Biomechanics and Mechatronics, Faculty of Mechanical Engineering, Czech Technical University in Prague, Technická 4, 166 07 Praha, Czech Republic*
[b] *Research Centre of Manufacturing Technology; Faculty of Mechanical Engineering, Czech Technical University in Prague; Technická 4, 166 07 Praha, Czech Republic*

The development of new production machines is driven with aim to improve their productivity and precision. Focusing on the mechanical properties of the machine structural parts assembly, the key properties are static and dynamic stiffness. For example in machine tools, machining limits depend strongly on the dynamic stiffness of machine tool – workpiece assembly, see Altintas [1]. Another aspect is to reduce inertia masses of motion axis components, as this is beneficial to the motion axis speed and acceleration. A possible improvement is in replacement of structural parts from steel, cast iron to composite or hybrid materials as they might improve the behavior due to their lower density, adequate stiffness and larger damping. A comprehensive study of composite and hybrid materials application into the machine tool was published by Mohring [2] stating that hybrid materials might be a future in machines design. However, a key question is whether a component with higher damping can improve a dynamic stiffness of the machine assembly as the most of the assembly damping happens in connection interfaces. This might lead to a situation, where a replacement of a single structural component by a new one with higher damping might not significantly influence the global assembly damping and the assembly stiffness.

A simulation model was assembled with aim to evaluate the effect of structural parts stiffness and damping on the dynamic behavior of the machine assembly. The model used description of the basic motion equation in modal coordinates y

$$[I]\{\ddot{y}\} + [\Phi]^T\,[C]\,[\Phi]\{\dot{y}\} + [\Lambda^2]\{y\} = [\Phi]^T\{F\}\,. \tag{1}$$

Aim of the model was to assembly the damping matrix C of the structural parts assembly. The basic equation for the damping matrix C in modal coordinates is given as

$$[\Phi]^T\,[C]\,[\Phi] = [\Phi]^T \sum_{j=1}^{m} \left(\frac{2\zeta_j}{\Omega}\right)[K_j]\,[\Phi] + \alpha + \beta[\Lambda^2] + [\Phi]^T \sum_{j=1}^{m} \beta_j[K_j]\,[\Phi] + \cdots. \tag{2}$$

In the Eq. (2), there are members corresponding to the Raleigh damping (α, β) of the whole assembly and members corresponding to the damping of each component (index j denotes the component and its part in the global stiffness matrix) using either constants β from the Rayleigh damping or modal damping ζ of component.

Generally, it is difficult to estimate Rayleigh parameters α, β for a model of production machine, as the assembly is full of connection interfaces, etc. For the evaluation of the single component material change effect on the global assembly behaviour, only the first member in Eq. (2) was taken into the account. This member is using a modal damping ζ of each component

of the model. The idea was to use the modal damping values, which are taken from the experimental modal analysis of the structural parts from various materials. And to make artificial modal damping ratios for the simplified models of connection interfaces, which would be estimated so that the average damping of the structural parts assembly corresponds to the damping of the real machines, which might be for example 2.0 - 4.5 % for the first structural mode shapes. Several values of modal damping ratios ζ of structural components from steel, cast-iron, composites and other materials were published by Novotny [3]. A brief overview is given in Table 1. Those values, together with the material stiffness were used in the simulation model.

The model was demonstrated on a case study using a 5-axis mill turn center, which is composed of a spindle, cross-slides, transverse beam and bed as the main structural components. A prediction of dynamic behavior when changing the structural material of each component from cast – iron to composite material with average damping ratio ζ = 1.0 % is given in Fig. 1. In the case study, damping ratio of connection interfaces (housings of linear guide-ways) was approximately 30 % to match the expected dynamic behaviour of assembly.

Table 1. Basic modal damping ratios for structural components

Material	ζ [%]
Steel	0.01-0.1
Cast iron	0.1-0.2
Polymer concrete	0.4
Fibre composites	0.1-0.6
Hybrid fibre composites	0.2-1.4
Hybrid particle composites	0.5-2.0

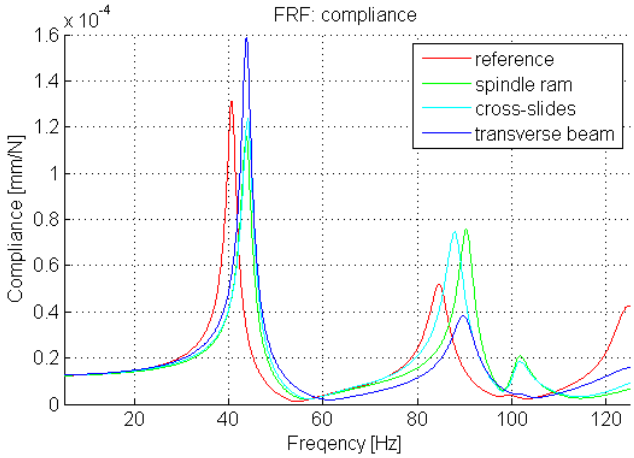

Fig. 1. Comparison of dynamic behavior of the machine tool assembly

The case study results in Fig. 1 showed that the application of composite materials to the transverse beam increased the dynamic compliance of assembly by 21 % with a slight frequency increase. Therefore, the design change would reduce the machine productivity. On the other hand, the application of composites to the spindle ram reduced the dynamic compliance by 13 % with a slight frequency shift. This would help the machining productivity, the question is if the higher material costs of composites can be justified by this improvement of the dynamic behaviour. The simulation model demonstrated a capability for predicting the dynamic behavior of the structural parts assembly using the modal damping of structural materials and modified damping in connection interfaces. Experimental verification will be the part of future works.

Acknowledgements

The work has been supported by the grant project of Czech Technical University in Prague with the project number SGS16/220/OHK2/3T/12.

References

[1] Altintas, Y., Weck, M., Chatter-stability of metal cutting and grinding, Manufacturing Technology 53 (2004) 619-642.
[2] Mohring, H.C., Brecher, C., Abele, E., at al., Materials in machine tool structures, Manufacturing Technology 64 (2015) 725-748.
[3] Novotny, L., Kolar, P., Sulitka, M., Smolik, J., Damping in machine tool structures. In Proceedings of the 14th International Conference on High Speed Machining, San Sebastian, Spain, 2018.

COMPUTATIONAL MECHANICS 2018
34th conference with international participation
Srní
October 31 - November 2, 2018

Influence of vertebrae and intervertebral disc on stresses in abdominal aortic aneurysms

O. Lisický [a], S. Polzer [b], J. Burša [a]

[a] *Institute of Solid Mechanics, Mechatronics and Biomechanics, Brno University of Technology, Czech Republic*
[b] *Department of Applied Mechanics, VSB Technical University of Ostrava, Ostrava, Czech Republic*

Computational modelling of stress-strain states in Abdominal Aortic Aneurysms (AAAs) has become an important tool in assessment of their rupture risk in the last decades. As its application potential in clinical practice is increasing with every additional influencing factor considered in the model, many factors have been analysed already. Up-to-date models are based on patient-specific AAA geometry obtained typically from CT-A imaging under a known level of blood pressure. Mean arterial pressure (MAP) is used to create their unloaded geometry [1] which (with other additional features such as residual stresses) may increase the credibility of the results. Material behaviour is also a very important feature to be described correctly. Large deformations of the arterial wall and intraluminal thrombus (ILT) are mostly described using constitutive models based on mean population data gathered from mechanical testing of patient-specific specimens [3]. ILT can be taken into consideration not only for his poroelastic structure reducing the blood pressure on the AAA wall but also for its significant load-bearing contribution. Different mechanical properties across the ILT thickness. Can be considered as a significant feature too. ILT with large thickness also reduces oxygen supply into the AAA wall underneath and consequently changes its mechanical properties (strength).

Nevertheless, very little attention has been devoted to the impact of the surrounding organs on the stresses in the AAA wall. Most computational models are just fixed on both ends of the AAA (boundary condition constraining all degrees of freedom). However, AAA is surrounded by less or more compliant connective tissues attached to other organs along its length which could lead to reduction of movements. Among lots of organs and tissues around the aorta, vertebrae along with intervertebral discs represent the stiffest ones and may have several contacts with the AAA, see Fig. 1. In these regions the AAA may be bent over the backbone which induces additional bending stresses in it and the contact regions may also change due to the movement of the AAA.

Taking most of the above features into consideration, the impact of backbone has been investigated in this preliminary study using a static stress-strain analysis of AAAs. The FE analysis of the idealized geometry shows a negligible impact on stresses in various vertebrae models (cylinder, vertebrae based on mean dimensions …). In contrast, significant differences in stresses have been found in case of patient-specific models. As expected, the impact of backbone does not occur under MAP because the deformed shape corresponds to that recorded from the CT-A imaging where the geometry and contacts were detected. However, when the elevated systolic pressure (assumed as 1.5 MAP in this study) was used to load the AAA wall, some patient-specific geometries showed significant differences in displacements and PWS, see Table 1. The relative increase of PWS due to the presence of backbone ranged from -2 to 81 %. Node-to-node comparison of the stresses between all the pairs of patient-specific models confirmed a global increase of stresses with consideration of backbone.

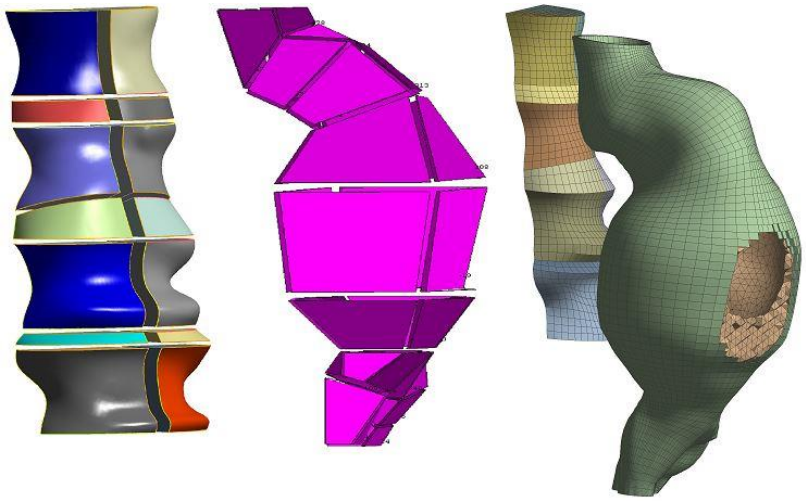

Fig. 1. Discretized model of vertebrae, intravertebral discs and AAA with pure hexahedral mesh using linear SOLID 185

Table 1. Comparison of PWS [MPa] in the patient-specific models with and without backbone

Patient [-]	1	2	3	4	5	6	7	8	9	10
WITHOUT backbone [kPa]	1450	783	3368	2089	1132	2468	3000	1136	882	1843
WITH backbone [kPa]	2630	783	3389	2630	1280	2530	3016	1420	921	1800
Difference [%]	81	0	1	26	13	3	1	25	4	-2

The results of FE analysis show NO significant increase or decrease in case of idealized models but significant variations in PWS (p = 0.034) have been found within the patient-specific models. As no indicator can be specified in what cases the backbone should be included, we recommend to include it in all FE models of AAA rupture.

Acknowledgements

This work was supported by project NETME CENTRE PLUS (LO1202), created with financial support from the Ministry of Education, Youth and Sports under the National Sustainability Programme I.

References

[1] De Putter, S., et al., Patient-specific initial wall stress in abdominal aortic aneurysms with a backward incremental method, Journal of biomechanics 40 (5) (2007) 1081-1090.
[2] Gasser, T., et al., Failure properties of intraluminal thrombus in abdominal aortic aneurysm under static and pulsating mechanical loads, Journal of Vascular Surgery 48 (1) (2008) 179-188.
[3] Polzer, S., et al., Importance of material model in wall stress prediction in abdominal aortic aneurysms, Medical Engineering and Physics 35 (9) (2013) 1282-1289.

COMPUTATIONAL MECHANICS 2018
34th conference with international participation
Srní
October 31 - November 2, 2018

Biomechanics of pelvic ring fixation techniques

L. Lobovský[a], J. Hartlová[a], M. Salášek[a,b], M. Krejčová[a], R. Tupý[c], T. Pavelka[b], J. Křen[a]

[a] *NTIS – New Technologies for the Information Society, Faculty of Applied Sciences, University of West Bohemia, Univerzitní 8, 301 00 Plzeň, Czech Republic*
[b] *Clinic for Orthopaedics and Traumatology of Locomotive Organs, University Hospital Plzeň, alej Svobody 80, 304 60 Plzeň, Czech Republic*
[c] *Clinic for Radiology, University Hospital Plzeň, alej Svobody 80, 304 60 Plzeň, Czech Republic*

The study focuses on development of computational tools for prediction and analysis of osteosynthesis of pelvic ring injuries. Fractures of pelvic bones may occur after high-energy impact events such as car accidents or sports injuries. For surgical treatment of unstable fractures either internal or external fixators can be applied in order to support the healing bone structures. In the following, a special attention is paid to minimally invasive internal fixation techniques for management of sacral bone injuries.

During osteosynthesis, the fractured bone parts are repositioned and the applied orthopaedic fixators prevent their relative motion. A set of ten fixation techniques is examined and a unilateral transforaminal sacral bone fracture (Denis type II [2]) is selected as the reference case for the study. The studied fixation techniques utilise a single or a combination of the four following orthopaedic fixators: iliosacral screw (ISS) [3], transiliac internal fixator (TIFI) [1], transiliac plate (TP) [5] or sacral bar (SB) [4].

The geometry of the computational model is developed based on CT scans of orthopaedic models of male pelvis. These solid foam models are also used in the experimental campaing that provides input data for validation of the numerical simulations. The experiments study a mechanical response of the model pelvic bones without fracture and a response of fractured bones with a selected fixation technique under physiological loading. The computational model itself is based on the finite element method. An example of the pelvic model geometry and the related computational mesh is provided in Fig. 1.

Due to the fact that each fixation technique is tested using orthopaedic plastic models, variations in cadaveric samples of pelves are avoided. Thus both experimental and computational studies provide a direct comparison of the stability of selected pelvic ring fixations. All pelvic models are tested in an intact condition as well as after creation of artificial unilateral transforaminal fracture and application of the selected fixation technique by an orthopaedic surgeon. In addition, the mechanical properties of the material, the orthopaedic models are made of, are determined experimentally during an extra set of tensile and compression tests.

Absolute and relative motion of the bone structures is examined, a symmetry of bone deformations along the median sacral crest is assessed, an evolution of the fracture line is tracked and a relative displacement of the fractured bone parts is quantified. The ratio between the stiffness of the treated pelvic structure and the stiffness of the intact model (each fixation technique is tested using an extra pelvic model) is determined. The gathered data are used to evaluate the stability of each applied fixation technique.

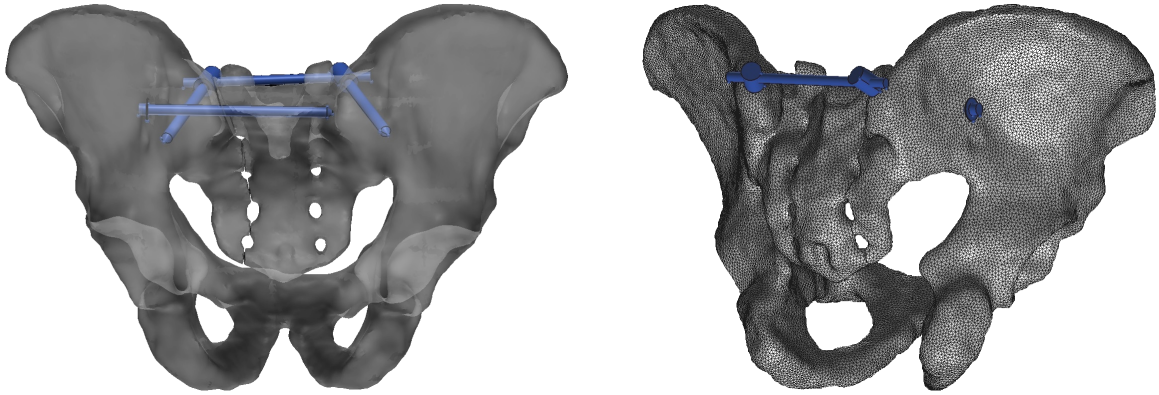

Fig. 1. The three-dimensional geometry reconstruction based on CT scans (*left*) and the computational mesh for the finite element analysis (*right*) of the fractured pelvis model with the TIFI+ISS fixation technique applied

In the experiments, a quasi-static loading is applied. The computational model reflects the experimental setup and material properties and the problem of elastostatics is solved using a finite element solver. The interaction of bone parts along the fracture line is modelled by a standard surface-to-surface contact algorithm with a finite sliding formulation and a non-zero friction. Results of the numerical simulations are compared to the experimental data and an analysis of the stability of the applied fixation techniques is provided.

Acknowledgements

This work is supported by the European Regional Development Fund-Project "Application of Modern Technologies in Medicine and Industry" (No. CZ.02.1.01/0.0/0.0/17_048/0007280) and by the project LO1506 of the Czech Ministry of Education, Youth and Sports under the program NPU I.

References

[1] Dienstknecht, T., Berner, A., Lenich, A., Zellner, J., Mueller, M., Nerlich, M., Fuechtmeier, B., Biomechanical analysis of a transiliac internal fixator, International Orthopaedics 35 (12) (2011) 1863-1868.

[2] Fakler, J.K.M., Stahel, P.F., Lundy, D.W., Classification of Pelvic Ring Injuries. In: Fractures of the pelvis and acetabulum, W.R. Smith, B.H. Ziran, S.J. Morgan (eds.), CRC Press, Boca Raton, 2007, pp. 11-26.

[3] Giráldez-Sánchez M. A., Lázaro-Gonzálvez, Á., Martínez-Reina, J., Serrano-Toledano, D., Navarro-Robles, A., Cano-Luis, P., Fragkakis, E.M., Giannoudis, P.V., Percutaneous iliosacral fixation in external rotational pelvic fractures. A biomechanical analysis, Injury 46 (2) (2015) 327-332.

[4] Gorczyca, J.T., Varga, E., Woodside, T., Hearn, T., Powell, J., Tile, M., The strength of iliosacral lag screws and transiliac bars in the fixation of vertically unstable pelvic injuries with sacral fractures, Injury 27 (8) (1996) 561-564.

[5] Suzuki, T., Hak, D.J., Ziran, B.H., Adams, S.A., Stahel, P.F., Morgan, S.J., Smith, W.R., Outcome and complications of posterior transiliac plating for vertically unstable sacral fractures, Injury 40 (4) (2009) 405-409.

COMPUTATIONAL MECHANICS 2018
34th conference with international participation
Srní
October 31 - November 2, 2018

Development of a simple helmet finite element model

W. Lyu [a,c], T. Bońkowski [b], L. Hynčík [b,d]

[a] NTIS – New Technologies for the Information Society, Faculty of Applied Sciences, University of West Bohemia, Technická 8, 301 00 Plzeň, Czech Republic
[b] Faculty of Applied Sciences, University of West Bohemia, Technická 8, 301 00 Plzeň, Czech Republic
[c] College of Mechanical Engineering, Tianjin University of Science and Technology, 1038 Dagu Nanlu, Hexi District, 300222, P. R. China
[d] New Technologies – Research Centre, University of West Bohemia, Univerzitní 8, 301 00 Plzeň, Czech Republic

Motorcycle riders belong to the group of so called vulnerable road users, which protection against an impact is an issue due to the multi-directional loading and the complex kinematics due to the impact. Virtual biomechanical human body models play an important role to assess injuries especially for such complex scenarios.

The major motorcycle rider's personal protective equipment is the helmet. There are not many numerical models of the motorcycle helmet available, which is probably caused by the fact that each helmet on the market has a different design and the condition for any helmet is just to fulfil the territory dependent regulations [7].

Whilst Deck et al. [2] used their model for helmet optimization based on the head injury assessment, Fernandez et al. [3] developed a concrete commercial road helmet model for its evaluation. The model developed by Ghajari et al. [4, 5] was used for the evaluation of the head response and the effect of the body influence in oblique impacts and also for the diverse population based Head Injury Criterion HIC assessment by Bońkowski [1]. Pavlata [6] used his model for the accident reconstruction.

The present work concerns the simple helmet finite element model development and validation for the European regulation [9] to be coupled to the existing human body model for motorcycle riders' safety assessment. The advantage of the helmet is the low calculation time step by fulfilling the ECE R22.05 regulation [9]. For the geometry, the AVG-T2 helmet [4, 5] was taken as a pattern. The finite element mesh was developed in order to be consistent with the human body model [8], which would be coupled to the helmet for future analyses. The helmet is composed of two parts, namely the outer shell with the thickness equal to 4 mm and the inner protective padding with the thickness of 40 mm. The material data were used the same as published by Deck et al. [2].

Each helmet entering the market must fulfil the ECE-R22.05 regulation [9], which concerns the dynamic test of the retention system, the rigidity test, the shock absorption test and the resistance to penetration visor test. For the head protection against an impact, the shock absorption test is done. According to the regulation, the helmet with the headform inside is dropped against an anvil with a velocity of 7.5 m/s. According to the ECE R22.05 regulation, the M size headform having the mass equal to 5.6 kg was used for the developed helmet size. Two anvils (flat and kerbstone) and four impact configurations points are defined. Fig. 1 shows the four impact configurations for the flat anvil.

The developed helmet is tested for 8 impact configurations (4 impact directions for both anvils). The ECE R22.05 regulation [9] defines, that the maximum acceleration must not exceed 275 g and the maximum HIC must not exceed 2400 for each impact and the helmet fulfils the requirement.

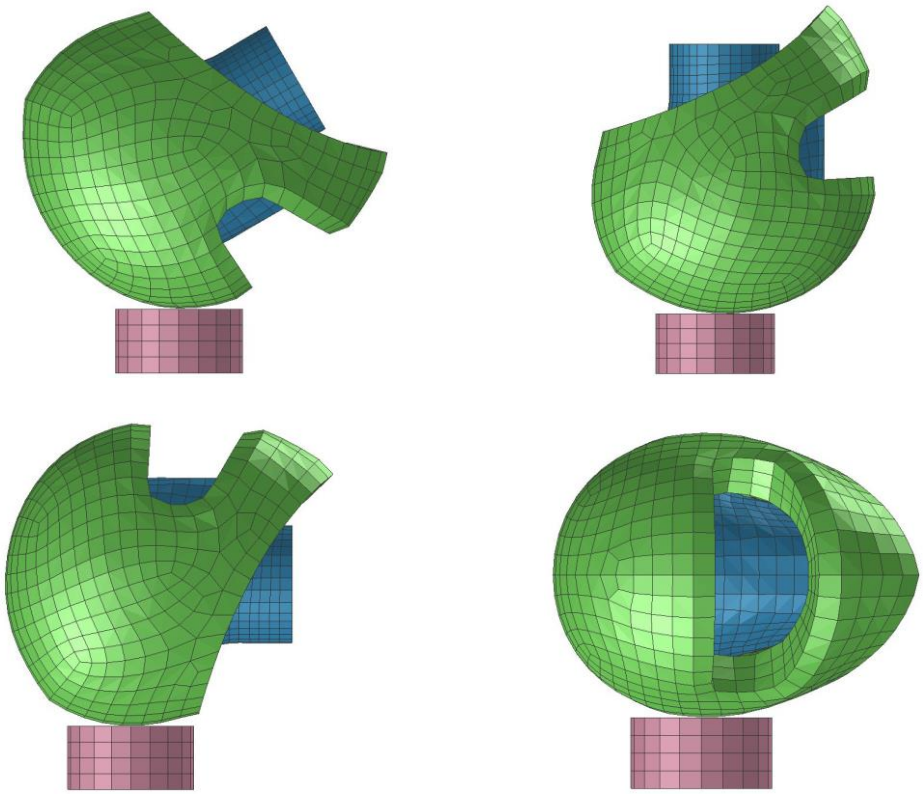

Fig. 1. Four helmet impact configurations against a flat anvil

Acknowledgements

W. Lyu was supported by the project LO1506 of the Czech Ministry of Education, Youth and Sports. L. Hynčík was supported by the project LTC17001 as the national link to the COST Action TU1407. T. Bońkowski was supported by the project SGS-2016-059.

References

[1] Bońkowski, T., Hynčík, L., Šoltés, L., Motorcycle helmets: the population diversity influence on head injury criterion assessment, Proceedings of the IRCOBI conference, Malaga, 2017, pp. 218-219.

[2] Deck, C., Willinger, B., Baumgartner, R., Helmet optimisation based on head-helmet modelling, Transactions on the Built Environment 67 (2003), pp. 319-328.

[3] Fernandes, F.A.O., et al., Finite element analysis of helmeted impacts and head injury evaluation with a commercial road helmet, Proceedings of the IRCOBI conference, Gothenburg, 2013, pp. 431-442.

[4] Ghajari, M., et al., Influence of the body on the response of the helmeted head during impact, International Journal of Crashworthiness 16 (3) (2011) 285-295.

[5] Ghajari, M., et al., Effects of the presence of the body in helmet oblique impacts, Accident Analysis and Prevention 50 (2013) 263-271.

[6] Pavlata, P., Calculation of motorcycle helmets according to ECE 22.05, Proceedings of the VPS User Forum, 2015.

[7] Smith, T.A., Kebschull, S.A., Comparison of the impact performance of motorcycle helmets: qualified to three different international motorcycle helmet standards, Proceedings of the IRCOBI ASI conference, Seoul, 2016, pp. 12-13.

[8] Vychytil, J., et al., Scalable multi-purpose virtual human model for future safety assessment, SAE Technical Paper 2014-01-0534, 2014.

[9] Regulation ECE R22.05, Uniform provisions concerning the approval of protective helmets and of their visors for drivers and passengers of motor cycles and mopeds, 2002.

COMPUTATIONAL MECHANICS 2018
34th conference with international participation
Srní
October 31 - November 2, 2018

Solution of bending and contact problems for Gao beam using control variational method

J. Machalová[a], J. Radová[a]

[a] *Department of Mathematical Analysis and Applications of Mathematics, Faculty of Science, Palacký University Olomouc, Czech Republic*

This contribution deals with a nonlinear beam model which was published by Gao in [1] and it is known as the *Gao beam*. Let us denote E the Young's modulus, I the area moment of inertia, q the distributed transverse load, ν the Poissons ratio, L the length of the beam, $2\mathrm{h}$ its height, while its width is b and it is considered as a unit. An axial force P is considered acting at the point $x = \mathrm{L}$. The Gao beam model is described by the fourth-order differential equation

$$EI\,w'''' - E\alpha(w')^2 w'' + P\mu\,w'' = f \qquad \text{in } (0,\mathrm{L}),$$

where w is an unknown deflection of the beam and

$$I = \frac{2}{3}\mathrm{h}^3\mathrm{b}, \quad \alpha = 3\mathrm{hb}(1-\nu^2), \quad \mu = (1+\nu)(1-\nu^2), \quad f = (1-\nu^2)q.$$

The axial load P is constant, $P > 0$ causes compression of the beam and $P < 0$ tension. We will focus on a contact problem for Gao beam and foundation which is situated under the beam. The gap between them is described by the function $\mathrm{g} \leq 0$. For simplicity it will be considered constant. The foundation is assumed to be deformable and governed by the Winkler one-parametric model with a foundation modulus k_F. The Gao beam equation is now modified in the following way

$$EI\,w'''' - E\alpha(w')^2 w'' + P\mu\,w'' = f + T(w) \qquad \text{in } (0,\mathrm{L}),$$

where $T(w)$ represents contact forces between the beam and the foundation and $T(w) = c_F(\mathrm{g}-w)^+$, with $c_F = (1-\nu^2)k_F$ and $v^+(x) = \max\{0, v(x)\}$. The variational formulation of the considered contact problem reads

$$\begin{cases} \text{Find } w^* \in V \text{ such that} \\ \Pi(w) = \min\limits_{v\in V} \Pi(v), \end{cases} \tag{1}$$

where $\Pi(v)$ is the functional of total potential energy in the form

$$\Pi(v) = \frac{1}{2}\int_0^{\mathrm{L}} EI\,(v'')^2 \mathrm{d}x + \frac{1}{12}\int_0^{\mathrm{L}} E\alpha\,(v')^4 \mathrm{d}x - \frac{1}{2}\int_0^{\mathrm{L}} P\mu\,(v')^2 \mathrm{d}x - \\ - \int_0^{\mathrm{L}} fv\,\mathrm{d}x + \frac{1}{2}\int_0^{\mathrm{L}} c_F\,((\mathrm{g}-v)^+)^2 \mathrm{d}x$$

and V is the space of kinematically admissible displacements.

The minimization problem (1) will be solved by using the control variational method. The main idea is to transform the problem into another one which is easier to solve. It is motivated by [4], where the contact of a cantilever Euler-Bernoulli beam with an obstacle was described. We will extend this conception for nonlinear Gao beam and for four different types of boundary conditions by introducing three different transformations. Each of them consists of several parts, firstly the transformation of variable and the loading function, secondly the definition of the state equation and finally the transformation of the total potential energy functional. For each transformation of variable the Lagrangian can be constructed and the corresponding saddle point equations enable us to define control variable u and state problem. Both of them are used in transformation of functional $\Pi(v)$, so as a result we have a new functional $J(w,u)$. After this process we are able to define a new problem, so called *optimal control problem*

$$\begin{cases} \text{Find } u^* \in U_{ad} \text{ such that} \\ J(w(u^*),u^*) = \min\limits_{u\in U_{ad}} J(w(u),u), \\ \text{where } w(u) \text{ solves the state problem} \\ \text{together with prescribed boundary conditions} \\ \text{and for control value } u \in U_{ad}. \end{cases}$$

The set of admissible controls is defined by

$$U_{ad} = \left\{u \in L^2((0,L)) : |u(x)| \le C \text{ a.e. in } (0,L)\right\},$$

where constant $C > 0$ is big enough. Under some assumptions the optimal control problem has the unique solution u^* and the function $w^* := w(u^*)$ solves the corresponding variational problem, see [2, 3].

The numerical realization of the optimal control problem consists of evaluation of the state problem and simultaneous minimization of the functional. State problem will be solved by using finite element method and will not make any problems. For minimization process it will be used *conditioned gradient method*. For a given control value u^k and computed state $w^k := w(u^k)$, the next iteration u^{k+1} is found by determining a descent direction and a suitable step size. The descent direction will be chosen as an anti-gradient of $J(w,u)$, which will be evaluated by means of the adjoint problem technique [5].

Acknowledgement

This work was supported by the IGA UPOL grant IGA_Prf_2018_024.

References

[1] Gao, D.Y., Nonlinear elastic beam theory with application in contact problems and variational approaches, Mechanics Research Communications 23 (1) (1996) 11-17.

[2] Machalová, J., Netuka, H., Control variational method approach to bending and contact problems for Gao beam, Applications of Mathematics 62 (6) (2017) 661-677.

[3] Machalová, J., Netuka, H., Solution of contact problems for Gao beam and elastic foundation, Mathematics and Mechanics of Solids 23 (3) (2018) 473-488.

[4] Sofonea, M., Tiba, D., The control variational method for contact of Euler-Bernoulli beams, Bulletin of the Transilvania University of Braşov, Series III. Mathematics, Informatics, Physics 2 (2009) 127-136.

[5] Tröltzsch, F., Optimal control of partial differential equations: Theory, methods and applications, American Mathematical Society, Providence, Rhode Island, 2010.

COMPUTATIONAL MECHANICS 2018
34th conference with international participation
Srní
October 31 - November 2, 2018

Biomechanical study of bone-dental implant interactions using patient-specific approach and multiscale computational modeling

P. Marcián [a], B. Thomková [a], Z. Florian [a], L. Borák [a]

[a] *Faculty of Mechanical Engineering, Brno University of Technology, Antonínská 548/1, 601 90 Brno, Czech Republic*

Dental implants are modern solutions for the cases of lost tooth replacements. Although the application of dental implants is relatively efficient solution, complications and failure of dental implant might occur [3]. This contribution is focused on the mechanical interaction of dental implants with the bone tissue with respect to different types of cancellous bone model. The solution is associated with a broader range of dental-implant-related clinical problems. The effective processing of data from CT and micro-CT devices enables achieving a high level of computational models that include detailed trabecular bone architecture as well as non-homogeneous material property distribution. Using such models allows local biomechanical analyses that are inevitable for better understanding of bone-implant contact (BIC) mechanisms.

Full human mandible was scanned using conventional CT device (pixel size of 0.5 mm) and a mandibular segment was scanned using micro CT scanner (General Electric v tome x L240, Boston, Massachusetts, USA; pixel size of 25 μm). Branemark implant was used in this study (diameter 3.3 mm and length 11.5 mm). Creation of geometry model is described in detail elsewhere [3]. To focus on the BIC in detail and in an effective way, the sub-modelling technique was adopted meaning the coarse model was used to provide boundary conditions for more detailed sub-model, see Fig. 1.

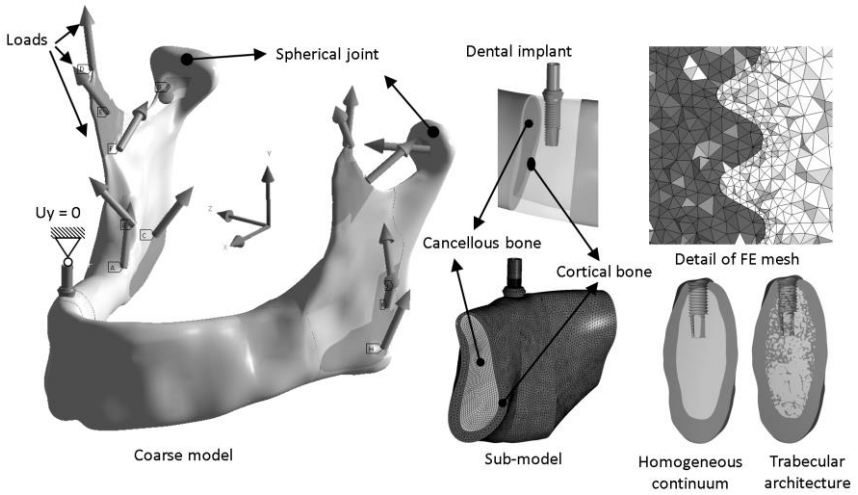

Fig. 1. Coarse model with load, sub-model, detailed mesh, model of cancellous bone

The sub-model consisted of a mandible segment with one implant of an approximate length 50 mm. Sufficiently fine mesh (0.05 mm) was defined around the threaded parts using SOLID187 elements, see Fig.1. All interacting components were connected to each other using contact elements TARGE160 and TARGE174. The total number of nodes was around 250,000 nodes for coarse model and 20 mil nodes for sub-model.

The materials of the implant and the cortical bone were assumed to be linearly elastic, homogeneous and isotropic (E_{imp} = 110000 MPa, μ_{imp} = 0.3; E_{cor} = 15000 MPa, μ_{cor} = 0.3) [3]. Cancellous bone in the sub-model was represented in three ways: 1. Assuming the cancellous bone to be homogeneous continuum with isotropic properties (E = 2840 MPa, μ = 0.3) [2]; 2. Same as 1 except for using orthotropic properties (E_x = 2000 MPa, E_y = 3180 MPa, E_z = 3340 MPa, μ_{xy} = 0.14, μ_{yz} = 0.21, μ_{xz} = 0.19, G_{xy} = 579 MPa, G_{yz} = 515 MPa, G_{xz} = 493 MPa) [2]; 3. Considering trabecular architecture (E_{trab} = 15000 MPa, μ_{trab} = 0.3). In the coarse model, the mandible was loaded by forces mimicking the muscle activity [1].

To investigate the influence of the cancellous bone type on the implant behavior, dental implant was evaluated for von Mises stress and total displacements. The stress and displacement distributions are shown in Fig. 2. The displacements, maximum stresses as well as the stress isolines indicate that the choice of cancellous bone representation has an insigificant effect on the implant results. Therefore, as far as the implant structural behavior is concerned, all investigated cancellous bone model types provide the same results if the stiffnesses of those bone types are equivalent.

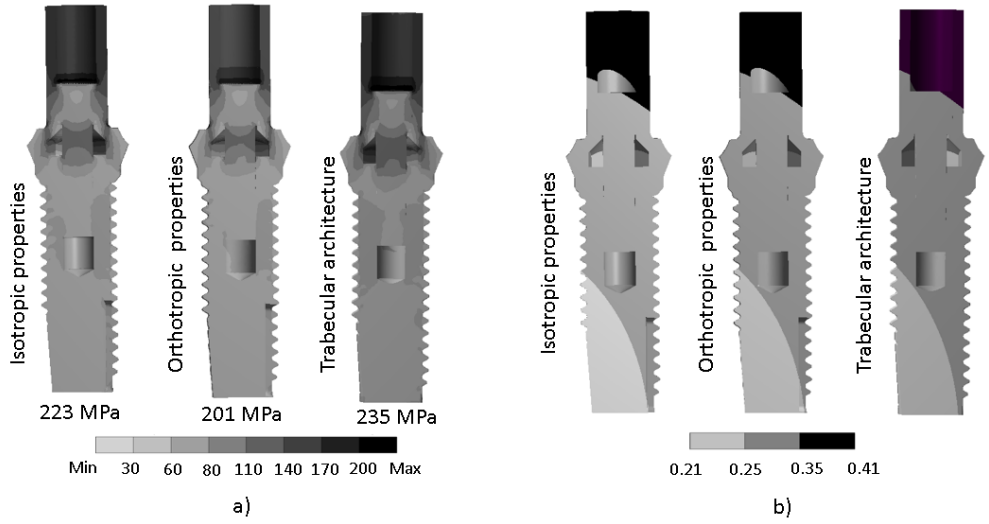

Fig. 2. a) von Mises stress [MPa] in dental implant; b) total displacement [mm]

Acknowledgements

The research was supported by the Czech Science Foundation: Grant No. 16-08944S.

References

[1] Korioth, T.W.P., 3-dimensional finite-element stress-analysis of the dentate human mandible, American Journal of Physical Anthropology 88 (1992) 69-96.

[2] Marcian, P., Losak, P., Kaiser, J., Borak, L., Estimation of orthotropic mechanical properties of human alveolar bone, Proceedings of the 22nd conference Engineering Mechanics, Svratka, 2016, pp. 370-373.

[3] Wolff, J., Narra, N., Antalainen, A.K., Valášek, J., Kaiser, J., Sándor G.K., Marcián, P., Finite elements analysis of bone loss around failing implants, Materials and Design 61 (2014) 177-184.

COMPUTATIONAL MECHANICS 2018
34th conference with international participation
Srní
October 31 - November 2, 2018

FEM simulation of elasto-plastic tube indentation

B. Marvalová [a], T. Hruš [a] and A. Hrouda [a]

[a] *Technical university of Liberec, Studentská 2, 461 17 Liberec, Czech republic*

Paper provides the summary of the FEM simulation of elasto-plastic strains and stresses in the course of the local indentation of a steel pipe by a spherical indenter. The FEM calculation was performed according to the recommendation of API 579-1 / ASME FFS-1 2007 [1] for Level 3 dent assessment. Series of 65 FE calculations of the elasto-plastic state of the indented tubes was performed. The combination of three tube diameters D = 508, 920 and 1420 mm with the ratios between the diameter and the wall thickness D/h = 91, 76, 64, 51 and 37 resp. were used. The diameters of the spherical rigid indenters were 100 and 200 mm, the depth of the indent varied gradually from 75 to 150 mm. The residual stresses and strains in the vicinity of the dent after the relieving of load were determined together with the depth and length of the resulting dent.

The configuration of the experimental loading of the indented tube has two planes of symmetry see Fig. 1. FE simulation model was adjusted as 1/4 of the whole with appropriate symmetrical boundary conditions see Fig. 2. The FE model of tube was supported equally as in the experiment i.e. the support was modeled as the rigid plane with the inclination of 15 degrees. The contacts were defined between the tube and the rigid spherical indenter and between the tube and the rigid support. The loading was controlled by the displacement of the indenter. The elasto-plastic material properties were obtained from the tensile test curve of pipe material which was converted to True Stress – True (Logarithmic) Strain curve for the FE calculation purpose.

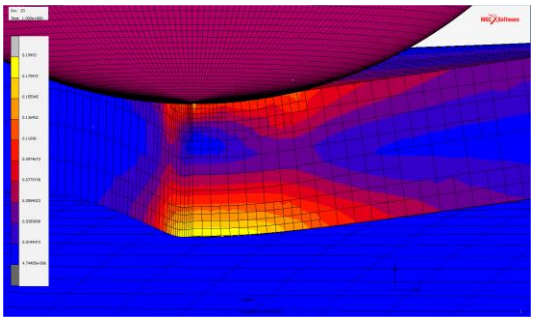

Fig. 1. Strain in contact region

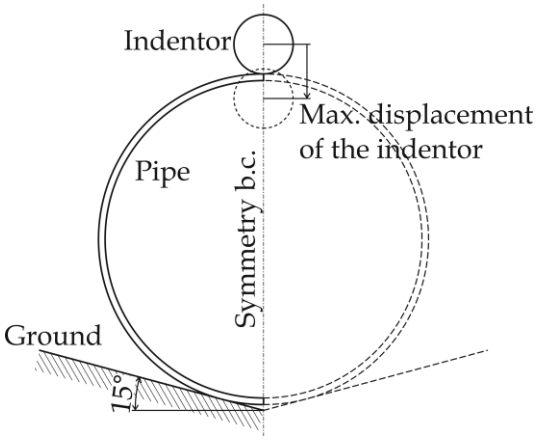

Fig. 2. FE 1/4 model of indentation

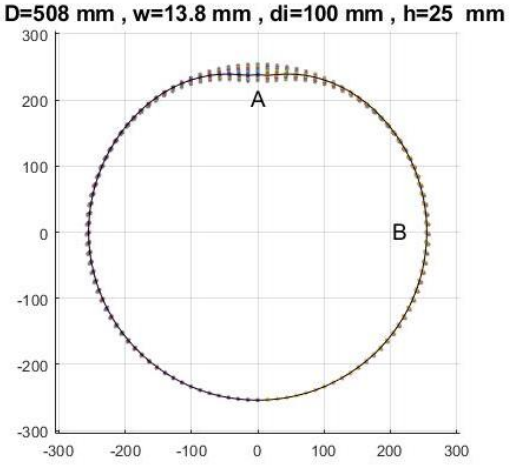

Fig. 3. Tube contour in course of indentation

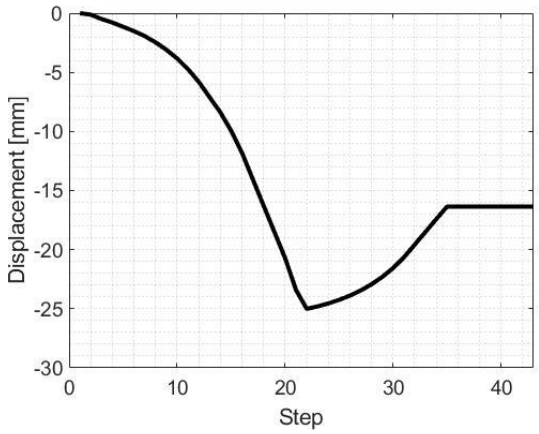

Fig. 4. Displacement of the point A

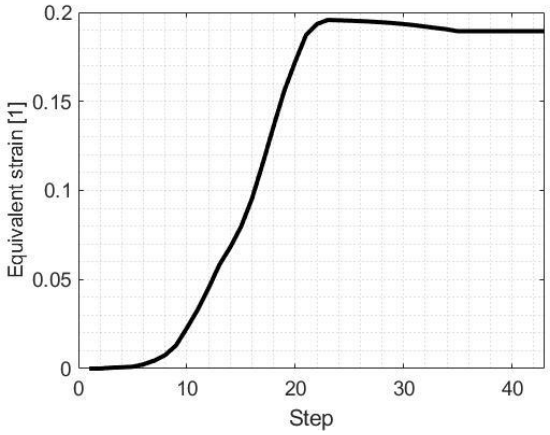

Fig. 5. Equivalent strain in point A

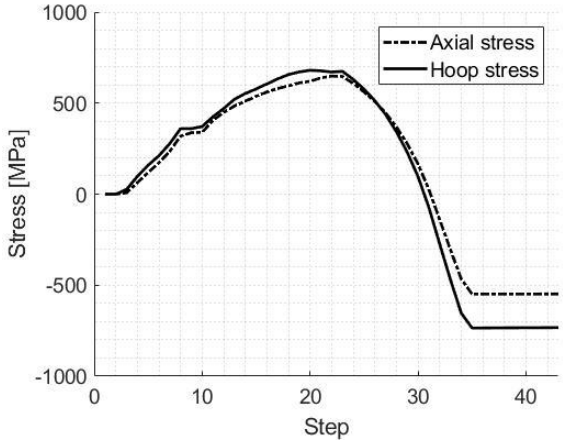

Fig. 6. Principal stresses in point A

FE mesh was created using 8-node hexahedron elements which allow the local adaptability of mesh that is necessary in large strains. Each single FE model from a series of 65 cases was created using a Python script which comprised the combinations of the tube diameter D, the wall thickness w, the indenter diameter di and the immersion depth of indenter h.

The evaluation of the FE results and the graphic processing were performed in Matlab. Some results for a particular case are shown in the Fig. 3 and 4 where the deformed contour of central cross-section is captured at the different steps of loading together with the displacement of the point A located inside the tube under the indenter. The successive equivalent strain and principal stresses at this point are shown in Fig. 5 and 6. The residual deformation of the tube and the residual strain and stresses are also apparent in these figures.

Acknowledgements

This work is supported by the SGS 2018 TUL grant 21120 provided by the Ministry of Education, Youth and Sports of the Czech Republic.

References

[1] Osage, D.A., Janelle, J.L., A joint API/ASME fitness-for-service standard for pressurized equipment, Proceedings of the Pressure Vessels and Piping Conference, Illinois, 2008, pp. 777-791

COMPUTATIONAL MECHANICS 2018
34th conference with international participation
Srní
October 31 - November 2, 2018

Numerical simulation of free-surface flow over a weir with non-reflective outlet boundary conditions

J. Musil[a,b]

[a] *Faculty of Mechanical Engineering, CTU in Prague, Karlovo nám. 13, 121 35 Praha, Czech Republic*
[b] *Institute of Thermomechanics, Czech Academy of Sciences, 182 00 Praha, Dolejškova 5, Czech Republic*

The non-reflective boundary conditions are essential ingredient in the procedure of computational domain restriction where presence of artificial/open boundaries requires prescription of appropriate boundary conditions in order to obtain numerical solution equivalent to the original one. Thus, these boundary conditions not only lead to reduction of computational cost by means of computational domain restriction but also allow to prescribe physical quantities on artificial boundary in correspondence with analytic form of solution.

This contribution is focused on non-reflective boundary conditions for two-phase incompressible VOF [4] method, which is mathematical model for Navier-Stokes equations described by following system of equations:

$$\partial_t(\rho\mathbf{u}) + \boldsymbol{\nabla}\cdot(\rho\mathbf{u}\otimes\mathbf{u}) + \boldsymbol{\nabla}p = \boldsymbol{\nabla}\cdot\boldsymbol{\tau} + \rho\mathbf{g}, \tag{1}$$

$$\boldsymbol{\nabla}\cdot\mathbf{u} = 0, \tag{2}$$

$$\partial_t\alpha + \boldsymbol{\nabla}\cdot(\alpha\mathbf{u}) = 0. \tag{3}$$

Here $0 \leq \alpha \leq 1$ is the liquid fraction in the mixture ($\alpha = 0$ corresponds to air, $\alpha = 1$ corresponds to water) and the density of the mixture is $\rho = \alpha\rho^{water} + (1-\alpha)\rho^{air}$. The symmetric tensor $\boldsymbol{\tau}$ expresses tangential stresses and $\mathbf{g}$ is the acceleration due to gravity.

The non-reflective boundary conditions for VOF model have been developed by employing similarity with theory of one-dimensional shallow water flows and afterwards have been implemented into the open-source package OpenFOAM [3]. This procedure was already presented at the Computational Mechanics conference in 2017 [1] or also in [2].

Whereas performance of these boundary conditions was not yet tested on outlet boundaries the aim here is to present results of numerical simulations of water flow over a weir with artificial boundary at the outflow. The computation has been performed on two-dimensional quadrilateral structured grid with 31 720 finite volume cells. The initial condition was set to $\mathbf{u} = \mathbf{0}$ and to $p + h\rho g$ as hydrostatic pressure in entire domain, α according to Fig. 1. At the bottom the no-slip boundary condition for $\mathbf{u}$ and homogeneous Neumann condition for $p + h\rho g$ and α was prescribed. At the inlet boundary (left) there was set homogeneous Neumann condition for $p + h\rho g$ and coupled boundary conditions for $\mathbf{u}$ and α respecting prescribed volumetric flow as 25 m^3/s. The top boundary is equipped with modified homogeneous Neumann conditions for $\mathbf{u}$ and α and total pressure is set as zero here. At the outlet (right) there were prescribed four variants of boundary conditions for $\mathbf{u}$ and α:

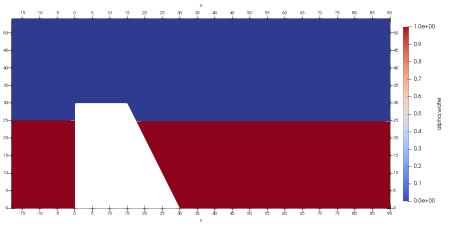

Fig. 1. Initial condition for α

I) homogeneous Neumann conditions for both $\mathbf{u}$ and α
II) OpenFOAM coupled boundary conditions allowing water height (i.e. α) to vary according to the prescribed volumetric flow rate (here set as negative value of inlet flow rate)
III) homogeneous Neumann condition for α, non-reflective boundary condition for $\mathbf{u}$
IV) non-reflective boundary conditions for both $\mathbf{u}$ and α.

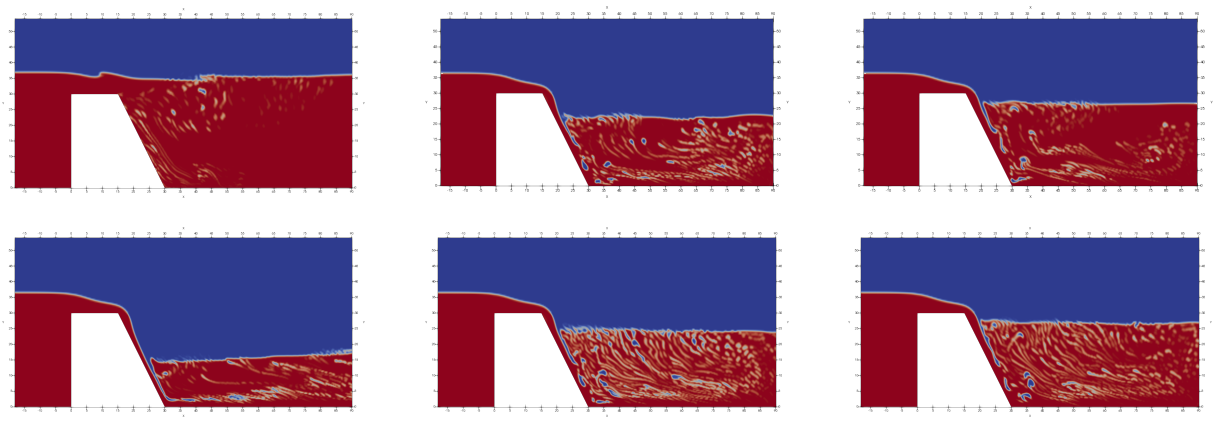

Fig. 2. Water height (α) in $t = 50$ s (upper row) and $t = 130$ s (lower row)

In the first column of Fig. 2 one can see I) variant of boundary conditions which lead to un-physical solution with large oscillations of water level. The second column shows variant II) which seems to perform well, but there is a problem with velocity at boundary being fixed according to the inflow and thus not respecting solution in the vicinity of boundary. In the third column III) variant is shown. Here the non-reflective condition for velocity gives satisfying results. Note that in all three aforementioned cases homogeneous Neumann condition (or its equivalent) for α was prescribed, though it is incorrect due to the fact that transport equation for α is 1st order PDE. The last, IV) variant of boundary conditions led to solver failure. That might have been caused by segregated approach employed in OpenFOAM for solving equations (1) and (3).

Further, the III) variant of boundary conditions was tested at the outlet of 3D case of a weir with more complex geometry.

Acknowledgement

This work was supported by the Grant Agency of the Czech Technical University in Prague, grant No. SGS16/206/OHK2/3T/12.

References

[1] Fürst, J., Musil, J., Development of non-reflective boundary condition for free-surface flows, Proceedings of the conference Computational Mechanics, Špičák, University of West Bohemia, 2017.

[2] Musil, J., Non-reflective boundary conditions for free-surface flows, Master thesis, Czech Technical University in Prague, Prague, 2018.

[3] Weller, H.G., Tabor, G., Jasak, H., Fureby, C., A tensorial approach to computational continuum mechanics using object-oriented techniques, Computers in Physics 12 (6) (1998), doi: 10.1063/1.168744.

[4] Yeoh, G.H., Jiyuan, T., Computational techniques for multiphase flows, Elsevier, 2009, pp. 215-232.

COMPUTATIONAL MECHANICS 2018
34th conference with international participation
Srní
October 31 - November 2, 2018

Elimination of edge-chipping phenomenon during rotary ultrasonic drilling

M. Naď, L. Kolíková, R. Ďuriš, Š. Šimon

[a] *Faculty of Materials Science and Technology in Trnava, Slovak University of Technology, J. Bottu 25, 917 24 Trnava, Slovak Republic*

Advanced materials such as ceramics, composites and other materials with superior properties are increasingly used in industries such as aerospace, automotive, electronics but they are also used in medical applications. Mechanical properties of such materials are characterized by specific properties such as high hardness, excellent wear resistance and brittleness. However, these properties usually cause difficulties and complications in machining and obtaining the desired shapes and dimensions of the products from these materials. As mentioned, these materials are hardly machinable by conventional machining processes. For these reasons, it is very important to develop efficient machining processes that will ensure the quality of the machining process and the energy and cost efficiency of machining.

One of the advanced processes used for drilling holes into the above mentioned materials is rotary ultrasonic drilling (RUD). This process can be classified as a hybrid process combining grinding process using diamond tool that simultaneously performs axial vibrations with frequency at the ultrasound level. The RUD process is characterized by sufficiently high removal rate while cutting pressures remain low with relatively small surface damage and strength degradation. Significant attention is paid to the processes and problems arising during the rotary ultrasonic drilling from both the theoretical and experimental points of view. One of the important problems that has to be solved in the RUD process is the formation of undesirable phenomenon called edge-chipping (Fig. 1).

During a hole drilling, the hole bottom thickness is changing and consequently an annulus plate area of the drilled hole bottom is subjected to transition through the resonance states. This resonant state can be considered as one of the important effects that leads to occur the ”edge-chipping“ phenomenon. As a consequence of this process, when the drilling tool is finishing the hole, the bottom edge of the hole is degraded by breaking the edge. In order to eliminate this phenomenon or to reduce the size of the edge damage of hole, it is necessary to examine the stress-strain state that arises as a result the ultrasonic vibration, workpiece structure and shape parameters of the drilling tool. The maximum stress states are analysed in critical zones of the drilled hole. The dependence of equivalent stresses on the edge radii of drilling tool and on the change in the bottom thickness of drilling hole is investigated.

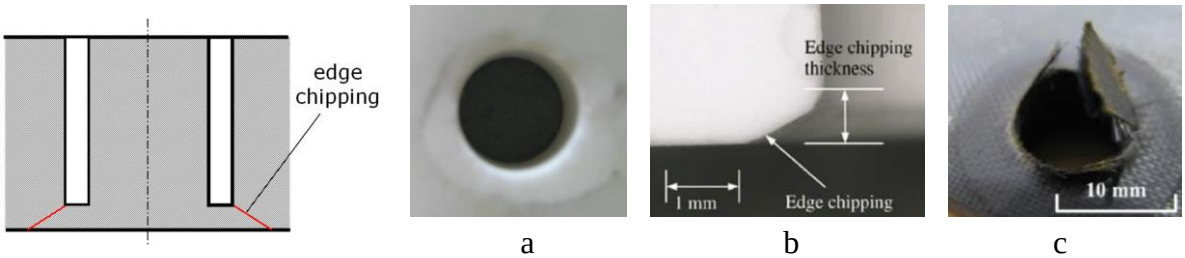

a b c

Fig. 1. Typical cases of edge-chipping formation (a - [4], b - [1], c - [2])

The edge-chipping phenomenon is investigated in two levels. The first approach is based on an investigation of the influence of the geometric parameters of the drilling tool [3] on the stress-strain state that occurs in the workpiece. The second approach is focused on the purposeful change in the workpiece structure, i.e. the structural modification of the workpiece by means of reinforcing layer (Fig. 2) on the lower surface of the workpiece.

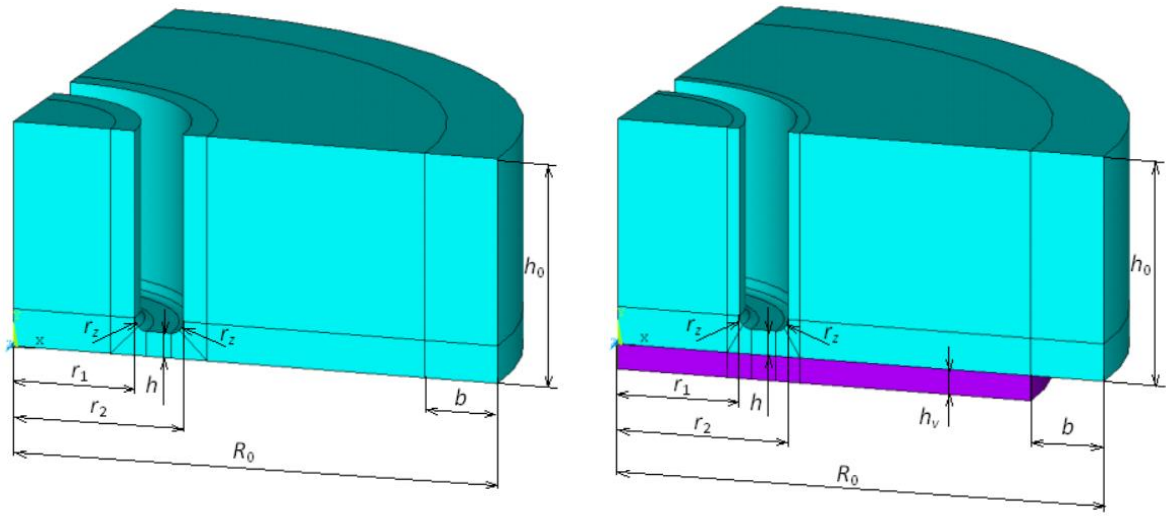

a b

Fig. 2. Model for simulation of RUD process: a - without reinforcing layer, b - with reinforcing layer

Rotary ultrasonic drilling process is a complex process with a large number of input parameters and variables that have to be taken into account in stress-strain analyses. The finite element analysis of RUD process is used to the prediction of edge-chipping phenomenon. The numerical simulation of drilling process using the RUD process are realized using the finite element models corresponding to models shown in Fig. 2. The structural modification effects based on additional reinforcing layers on the stress-strain states and prediction of "edge-chipping" phenomenon occurring during RUD are analysed in this paper.

Acknowledgements

The work was supported by the grant project KEGA 029STU-4/2018 and institutional project IP MTF 1603/2017.

References

[1] Li, Z.C, et al., Edge-chipping reduction in rotary ulrasonic machining of ceramics: finite element analysis and experimental verification, International Journal of Machine Tools and Manufacture 46 (2006) 1469-1477.

[2] Liu, D.F., et al., A cutting force model for rotary ultrasonic machining brittle materials. International Journal of Machine Tools and Manufacture 52 (2012) 77-84.

[3] Nad, M., Kolíková, L., Rolník, L., Ďuriš, R., Analysis of vibration effects on edge-chipping occurence during rotary ultrasonics drilling, Proceedings of the 14th International Conference "Dynamical Systems - Theory and Applications", Lodz, Poland, 2017, pp. 335-344.

[4] Zvončan, M., Research of edge-chipping in rotary ultrasonic machining., Ph.D. thesis, Slovak University of Technology, Faculty of Materials Science and Technology in Trnava, Trnava, 2012.

COMPUTATIONAL MECHANICS 2018
34th conference with international participation
Srní
October 31 - November 2, 2018

Influence of humidity of environment on fatigue crack propagation in railway axle

L. Náhlík [a,b], P. Pokorný [a], T. Vojtek [a], P. Hutař [a]

[a] CEITEC IPM, Institute of Physics of Materials, Czech Academy of Sciences, Žižkova 22, 616 62 Brno, Czech Republic
[b] Institute of Solid Mechanics, Mechatronics and Biomechanics, Brno University of Technology, Techniocká 2, 616 69 Brno, Czech Republic

The presentation is devoted to the crack propagation in the railway axle made of EA4T steel. The propagating fatigue crack is subjected to the different kinds of crack closure. The paper describes contribution of plasticity induced crack closure, roughness induced crack closure and oxide induced crack closure to the total crack closure and their influence on the residual fatigue lifetime of the railway axle. Special attention is devoted to the influence of humidity of the air to the fatigue crack propagation and railway axle residual fatigue lifetime. Fig.1 shows detail of fracture surfaces with different width of oxide layers occurred during fatigue testing under different humidity of laboratory air. It is evident the increase of oxides on the fracture surfaces with the increase of absolute air humidity. The experimental results were obtained using chamber developed at Institute of Physics of Materials CAS for fatigue testing machine, which enables fatigue tests under different air humidity. The chamber used is shown in Fig. 2.

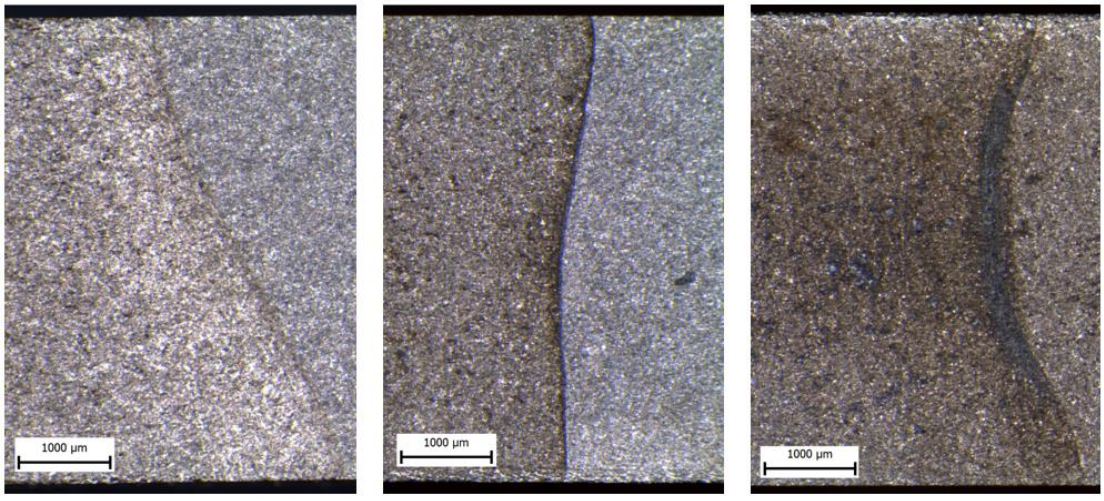

Fig. 1. Fracture surfaces of specimens tested under different humidity conditions (abbreviations RH = relative humidity, AH = absolute humidity)

Experimentally measured data were used for following analysis of residual fatigue lifetime of the railway axle designed in Bonatrans company. All necessary numerical calculations based on finite element method (stress-strain analysis, calculations of fracture parameters, etc.) were performed and own procedure for determination of residual fatigue lifetime of railway axles was applied. Detailed description of the procedure can be found in [1]. It can be

concluded that different air humidity leads to the important change of fatigue crack closure due to existence of oxide layers on the fracture surfaces. The existence of oxides result in important change of residual fatigue lifetime, therefore for reliable estimation of residual fatigue lifetime air humidity should be taken into account during material testing.

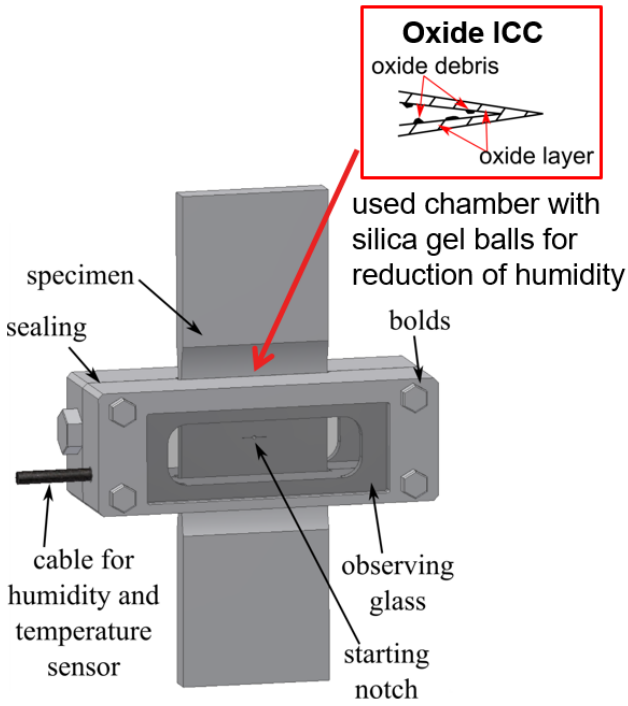

Fig. 2. Chamber for fatigue crack testing under different air conditions (author P. Pokorný, Institute of Physics of Materials CAS)

The presentation contributes to the better understanding of fatigue damage of engineering structures and higher reliability of railway axles.

Acknowledgements

This work was supported through the project m-IPMinfra No. CZ.02.1.01/0.0/0.0/16_013/0001823 of the Ministry of Education, Youth and Sports of the Czech Republic and by research infrastructure IPMinfra supported by the project No. LM2015069 of the same provider.

References

[1] Pokorný, P., Vojtek, T., Náhlík, L., Hutař, P., Crack closure in near-threshold fatigue crack propagation in railway axle steel EA4T, Engineering Fracture Mechanics 185 (2017) 2-19.

COMPUTATIONAL MECHANICS 2018
34th conference with international participation
Srní
October 31 - November 2, 2018

Lagrange and Appell-Gibbs approaches in problems of non-holonomic dynamic systems

J. Náprstek[a], C. Fischer[a]

[a] *Institute of Theoretical and Applied Mechanics, CAS v.v.i., Prosecká 76, CZ-190 00 Praha, Czech Republic*

Hamiltonian functional and relevant Lagrange equation system are popular tools in investigation of dynamic systems. Various generalizations enable to extend the class of problems concerned slightly beyond conventional limits of a Hamiltonian system. This strategy is very effective particularly concerning 2D and simpler 3D systems. However, the governing differential systems of most non-holonomic 3D systems suffer from inadequate complexity, when deduced using this way. Any analytical investigation of such a governing system is rather impossible and its physical interpretation can be multivalent. For easier analysis particularly of systems with non-holonomic constraints the Appell-Gibbs approach seems to be more effective providing more transparent governing systems.

Both Lagrangian as well as Appell-Gibbs procedures originate from a balance of internal energy change in time on one hand and external energy supply (e.g. excitation) and dissipation on the other hand. Formulating an adequate functional equivalence a suitable variational principle is applied. It claims that among all admissible shapes of the system reaction, the selected one is that which represents the minimal energy requirement.

This manipulation being based on the third form of the basic equation of dynamics can bring us to the system of Lagrangian equations of the 2nd kind. It reads for dynamic system with n Degrees of Freedom (DOF) as follows:

$$\frac{\mathrm{d}}{\mathrm{d}t}\Big(\frac{\partial \mathcal{T}}{\partial \dot{q}_s}\Big) - \frac{\partial \mathcal{T}}{\partial q_s} + \frac{\partial \mathcal{V}}{\partial q_s} = Q_s + \frac{\partial \mathcal{R}}{\partial \dot{q}_s} + \sum_{r=1}^{l} \lambda_r C_{rs}, \quad s = 1, .., n, \tag{1}$$

where $q_s, s = 1, .., n$ are Lagrange coordinates, $\mathcal{T}, \mathcal{V}$ is kinetic and potential energy, respectively, Q_s are generalized forces, $\mathcal{R}$ is the Rayleigh function representing a potential of damping forces, if it exists. Otherwise individual expressions characterizing more complex laws of the damping should be included. For more information, see either monographs [2, 5] or hundreds of papers, e.g., [3, 4].

The system of equations (1) should be completed by $l < n$ equations of links, which can be expressed in a form inherent to both holonomic/non-holonomic links

$$\sum_{s=1}^{n} C_{rs}\dot{q}_s + D_r = 0,\ r = 1, .., l,\ \mathbf{D} = |D_r(\mathbf{q}, t)|\} \in \mathbb{R}^l\ ,\ \mathbf{C} = |C_{rs}(\mathbf{q}, t)| \in \mathbb{R}^{ln}. \tag{2}$$

Eqs. (1) and (2) represent the system of $n + l$ differential equations with $n + l$ unknowns $\mathbf{q}, \boldsymbol{\lambda}$. After rewriting into the normal form, we obtain the system

$$\dot{\mathbf{u}} = \mathbf{f}(\mathbf{u}, t), \qquad \mathbf{u},\ \mathbf{f} \in \mathbb{R}^{2n}, \tag{3}$$

which includes $2n + l$ equations with $2n + l$ unknowns $\mathbf{q}, \dot{\mathbf{q}}, \boldsymbol{\lambda}$. Functions $\mathbf{f}(\mathbf{u}, t)$ are nonlinear functions (smooth enough) of displacements, time t and system parameters representing geometry and physical properties of the system. If the dynamic system is holonomic and constraints (2) are integrable, then it is (sometimes) possible to reduce the number of unknowns eliminating relevant "fixed" degrees of freedom and multipliers $\boldsymbol{\lambda}$. Then we have $2k$ unknowns, where $k = n - l$.

Let us pay attention to Appell-Gibbs approach. The method follows from the 5th Gaussian form of basic equation of Dynamics, for details see, e.g., [1]. The core consists in the Gibbs function $\mathcal{G}$ and function $\mathcal{H}$

$$\mathcal{G} \;=\; \frac{1}{2}\sum_{r=1}^{k} m_r \ddot{q}_r^2, \quad \mathcal{H} = \mathcal{G} - \sum_{r=1}^{k} Q_r \ddot{q}_r. \tag{4}$$

Take a note that summations (4) reflect only "live" degrees of freedom $k = n - l$. It can be shown, that the governing differential system follows from minimization of the function $\mathcal{H}$ with respect to acceleration coordinates. In other words it holds

$$\frac{\partial \mathcal{G}}{\partial \ddot{q}_r} \;=\; Q_r, \quad r = 1, .., k. \tag{5}$$

The energy dissipation terms on the right side of Eq. (5) are to be added similarly like generalized forces using the virtual works principle. The system (5) should be completed by geometric links (2). The differential system of equations (2) and (5) includes $k+l$ unknowns. It represents the most simple and in the same time the most general form of equations of the dynamic system movement. The form of this system is very simple and it can be used with the same effectiveness to investigation of holonomic as well as non-holonomic systems, as the constraints can represent non-holonomic but also holonomic type of links. Unlike the Lagrangian approach the non-holonomic links do not augment the number of differential equations.

The procedure working with accelerations instead of velocities provides incomparably simpler and more transparent governing differential system. It enables easier and more effective analytical investigation and qualitative analysis unlike the Lagrangian governing system. Also the number of unknowns and equations in general is either the same or lower than that provided using the Lagrangian procedure.

Acknowledgements

The kind support of the Czech Science Foundation project No. 17-26353J and of the RVO 68378297 institutional support is gratefully acknowledged.

References

[1] Lewis, A., The geometry of the Gibbs-Appell equations and Gauss's principle of least constraints, Reports on Mathematical Physics 38 (1996) 11-28.

[2] Lurie, A., Analytical mechanics, GIFML, Moscow, 1961. (in Russian)

[3] Náprstek, J., Fischer, C., Non-holonomic dynamics of a ball moving inside a spherical cavity, Proceedings of the conference EURODYN 2017 – 10th Int. Conf. on Structural Dynamics, Elsevier – Procedia Engineering 199 (2017) 613-618.

[4] Náprstek, J., Fischer, C., Pirner, M., Fischer, O., Non-linear dynamic behaviour of a ball vibration absorber, Proceedings of the conference COMPDYN 2011, ECCOMAS - NTU Athens, Kerkyra, Corfu, 2011, pp. 1-14.

[5] Pars, L., A treatise on analytical dynamics, 2nd edition, Ox Bow Press, Connecticut, USA, 1972.

COMPUTATIONAL MECHANICS 2018
34th conference with international participation
Srní
October 31 - November 2, 2018

Urogynecologic surgical mesh and associated complications: Can computational biomechanics help?

V. Nováček [a], L. Havelková [a]

[a] *New Technologies – Research Centre, University of West Bohemia, Univerzitní 8, 306 14 Plzeň, Czech Republic*

Pelvic organ prolapse is a pelvic floor disorder occurring when the tissue and muscles of the pelvic floor no longer support the pelvic organs resulting in the drop from their normal position. The pelvic organs include the vagina, uterus, bladder, urethra, and rectum. The bladder is the most commonly involved organ in pelvic organ prolapse. Pelvic organ prolapse can also be associated with stress urinary incontinence. Stress urinary incontinence is a leakage of urine during moments of physical activity that increases abdominal pressure, such as coughing, sneezing, laughing, or exercise.

Pelvic organ prolapse without or with stress urinary incontinence is a major health care problem negatively affecting patients and their quality of life. It also represents a significant socioeconomic burden. Around 200,000 women undergo one or more surgical treatment for pelvic organ prolapse in the U.S. annually [1]. The total cost for surgical interventions for pelvic organ prolapse in the U.S. was estimated to §1 billion in 1997 [6].

Nonsurgical treatment options for pelvic organ prolapse include pelvic floor exercises and pessary, a removable device that is inserted into the vagina to support the pelvic organs that have prolapsed. Surgery may be recommended for women with significant discomfort or pain from pelvic organ prolapse that impairs their quality of life. Surgery to repair pelvic organ prolapse can be done through either the abdomen or vagina, using sutures alone or with the addition of surgical mesh.

Urogynecologic surgical mesh is a medical device used to treat pelvic floor disorder. The implant is expected to provide additional mechanical support to weakened and/or diseased tissue of the pelvic floor, thus, restoring normal physiological position of the pelvic organs. It is frequently a non-absorbable knitted textile implant made of polypropylene or polyethylene terephthalate mono or multi-filaments. Absorbable and non-woven products are also available.

U.S. Food and Drug Administration (FDA) issued a Public health notification on serious complications associated with transvaginal surgical mesh in 2008 and a notification update in 2011 warning that these complications are not rare events, the efficacy of the treatment compared to non-mesh repair is not demonstrated and patients with mesh may be exposed to greater risk [8, 7].

The most frequent complications reported include but are not limited to mesh erosion, pain, infection, bleeding, pain during sexual intercourse, organ perforation, and urinary problems. Many of these complications require additional intervention, including medical or surgical treatment and hospitalization. Erosion of mesh through the vagina was found the most common and consistently reported mesh-related complication from transvaginal pelvic organ prolapse surgeries using mesh. Mesh contraction (shrinkage) was a previously unidentified risk of transvaginal pelvic organ prolapse repair with mesh that had been reported in the published scientific literature and in adverse event reports to FDA [8].

Todros et al. [7] published a review of several computational models of pelvic floor that have been developed to investigate vaginal childbirth biomechanics or pelvic floor dysfunction. Computational models of knitted textile-based implants have recently appeared based on textile structure [5, 3] or exhaustive experimental data [4].

The authors of this publication expect that the recently developed finite element model of pelvic floor [2] will be adapted to simulate pelvic organ prolapse and its repair as well as its biomechanical performance during various physiological activities. The model [2] will need to be completed by the implant. Constitutive relations for both the tissue and implant will need to be revised to take into account possible non-linearity, anisotropy, permanent set, Mullins effect and muscle contraction. Boundary conditions will need to be assessed for relevant daily activities. It is hypothesized that material and structural plasticity of the implant under specific cyclic load leads to unexpected deformation modes which could imply inadvertent response of the implant. Thus, simulating pelvic organ prolapse repair and its biomechanical performance would provide more insight in pelvic organ prolapse repair biomechanics and could eventually contribute to explain the complications associated with transvaginal surgical mesh.

Acknowledgements

This publication was supported by the project CZ.02.1/0.0/0.0/17_048/0007280 of the Czech Ministry of Education, Youth and Sports under the operational program Research, Development and Education.

References

[1] Boyles, S.H., Weber, A.M., Meyn, L., Procedures for pelvic organ prolapse in the United States, 1979-1997, American Journal of Obstetrics and Gynecology 188 (1) (2003) 108-115.

[2] Krofta, L., Havelková, L., Urbánková, I., Krčmář, M., Hynčík, L., Feyereisl, J., Finite element model focused on stress distribution in the levator ani muscle during vaginal delivery, International Urogynecology Journal 28 (2) (2017) 275-284.

[3] McKee, P.J., Sokolow, A.C., Yu, J.H., Long, L.L., Wetzel, E.D., Finite element simulation of ballistic impact on single jersey knit fabric, Composite Structures 162 (2017) 98-107.

[4] Pierrat, B., Nováček, V., Turquier, F., Avril, S., Mechanical characterization and constitutive modelling of textile-based implants, Proceedings of the 5th International Conference on Computational and Mathematical Biomedical Engineering, United States, 2017.

[5] Rohrnbauer, B., Kress, G., Mazza, E., A physically based structural model for a textile prosthetic mesh, International Journal of Solids and Structures 51 (3-4) (2014) 633-646.

[6] Subak, L.L., Waetjen, L.E., van den Eeden, S., Thom, D.H., Vittinghoff, E., Brown, J.S., Cost of pelvic organ prolapse surgery in the United States, Obstetrics & Gynecology 98 (4) (2001) 646-651.

[7] Todros, S., Pavan, P.G., Natali, A.N., Biomechanical properties of synthetic surgical meshes for pelvic prolapse repair, Journal of the Mechanical Behavior of Biomedical Materials 55 (2016) 271-285.

[8] US Food and Drug Administration, FDA safety communication: update on serious complications associated with transvaginal placement of surgical mesh for pelvic organ prolapse, 2011.

COMPUTATIONAL MECHANICS 2018
34th conference with international participation
Srní
October 31 - November 2, 2018

Sensitivity analysis of total energy in electronic structure calculations

M. Novák[a,b], J. Vackář[b], R. Cimrman[c]

[a] Faculty of Applied Sciences, University of West Bohemia, Univerzitní 8, 306 14 Plzeň, Czech Republic
[b] Institute of Physics, Academy of Sciences of the Czech Republic, Na Slovance 2, 182 21 Praha 8, Czech Republic
[c] New Technologies Research Centre, University of West Bohemia, Univerzitní 8, 306 14 Plzeň, Czech Republic

A variation of the total energy of a system of atoms with respect to a change in atomic positions, i.e., the sensitivity of the total energy, also known as Hellmann-Feynman forces (HFF), is a very important quantity in the physics of materials. Its efficient evaluation has many applications such as finding stable atomic positions or in molecular dynamics calculations.

The HFF are the gradients of the total energy (including the interaction energy of atomic cores) with respect to the movement of atomic centers. According to the Hellmann-Feynman theorem [3], supposing that a fixed discretization basis is used, the forces can be calculated from the gradient of the Hamiltonian (energy operator) H

$$\vec{f_i} = -\nabla e_{\text{TOT}} = -\nabla \left(\psi^+ H \psi\right) = -\psi^+ \nabla \left(H\right) \psi \,, \tag{1}$$

where the gradient is considered with respect to the shift of atomic centers, $^+$ denotes Hermitian transpose and ψ is the wave function describing a quantum state.

We present several approaches for evaluating the HFF within the density functional theory in combination with nonlocal ab-initio pseudopotentials and the finite-element method, as implemented in our new real space code for electronic structure calculations [6, 2, 1].

The total energy in the density functional theory is given by (see e.g. [4, 5])

$$e_{\text{TOT}} = \sum_{i=1}^{n} w_i \int \psi_i^+ \frac{1}{2} \nabla^2 \psi_i + \int \psi_i^+ V_{\text{EXT}} \psi + \int E_{\text{H}}(\rho) + \int E_{\text{XC}}(\rho) + e_{\text{ION}} \,, \tag{2}$$

where V_{EXT} is the external potential, E_{H} is the electrostatic energy, E_{XC} is the exchange-correlation energy, ρ is the charge density and e_{ION} is the atomic core repulsion energy. In our case V_{EXT} is the sum of pseudopotentials of atomic cores, each of them constituted by a long-range local part and a short-range nonlocal l-dependent part:

$$V_{\text{EXT}} = \sum_a \left(V_{\text{LOC}}^a + \sum_l V_{\text{NL}}^{a,l} P_l^a \right) \,, \tag{3}$$

where P_l^a is a projection operator into a l-subspace, spanned by the spherical harmonics basis $Y_{l,m}$, of the a-th center.

Following from (1), the gradient of the total energy contains only the terms with the explicit dependence on atom positions:

$$\nabla_a e_{\text{TOT}} = \int \nabla V_{\text{LOC}}^a \rho + \sum_{l,i} w_i \int \psi_i^+ \nabla \left(V_{\text{NL}}^{a,l} P_l^a \right) \psi_i + \nabla e_{\text{ION}} \,. \tag{4}$$

The most difficult term of equation (4) is the middle one: the nonlocal part of electron-ion interaction. In the contribution, several approaches to evaluating this term will be analyzed in terms of convergence properties and computing demands using test calculations on simple molecules of nitric oxide, carbon dioxide and tetrafluormethane, see Fig. 1, with interatomic distances scaled by a variable factor.

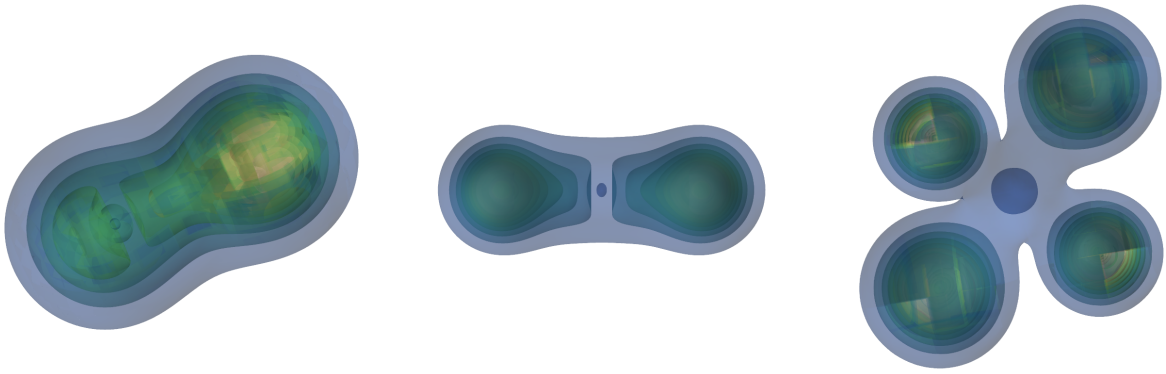

a NO molecule a CO_2 molecule a CF_4 molecule

Fig. 1. The self-consistent charge densities ρ of the test molecules

Acknowledgements

This work was supported by the Czech Science Foundation, projects no. GA17-12925S and GA17-14840S. The first author acknowledges the support by CEDAMNF project, reg. no. CZ. 02.1.01/0.0/0.0/15_003/0000358, co-funded by the ERDF as part of the Ministry of Education, Youth and Sports OP RDE programme.

References

[1] Cimrman, R., Novák, M., Kolman, R., Tůma, M., Plešek, J., Vackář, J., Convergence study of isogeometric analysis based on Bézier extraction in electronic structure calculations, Applied Mathematics and Computation 319 (2018) 138-152.

[2] Cimrman, R., Novák, M., Kolman, R., Tůma, M., Plešek, J., Vackář, J., Isogeometric analysis in electronic structure calculations, Mathematics and Computers in Simulation 145 (2018) 125-135.

[3] Hellmann, H., A new approximation method in the problem of many electrons, The Journal of Chemical Physics 3 (1) (1935) 61-61.

[4] Ihm, J., Zunger, A., Cohen, M.-L., Momentum-space formalism for the total energy of solids, Journal of Physics C: Solid State Physics 12 (21) (1979) 4409.

[5] Pask, J.E., Sterne, P.A., Finite element methods in ab initio electronic structure calculations, Modelling and Simulation in Materials Science and Engineering 13 (3) (2005) R71.

[6] Vackář, J., Čertík, O., Cimrman, R., Novák, M., Šipr, O., Plešek, J., Finite element method in density functional theory electronic structure calculations, In: Advances in the theory of quantum systems in chemistry and physics, Springer, 2012, pp. 199-217.

COMPUTATIONAL MECHANICS 2018
34th conference with international participation
Srní
October 31 - November 2, 2018

Numerical modelling of plasticity induced crack closure

T. Oplt [a,b], P. Hutař [b], M. Šebík [a]

[a] Faculty of Mechanical Engineering, Brno University of Technology, Technická 2896/2, Brno, Czech Republic
[b] Institute of Physics of Materials, Academy of Sciences of the Czech Republic, Žižkova 22, Brno, Czech Republic

Plasticity-induced crack closure (PICC) is the phenomenon discovered by Elber [1] in 1970. Since then, additional closing mechanisms have been introduced, but the plasticity remained the most significant mechanism under various loading conditions. As the crack is loaded, tensile strains are developed near the crack tip, but they are not fully reversed with unloading. Propagating crack than leaves behind so called plastic wake, which is formed by the residual plastic deformations in the direction normal to the crack propagation, causing the crack faces come to the contact before the crack is actually closed. Employing finite element (FE) methods on PICC phenomenon provides closer insight into the closure mechanics, leading to improving the physical background and ability to develop accurate models for fatigue life prediction.

For the purpose of the study, MT specimen with dimensions $2L$ = 200 mm, $2W$ = 60 mm, $2h$ = 5 mm was used (Fig. 1). Specimen was made of steel EA4T (σ_Y = 611 MPa and σ_{UTS} = 727 MPa). Specimen was cyclically loaded with various stress intensity factor range ΔK and also various crack lengths, both following experimentally measured results [2].

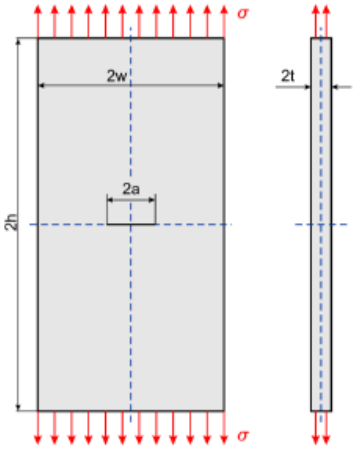

Fig. 1. MT specimen dimensions

Wide research of crack closure aspects in finite element modelling have been published. PICC is a complex problem and FE results depend on many different preprocessing inputs, where finite element mesh is typical example. Most of the researchers prefer linear elements to quadratic, which may create artefacts of residual stresses around the crack tip and edges might have different stiffness due to the middle node. Element size is estimated in connection with the forward plastic zone size r_p, where suggested is to use at least 10 elements through the plastic zone. Important is also the ratio of the element's edges, which should be ideally equal [3].

In order to create plastic wake, it is necessary to introduce cyclic loading followed by crack propagation. Crack growth usually doesn't follow physical laws (Paris law), which is not in the area of interest in this case, but one crack increment is equal to the element size. Therefore, the easiest and most common way of crack propagation is the debonding of constrained nodes. Moment when the node is released differs. Closest to the physical basis is releasing nodes when the load reaches maximum value, although some authors tried to release nodes in different cycle stages. Crack is recommended to let grow at least through the initial plastic zone size, although in some cases solution needs more cycles to reach convergency [3, 4].

Crack closure itself offers also many options how to be determined. Elber noticed the sudden change in geometry stiffness while unloading, which he assigned to the crack faces closure. Based on this, experimentally measured closure uses this technique up today. FE modelling

offers apart from the stiffness change, Fig. 2, also another options. Most common is to evaluate the closure by the monitoring of the displacement sign change of the first node behind the crack tip. When the sign changes from positive to negative, crack is closed and the closing force can be estimated, Fig. 3. In order to capture correct closing force, it is essential to use reasonable amount of substeps in each iteration cycle. Similar approach is the monitoring of stresses sign change right on the crack tip. Other possibility is to check contact pressure on the crack faces.

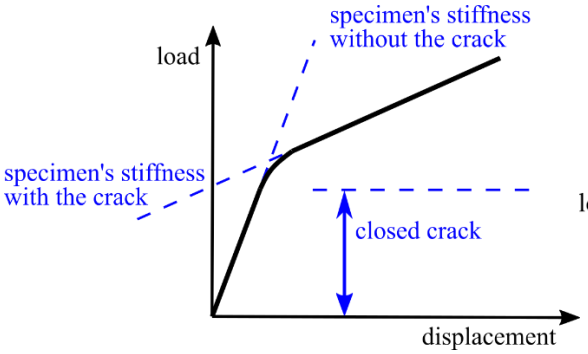

Fig. 2. Stiffness change when the closure occurs

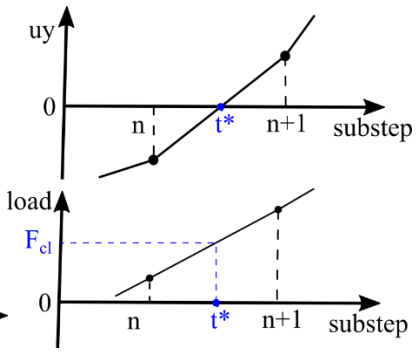

Fig. 3. Closure determination by first node displacement monitoring

These are most significant inputs which have significant impact on the crack closure determination. Most of researchers put their effort into the clarification of these relations in terms of finite element modelling only (e.g. mesh refinement in order to obtain converged solution). However, wide confrontation with experimental results is missing. Presented research aims for finding optimal finite element model configuration, which takes into account agreement with experimental results. Results presented can help to clarified methodology of plasticity induced crack closure numerical simulations.

Plasticity induced crack closure was numerically estimated on two-dimensional FE models. Different methods of determinations were compared and discussed. Optimal FE model configuration was defined, particularly in connection with experimental results. This could be a first step for full three dimensional model of the crack to determined plasticity induced crack closure.

Acknowledgements

This research has been supported by the Ministry of Education, Youth and Sports of the Czech Republic under the project m-IPMinfra (CZ.02.1.01/0.0/0.0/16_013/0001823) and specific research project FSI-S-17-4386 of the Faculty of Mechanical Engineering, BUT.

References

[1] Elber, W., Fatigue crack closure under cyclic tension, Engineering Fracture Mechanics 2 (1) (1970) 37-45.
[2] Pokorný, P., et al., Crack closure in near-threshold fatigue crack propagation in railway axle steel EA4T, Engineering Fracture Mechanics 185 (2017) 2-19.
[3] Solanki, K., Daniewicz, S.R., Newman, J.C.J., Finite element analysis of plasticity-induced fatigue crack closure: an overview, Engineering Fracture Mechanics 71 (2004) 149-171.
[4] Singh, K.D., Parry, M.R., Sinclair, I., Some issues on finite element modelling of plasticity induced crack closure due to constant amplitude loading, International Journal of Fatigue 20 (2008) 1898–1920.

COMPUTATIONAL MECHANICS 2018
34th conference with international participation
Srní
October 31 - November 2, 2018

Design and analysis of shaft and bonded joints for electric car gearbox

Z. Padovec [a], B. Kropík [a], T. Zavřelová [a]

[a]*Czech Technical University in Prague, Faculty of Mechanical Engineering, Department of Mechanics, Biomechanics and Mechatronics, Technická 4, 166 07, Praha, Czech Republic*

Main goal of this work is to analyze loading of current steel input shaft of electric car gearbox and then design lightweight alternative version. Designed shaft will have hybrid construction from composite and steel parts. Gears will be bonded to the shaft, so it is necessary to do several shear experiments for choosing suitable adhesive.

At first the original steel shaft was analysed with unit force (1 000 *N*) and torque (10 000 *N·mm*) load to obtain deflection and rotation of the shaft. FE software Abaqus was used for this analysis. Then designed hybrid shaft was loaded in similar way for stiffness comparison. Several designed ideas of hybrid shafts were analysed with the – shaft with steel mandrel, shaft without steel mandrel (both versions have same lay-up), and shaft with steel mandrel with optimized lay-up. Comparison of deflection/rotation of designed version can be seen in Table 1.

Table 1. Comparison of deflection/rotation for designed versions

Version	Deflection [*mm*]	Rotation [*rad*]
Original steel shaft	-3.411e-04	-1.182 e-04
Designed hybrid shaft	-9.738 e-04	3.289 e-04
Optimized lay-up	-8.197 e-04	6.607 e-04
Hybrid shaft without mandrel	-9.863 e-04	3.327 e-04

Designed shaft will be tested on CTU´s experimental stand with maximal torque equal to 300 *N·m*. This torque was distributed to the shaft though the helical gears, so we have to compute the real loading of our model – radial, axial and tangential forces in gears and corresponding force, torque and bending moments in shaft. Values of deflection/rotation for real load can be seen in Table 2. Deformed FE model (displacement) can be seen in Fig. 1. Designed shaft (without steel parts and gears) can be seen in Fig. 2.

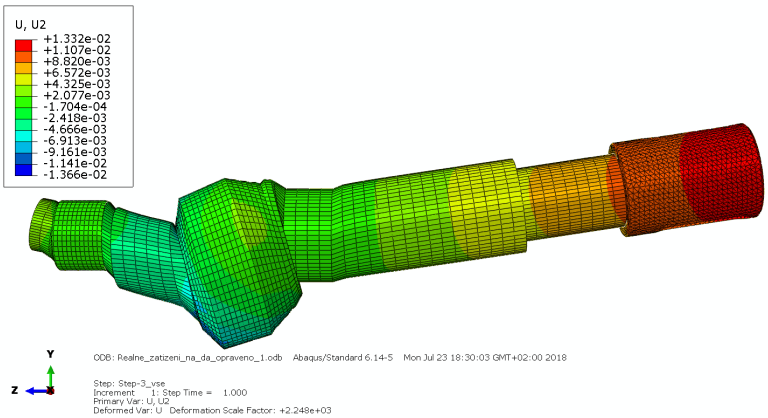

Fig. 1. Deflection of designed shaft

Table 2. Deflection/rotation for real load

Version	Deflection [*mm*]	Rotation [*rad*]
Designed hybrid shaft	-136.6 e-04	2.178 e-04

Fig. 2. Designed composite shaft

Real shaft will be manufactured by filament winding technology and gears will be bonded to the shaft. Several shar tests on flat specimens according to [1] were done to choose suitable adhesive. Six material combinations and eight adhesives were tested which means around about 225 specimens. Results of the experiments were average shear strengths for each type of adhesive/material combination – typical graph from shear experiment can be seen in Fig. 3. Experiments were also simulated in Abaqus with the use of cohesive elements and simulation results were compared with experiment. Based on the results from flat specimens, four adhesives were chosen for testing on tubular specimens steel/composite. Bonded joint was created with the use of injection technology.

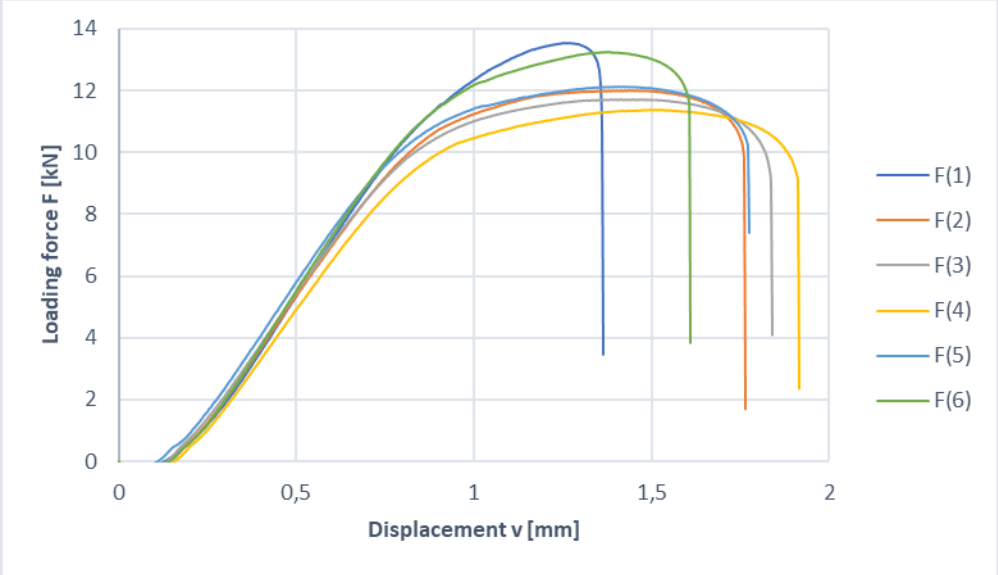

Fig. 3. Relationship between loading force and displacement for steel adherends and Acralock adhesive

Acknowledgements

This work has been supported by project TF03000050 of the Technological Agency of the Czech Republic and by the Grant Agency of the Czech Technical University in Prague, under grant No. SGS18/175/OHK2/3T/12.

References

[1] ČSN EN 1465, Lepidla - stanovení pevnosti ve smyku při tahovém namáhání přeplátovaných lepených sestav, 2009.

COMPUTATIONAL MECHANICS 2018
34th conference with international participation
Srní
October 31 - November 2, 2018

Computer simulation of the frontal collision of the articulated urban bus into the column of the traffic board portal

P. Pavlata [a]

[a] *Vision Consulting Automotive s.r.o., Rumunská 12, CZ – 120 00 Praha 2, Czech Republic*

There are currently many active and passive systems designed to protect passengers in modern vehicles. These systems are now developed purely on the basis of virtual approaches. The first aim of this paper is to demonstrate the process of computer reconstruction of the urban articulated 18 m long bus accident caused in January 2016 in Bratislava. Because of an acute health indisposition of a woman driver, the vehicle with passengers crashed into the column of the traffic boards portal.

Two different approaches were used and compared together. The first approach introduces an usage of software Virtual Crash used mainly by forensic experts of traffic accident branch in their simulation. Virtual Crash is based on MBS algorithms and uses rigid bodies in dynamic calculation. The second approach presents a dynamic nonlinear calculation performed in the PAM-Crash explicit system with a validated fully deformable FE vehicle model.

This model was built from about 2.5 milions elements and have over 12 milions degree of freedom. Time step of converging solution is about 1μs in this case. Similar model of 10 m long intercity bus of the same design family made by the same production technology was built in beginning 2013 and later validated by a full scale test in October 2013, Fig. 1. This experiment showed a very good agreement to computer model results and enabled the use of a computer model of 18 m long urban bus for our future computer simulations.

Fig. 1. Comparing computer simulation results with results of full scale test

The second aim of this paper is to introduce the methodology that could easily be implemented for the category of buses, where no similar methods have yet been used to assess the level of passive safety.

The paper further deals with the use of numerical simulations to assess passenger wounding in a general collision scenario that helps identify interior elements to improve passenger safety at the early stages of the design proposal to assess passenger protection with respect to human population variability. To assess the impact of population variability for defined impact scenarios, the scalable virtual model of the human body Virthuman can be used effectively. This model allows to cover passengers of various sizes (gender, age, height, weight, ...) and extends the conventional virtual evaluation of new security designs through existing standard test dummies and models based on the finite element method. The advantage of the Virthuman instrument used in the project is its computational efficiency when the MBS approach allows the use of up to 99 passengers in one model without increasing the computational time of the deformable model.

Using presented techniques, the reconstruction of traffic accidents as well as the safety risk for occupants on a vehicle board can be efficiently assesed.

Acknowledgements

The work has been partially supported by the research project MIT CZ No. FR-TI2/489.

References

[1] EuroNCAP, Assessment protocol – adult occupant protection, version 7.0.3, 2015.
[2] EuroNCAP, Oblique pole side impact testing protocol, version 7.0.2, 2015.
[3] EuroNCAP, Pole side impact testing protocol, version 5.1, 2011.
[4] Hirt, M., Vorel, F., Soudní lékařství, Grada Publishing, Praha, 2016.
[5] Hyncik, L., Cechova, H., Kovar, L., Blaha, P., On scaling virtual human models, SAE Technical Paper, 2013.
[6] Kahane, C.J., Evaluation of the 1999-2003 head impact upgrade of FMVSS No. 201 Upper-interior components: Effectiveness of energy-absorbing materials without headprotection air bags, NHTSA, 2011.
[7] Vychytil, J., Manas, J., Cechova, H., Spirk, S., et al., Scalable multi-purpose virtual human model for future safety assessment, SAE Technical Paper, 2014.
[8] Vychytil, J., Hyncik, L., Manas, J., Pavlata, P., et al., Prediction of injury risk in pedestrian accidents using virtual human model VIRTHUMAN: Real case and parametric study, SAE Technical Paper, 2016.

COMPUTATIONAL MECHANICS 2018
34th conference with international participation
Srní
October 31 - November 2, 2018

Flutter boundary assessment for a blade cascade using developed discontinuous Galerkin code

A. Pecka[a], O. Bublík[a], J. Vimmr[a]

[a] *NTIS – New Technologies for the Information Society, Faculty of Applied Sciences, University of West Bohemia, Univerzitní 8, 301 00 Plzeň, Czech Republic*

This contribution builds on the last year contribution [5], where the flutter boundary was assessed for a single aerofoil with the aid of the fluid-structure interaction (FSI) code developed for the purpose of aeroelastic flutter analysis as a part of FlowPro. FlowPro is a multipurpose numerical software developed by the authors of this contribution. Flutter boundary established in [5] was compared with the results of Kirshmann [4] and Hall [2]. Since the results agreed reasonably well to say the least, the FSI code is now considered as validated. The aim of this contribution is to establish the flutter boundary for a blade cascade.

The developed algorithm for fluid flow modelling is based on the discretisation of the system of Navier-Stokes equations by the discontinuous Galerkin method with the Lax-Friedrichs numerical flux. Furthermore, the time integration is performed by the second order backward difference formula (BDF2), which is an unconditionally stable implicit method. In its general form, it also allows us to adaptively change the size of time steps.

Let us move on to the flutter boundary prediction. The flutter boundary is a curve in $\mathbb{R}^2$ which determines the threshold for the occurrence of the instability of type flutter depending on two variables, namely the far-field Mach number M and speed index U_F. Here, we study the flutter boundary for a blade cascade consisting of four flat plates with periodic boundary condition as show in Fig. 2. For each blade, we considering the wing model of Isogai [3] shown in Fig. 1. The dynamics of each blade is determined by the following system of two differential equations

$$m\ddot{y} + S_\alpha \ddot{\alpha} + K_y y = L,$$
$$S_\alpha \ddot{y} + I_\alpha \ddot{\alpha} + K_\alpha \alpha = M_A,$$

where

$$m = \mu\pi\varrho_\infty b^2, \qquad S_\alpha = mbx_a,$$
$$I_\alpha = mr_a^2, \qquad K_y = m\omega_y^2,$$
$$K_\alpha = I_\alpha\omega_\alpha^2, \qquad \omega_\alpha = U_\infty/U_F b\sqrt{\mu}.$$

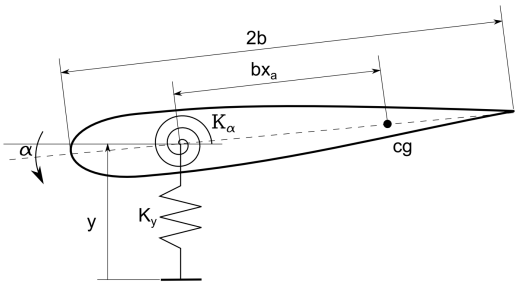

Fig. 1. Isogai wing model

On the right-hand side of the equations of motion we have the lift L and torque M_A acting on the aerofoil due to the aerodynamic forces. The structural parameters are $x_a = 1.8,\ r_a^2 = 3.48,\ \mu = 60$ and the heat capacity ratio is $\kappa = 1.4$. Far-field velocity U_∞ and density ϱ_∞ can be readily calculated using M and κ. In order to solve the system of second order ordinary differential equations, we first rewrite it as a system of first order ordinary differential equations

and consequently apply the two-step Adams-Bashforth scheme. We solve the FSI problem as a whole by solving the flow field and the rigid body dynamics in turns using the weak coupling. The fluid flow influences the rigid body through the lift L and torque M_A. Conversely, the rigid body influences the fluid flow by changing its own position given by the displacement y and angle α. Hence, the mesh vertices must be recalculated at each time step, which we achieve by the blending function approach [1].

The flutter boundary is established using an iterative process in which aeroelastic simulations are performed for many combinations of values of the far-field Mach number M and speed index U_F. If the resulting motion grows in an unbounded fashion with time, the system is considered unstable and prone to aeroelastic flutter. If the disturbances are damped with time, the system is stable and flutter does not occur. If the system continues to oscillate with constant amplitude, the system is neutrally stable and the flutter boundary is established. The flutter boundary determined by the developed FSI software is plotted in Fig. 3. The green and red dots correspond to the combinations of U_F and M for which the system is stable and unstable, respectively. The flutter boundary drawn by the black line was found using bisection method.

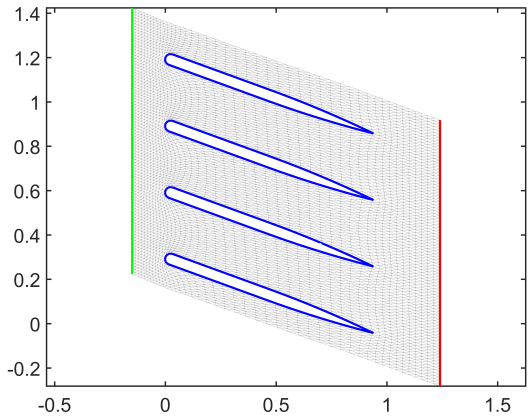

Fig. 2. Geometry and mesh

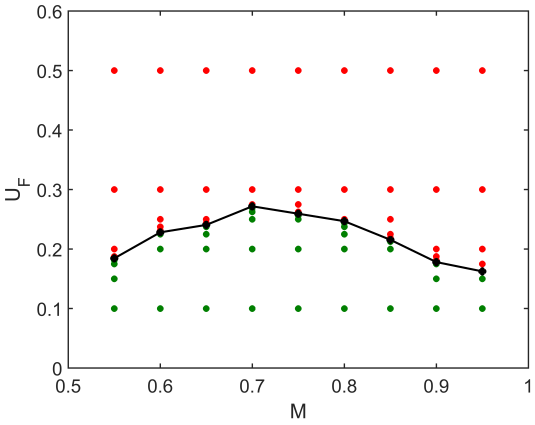

Fig. 3. Flutter boundary

Acknowledgements

The authors appreciate the kind support of the grant GA 16-04546S "Aero-elastic couplings and dynamic behaviour of rotational periodic bodies" of the Czech Science Foundation and of the student grant project SGS-2016-038.

References

[1] Bublík, O., Vimmr, J., Jonášová, A., Comparison of discontinuous Galerkin time integration schemes for the solution of flow problems with deformable domains, Applied Mathematics and Computation 267 (2015) 329-340.

[2] Hall, K.C., Jeffrey, T.P., Dowell, E.H., Proper orthogonal decomposition technique for transonic unsteady aerodynamic flows, AIAA Journal 38 (10) (2000) 1853-1862.

[3] Isogai, K., On the transonic-dip mechanism of flutter of a sweptback wing, AIAA Journal 17 (6) (1979) 793-795.

[4] Kirshman, D.J., Liu, F., Flutter prediction by an Euler method on non-moving Cartesian grids with gridless boundary conditions, Computers and Fluids 35 (6) (2006) 571-586.

[5] Pecka, A., Bublík, O., Vimmr, J., Validation of a fluid-structure interaction code based on the discontinuous Galerkin method, Proceedings of the 33rd conference with international participation Computational Mechanics 2017, University of West Bohemia, Špičák, 2017.

COMPUTATIONAL MECHANICS 2018
34th conference with international participation
Srní
October 31 - November 2, 2018

Damping of flutter oscillations by dry friction contacts

L. Půst [a], L. Pešek [a], P. Šnábl [a]

[a] *Institute of Thermomechanics, Czech Academy of Sciences, Dolejškova 5, 182 00, Praha, Czech Republic*

Self-excited flutter vibrations of turbine blades are very dangerous phenomena for the service life of turbines [1], [2]. The various design treatments are therefore applied for suppression of blades' flutter vibrations. The introduction of dry friction elements is one of the very effective methods. The dynamic behavior of a computational model of 30-blades turbine wheel is investigated in the proposed paper. The blades in the rotating cascade are excited by aerodynamic forces arising from the spatially periodical flow of steam through the stator blades cascade. This flow produces both forced vibration and self-excited vibrations – flutter. The application of dry friction elements on reduction of these dangerous vibrations is presented on several examples.

The computational model of thirty blades turbine wheel with elastic connections between neighbouring blades modelled approximately the experimental wheel investigated in our institute. A small blades' section is in Fig. 1. Spring connections between blades (stiffness k_1) model the elastic properties of disc.

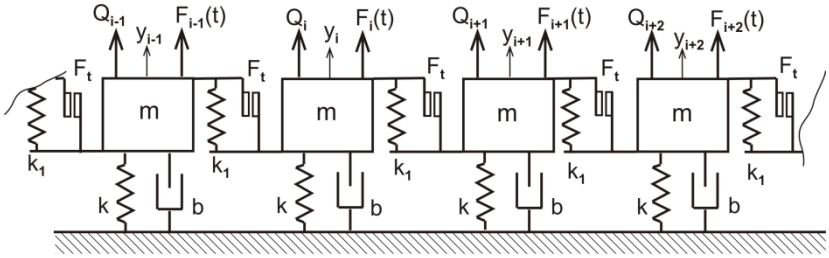

Fig. 1. Section of computational model of closed 30-blades cascade with dry friction inter-blades connections

Due to the different numbers of blades of stationary and of rotating wheels, the wakes from the stationary cascade flow excite the forced running waves. These forced waves serve as initial impulses for aero-elastic self-excited oscillations – flutter running waves. In order to investigate the behaviour of bladed cascade also in the unstable regions, the simple Van der Pol expression for description of self-exciting forces is used. These self-exciting forces are controlled by only one blade's motion parameters – similar as at aeroplane wing:

$$Q_i = -\mu(1-(y_i/r)^2)\dot{y}_i, \qquad i = 1, \ldots, 30,$$

where r is the displacement at which the negative aerodynamic force changes into positive one, μ is a scalar parameter indicating the intensity of this non-linear force.

The dry friction elements used for suppression of flutter vibrations are described by smooth modification of Coulomb law with arctangent function F_{ti}:

$$F_{ti} = fF_N arctg(\gamma(\dot{y}_i - \dot{y}_{i+1}))2/\pi \qquad i = 1, \ldots, 30,$$

with sufficiently high parameter γ.

The first step in study of bladed wheel dynamics is analysis of free vibration. This cyclic structure with parameters m = 0.182 kg, k = 105000 kg s^{-2}, k_1 = 10000 kg s^{-2} has 30 eigen-frequencies in the range 759.55 – 899.48 rad/s (majority twofold) and 15 modes with 0 –15

nodal diameters (nd). In this paper only 5 selected cases with 0, 4, 8, 12, 15 nd is presented. The aerodynamic forces of the interrupted steam flowing from stator cascade with *l*s blades produce spatial generally periodic forces, acting on the rotating blade cascade with different numbers *lr* of blades. These periodic forces have many components that can excite forced vibrations corresponding to all above mentioned natural frequencies.

Let us concentrate on the damping of flutter oscillation of bladed wheel with 12 nodal diameters at $\Omega = 880.74$ rad/s (140.17 Hz). Mode of un-damped flutter (F_{t0} = 0) vibrations are shown in Fig. 2. Using dry friction elements (F_{t0} = 0.93 N) between neighboring blades reduces flutter oscillations on acceptable value.

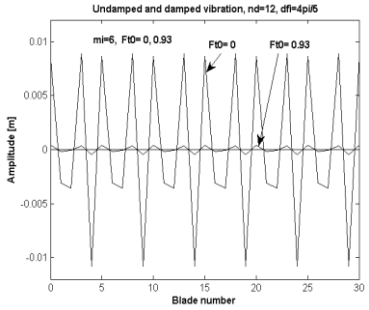

Fig. 2. Mode at 880.74 rad/s

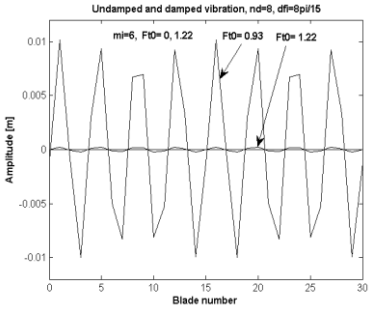

Fig. 3. Mode at 835.64 rad/s

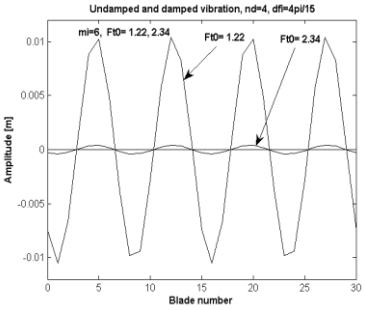

Fig. 4. Mode at 783.12 rad/s

However, this dry friction element does not suffice for suppression of bladed wheel flutter oscillation with 8 nodal diameters ($\Omega = 835.64$ rad/s, 133.00 Hz) as it is evident from record in Fig. 3, where the dry friction element (F_{t0} = 0.93 N) does not reduce the amplitudes and they stay roughly the same as of un-damped system. Only when the dry friction forces increase to F_{t0} = 1.22 N, the danger flutter oscillations disappear.

Similar damping properties have also the resonance vibrations with 4 nodal diameters ($\Omega = 783.12$ rad/s, 124.62 Hz) as it is seen from Fig. 4. Application of the same dry friction dampers as in previous case (F_{t0} = 1.22 N) does not reduce the flutter oscillations and the dry friction force has to increase to F_{t0} = 2.34 N in order that these oscillations are strongly diminished.

The same properties have all 15 resonances of investigated bladed wheel. The simpler is the mode of vibrations, the higher dry friction force is needed for suppression of the flutter vibrations. E.g. the lowest eigen-frequencies need very high dry friction for their reduction and the first frequency with umbrella mode (all blades vibrate in phase) cannot be suppressed by any value of dry friction situated between neighbouring blades.

This phenomenon is typical for all multi-degree-of-freedom systems, where damping forces act in another place than excitation forces work.

Acknowledgement

This work has been supported by the grant project of the Czech Science Foundation No 16-04546S “Aero-elastic couplings and dynamic behaviour of rotational periodic bodies”.

References

[1] Půst, L., Pešek, L., Blades forced vibration under aero-elastic excitation modelled by Van der Pol, International Journal of Bifurcation and Chaos 27 (11) (2017)

[2] Půst, L., Pešek, L., Byrtus, M., Flutter running waves in turbine blades cascade, Proceedings of the DSTA, Lodz, Poland, 2017, pp. 483-492.

COMPUTATIONAL MECHANICS 2018
34th conference with international participation
Srní
October 31 - November 2, 2018

Experimental simulation of unilateral paralysis of human vocal folds

V. Radolf [a], J. Horáček [a], V. Bula [a], J. Košina [a], J. Švec [b]

[a] *Institute of Thermomechanics, The Czech Academy of Sciences, Dolejškova 1402/5, 182 00 Praha, Czech Republic*
[b] *Department of Biophysics, Faculty of Science, Palacký University, 17. listopadu 12, 771 46 Olomouc, Czech Republic*

Unilateral paralysis of the superior laryngeal nerve affecting the cricothyroid muscle produces an imbalance in the longitudinal tension of the vocal folds during phonation. Such an asymmetry causes changes in the vibratory pattern of the vocal folds and in the resulting voice quality, e.g. hoarseness, voice breaks, limited pitch and loudness range. This problem was studied by means of a physical model of the human voice production.

The model consists of vocal fold replica made of silicon and a plexiglass tube representing the vocal tract configured for [u:] vowel. For the measurement setup see [2]. A two-layer water-filled silicone vocal fold replica [2] was excited by the airflow coming from a compressor through a regulating valve into the float flow meter, based on which the control flow rate was manually set to 0.25 l/s. The air entered the model of subglottal spaces consisting of a simplified model of lungs and trachea. Thereafter, the air flew into the part where the vocal folds were installed. The hydrostatic pressure inside the vocal fold model was regulated by a syringe to pre-set the fundamental frequency of phonation to a fixed value 110 Hz. The mean subglottal and oral pressures were measured by NXP (Freescale) MPXV5010GC6U integrated pressure semiconductor sensors mounted in the walls of the trachea and the oral cavity. The fluctuations of the subglottal and oral pressures were measured by a B&K 4138 miniature microphone (range 6.5 Hz–140 kHz) and by a special B&K 4182 microphone probe (range 1 Hz–20 kHz), respectively. Vocal fold vibrations were recorded by the high-speed camera (NanoSense MkIII) positioned at a 90 degree bend of the trachea model where a glass window was installed; this enabled the viewing of the vocal fold vibration from the subglottal side.

All the pressure signals were synchronously sampled and recorded using the measurement system B&K Pulse 3560 C controlled by a personal computer equipped by the SW PULSE LabShop Version 10. The sampling frequency of the signals was 16.4 kHz, and 1000 frames were synchronously recorded by the high-speed camera with the rate of 3000 frames/s.

Fig. 1 shows the videokymogram of the vibratory pattern of the vocal folds constructed from the perpendicular cross line at the position of the maximal glottal width amplitude. The black pixels represent the glottal width *GW(t)* at the individual time instants of video recording. This vibration pattern resembles pathological asymmetric vibration patterns observed in vivo in patients with unilateral vocal fold paralysis [4, 1]. Notice the period irregularities on both the vocal folds which are typical for rough or diplophonic voices [5]. Also, notice the reduced amplitude of vibration of the left (lower) vocal fold, which suggests a mass imbalance rather than a stiffness imbalance of the vocal folds or extremely tensed left vocal fold, see [3].

Fig. 2 demonstrates time records of the following measured signals: oral pressure $P_{oral}(t)$ measured in the mouth cavity of the vocal tract model, glottal area *GA(t)* and subglottal

pressure $P_{sub}(t)$ measured just below the vocal folds. The beats-like vibration pattern of all the signals is similar to that seen in the videokymogram.

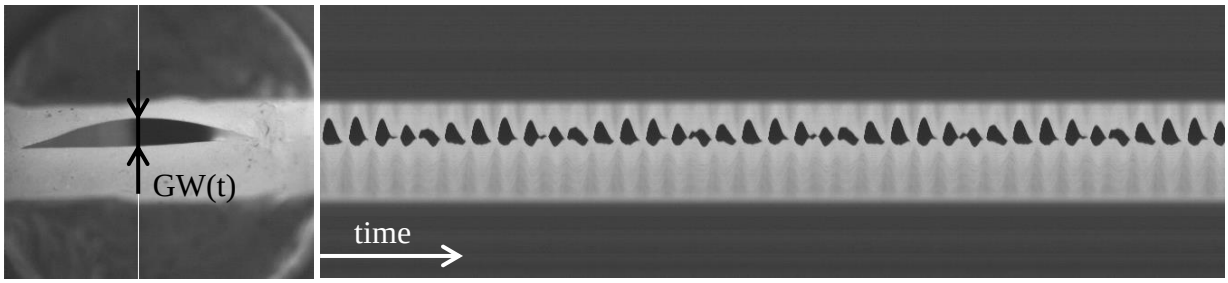

Fig. 1. Position of the cross line for videokymogram construction (left), videokymogram of vibrating paralysed vocal folds model (right)

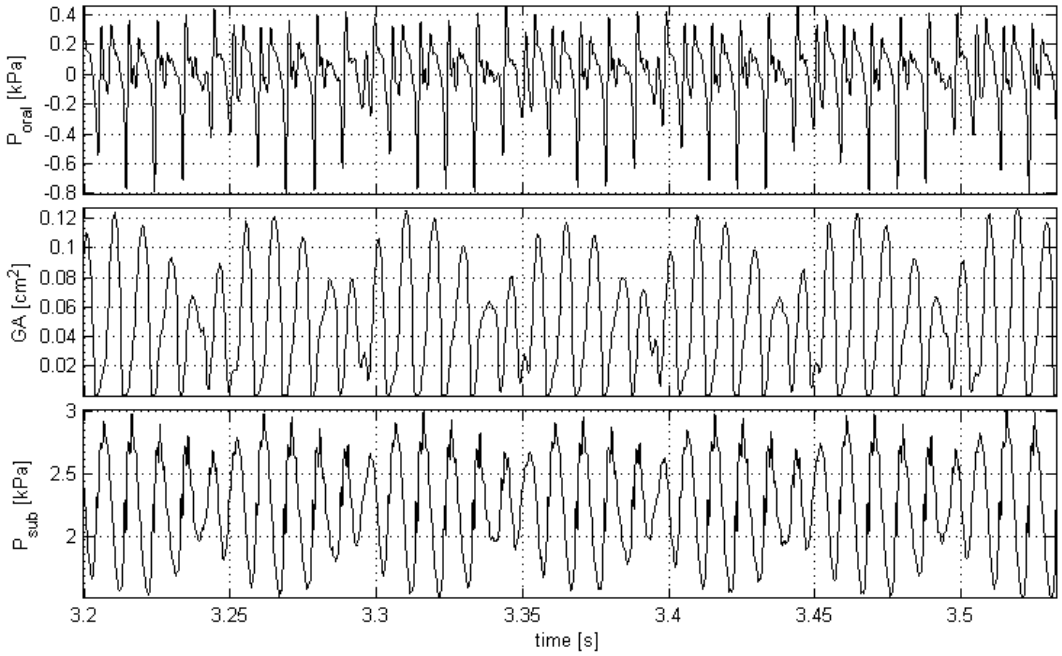

Fig. 2. Waveforms of vibrating paralysed vocal folds model: oral pressure (top), glottal area, subglottal pressure (bottom)

Acknowledgements

The study was supported by a grant from the Czech Science Foundation No. 16-01246S "Computational and experimental modelling of self-induced vibrations of vocal folds and influence of their impairments on human voice."

References

[1] Eysholdt, U., Rosanowski, F., Hoppe, U., Vocal fold vibration irregularities caused by different types of laryngeal asymmetry, European archives of otorhinolaryngology 260 (2003) 412-417.

[2] Horáček, J., et al., Experimental modelling of phonation using artificial models of human vocal folds and vocal tracts, Proceedings of the 23rd International Conference Engineering Mechanics, Svratka, 2017, pp. 382-385.

[3] Isshiki, N., et al., Clinical significance of asymmetrical vocal cord tension, The Annals of otology, rhinology and laryngology 86 (1977) 58-66.

[4] Sram, F., Schutte, H.K., Svec, J.G., Clinical applications of videokymography, Proceedings of the 16th World Congress of Otorhinolaryngology Head and Neck Surgery, Sydney, 1997, pp. 1681-1684.

[5] Svec, J.G., Sram, F., Schutte, H.K., Videokymography in voice disorders: what to look for?, The Annals of otology, rhinology and laryngology 116 (2007) 172-180.

COMPUTATIONAL MECHANICS 2018
34th conference with international participation
Srní
October 31 - November 2, 2018

Optimal control method for solution of inverse problem

J. Radová[a], J. Machalová[a]

[a] Faculty of Science, Palacký Univerzity Olomouc, 17. listopadu 1192/12, 771 46 Olomouc, Czech Republic

In this contribution we deal with using of the optimal control method for solution of an inverse problem for nonlinear Gao beam which was published by Gao in [1]. The inverse problem will be formulated as the minimization of a cost functional which depends on a state problem. The state problem is represented by the Gao beam equation

$$\begin{cases} \sigma I u^{IV} - \sigma\alpha(u')^2 u'' = f & \text{in } (0,L), \\ u(0) = u'(0) = 0, \\ u(L) = u'(L) = 0, \end{cases} \tag{1}$$

where u is an unknown deflection of the beam, σ is the Young's elastic modulus, $I = \frac{2}{3}h^3$ is the area moment of inertia, h is the thickness of the beam and L is the length of the beam. The remaining symbols indicate the following

$$\alpha = 3h(1-\nu^2) \qquad \text{and} \qquad f = (1-\nu^2)q,$$

where ν denotes Poisson ratio and q is the given vertical load. The clamped beam is considered which corresponds to the prescribed boundary conditions.

It remains to specify the cost functional. Let $||\cdot||$ be L^2-norm and let $z \in L^2((0,L))$ be a given function. Then we define the cost functional $J(\sigma, u(\sigma)) : U_{ad} \times H_0^2((0,L)) \to \mathbb{R}^1$ by

$$J(\sigma, u(\sigma)) = \frac{1}{2}||u(\sigma) - z||^2,$$

where

$$U_{ad} = \{\sigma \in L^\infty((0,L)) \,|\, \sigma_{\min} \le \sigma \le \sigma_{max} \text{ in } (0,L), \sigma|_{K_i} \in P_0(K_i), i = 1,\dots,n\}$$

is the set of admissible parameters with given constants $0 < \sigma_{\min} < \sigma_{\max}$ and $K_i = [x_{i-1}, x_i]$, $i = 1,\dots,n$, where $x_0 = 0 < x_1 < x_2 < \dots < x_n = L$. It means that $U_{ad} \subset \mathbb{R}^n$ is the set of piecewise constant functions over the partition of $(0,L)$.

Now we can define the inverse problem as a following minimization problem

$$\begin{cases} \text{Find function } \sigma^* \in U_{ad} \text{ such that} \\ J(\sigma^*, u(\sigma^*)) = \min\limits_{\sigma \in U_{ad}} J(\sigma, u(\sigma)), \\ \text{where } u(\sigma) \text{ solves the state problem } (1). \end{cases} \tag{2}$$

The numerical realization of this problem is based on using finite element method and consists of two parts. The first part is the discretization of the state problem which does not make

any troubles and it is described for example in [2, 3]. The second part concerns the minimization of a cost function $\mathbf{I}$ which arises from the discretization of the cost functional J and can be written in the form

$$\mathbf{I}(\boldsymbol{\sigma}) \ := \ J(\boldsymbol{\sigma}, \mathbf{u}(\boldsymbol{\sigma})).$$

The minimization is based on iterative process which generates a sequence $\left\{\boldsymbol{\sigma}^k\right\}$ with the given initial approximation $\boldsymbol{\sigma}^0$ such that

$$\lim_{k\to\infty} \mathbf{I}(\boldsymbol{\sigma}^k) \ = \ \mathbf{I}(\boldsymbol{\sigma}^*), \qquad \text{where} \quad \mathbf{I}(\boldsymbol{\sigma}^*) \ = \ \min_{\boldsymbol{\sigma}\in\mathbf{U}} \mathbf{I}(\boldsymbol{\sigma}).$$

For the given $\boldsymbol{\sigma}^k$ we compute $\mathbf{u}(\boldsymbol{\sigma}^k)$ as a solution of the discretized state problem and the next iteration $\boldsymbol{\sigma}^{k+1}$ is found in the form $\boldsymbol{\sigma}^{k+1} = \boldsymbol{\sigma}^k + \alpha \mathbf{d}^k$, where $\alpha > 0$ and $\mathbf{d}^k$ is a descent direction. This direction is chosen in such a way that $\mathbf{I}(\boldsymbol{\sigma}^k + \alpha\mathbf{d}^k) \ < \ \mathbf{I}(\boldsymbol{\sigma}^k)$ for all $\alpha \in (0, \overline{\alpha}), \overline{\alpha} > 0$. The important step for this algorithm is the choice of the step length α which is obtained by using line search techniques. The cost function can be written in the form

$$\mathbf{I}(\boldsymbol{\sigma}) \ = \ \frac{1}{2} \left(\mathbf{S}\mathbf{u}(\boldsymbol{\sigma}) - \mathbf{z}, \mathbf{S}\mathbf{u}(\boldsymbol{\sigma}) - \mathbf{z}\right)_p,$$

where $\mathbf{z} \in \mathbb{R}^p$ is a given vector, $(.,.)_p$ denotes the inner product in $\mathbb{R}^p$ and $\mathbf{S} \in \mathbb{R}^{p\times n}$ is a matrix representing the restriction mapping from $\mathbb{R}^n$ onto $\mathbb{R}^p$. For computation of the descent direction we need to derive the expression for the gradient of the function $\mathbf{I}$. It is obvious that

$$\begin{aligned} \mathbf{I}'(\boldsymbol{\sigma}) \ &= \ \frac{1}{2} \left(\mathbf{S}\mathbf{u}'(\boldsymbol{\sigma}), \mathbf{S}\mathbf{u}(\boldsymbol{\sigma}) - \mathbf{z}\right)_p + \frac{1}{2} \left(\mathbf{S}\mathbf{u}(\boldsymbol{\sigma}) - \mathbf{z}, \mathbf{S}\mathbf{u}'(\boldsymbol{\sigma})\right)_p = \\ &= \ \left(\mathbf{S}\mathbf{u}(\boldsymbol{\sigma}) - \mathbf{z}, \mathbf{S}\mathbf{u}'(\boldsymbol{\sigma})\right)_p = \left(\mathbf{S}^T \left(\mathbf{S}\mathbf{u}(\boldsymbol{\sigma}) - \mathbf{z}\right), \mathbf{u}'(\boldsymbol{\sigma})\right)_p. \end{aligned}$$

The problematic part $\mathbf{u}'(\boldsymbol{\sigma})$ can be eliminated by using adjoint state problem, for more details see in [5].

Numerical results for the nonlinear Gao beam are compared with results for the classical linear Euler-Bernoulli beam [4] and numerical computations are realized by using MATLAB.

Acknowledgement

This work was supported by the IGA UPOL grant IGA_Prf_2018_024.

References

[1] Gao, D.Y., Nonlinear elastic beam theory with application in contact problems and variational approaches, Mechanics Research Communications 23 (1) (1996) 11-17.

[2] Machalová, J., Netuka, H., Control variational method approach to bending and contact problems for Gao beam, Applications of Mathematics 62 (6) (2017) 661-677.

[3] Machalová, J., Netuka, H., Solution of contact problems for Gao beam and elastic foundation, Mathematics and Mechanics of Solids 23 (3) (2018) 473-488.

[4] Marinov, T.T., Vatsala, A.S., Inverse problem for coefficient identification in the Euler-Bernoulli equation, Computers & Mathematics with Applications 56 (2) (2008) 400-410.

[5] Tröltzsch, F., Optimal control of partial differential equations: Theory, methods and applications, American Mathematical Society, Providence, Rhode Island, 2010.

COMPUTATIONAL MECHANICS 2018
34th conference with international participation
Srní
October 31 - November 2, 2018

On approaches, methods and problems related to wave dispersion in porous media

E. Rohan[a], V.-H. Nguyen[b], V. Lukeš[a], R. Cimrman[a], S. Naili[b]

[a] *NTIS – New Technologies for the Information Society, Faculty of Applied Sciences, University of West Bohemia, Univerzitní 8, 301 00 Plzeň, Czech Republic*

[b] *Laboratoire Modélisation et Simulation Multi Echelle, Université Paris Est Creteil,MSME UMR 8208 CNRS, Créteil cedex, France*

The paper is devoted to modelling of wave propagation in fluid saturated porous media. The aim is to compare two approaches suitable for wave analysis in periodic structures. The homogenization-based method provides macroscopic models and relies on scale separation, such that the wave length should be much longer than the heterogeneity size. The method based on the Bloch-Floquet theory is applicable for analyzing plane wave propagation in infinite continua only, but enables to capture also effects of Bragg's scattering. Application of these two methods for computing the dispersion curves of the two-phase media with deformable and rigid skeletons is discussed in the context of two kinds of porous media: 1) deformable fluid-saturated porous media described by the Biot model at the mesoscopic scale, 2) waves in fluids saturating rigid porous structures. Computational studies based on the Bloch wave decomposition were performed for numerical models obtained using the finite element discretization of the corresponding problems imposed in the representative volume element. The results presented in terms of dispersion curves are compared with analogous results obtained using the homogenized models providing directly the shear and pressure wave responses.

Waves in deformable fluid-saturated porous media. The mathematical model governing the wave propagation in fluid-saturated porous media (FSPM) made of an elastic solid skeleton whose pores constitute a connected pore network was first proposed by Biot [2]. It is well known that, in (mesoscopically) homogeneous media in $\mathbb{R}^n$, there are $n+1$ principle modes of plane waves propagating as the $n-1$ shear waves (S), fast quasi-compressional waves (P1) and slow quasi-compressional waves (P2), cf. [7] and [6], where the homogenization based approach was reported. For the rigid double porosity media, the dispersion properties of the homogenized model were considered in [3], whereas the single porosity model was obtained in [4]. In this paper, we consider FSPM governed by the Biot model relevant to a mesoscopic scale whereby the material coefficients oscillate with a given spatial period. To analyze the wave propagation in such media, as an alternative to the homogenization based approach, we have derived a formulation based on the Bloch wave decomposition which yields a quadratic eigenvalue problem for complex wave numbers within the first Brillouin zone associated with the periodic structure.

Waves in fluid saturating rigid periodic scaffolds. We consider acoustic waves in a compressible fluid saturating rigid porous periodic structure. Models of homogenized media, cf. [1], were derived for two types of fluids and flow regime: a) acoustic fluid (inviscid), b) viscous fluid, but no convection flow. Obviously the case a) leads to the homogenization of the Helmholtz equation. Using homogenization in the case b) leads to the dynamic permeability

For these kinds of homogenized media, the dispersion curves are presented and compared with corresponding results computed using the Bloch wave decomposition.

Acknowledgments

This research is supported by project GACR 17-01618S and in part by the project LO1506 of the Czech Ministry of Education, Youth and Sports.

References

[1] Allaire, G., Homogenization of the unsteady Stokes equation in porous media, In: Progress in PDE: Calculus of variation, applications, Pitman Research notes in Mathematics Series vol. 267, 1992, pp. 109-123.

[2] Biot, M.A., Theory of propagation of elastic waves in a fluid-saturated porous solid. I. Low-frequency range, Journal of the Acoustical Society of America28 (2) (1956) 168-178.

[3] Rohan, E., Homogenization of acoustic waves in strongly heterogeneous porous structures, Wave Motion 50 (2013) 1073-1089.

[4] Mielke, A., Rohan, E., Homogenization of elastic waves in fluid-saturated porous media using the Biot model, Mathematical Models and Methods in Applied Sciences 23 (5) (2013) 873-916.

[5] Rohan, E., Naili, S., Nguyen, V.-H., Wave propagation in a strongly heterogeneous elastic porous medium: Homogenization of biot medium with double porosities, Comptes Rendus Mecanique 344 (6) (2016) 569-581.

[6] Rohan, E., Nguyen, V.-H., Naili, S., Numerical modelling of waves in double-porosity Biot medium, Computers & Structures (2017), doi:10.1016/j.compstruc.2017.09.003. (in press)

[7] Rohan, E., Nguyen, V.-H., Naili, S., Dynamics and wave dispersion of strongly heterogeneous fluid-saturated porous media, Procedia Engineering 199 (2017) 1507-1512.

COMPUTATIONAL MECHANICS 2018
34th conference with international participation
Srní
October 31 - November 2, 2018

Intra- and inter-somatotype differences in a manual material handling task

A. Sánchez-Alvarado [a,d], O. Sánchez-Brenes [b], M. Sánchez-Brenes [a], M. Zerpa-Catanho [c], C. Vargas-Del Valle [c], G. Céspedes-Calderón [c]

[a] *Applied Ergonomics Laboratory – ErgoTEC, Faculty of Industrial Production Engineering, Costa Rica Institute of Technology in Cartago, Costa Rica.*
[b] *Applied Ergonomics Laboratory – ErgoTEC, Faculty of Industrial Design Engineering, Costa Rica Institute of Technology in Cartago, Costa Rica.*
[c] *Research Assistant, Applied Ergonomics Laboratory – ErgoTEC, Costa Rica Institute of Technology in Cartago, Costa Rica.*
[d] *Faculty of Applied Sciences, University of West Bohemia in Pilsen, Univerzitní 8, 306 14 Plzeň, Czech Republic*

The Manual Material Handling (MMH) of loads is considered worldwide one of the main components in musculoskeletal disorders in various industries, which also carries a high cost [1]. Prior research has shown that there are limited studies comparing different bodily characteristics for both genders during MMH [4] and that individuals severely obese are in greater risk than normal weight individuals when performing a MMH task [5].

A total of 37 subjects were assessed for this study, each subject signed an informed consent form and anthropometric measures were taken in addition to age, weight, and height, using a skinfold caliper. Table 1 summarizes the somatotype (endomorph: soft round body type, mesomorph: athletic body type) data according to each gender, based on Heath-Carter formula.

Table 1. Average (standard deviation) of the participants according to their somatotype

	Mesomorph (athletic body type)		**Endomorph (gain weight easily)**	
Gender	**Male n=16**	**Female n=10**	**Male n=3**	**Female n=8**
Age (years)	23.50 (3.69)	22.30 (2.54)	21.33 (2.52)	21.71 (1.11)
Weight (kg)	68.51 (5.77)	63. 17 (13.43)	78.97 (5.44)	64.31 (11.15)
Height (cm)	171.33 (6.89)	159.63 (5.29)	175.87 (2.11)	162.41 (5.45)
BMI	23.26 (1.73)	24.66 (4.33)	25.51 (1.19)	24.23 (9.14)
FAT %	19.21 (0.04)	22.68 (0.04)	24.46 (0.01)	33.39 (0.00)

The kinematic data were recorded with Qualisys motion capture system (Stockholm, Sweden), with 8 Miqus M1 and 1 Miqus Video cameras, at 150 frames per second. A total of 57 passive markers were used. The data was analyzed and processed on Visual 3D software (C-Motion, Inc, MD, USA), using an inter-linked segments model. The kinematic data was processed and filtered using a fourth-order, bidirectional, low-pass Butterworth filter, with cutoff frequencies of 6 Hz.

A 15.0 kg load was lifted from a height of 15 cm above ground level and unloaded at shoulder height (relative to each person), the load was lifted twice, with an interval of 30 seconds between each series. In addition, two different lifting conditions were carried out, without any instructions (free condition) for each participant, and then with specific instructions (instructed condition) for an appropriate MMH, based on [2] and [3].

Endomorph female participants presented an increased trunk-lab angle during the free condition compared to instructed trials (74.50° vs 49.39°, respectively, t = 4.48, df = 10,

$p < 0.05$, $r = 0.82$). In the case of female mesomorph participants, trunk-pelvis and trunk-lab angles were higher for the free condition compared to the instructed trials ($r = 0.79$, $r = 0.82$, respectively), and on the contrary knee and ankle joint angles were lower ($r > 0.50$ in both cases). Fig. 1(a) shows this situation in a schematic representation from one of the participants for both conditions.

a) 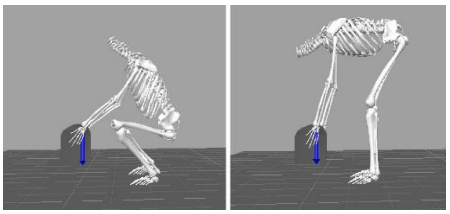 b) 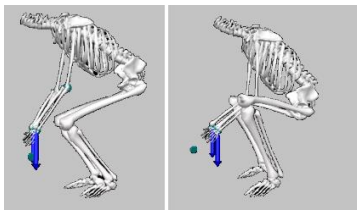

Fig. 1. a) Lift start visualization for one endomorph female, instructed (left) vs. free. b) Inter-somatotype differences for the 15-kg load on instructed trials, endomorph (left) vs. mesomorph

A similar behavior was presented on mesomorph male participants, where knee, hip, trunk-pelvis and trunk-lab angles were significantly different ($t = 4.35$, $df = 24$, $p < 0.05$, $r = 0.66$; $t = -3.17$, $df = 24$, $p < 0.05$, $r = 0.54$; $t = -3.13$, $df = 24$, $p < 0.05$, $r = 0.54$, and $t = -4.42$, $df = 12$, $p < 0.05$, $r = 0.79$, respectively). Endomorph male participants did not show any statistical differences.

Concerning inter somatotypes differences (mesomorph vs endomorph) for the instructed condition, no differences were found from a statistical point of view ($p > 0.05$). Nevertheless, male mesomorphs bent more the hips (106.86° vs 88.00°) and presented a more extended trunk-pelvis angle (-33.17° vs -56.20°), though mesomorph male participants performed a marginally more extended trunk inclination (42.94° vs 46.53°). Fig. 1(b) exhibits inter-somatotype differences. This might be attributed to a stronger body composition on mesomorph participants compared to endomorph.

In conclusion, when subjects executed free trials, they bent their knees less than following lifting instructions, leading to a greater trunk inclination to reach the load. On the other hand, despite instructions were given, small inter-somatotypes variations were found in instructed trials, however, these differences were not significant.

Acknowledgements

This publication was supported by the project CZ.02.1/0.0/0.0/17_048/0007280 of the Czech Ministry of Education, Youth and Sports under the operational program Research, Development and Education.

References

[1] Haines, T., Bowles, K., Cost-effectiveness of using a motion-sensor biofeedback treatment approach for the management of sub-acute or chronic low back pain: Economic evaluation alongside a randomized trial, BMC Musculoskeletal Disorders 18 (1) (2017).
[2] Kingma, I., Faber, G., Van Dieën, J., How to lift a box that is too large to fit between the knees, Ergonomics 53 (10) (2010) 1228-1238.
[3] Kingma, I., Faber, G., Van Dieën, J., Supporting the upper body with the hand on the thigh reduces back loading during lifting, Journal of Biomechanics 49 (6) (2016) 881-889.
[4] Plamondon, A., Lariviere, C., Denis, D., St-Vincent, M., Delisle, A., Sex differences in lifting strategies during a repetitive palletizing task, Applied Ergonomics 45 (6) (2014) 1558-1569.
[5] Singh, D., Park, W., Hwang, D., Levy, M., Severe obesity effect on low back biomechanical stress of manual load lifting, Work 51 (2) (2015) 337-348.

COMPUTATIONAL MECHANICS 2018
34th conference with international participation
Srní
October 31 - November 2, 2018

Elementary approach to monitoring and evaluation of aerodynamics simulations of moving parts in computational domain

M. Schuster [a]

[a] *Výzkumný a zkušební ústav Plzeň s.r.o., Tylova 1581/46, 301 00 Plzeň, Czech Republic*

This paper is generally focused on modelling of aerodynamics with motion in computational domain. Basic approach to modelling of domain zones motion using so called "sliding-mesh" method and setting relevant boundary conditions for simulate calculations are described. These engineering cases were selected: CFD simulations of the hydrodynamic situation around the model of moving control rods and CFD simulations of the aerodynamic situation in the tunnel through which a train pass. Results of simple case studies of trains riding through a tunnel are showed. Relationship between the resulting values of CFD calculations and values mentioned in standards and other rules determining the operating condition in tunnels are discussed.

Modelling of aerodynamics with a motion in the computational domain is a problem where separate domain parts move relatively to each other. The relative motion of stationary and moving components of domain generates transient interactions and time dependent aerodynamic load. This motion can be translational or rotational.

One possible approach how to simulate "motion in domain" is the method of "sliding-mesh" which is often used in CFD simulation of aerodynamics [1]. This method is based on the motion of one or more moving zones relatively to stationary non-moving zones. 3D-case domain includes moving/stationary zones as volumes with "unchanging shape and size" and non-deforming computational mesh in domain.

The "sliding-mesh" modelling is used in many applications of engineering praxis:

- rotating machines, turbines, compressors, fans,
- control valves,
- control and nuclear fuel rods,
- moving and passing vehicles.

Important part of the "sliding-mesh" setup model is the "interface-zone". Each domain cell zone is bounded by at least one "interface zone". These cell zones slide (rotate or translate) relatively to each other along the mesh interface in discrete steps during the calculation.

Basic setup of "sliding-mesh" models is common and consists of several main steps (moving/stationary zones, interfaces, time-dependent solvers, etc.). Each "sliding-mesh" model application is different in many details corresponding to the particular engineering case. Size and dimensions of domain, types of mesh elements, boundary layer requirements, boundary conditions, medium materials (aero/hydro) or time background of model play important role and have significant influence on other parameters of the calculation setup. Time management of calculation is often crucial because choice of time-step size, number of time steps or number of iterations per time-step affect the process of convergence of the

calculation. Of course, set-up parameters of currently solved task are always very different from others cases.

Simulation of the slow motion of a control rod in channel was chosen as the first illustrating case from engineering praxis. Small cylindrical rod was shifted in shaped channel. Domain dimensions size were several millimetres, high-pressure water was used as the surrounding medium, rod shifts several millimetres. The pressure load of the rod was investigated as the main result of simulation.

The simulation of train aerodynamics in tunnels was chosen as the second illustrative example from the engineering praxis. [2]. This category of tasks contains wide variety of ride regimes to simulate: the train enters the tunnel, the train rides through the tunnel and passing and crossing trains in the tunnel (at various speed, various shape of tunnel, various types of trains – loco, electric/motor-unit, etc). Results of simulations allowed us to judge the aerodynamic influence of moving vehicles or influence of a moving vehicle to the surroundings and then to examine:

- the design of a train shape,
- the aerodynamic load of a train body or its parts,
- the influence of the riding train to the surroundings,
- the design of the tunnel and tunnel portals.

The setup, post processing and the result analysis of these tasks correspond to the requirements given by standards or ride regulations (e.g. maximal running speed, line speed) of pressure strain of train parts, tunnel and surroundings. The graph of the time-dependant value of pressure on front part of the moving locomotive or the graph of the time-dependant value of pressure in fixed point along the railway tracks are often used as relevant results.

It should be noted that other approaches to model a “motion in domain” is to use the method of “dynamic-mesh” with deforming meshes of moving zones [1]. The “dynamic-mesh” model allows us to move the boundaries of a cell zone relatively to other boundaries of the zone. Simulations of aero/hydrodynamic situation in the model as “moving piston in cylinder” are typical engineering cases for this method.

Conclusion of this extended abstract is simple: CFD simulations allow us to model engineering cases with “complicated” aerodynamics when one or more parts of computational domain are in motion. The methodology of the simulation itself is clear, but it should be noted that the approach how to compare the results to the requirements of standards is not. It should be clearly defined what monitoring is required, which aerodynamic loads should be studied and how and where they act.

Acknowledgements

The paper has originated in the framework of institutional support for the long-time conception development of the research institution provided by the Ministry of Industry and Trade of the Czech Republic to Research and Testing Institute Plzen.

References

[1] ANSYS Fluent User’s and Theory Guides, ANSYS, Inc., Canonsburg, 2015 – 2018.
[2] Schuster, M., et all., External aerodynamics of rail vehicles and aerodynamics in railway tunnels, Internal research reports, VZÚ Plzeň, 2003 – 2018. (most in Czech)

COMPUTATIONAL MECHANICS 2018
34th conference with international participation
Srní
October 31 - November 2, 2018

Optimized Wang Cubes for reconstruction of heterogeneous materials

D. Šedlbauer [a]

[a] *Department of Mechanics, Faculty of Civil Engineering, CTU in Prague, Thákurova 7/2077, 166 29 Prague, Czech Republic*

The term (re)construction of either 2D or 3D random heterogeneous material models used to be linked with the traditional concept of the Periodic Unit Cell (PUC). Unfortunately principles of the PUC approach with periodic boundary conditions are in direct conflict with definitions of randomness and heterogeneity. Few years ago a group of researches started to reduce consequences of this approach by utilization of the Wang tiling concept [3], which allows us to create aperiodic planes/spaces with relative small set of Wang Tiles/Cubes. This contribution deals with an upgrade of methods for generation of Wang tiles based on molecular dynamic algorithms. We will focus on 3D material samples representing domains with impenetrable hard spherical particles of identical radii in a matrix.

The main building block for tiling in 3D, Wang cube, can be described as a cube with different codes (information) on walls allowing compatibility within tiling process. The stochastic CSHD algorithm [1] is applied, since for material engineering there is no need to create strictly aperiodic samples. We consider the smallest set of Wang cubes based on two possible types of codes on walls for each of axis *x*, *y*, *z* in coordinate system. This assumption together with stochastic principles of tiling form basic set of sixteen Wang Cubes, Fig. 1.

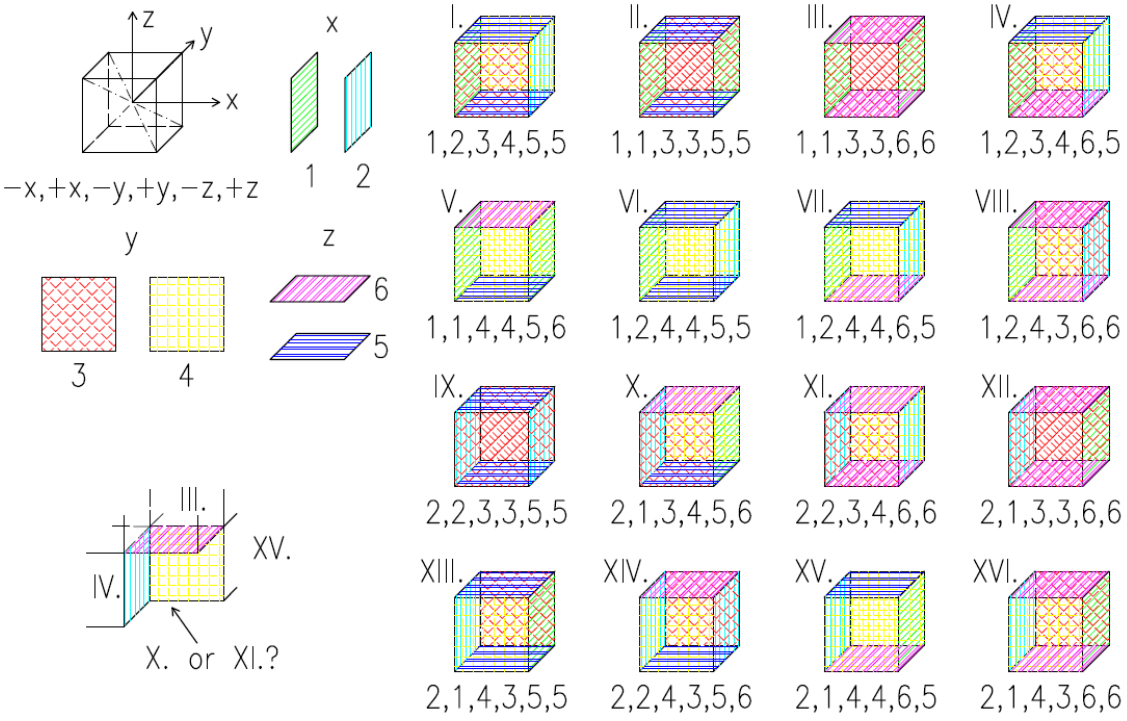

Fig. 1. Principles of stochastic tiling, basic set of 16 Wang Cubes

In previous works [2] a dynamic algorithm was used for generation of Wang cubes in order to efficiently prevent particles overlapping. Here particles collide from each other and rebound from walls of Wang cube volume border parts. Every single cube of the set was divided into six border and one central box to meet requirements for both tiling principles and particle volume fraction. Despite the reduction of unwanted periodicity in comparison with the PUC concept, approach with the cube volume division leads to secondary periodic peaks in lower order statistic description. In this contribution we present a significant upgrade of dynamic algorithm based on adaptive walls, Fig. 2.

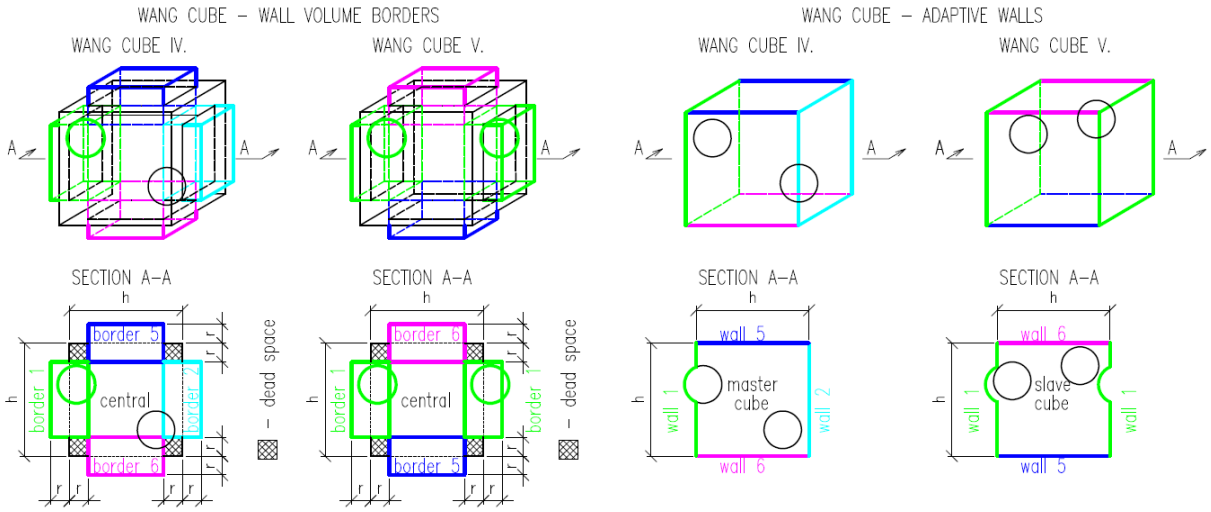

Fig. 2. Simplified comparison of algorithms for Wang Cubes generation: Wall volume borders vs Adaptive Walls

In Fig. 2 are shown only two representatives of the set with just codes in *x*, *z* axis and with only two particles to keep visual comparison clear for the reader. In the first case particles in border volume parts have to be copied to all cubes with appropriate code on wall. On the other hand with adaptive walls there is a master cube, where the particle forms the wall deformation. The walls on slave cubes with the same code then only follow the deformation without copying particles from the master cube, which increase heterogeneity of the tiling.
This contribution briefly introduced Wang tiling for reconstruction of 3D random heterogeneous material domains. Described modification of algorithm for Wang cubes generation together with particle swarm optimization method reduce unwanted secondary artefacts in lower order statistical descriptors. All of these improvements represent promising ways how to get closer to heterogeneous material models of required properties as fundamentals for various fields of material engineering.

Acknowledgements

The financial support of the Grant Agency of the Czech Technical University in Prague, grant No. SGS18/036/OHK1/1T/11, is gratefully acknowledged.

References

[1] Cohen, M., Shade, F.J., Hiller, S., Deussen, O., Wang tiles for image and texture generation, ACM Transactions on Graphics 22 (3) (2003).
[2] Šedlbauer, D., Dynamic packing algorithm for 3D Wang Cube generation, In: Proceedings of the 5th Conference Nano & Macro mechanics. Prague: Czech Technical University, 2014, pp. 173-180.
[3] Wang, H., Proving theorems by pattern recognition-II. Bell system technical journal **40** (1) (1961) 76-102.

COMPUTATIONAL MECHANICS 2018
34th conference with international participation
Srní
October 31 - November 2, 2018

Control of vibration suppression of plate with a grid of actuators and sensors

Z. Šika [a], F. Svoboda [b], J. Volech [a], R. Krejza [a], M. Hromčík [b], J. Zavřel [a]

[a] *Faculty of Mechanical Engineering, Czech Technical University in Prague, Technická 4, 166 07 Prague 6, Czech Republic*
[b] *Faculty of Electrical Engineering, Czech Technical University in Prague, Karlovo náměstí 13, 121 35, Prague 2, Czech Republic*

The paper deals with the optimization of active vibration suppression of plate demonstrator equipped by regular grid of 5x5 actuators and their collocated 5x5 sensors realized by planar piezo patches [1]. Robust H-infinity design with fixed order controller of predefined structure and LQR design using implementation with the states observer have been investigated. The influence of different boundary conditions (examples in Fig. 1) of the plate to efficiency of different control law concepts is the main topic of research. The ideal target is an easy tunable, scalable, active vibration suppression control law, defined by a limited number of independent parameters and optimized dominantly based on the local dynamical properties of the compact actuator-sensor-matrices and only finally tuned taking into account the particular global mechanical configurations (e.g. boundary conditions).

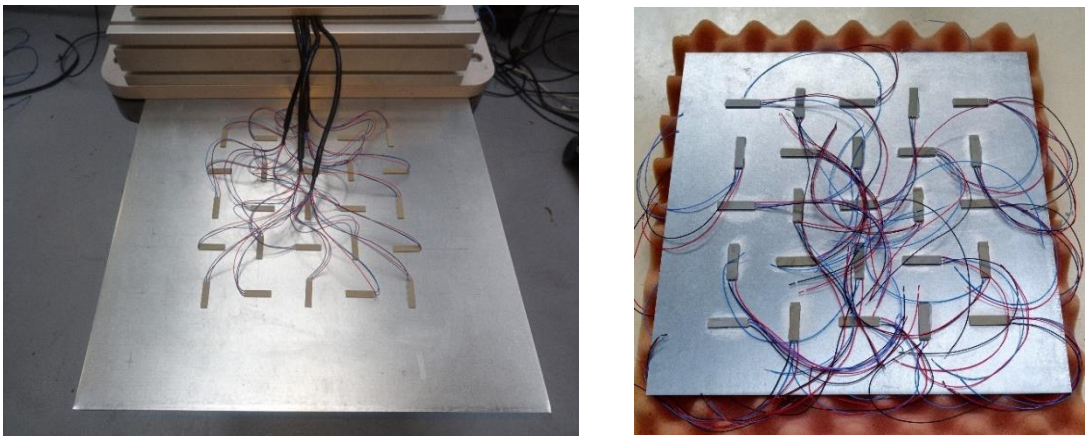

a) cantilever active plate b) "free" active plate

Fig. 1. Plate demonstrator with grid of piezo patches as actuators and sensors

H-infinity synthesis with predefined controller structure is frequency-domain optimization method for controller tuning. HIFOO solver [2] or *hinfstruct* function in Robust control toolbox in MATLAB have been the first method used for solving this task. Simulation model of the plate equipped with 25 actuators (control inputs U_i) and 25 collocated sensors (measured outputs Y_i) has been used for design and validation of selected control laws. They are designed using the H infinity structured optimization methodology to attenuate resonant modes of this flexible structure. The local controllers were considered in simple decentralized form

$$U_i = -k_i Y_i = -p_i \frac{s}{s+f_c} Y_i \,, \tag{1}$$

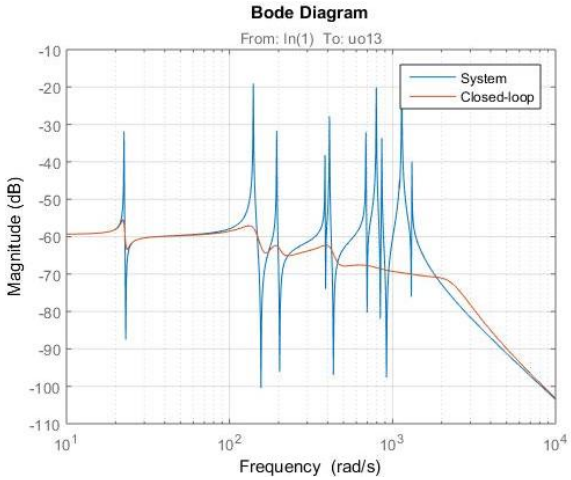

Fig. 2. Example of Bode diagram for H-inf decentralized feedback control

or in more complex form, where the control action applied to each patch depends also on measured outputs at the neighboring sensoring patches. Example of achievable results are presented in the form of Bode diagram (Fig. 2).

The second variant of the control law has been synthetized using well known LQR method with a state observer using sensory piezo-patches outputs. The achievable results have been comparable with the fixed order H-inf strategy. The different variants of excitation/disturbance have been considered and tested. The limits of control voltage of actuators have been taken into account using penalization matrix. The comparison of response of original and actively damped cantilever plate is in Fig. 3 for chirp excitation/disturbance by couple of perpendicular piezo patches no. 13 and 14. The control design using both mentioned techniques and the verification experiments are still in intense development.

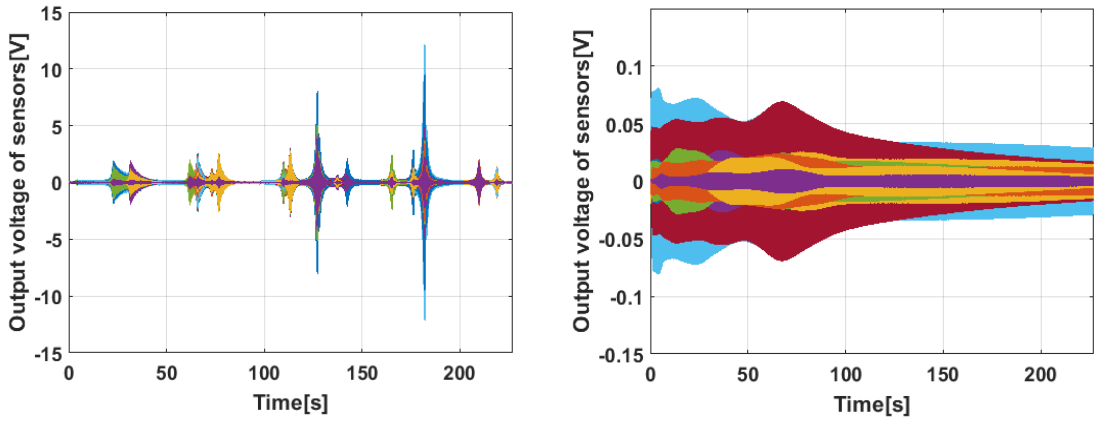

a) response of original system b) response with feedback control

Fig. 3. Example of simulation time responses of all piezo-patch sensors to chirp excitation

Acknowledgements

The work has been supported by the Czech Science Foundation project 16-21961S „Mechatronic structures with heavily distributed actuators and sensors”.

References

[1] Preumont, A., Mechatronics, dynamics of electromechanical and piezoelectric systems, Springer, 2006.
[2] Burke, J.V., Henrion, D., Lewis, A.S., Overton, M.L., "HIFOO - A MATLAB Package for fixed-order controller design and H-infinity optimization, In *IFAC Symposium on Robust Control Design*, Toulouse, 2006.

COMPUTATIONAL MECHANICS 2018
34th conference with international participation
Srní
October 31 - November 2, 2018

Combining adaptive mesh refinement with a parallel multilevel BDDC solver

J. Šístek[a], P. Kůs[a,b]

[a] *Institute of Mathematics, Czech Academy of Sciences, Žitná 25, 115 67 Praha 1, Czech Republic*
[b] *Max Planck Computing and Data Facility, Max Planck Institute, Giessenbachstrasse 2, 85748 Garching bei München, Germany*

Adaptive mesh refinement and domain decomposition. Adaptive mesh refinement is an important part of solving problems with complicated solutions or when a prescribed accuracy needs to be achieved. In this approach, solution is found on a given mesh and its local error is estimated. Regions where the estimated error is high are then refined to improve the accuracy, and the solution is recomputed. This strategy leads to accumulation of degrees of freedom to regions with abrupt changes in the solution, such as boundary or internal layers.

The growing size of the problems, especially in 3D, more and more often requires solving these on a parallel computer. To this end, partitioning of the computational mesh into subdomains is required. If the partitioning is not adjusted to the new meshes in the adaptive process, large imbalances in subdomain sizes quickly emerge, and utilization of the parallel computer becomes inefficient.

A viable way to maintain the subdomain sizes balanced is repartitioning using the space-filling curves, which maintains approximately equal number of elements in each subdomain. Such approach is offered by the *p4est* library [1]. However, this repartitioning strategy typically produces subdomains composed of several disconnected components.

Another important ingredient of simulations based on FEM is the solver for the arising system of linear equations. A good match for a parallel computation is using a domain decomposition method, and a recent member of this family is the multilevel Balancing Domain Decomposition based on Constraints (BDDC) [2, 4]. This method is implemented in our parallel solver *BDDCML*[1] [5].

We have developed a custom implementation of the FEM to study the impact of the special structure of the subdomains created by the *p4est* library on the BDDC solver. Disconnected components of subdomains are detected using subdomain mesh graphs while hanging nodes are incorporated naturally into the computation by the non-overlapping domain decomposition.

Numerical results and discussion. The solver has been applied to a number of benchmark Poisson and linear elasticity problems. The problem geometry was a unit cube in all our experiments. These experiments were performed using up to about 1 billion unknowns and 4 096 CPUs of the *Salomon* supercomputer at the IT4Innovations supercomputing centre.

In the first set of experiments, we have generated a mesh refined in several predefined regions. The behaviour of the solver was compared to uniformly refined meshes resulting in approximately half of the iterations, yet comparable in time to solution.

[1] `http://users.math.cas.cz/~sistek/software/bddcml.html`

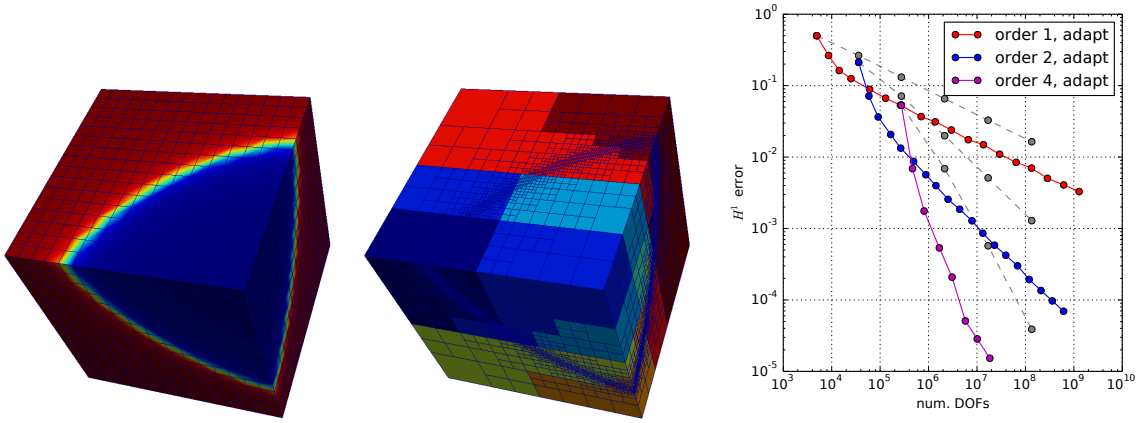

Fig. 1. A benchmark for a parallel adaptive computation: visualization of the exact solution (*left*), adaptively refined mesh partitioned into subdomains (*middle*), and convergence of the H^1 norm of the error on 2048 subdomains for different polynomial orders (*right*), adaptive (*colour lines*) vs. uniform (*grey lines*) mesh refinements.

The next experiment was running a benchmark adaptive computation, see Fig. 1. This test was performed for the Poisson problem using linear, quadratic, and fourth-order finite elements. The solver has allowed us to verify the convergence rate for problems refined up to 1 billion unknowns using 2 048 subdomains (and CPU cores). More details can be found in our paper [3].

Acknowledgements

This research was supported by the Czech Science Foundation through grant 18–09628S, and by the Czech Academy of Sciences through RVO:67985840. Computational time on the *Salomon* supercomputer has been provided by the IT4Innovations Centre of Excellence project (CZ.1.05/1.1.00/02.0070), funded by the European Regional Development Fund and the national budget of the Czech Republic via the Research and Development for Innovations Operational Programme, as well as Czech Ministry of Education, Youth and Sports via the project Large Research, Development and Innovations Infrastructures (LM2011033).

References

[1] Burstedde, C., Wilcox, L., Ghattas, O., p4est: Scalable algorithms for parallel adaptive mesh refinement on forests of octrees, SIAM Journal on Scientific Computing 33 (3) (2011) 1103-1133.

[2] Dohrmann, C.R., A preconditioner for substructuring based on constrained energy minimization, SIAM Journal on Scientific Computing 25 (1) (2003) 246-258.

[3] Kůs, P., Šístek, J., Coupling parallel adaptive mesh refinement with a nonoverlapping domain decomposition solver, Advances in Engineering Software 110 (2017) 34-54.

[4] Mandel, J., Sousedík, B., Dohrmann, C.R., Multispace and multilevel BDDC, Computing 83 (2-3) (2008) 55-85.

[5] Sousedík, B., Šístek, J., Mandel, J., Adaptive-Multilevel BDDC and its parallel implementation, Computing 95 (12) (2013) 1087-1119.

COMPUTATIONAL MECHANICS 2018
34th conference with international participation
Srní
October 31 - November 2, 2018

Self-oscillation of the two-axis gyroscopic stabilizer

J. Škoda [a], J. Šklíba [a]

[a] *Faculty of Mechanical Engineering, Technical University of Liberec, Studentská 2, 461 17 Liberec, Czech Republic*

Van der Pol introduced a solution of the self-oscillations of spring suspended body siting upon the uniform velocity moving rough conveyor belt in 1934. Friction between body and conveyor belt was non-Coulomb, which characteristics has negative slope in the certain interval – see Fig. 1. This classic problem, which is introduced in lots of non-linear vibrations related textbooks, motivated several works (see [1, 2, 3, 5]) whose refer to the fact that solution leads to the same equation (such as pin rotating in hub). Chernikov in [3] demonstrates that transformation of one-axis gyrostabilizer self-oscillations lead to the same equation in certain case. Mentioned Chernikov's work motivated us to analyze self-oscillations of two-axis gyroscopic stabilizer with non-Coulomb friction in the axis of stabilizer outer gimbal caused by uniform rotation speed of the stabilizer base.

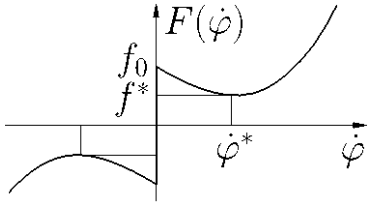

Fig. 1. Non-Coulomb friction characteristics

$$M_T(\dot\varphi) = f_0\left[\operatorname{sign}\dot\varphi - d_1\dot\varphi + d_3\dot\varphi^3\right] \qquad (1)$$

Similarly to Chernikov, we base our analysis on the system simplified as much as possible, using the following assumptions:

1. Mechanical system is in basic configuration – axes of gimbals are mutually perpendicular and horizontal, while flywheel's axes are vertical.
2. Correction and compensation feedbacks are deactivated – so that skew symmetric matrix of non-conservative forces is zero.
3. All gimbals and flywheels are static and dynamic balanced.
4. Flywheels angular momentum is sufficiently high.

Routh equations of motion are:

$$\begin{aligned} a_{11}\ddot\varphi + a_{13}\ddot\varepsilon - H\dot{\mathrm{E}} &= M_{T1}, \\ a_{22}\ddot\psi - H\dot\varepsilon + a_{24}\ddot{\mathrm{E}} &= M_{T2} = 0, \\ a_{31}\ddot\varphi + H\dot\psi + a_{33}\ddot\varepsilon &= 0, \\ H\dot\varphi + a_{42}\ddot\psi + a_{44}\ddot{\mathrm{E}} &= -H\dot\beta_0, \end{aligned} \qquad (2)$$

where a_{11} to a_{44} stand for algebraic functions of moments of inertia, H stands for angular momentum of the flywheels, M_{Ti} are for dry friction torques and $\dot\beta_0$ stands for a constant rotation speed of the stabilizer base. Second third and fourth equations have first integrals. According to Merkin [4], roots of characteristic polynomial are divided into two groups – nutation and precession, if angular momentum H is sufficiently high. But in spite of the absence of non-conservative positional forces (so called radial corrections), roots of the

precession motion are identically zero. The only torque acting on the system is non-Coulomb friction in the first Eq. (2), which describes a motion of the outer gimbal. Thus the characteristic polynomial of the system Eq. (2) with no damping has two pairs of the pure imaginary roots whose imaginary parts represents the nutation frequencies.

Discontinuity at zero mutual velocity and a cubic part of the non-Coulomb friction torque characteristics Eq. (1) are the only nonlinearities in the system. We are tackling this nonlinearity using a harmonic linearization method, similarly to [3]. We are assuming that the frequency of the self-oscillations will be close to one of the natural frequencies. We can determine the amplitudes of the self-oscillations using the condition of the real part of characteristic polynomial root of the system with a linearized damping force to be identically zero at the natural frequency.

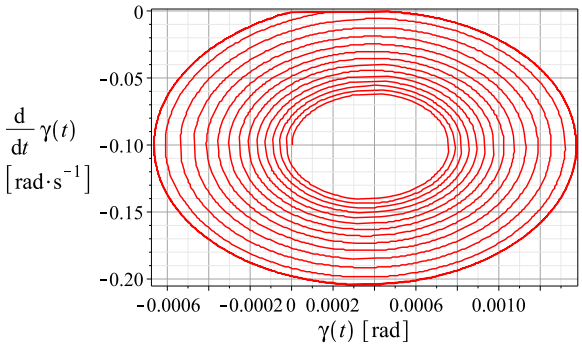

Fig. 2. Phase trajectory of outer gimbal with respect to inertial system – amplitudes reaching a limit cycle

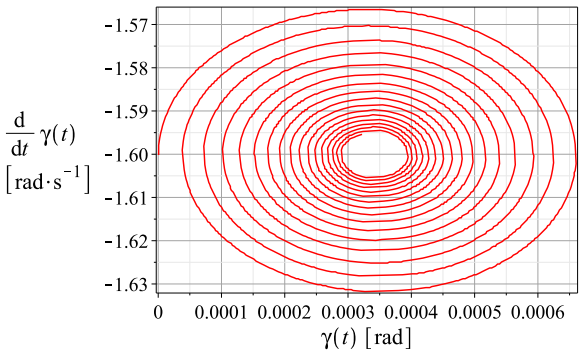

Fig. 3. Phase trajectory of outer gimbal with respect to inertial system – asymptotic stable

Limiting ourselves on the semi-trivial solution (assuming motion only with one frequency) and using table of the non-Coulomb friction characteristics according to Chernikov [1], we can show, by the numeric simulation of the system Eq. (2) , e.g. Fig. 2 and Fig. 3, that the phase trajectories of the motion for the certain setting of base rotation speed $\dot{\beta}_0$ are converging to the limit cycle and their amplitudes corresponds to the approximate solution of the linearized system. This can be considered as a proof of the self-oscillations existence.

Acknowledgements

This article was written at the Technical University of Liberec, Faculty of Mechanical Engineering with the support of the Institutional Endowment for the Long Term Conceptual Development of Research Institutes, as provided by the Ministry of Education, Youth and Sports of the Czech Republic in the year 2018.

References

[1] Andronov, V.V., Zhuravlev, V., Dry friction in problems of mechanics, Moscow, 2010.
[2] Blekhman, I.I., Vibracionnaya mekhanika, Moskva, 1994. (in Russian)
[3] Chernikov, S.A., Self-oscillation of a gyroscopic system with dry friction in gimbal axes during angular motion of the support, Herald of the Bauman Moscow State Technical University 95 (2) (2014) 28-39. (in Russian)
[4] Merkin, D.R., Giroskopicheskie systemy, Leningrad, 1974. (in Russian)
[5] Zhuravlev, V.V., Klimov, D., Prikladnie metody v teorii kolebanii, Moskva, 1998. (in Russian)

COMPUTATIONAL MECHANICS 2018
34th conference with international participation
Srní
October 31 - November 2, 2018

Numerical simulation of a cylindrical fatigue specimen loaded under mixed-mode conditions

O. Slávik [a], T. Vojtek [b], J. Poduška [a], L. Náhlík [b,c], P. Hutař [b,c]

[a] *Institute of Physics of Materials, AS CR, and Institute of Solid Mechanics, Mechatronics and Biomechanics, BUT Faculty of Mechanical Engineering; Brno, Czech Republic*
[b] *Institute of Physics of Materials, AS CR, Brno; Czech Republic*
[c] *CEITEC IPM, Brno, Czech Republic*

Although a significant number of service failures occur due to the fatigue crack propagation under mixed-mode loading conditions, this area is still relatively unexplored [3]. That is why study of mixed mode fatigue crack propagation has become much more relevant recently. The mixed mode crack behaviour is also the subject of this paper. It is focused mainly on numerical modelling of cylindrical fatigue specimen containing small cracks, loaded under mixed mode conditions. The simulation results are needed to successfully evaluate experimental measurements of crack propagation in the cylindrical fatigue specimens made of the austenitic stainless steel 316L. Some of the experimental data are also presented in this paper. Comparison of mixed mode results and pure mode I data is also carried out.

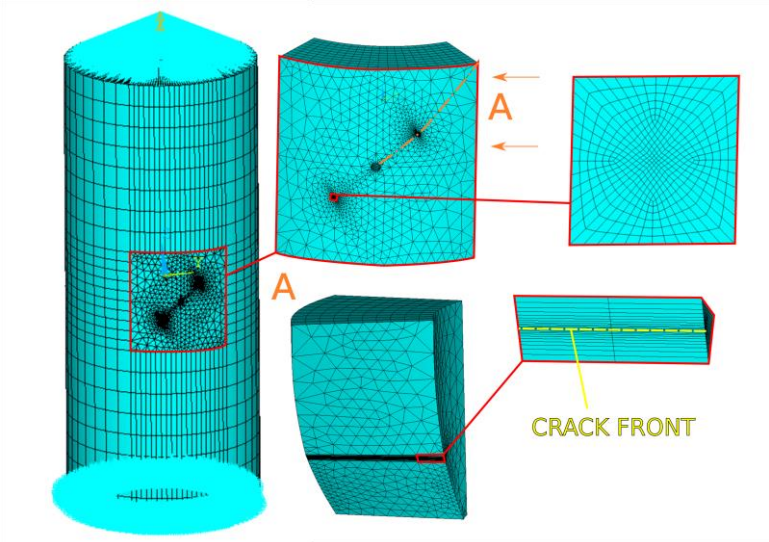

Fig. 1. Meshed model with boundary conditions and details of mesh

It is important to note that cracks that are dealt with in this paper belong to short cracks area of fracture mechanics [4]. In case of short cracks, large scale yielding conditions at the crack tip are typical. Therefore, linear elastic fracture mechanics cannot be applied [2] and non-linear fracture mechanics approach has to be used. Therefore, in our case, the parameter describing the fatigue crack growth rate is the plastic part of the J-integral, see [1].

A numerical model of the cylindrical fatigue specimen with cracks was set up to calculate J-integrals of cracks at several crack lengths. An important aspect of numerical model concerning fracture mechanics was the quality of the mesh. Very fine mesh had to be created in the close vicinity of the crack tip. Meshed specimen with boundary conditions, zoomed

details and cross sections can be seen in Fig. 1. The boundary conditions of the model were set up to simulate torsional loading. Upper surface was loaded by structural displacement – rotation around Z axis (see Fig. 1). Bottom surface was fixed.

The numerical model was solved twice for every crack length – at first using a simple linear elastic material model and then again with an elastic-plastic multilinear model based on cyclic stress-strain curve of the 316L steel. After solving the numerical models, J-integral could be calculated along the crack front. The plastic part of J-integral was evaluated as the difference between J-total (elastic-plastic problem) and elastic part of J-integral (linear elastic problem). Finally, the results of the simulation were used to calculate plastic part of J-integral of crack lengths measured in the experiments on real specimens. Plastic part of J-integral was then used for description of crack growth rate and compared with pure mode I data, see Fig. 2.

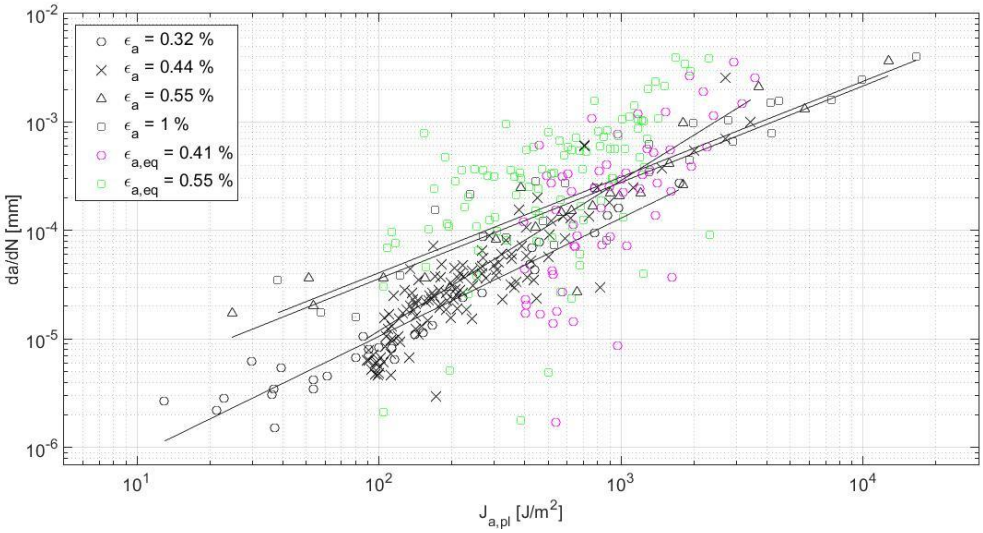

Fig. 2. Comparison of crack growth rates for mixed mode (purple, green) and pure mode I (black)

Conclusion: Numerical model was created in order to calculate the J-integral, which was afterwards used for description of the crack growth rate under mixed mode loading. Results were compared with pure mode I data [1]. Two sets of data with equivalent strain 0,41% and 0,55% was calculated. Obtained data indicate a significant amount of similarity compared to the pure mode I results.

Acknowledgements

This research has been supported by the Ministry of Education, Youth and Sports of the Czech Republic under the project m-IPMinfra (CZ.02.1.01/0.0/0.0/16_013/0001823) and the equipment and the base of research infrastructure IPMinfra were used during the research activities. Also, thanks are due to the specific research project FSI-S-17-4386 of the Faculty of Mechanical Engineering, BUT.

References

[1] Hutař, P., Poduška, J., Šmíd, M., Kuběna, I., Chlupová, A., Náhlík, L., Polák, J., Kruml, T., Short fatigue crack behaviour under low cycle fatigue regime, International Journal of Fatigue 103 (2017) 207-215.
[2] Hussain, K., Short fatigue crack behaviour and analytical models: a review, Engineering Fracture Mechanics 58 (4) (1997) 327–354.
[3] Qian, J., Fatemi, A., Engineering Fracture Mechanics 55 (1996) 969.
[4] Ritchie, R.O, Peters, J.O., Small fatigue cracks: mechanics, mechanisms and engineering applications, Materials Transactions 42 (1) (2000) 58–67.

COMPUTATIONAL MECHANICS 2018
34th conference with international participation
Srní
October 31 - November 2, 2018

Non-linear vibration of planar case of three-blade bundle with dry friction contacts

P. Šnábl[a], L. Pešek[a], L. Půst[a]

[a] *Institute of Thermomechanics of the Czech Academy of Sciences, Dolejškova 5, 18200 Prague, Czech Republic*

Using dry friction couplings (so called tie-bosses) between the blades in turbine rotors can be used to suppress dangerous resonant vibrations of turbine blades and it has been studied on our institute on various models [1, 3].

Experimental setup of three-blade bundle was built along with bladed wheel [2]. The first set-up of the bundle was with blades turned 45 degrees to the disc plane. In that case the deformation of the blades causes turning of the ends of tie-bosses and edge contact together with multi-directional slip occurs. The experimental set-up was simplified herein so that the blades are parallel to the disc plane and in-line slip occurs. Although single electromagnet was used to excite the system, the first mode of vibration with no slip in tie-bosses just occurred. In case of bladed wheel, all blades have coupling through tie-bosses with neighbouring blades which stiffen them and raise their eigenfrequency. In our case, a mistuning by reducing mass of side blades caused similar behaviour. Steel to steel contact pair was used for the first tests.

Analytical non-linear model of three-blade bundle has been created in Simulink to study the effect of dry friction on system damping. Each blade is represented by single-DOF element connected with Kelvin-Voigt element to another single-DOF element representing part of the disc. That part of the disc is connected to the frame and neighbouring disc parts also with Kelvin-Voigt elements. Between neighbouring blades a friction coupling consisting of serially connected dry friction element and spring was used [3].

Parameters of the Simulink model were tuned so that the resonance amplitudes of the middle blade during sweep excitation from 30 to 70 Hz for 60 s with measured peak of excitation force 3.8 N with open tie-bosses (with no friction force) and closed tie-bosses (with high friction force so that no slip occurs) match with the experiment as can be seen on Fig. 1.

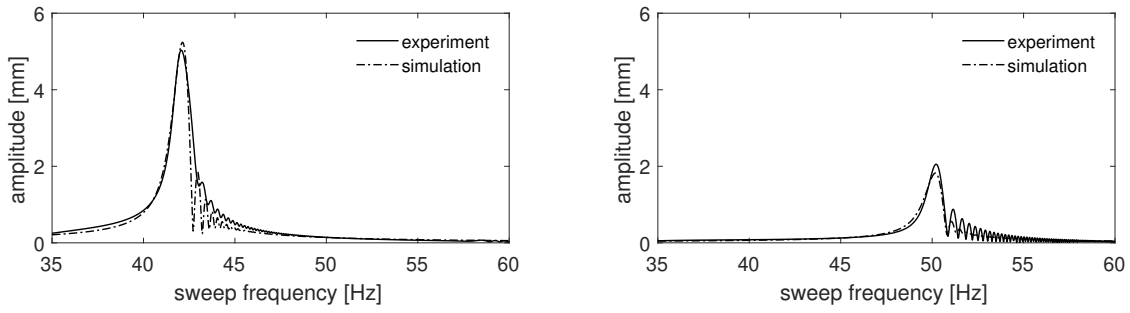

(a) open tie-bosses (b) closed tie-bosses

Fig. 1. Comparison of resonances during sweep excitation from experiment and simulation

Parameters are following: mass of the side blades 0.473 kg, mass of the middle blade 0.908 kg, stiffness of the blades (measured on experimental set-up) 6 300 N/m, damping coefficient of the blades 2.2 Ns/m, mass of the disc parts 0.7 kg, stiffness of the disc part to the frame 2×10^6 N/m and to the neighbouring disc part 4×10^6 N/m, damping coefficient of the disc parts 0 Ns/m and stiffness of the spring serial to the friction element 2×10^5 N/m. Coulomb friction law was used in the friction element.

Simulation responses on sweep excitation with various friction forces is shown on Fig. 2. Dashed line shows resonance peak of the system with closed tie-bosses. Allowing system to slip by reducing friction force, the resonance peak is being cut off till the amplitude of the middle blade reaches it's minimum for friction force around 2 N and by further reduction of the friction force the open-contact resonance arises.

Dash-dotted line on Fig. 3 shows measured data from the experiment with pre-stressed contacts. It corresponds with the simulation data with friction force 2.4 N.

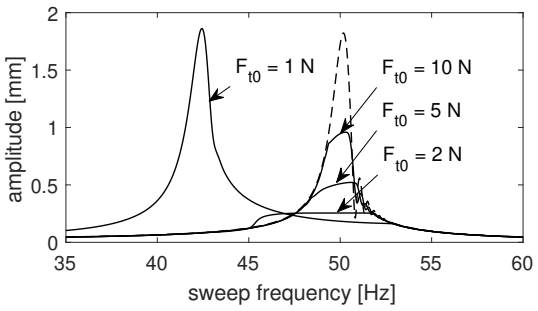

Fig. 2. Change of amplitude with varying friction force

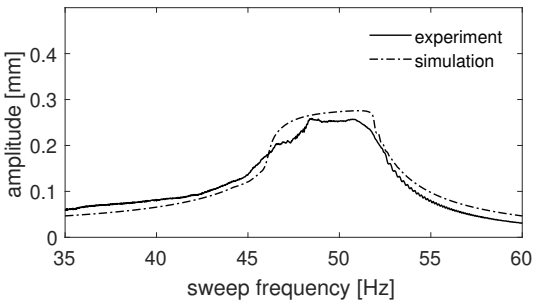

Fig. 3. Comparison of experimental and simulation results for $F_{t0} = 2.4$ N

The first results show very good agreement between experimental results and those from analytical model. According to the simulation, ideal friction force for this setup is 2 N and for excitation force 3.8 N it reduced the maximal amplitude 20x (from 5.24 to 0.26 mm) compared to open-contact resonance and 7x (from 1.82 to 0.26 mm) compared to close-contact resonance.

Acknowledgement

This work was supported by the research project of the Czech Science Foundation No. 16-04546S "Aero-elastic couplings and dynamic behaviour of rotational periodic bodies".

References

[1] Pešek, L., Bula, V., Šnábl, P., Cibulka, J., Experimental analysis of bladed wheel model with tie-boss couplings – steady and rotational states. Proceedings of the conference DYMAMESI 2018, Prague, Institute of Thermomechanics of the CAS, 2018, pp. 47-50.

[2] Pešek, L., Půst, L., Šulc, P., Šnábl, P., Bula, V., Stiffening effect and dry-friction damping of bladed wheel model with tie-boss couplings – Numerical and experimental investigation. Proceedings of the 10th International Conference on Rotor Dynamics – IFToMM, Cham, Springer International Publishing, 2019, pp. 148-162, doi: 10.1007/978-3-319-99270-9_11.

[3] Půst, L., Pešek, L., Radolfová, A., Blade couple with dry friction connection, Applied and Computational Mechanics 9 (1) (2015) 31-40.

COMPUTATIONAL MECHANICS 2018
34th conference with international participation
Srní
October 31 - November 2, 2018

Influence of the pilot on the modal parameters of the control system lightweight aircraft

T. Sommer [a], P. Steinbauer [a], M. Vilímek [a], S. Slavík [a], A. Kratochvíl [a]

[a] *Faculty of Mechanical Engineering, Czech Technical University in Prague, Technická 4, 166 07 Praha 6, Czech Republic*

This paper is focused on creation of experiment and experimental determination of pilot influence on the modal parameters of the longitudinal mechanical control system of lightweight aircraft. There are some publications which describes pilot response and traffic delay in relation to flight dynamics. Several studies on the description of the pilot's muscular activity have been published. The paper [1] deals with the recent studies of the human controller. At first describes linear models of human controllers, discus results of linear model studies, next describes nonlinear models like "bang bang" model for high-order system. The paper [2] deals with the lumbar muscular activity during real flight conditions, using surface electromyography sensors. With focus on type and duration of flight, type of helicopter, pilot dimensions. The paper [3] deals with vibration of helicopters during flight at very low frequencies 0.315-5 Hz. The paper [4] discusses mathematical models of human pilot behaviour at low frequencies till 1.6 Hz. Publication [5] describes influence of muscle responses in higher frequency up to 300Hz in relation to heavy tools such as drilling machine, drilling hammer, jackhammer. Main aim is description of influence of pilot arm on dynamical characteristics mechanical control route in the frequency range 1-70Hz. Determining where pilot´s properties are among the test boundary conditions of free and blocked control.

Test setup: During experiment pilot was sitting on the chair and hold the control stick. On the scheme are control stick, wrist, elbow and shoulder moving parts, other are without moving. On the pilot arm was placed seven sensors for measuring muscle activity. Measured muscles were brachialis, brachioradialis, biceps long head, biceps short head, triceps medial, triceps long head and triceps lateral. This measuring of the muscle activity called Electromyography (EMG) and usually is used for medicine purposes. On the control stick was placed three one-directional piezoelectric accelerometers from Bruel and Kjaer company with 14g range (position 2) on the frame and 71g range on the moving control stick (position 1,3). Point 4 wasn´t measured, dimensions are in millimeters. On the shaker was placed forcemeter from Bruel and Kjaer company.

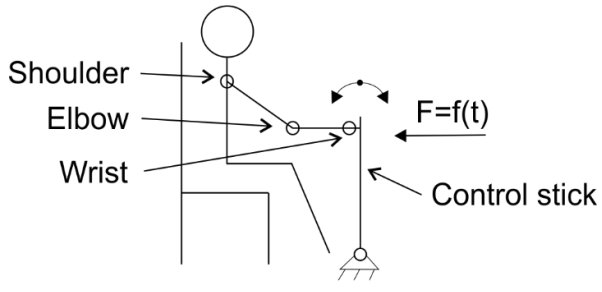

Fig. 1. Experiment layout

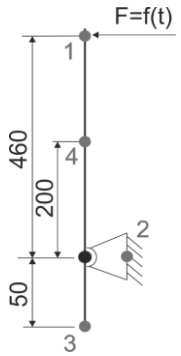

Fig. 2. Control stick scheme

Few boundary conditions were defined for this experiment. First one is a standard holding of control stick by a pilot. This boundary condition attempts to simulate the standard holding during balanced steady state flight with minimal or zero forces in control.

The second boundary condition is a state in which pilot tries to supress or minimize the movement of control stick within the range of vibration. Next boundary condition is a level of amplitude of excitation signal 1V, 2V, 3V.

The experiment was done with few types of excitation signals exactly sinesweep with linear and logarithm distribution and random burst. Excitation signal has frequency range 0.5-75 Hz. Sampling frequency was 1024 Hz, duration of one sample was 32s. Useful bandwidth was 400 Hz and has 32768 spectral lines.Measuring was done few times, first block was measured without averaging and it was done 3 times with the same boundary conditions. From this type of measuring we obtain EMG data. For calculating transfer function (further TF) from accelerometers and forcemeter we used data from averaged measurement. The setup of averaging was 66.6% of overlap with 12 averaging which consist of 5 full samples length.

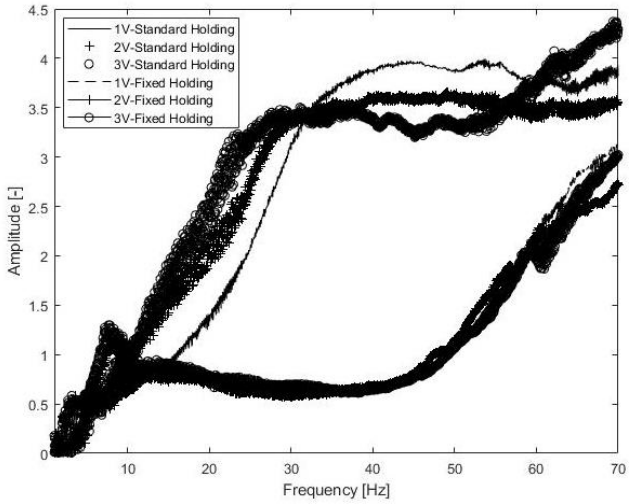

Fig. 3. Measured frequency response functions

Fig. 3 shows that there is some change in the measured TF when changing the amplitude of the excitation signal of "standard holding". This change is not so clear on the second boundary condition "fixed holding". A major change in the TF occurs in the case of a change of the handle type of the control stick. At higher frequencies, it is obvious, that the pilot is unable to suppress the movement and the TF is closer to the TF of the "standard holding".

Measured data was postprocessed. The obtained postprocessed data was used for creation of a state-space model of description human pilot operator. State space model was created by using subspace method without disturbance matrix.

References

[1] Brian, R., Gaines linear and nonlinear models of the human controller, International Journal of Man-Machine Studies 1 (1969) 333-336.

[2] Lopez-Lopez, J.A., Vallejo, P., Rios-Tejada, F., Determination of lumbar muscular activity in helicopter pilots: A new approach, Aviat Space Environ Med 72 (2001) 38 –43.

[3] de Oliveira, C.G., Simpson, D.M., Nadal, J., Lumbar back muscle activity of helicopter pilots and whole-body vibration, Journal Biomech 43 (2001) 1309–1315.

[4] McRuer, D.T., Krendel, E.S., Mathematical models of human pilot behaviour, Advisory Group for Aerospace Research and Development, Paris, France, 1974.

[5] Meltzer, G., A vibration model for the human hand-arm-system, Central Institute of Occupational Safety, Dresden, G.D.R.

COMPUTATIONAL MECHANICS 2018
34th conference with international participation
Srní
October 31 - November 2, 2018

Development of a personalized musculoskeletal human shoulder model

J. Špička[a], J. Vychytil[a], T. Ryba[b], L. Havelková[a]

[a] New Technologies – Research Centre, Univerzitní 8, 306 14 Plzeň, Czech Republic
[b] Faculty of Applied Sciences, University of West Bohemia, Univerzitní 8, 306 14 Plzeň, Czech Republic

Musculoskeletal disorders of the upper extremity are extremely common and one of the major causes of disability, sickness absence and health care usage worldwide [3]. In fact, musculoskeletal conditions is the most frequent cause of disability severely affecting individuals' daily lives [2]. With an ever growing and aging population, number of diseases typical for elderly people is expected to increase. To address these issues, detailed knowledge of the human body biomechanics is essential.

The aim of this study is to contribute to the development of personalized musculoskeletal human shoulder model for the prevention, therapy and rehabilitation strategies. Namely, we participate in the development of the virtual shoulder model in the AnyBody Modeling System (AMS). This model consists of bones that are interconnected via kinematic joints, muscles with corresponding tendons and ligaments. The bones are considered as rigid bodies. Each muscle with corresponding tendon is represented with several virtual elements in the model that are usually referred to as lines of action. These lines are considered as hill-type models and allows for the active motion of the model as a whole. An important task in the model development is setting realistic muscle paths in order to predict accurate acting forces and moments. To achieve that, artificial obstacles are used in the AMS model to avoid unreal muscle shapes and excessive sliding. Namely, the torus obstacle method is used [1]. It means that for each muscle line, tori obstacles are defined. The path is then given as a shortest connection of muscle attachments, closely wrapping the torus surface. Hence, the key issue of the model development is to define proper position and radii of each torus obstacle. These parameters differ in general for different individuals. The aim of this study is to develop methodology for setting the parameters of tori obstacles based on magnetic resonance imaging (MRI) of a particular shoulder. That is, patient-specific approach is adopted.

The shoulder of a patient is investigated using MRI to obtain anatomy data regarding glenohumeral joint and relevant muscles, see Fig. 1. In fact, we use standard MRI scanning of a shoulder that is common in medical practice. To process these data, semi-automatic tool has been developed. It enables us to identify individual bones and muscles. In this particular application, we use it to identify humerus and the deltoid muscle. Consequently, we create a 3D geometrical representation of these tissues.

The deltoid muscle is represented in the model with several lines of action. To obtain these, section cuts of the 3D geometrical model of the deltoid muscle in corresponding planes are performed. For each section, centerline of the muscle is obtained, see Fig. 2. Here, the centerline is depicted as a green line. The crucial task is to represent this centreline with the line of action within the musculoskeletal model using a torus obstacle. In fact, an optimization method is used

Fig. 1. MRI scan of a shoulder (frontal plane).

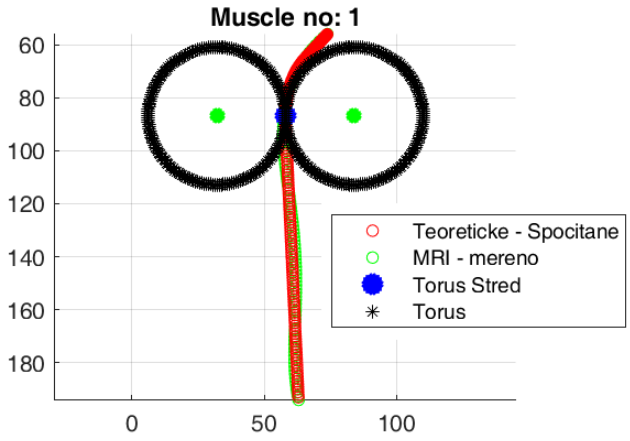

Fig. 2. The best fit of virtual muscle line (red) and a real centerline from MRI image (green) and the corresponding torus obstacle (black)

to find the parameters of the torus obstacle (position and radius) in order to find the best fit of the virtual muscle line and the real centerline. The result is depicted in Fig. 2. The virtual muscle line is depicted as a red line. The section of the corresponding torus obstacle is also depicted (black circles). The virtual line passes through the torus which has a zero inner diameter in this case.

The optimization process is done for each section cut. Hence, virtual lines of action and corresponding parameters of tori obstacles in terms of radii and positions are obtained. These are used as an input data for the musculoskeletal model of a shoulder in AMS. The proposed process is based on a patient-specific anatomy data. Hence, it contributes to the personalization of resulting musculoskeletal model.

Acknowledgements

This work was supported by the project n. 38 ”Virtual human body model for prevention, therapy and rehabilitation of shoulder disease” realised within the frame of the Program INTERREG V-A: Cross-border cooperation between the Czech Republic and the Federal State of Germany Bavaria, Aim European Cross-border cooperation 2014-2020. The realisation is supported by financial means of the European Regional Development Fund (85% of the costs) and the state budget of the Czech Republic (5%).

References

[1] Havelková, L., Špička, J., Vychytil, J., Aurbach, M., Krnoul, Z., Torus-obstacle method used for representing muscle path in musculoskeletal models, Proceedings of the 8th World Congress of Biomechanics, Dublin, 2018.

[2] Holtz, C., Global health care: Issues and policies, 2nd edition, Jones & Bartlett Learning, Burlington, MA, 2013.

[3] Huisstede, B., Complaints of the arm, neck and/or shoulder. A new approach to its terminology and classification: the CANS model, Ph.D. thesis, Erasmus University Medical Center, Rotterdam, 2007.

COMPUTATIONAL MECHANICS 2018
34th conference with international participation
Srní
October 31 - November 2, 2018

Tramway front end design safe for pedestrian

S. Špirk [a], J. Špička [a,b]

[a] Faculty of Mechanical Engineering, University of West Bohemia in Pilsen, Univerzitní 8, 306 14 Plzeň, Czech Republic
[b] New Technologies - Research Centre , University of West Bohemia in Pilsen, Univerzitní 8, 306 14 Plzeň, Czech Republic

This paper is focused on the field of rail vehicles passive safety. The really intensive research was dedicated to the safety tram front end design in last two years. The main point of this research is to reduce the severity of the consequences of a collision between tramway and pedestrian.

The collision of pedestrian and tramway is complicated problem. Some interesting researches were published early before the interest of European rail industry. The work has tended to a new tram safety systems, proposal from the pedestrian, passenger and driver points of view. [1] Today the most interesting researches were published by the "Technical Agency for ropeways and Guided Transport Systems" [2]. This is connected with the preparation of a new regulation. The collision scenario is based on statistical research and moreover the local research in Czech Republic is in the agreement with these statistics. The statistic of accidents is important for the definition of boundary conditions. The testing collision scenario consists of the tramway with the initial velocity equalling to 20 km/h, the initial position of the pedestrian with respect to the front-end of tram. The monitored value of the pedestrian is HIC (Head Injury Criterion) with its maximum threshold value equal to1000. The research is more focused on the tram design and less on the road (which can also produce several injuries by secondary impact of pedestrian). However, this is not a case of this research and it cannot be solved by the tramway producers. The result of pedestrian collision is most influent by geometry and material of the tram front-end.

For assessment of influence of tram geometry, it is necessary to investigate in the numerical simulations with different shapes of tram face. To avoid some unpredictable stochastic phenomena, it would be best to provide simulations with maximum number of possible geometries. One possible approach is to simplify the tram front-end design to the discreet description. The tram face can be divided to the finite number of linear flats with the finite number of positions [3]. Each flat has its own stiffness, damping and slope (inclination angle) definition. This approach is not as perfect as continuous reality, because the number of variants increase rapidly (1), but it can evaluate the safety of most geometries, where some of them are quite unpredictable.

$$V'(r,n) = n^r = 5^4 = 625 \ , \tag{1}$$

where the constant **n** is number of bodies and **r** is number of possible positions for each body. From this simple formula (1) it is obvious then the computations cannot be provided manually although this approach leads to the fast rigid body simulations.

With advantages of numerical software Virtual Performance Solution and its module Pam-Crash (which allows implement the python code to the input file), the simulation with next partition can be prepared. The main input file (*.pc) contains the minimum necessary settings and python variables for the geometry definition. This input file consists of another include

files (*.inc) with Multibody systems definitions (Human body model Virthuman, the ground definition, and the tram front-end design). The last include file contains python code which can create the simply Multibody model of tram face with basic trigonometry transformations (with known python variables defined in main input file) at the start of simulation.

This definition of simulation allows us to use another code for creating and running all possible variants of tram design. The first fast solution was prepared in Matlab which runs specific multibody computations on Linux based cluster through shell bash script (*.sh). The Matlab was selected cause its suitable and known possibilities to format text correctly and readable for Pam-Crash (close to Fortran syntax). Probably this work could be done with Linux shell script only (with significant effort) in the future. Although the multibody is not much suitable for parallelization, solving more of multibody simulations allows very simply parallelism. Each simulation can run in separate thread or node of cluster. This approach allows solver to finish optimization process in hours instead of days (on one CPU). The results of many simulations can be finally post-processed with Visual viewer scripts (*.tpl).

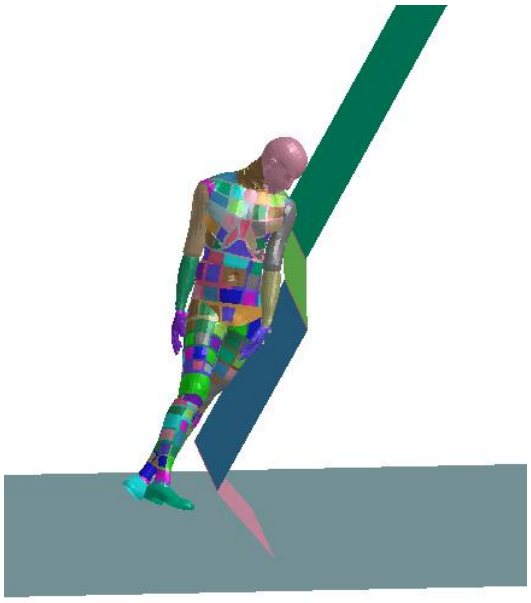

Fig. 1. The Multibody simulation of pedestrian collision with variable tram shape

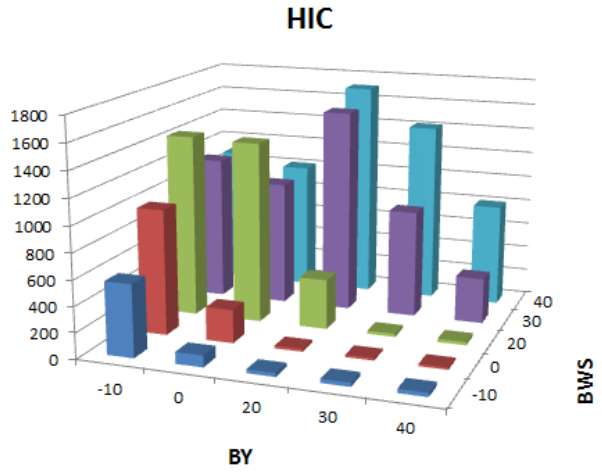

Fig. 2. The influence of two variable angles on the Head Injury Criterion value

Acknowledgements

The work has been supported by the project TRIO FV20441 „Výzkum a vývoj bezpečného čela tramvaje" provided by the Ministry of Industry and Trade of Czech Republic.

References

[1] Hyncik, L, Kockova, H., Číhalová, L., Cimrman R., Optimization of tram face with respect to passive safety, Engineering and Computational Mechanics 2 (2008) 53-62.

[2] Jubin, E., Tram to pedestrial collision, Proceedings of the 11th International Symposium PASSIVE SAFETY of RAIL VEHICLES, 2017, pp. 21-35.

[3] Špirk, S., The collision of unbelted passenger with assessment of various vehicle interior, Manufacturing Technology 17 (2017) 962-969.

COMPUTATIONAL MECHANICS 2018
34th conference with international participation
Srní
October 31 - November 2, 2018

Mechatronic modal hammer

P. Steinbauer [a]

[a] Department of Mechanics, Biomechanics and Mechatronics, Faculty of Mechanical Engineering, Czech Technical University in Prague

Many types of engineering structures exhibit nonlinear behavior under real operating conditions, e.g. brake sequel and undesirable engine mounting oscillations. In the aerospace industry, nonlinear motions may have serious implications for fatigue life ([4]). Even modal properties of advanced materials (plastics, glass or carbon fiber composites etc.) exhibit non-linear characteristic ([5]). In addition, current components are often lightweight, with thin walls and complicated internal structure.

Experimental modal analyses is well known and widely used tool for FEM model verification, calibration and recently quality assurance as well. The range of measured problems increased. Components with some level of non-linearity are measured. The quality control requires rapid measurement set-up. Accurate determination not only eigen-frequencies and eigen-modes, but also modal damping is essential ([2], [3]). Source of excitation force is essential part of the measurement chain. Influence of the measurement set-up of the measured item needs to be minimized. This disqualify modal shakers. They have to be connected (by screws or glue) to the item and it adds artificial damping and measurement uncertainty. Bending torques and added stiffness substantially modify the modes. Classical modal hammers do not influence properties of measured item. However, their usage requires skilled worker, it is exhausting, thus unreliable and impact force varies extremely between measurements.

Spatial vibration modes needs to be investigated accurately. So huge number of measured points (at least twice per highest mode wavelength) is necessary to mitigate spatial aliasing or mode shape misinterpretation. The scanning vibrometer allows automatic measurement of all measured points. But stable, robust, automatic excitation without influencing measured item used to be a problem.

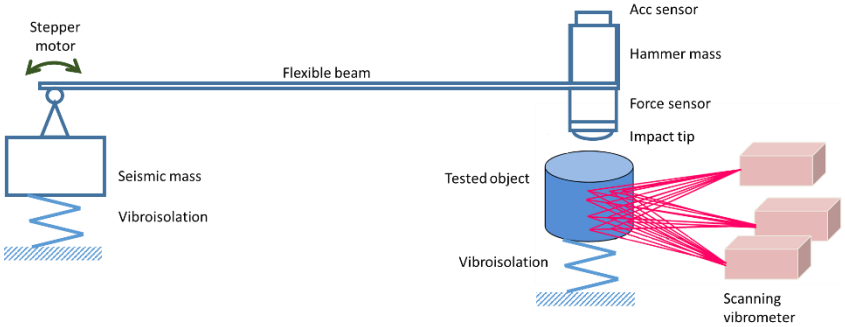

Fig. 1. Hammer structure

The paper introduces automatic modal hammer, which ensures high repeatability of impacts, clean impacts without double hits and controlled impact force level. Mechatronic design (Fig. 1) is based on highly flexible beam holding impact tool with force sensor. This enables clear single impact as the drive can reverse motion. The residual vibrations of the beam

are suppreesed by input shaping control ([1]) of the backward hammer motion. On-line tuning and feedback control based on hammer accelerometer to compensate unknown coefficient of restitution.

Fig. 2a shows functional prototype of the mechatronic modal hammer working together with 3D laser Doppler vibrometer Polytec. The setup enabled 17 hours of continuous experimental modal analyses measurement with impact excitation. Fig. 2b demonstrates spatial mode, which could hardly be measured accurately with modal shakers.

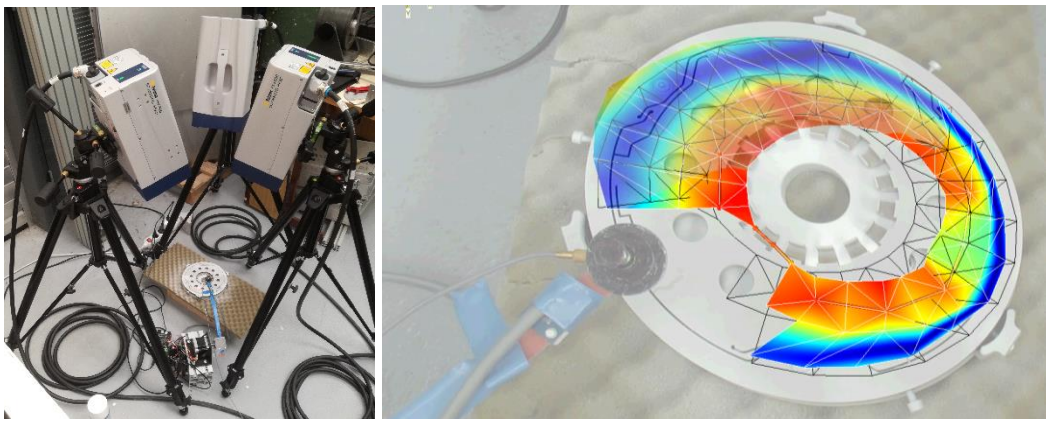

Fig. 2. Mechatronic modal hammer working with 3D laser doppler vibrometer (a), spatial eigen mode at frequency 685,16Hz excitated by mechatronic modal hammer (b)

The mechatronic modal hammer was designed and manufactured. Basic structure is relatively simple. However, suitable choice of mechanical parameters and smart control (feedback and feedforward) enables the device to achieve high parameter stability of impact excitation. The repeatability of the excitation force pulse is thus very high and long time measurement of experimental modal analyses is reliable and accurate. Furthermore, the mechatronic modal hammer is significantly cheaper then shaker. Mechatronic hammer installation is also very easy. This increases measurement quality, because several positions of excitation can be quickly tested to avoid modal nodes.

Acknowledgements

This research has been realized using the support of EU Regional Development Fund in OP R&D for Innovations (OP VaVpI) and The Ministry of Education, Youth and Sports, Czech Republic, project # CZ.1.05/2.1.00/03.0125 Acquisition of Technology for Vehicle Center of Sustainable Mobility and The Ministry of Education, Youth and Sports program NPU I (LO), project # LO1311 Development of Vehicle Centre of Sustainable Mobility. This support is gratefully acknowledged.

References

[1] Beneš, P., Valášek, M., Optimized re-entry input shapers, Journal of Theoretical and Applied Mechanics 54 (2) (2016) 353-368.
[2] Balmes, E., Wright, J.R., Garteur group on ground vibration testing, Results from the test of a single structure by 12 laboratories in Europe, OFFICE NATIONAL D ETUDES ET DE RECHERCHES AEROSPATIALES ONERA-PUBLICATIONS-TP, 1997.
[3] Steinbauer, P., Němec, J., Modal testing as a tool for composite damage detection?, 33rd conference with international participation Computational Mechanics 2017 - Extended Abstracts, Pilsen, University of West Bohemia, 2017.
[4] Worden, K., Tomlinson, G., Nonlinearity in structural dynamics, Boca Raton, CRC Press, 2000.
[5] Youzera, H., Meftah, S.A., Challamel, N., Tounsi, A., Nonlinear damping and forced vibration analysis of laminated composite beams, Composites Part B: Engineering 43 (3) (2012) 1147-1154.

COMPUTATIONAL MECHANICS 2018
34th conference with international participation
Srní
October 31 - November 2, 2018

Fast calculation of collapse load of shell structures

V. Štembera[a]

[a] *Institute for Mechanics of Materials and Structures, Vienna University of Technology, Karlsplatz 13, 1040 Vienna, Austria*

Numerical calculation of collapse load (limit load) of a structure, made of elastic-plastic material, is often of practical interest. Standard approach is based on repetitive use of nonlinear finite element calculation, where the collapse load is determined iteratively. However, more efficient approach called *finite element limit analysis* (FELA) is possible. In this approach the collapse load is searched as a minimum of a certain optimization problem.

Practical interest of the FELA was raised, when it was combined with the so-called second order cone programming (SOCP). This combination firstly appeared in literature in first decade of 21st century [1, 3], which made the FELA numerically very atractive. The FELA approach has also some drawbacks, mainly the assumption of ideal plasticity and geometrical linearity.

Let us demonstrate efficiency of the FELA approach on a symmetrical steel frame structure proposed in [2], see Figs. 1 – 3. The table in Fig. 1 compares calculation times of both approaches, which shows factor 34 in favour of the FELA approach. However, calculation efficiency is not the only benefit of the FELA approach – another one is high robustness of the calculation contrary to typical slow convergence of the nonlinear plastic calculations, when run near collapse load and when no hardening can be used.

Method	Calculation time
FELA ([4])	139 s
standard nonlinear FEM ([4])	4692 s

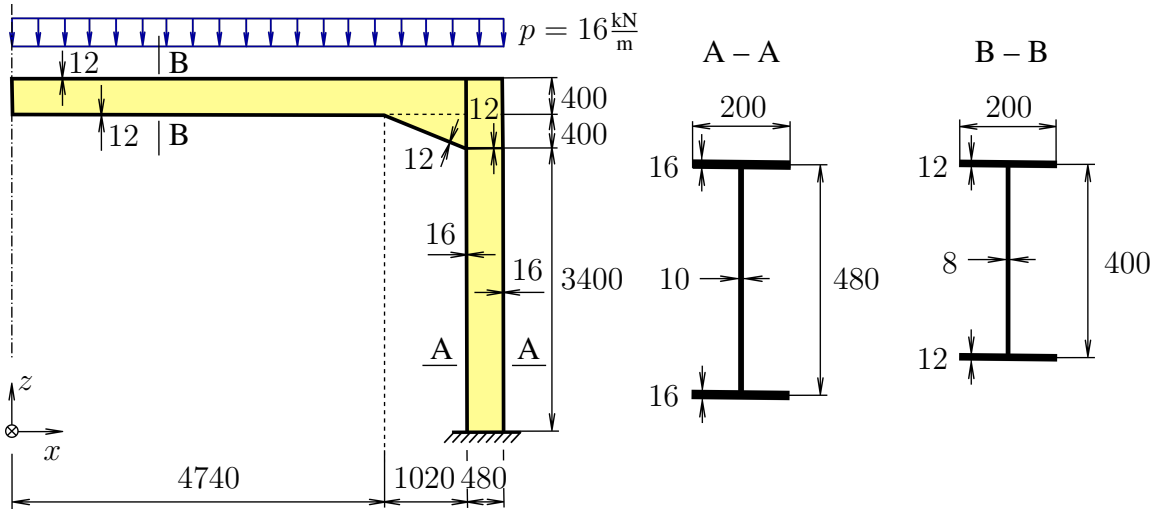

Fig. 1. Steel frame structure – problem sketch. Half of the structure is modeled due to symmetry

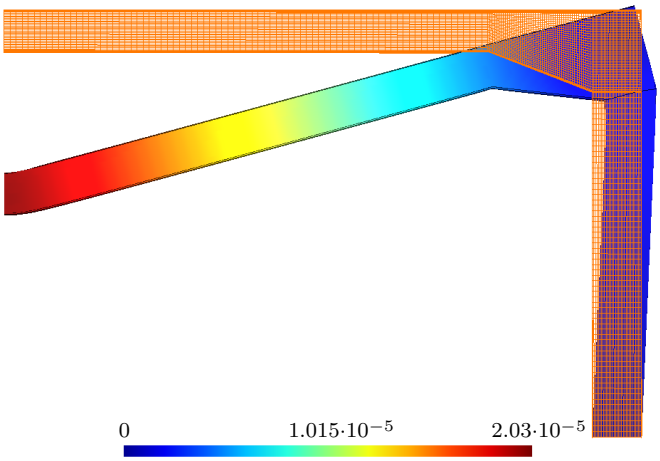

Fig. 2. Steel frame structure – undeformed mesh and absolute value of velocity of the plastic flow u is shown in colour. Structural deformation shows tendency of collapse

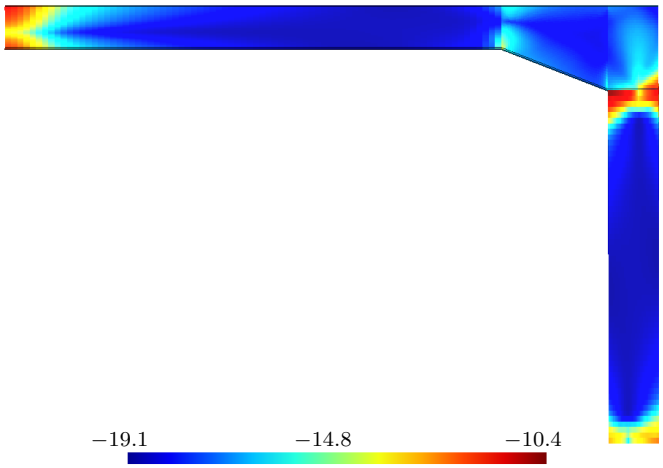

Fig. 3. Steel frame structure – logarithm of the dissipation energy $\log(e_{\text{dis}})$ is shown in colour. Note the plastic hinge created under the right upper corner

References

[1] Ciria, H., Peraire, J., Computation of upper and lower bounds in limit analysis using second-order cone programming and mesh adaptivity, Proceedings of the 9th ASCE Specialty Conference on Probabilistic Mechanics and Structural Reliability, Massachusetts Institute of Technology, Cambridge, 2004, MA 02139.

[2] Gruttmann, F., Wagner, W., A linear quadrilateral shell element with fast stiffness computation, Computer Methods in Applied Mechanics and Engineering 194 (2005) 4279-4300.

[3] Makrodimopoulos, A., Martin, C.M., Lower bound limit analysis of cohesive-frictional materials using second-order cone programming, International Journal for Numerical Methods in Engineering 66 (2006) 604-634.

[4] The femCalc finite element software. [online] www.femcalc.eu.

COMPUTATIONAL MECHANICS 2018
34th conference with international participation
Srní
October 31 - November 2, 2018

Modeling of the mechanical behavior of polymer hydrogels

J. Štorkán [a], T. Vampola [a], M. Dušková-Smrčková [b], K. Dušek [b]

[a] Faculty of Mechanical Engineering, Czech Technical University in Prague, Technická 4, 160 00 Praha, Czech Republic
[b] Institute of Macromolecular Chemistry, Czech Academy of Sciences, Heyrovského nám. 2, 162 06 Praha, Czech Republic

Polymeric hydrogels are interesting materials for biomechanics applications. These materials can be used as carriers for the cultivation of different types of biological materials. Hydrogels exist in many species, differing in chemical composition. The chemical composition, together with internal topology and external geometry, defines mechanical properties of the polymer hydrogels. The topology of hydrogels is a porous structure. The shape and size of the pores is affected by their production. It is shown that the mechanical properties of the inner structure significantly affect to cell production. Therefore, there is area for research into the mechanical properties of hydrogels. The goal of the whole research is to be able to design a topology so that the resulting mechanical properties are optimal for biological materials cultivation. This article deals with FEM modeling of hydrogel as homogeneous body without internal topology. This involves problems with the non-standard behavior of the material model over models commonly used in machine practice.

Hydrogels are very soft and flexible materials with a very great strains. Therefore, their material models are hyperelastic. The second significant feature of hydrogels is swelling. During production, they absorb the solvent. Mostly water. When swelling, the volume changes as long as a balance is established between the cohesive forces that hold the solvent in the material and the elastic forces that prevent the volume change of the body. This phenomenon is described by changing Gibbs' free energy, such as Flory-Huggins' formula (2). The overall change in Gibbs' free energy is the sum of the mixing component (2) and the elastic component (3). The elastic component represents any hyperelastic model. The material model based on the Gents' model of material with limited stretchability was used. For simplicity, we do not distinguish between Gibbs' free energy and Helmholts' free energy.

$$\Delta G = \Delta G_{mix} + \Delta G_{el,n} \,, \tag{1}$$

$$\Delta G_{mix} = RT \frac{\phi_2^0}{V_{1mol}} \frac{\phi_1}{\phi_2} (\ln \phi_1 + g(\phi_2)\phi_2) - RT \frac{f_e - 2}{f_e} v_e \phi_2^0 \ln \phi_2 \,, \tag{2}$$

$$\Delta G_{el,n} = -RTv_e\phi_2^0 \left(\ln(\lambda_1\lambda_2\lambda_3) + \frac{n-1}{2}\left(\ln\left(1-\frac{\lambda_1^2}{n-1}\right) + \ln\left(1-\frac{\lambda_2^2}{n-1}\right) + \ln\left(1-\frac{\lambda_3^2}{n-1}\right) - 3\ln\left(1-\frac{1}{n-1}\right)\right)\right) . \tag{3}$$

Parameters ϕ_1 and ϕ_2 are the volume fractions of solvent and gel. Volume fractions can be expressed by volume ratio. The volume ratio is a deformation function. Parameters λ_i are stretch. Other parameters are constants. Overall, the change of Gibbs' free energy is a function of only the main deformations. With this material model, it is possible to work with conventional continuum mechanics.

When computing, there is a problem with model convergence. Because the description contains a swelling component, the model changes the volume. With free swelling, the volume increases by about 350% and causes a deformation of about 65%. This of course depends on input parameters. Such large deformations must result in the first increment, and this causes numerical instability. The biggest problem is when the body is statically undefined. Another

problem is the shape of the function (1). For some combinations of input parameters it may not be convex. And it may contain more extremes. Such a case is shown in Fig. 1. The solution is not clear and you need to select the correct minimum Gibbs' free energy and avoid the maximum.

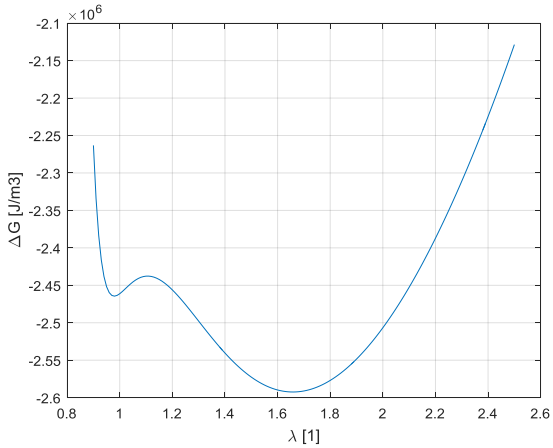

Fig. 1. Change of Gibbs' free energy for free isotropic swelling

The model shown in the figure shows 3 solutions for free isotropic swelling. One is the maximum and is unstable, the other two need to choose one. The easiest way is to choose a solution with lower energy (greater stability), or use the Maxwell construction for choice.

Swelling deformations are large. The calculation may not converge. This can be solved by the correct estimation of nodal displacements in numerical solution. This estimate determines which solution will be found. Nodal displacements estimates are simple for static defined tasks only. For general tasks, it is a very complicated estimate to carry out because it must respect kinematic boundary conditions. Therefore, another method is used. The calculation is made with another material model that does not show swelling. With this model, it is not a problem to calculate the task with all the boundary conditions. After applied boundary conditions, the material model switches to the desired swelling. The switching of the material model can be controlled incrementally. The incremental scheme will ensure convergence. In the case of a model with multiple solutions, the non-swelling model switches to swelling with a clear solution. This solution is consistent with one of the final material model solutions for the isotropic task. This ensures convergence to the chosen solution - choice of solution. And in the last phase it switches to the final material model.

The paper describes the possible procedure of FEM calculation of hydrogel materials. The basis of the calculation is to perform a calculation with a common material model. Only after the application of boundary conditions is the material model incrementally changed to the desired. This procedure reduces the risk of non-convergence. In addition, this allows you to choose a solution to which the model converges, if they exist.

Acknowledgements

The research is supported by Grant Agency of the Czech Republic by project No 17-08531S Computationally designed hydrogel cell supports.

References

[1] Koningsveld, R., Stockmayer, W.H., Nies, E., Polymer phase diagrams: A textbook, Oxford University Press, 2001.

[2] Dušek, K., Dušková-Smrčková, M., Šomvársky, J., Effect of constraints on swelling of polymer networks, Macromol, Symposia 2015, 358, pp. 120–127.

COMPUTATIONAL MECHANICS 2018
34th conference with international participation
Srní
October 31 - November 2, 2018

Prediction of hub-seal effect on efficiency drop in axial turbine stage

P. Straka [a]

[a] Czech aerospace research centre, Beranových 130, 199 05 Prague, Czech Republic

In axial turbine stages the secondary flows have an important impact on the drop of the stage efficiency. Significant sources of the secondary flows are shroud- and hub-seals [1,2]. This paper deals with numerical simulation of the hub-seal leakage flow effect on the axial turbine stage efficiency drop. Simulation was done using in-house numerical software [3] based on solution of RANS equation closed with $k-\omega$ turbulence model.

Fig. 1 shows scheme of the computational domain containing stator and rotor blades and simplified hub-seal with two seal-fins and with separated inlet boundary. The mass flow rate through the hub-seal is controlled with the size of the radial clearance c_{rad} in range 0.1 – 1.5 mm. The isentropic outlet Mach number is $M_{is,out}$ = 0.24, the isentropic outlet Reynolds number is $Re_{is,out} \approx 5.1\times10^6$, rotational speed of the rotor blade is 3810 RPM. Two axial clearances c_{ax} = 5 and 10 mm are tested.

Fig. 2 shows streamlines in meridian plane inside the hub-seal colored by normalized mass-flux density $\dot{m}/\dot{m}_{nom}$, where $\dot{m} = \rho(u_{ax}^2 + u_{rad}^2)^{0.5}$, ρ is the density, u_{ax} and u_{rad} are axial and radial velocity vector components and $\dot{m}_{nom}$ is nominal value. Fig. 3a documents an ele-

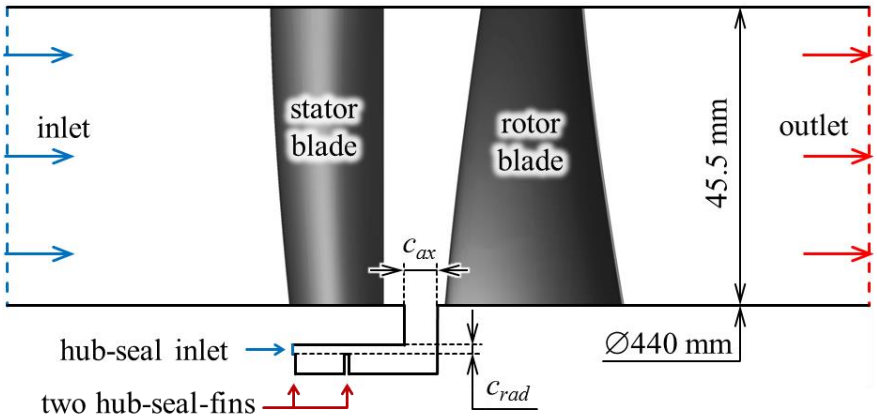

Fig. 1. Scheme of the axial turbine stage with the hub-seal

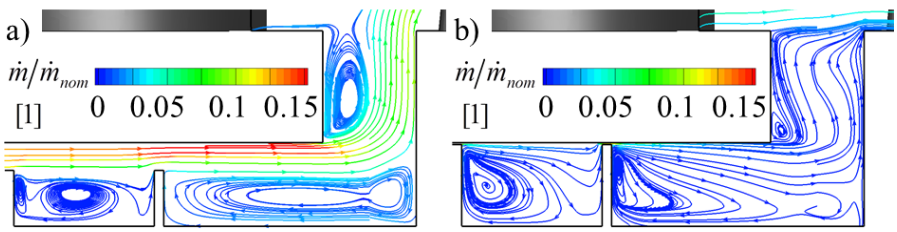

Fig. 2. Projection of streamlines to the meridian plane in the hub-seal region; the streamlines are colored by normalized mass-flux density; radial clearance: a) c_{rad} = 1.5 mm, b) c_{rad} = 0.1 mm

vation effect of the rotor blade on the stream from the hub-seal. The normalized efficiency drop dependency on the mass flow rate through the hub-seal is shown in fig. 3b. In fig. 3b there is $\Theta = q_{seal} / q_{tot}$, q_{seal} is mass-flux through the hub-seal and q_{tot} is total mass-flux through the outlet boundary. The normalized efficiency drop is defined as $\hat{\eta}_{TT} = (\eta_{TT} - \eta_{min}) / (\eta_{max} - \eta_{min})$, where $\eta_{TT} = (T_{Tin} - T_T) / (T_{Tin} - T_{Tis})$, T_{Tin} is the total inlet temperature, T_T is local total temperature, T_{Tis} is local isentropic total temperature, η_{min} and η_{max} are chosen minimal and maximal values for normalization. Fig. 4 compares distribution of the normalized efficiency drop in axial section behind the rotor blades for radial clearance c_{rad} = 0.1 and 1.5 mm.

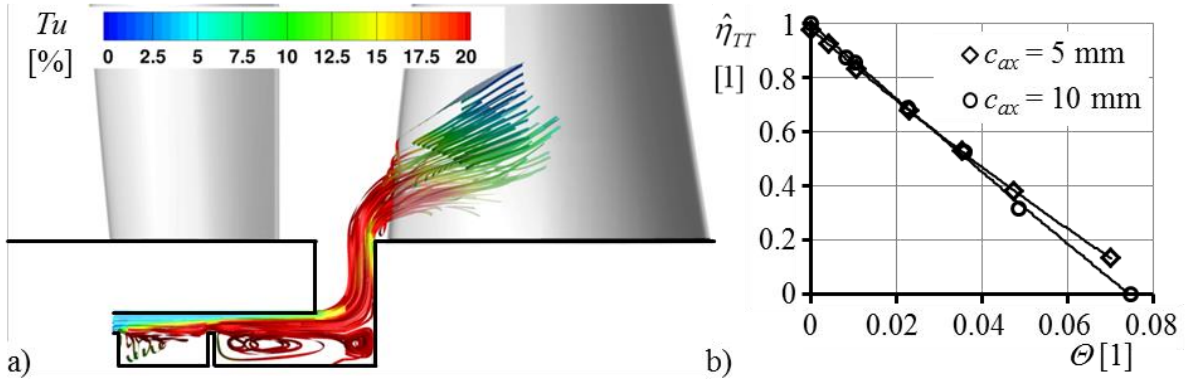

Fig. 3. a) detail of the streamlines (colored by local turbulence intensity) from the outflow-slot of the hub-seal; b) dependency of the normalized efficiency on the hub-seal mass-flux to total mass-flux ratio

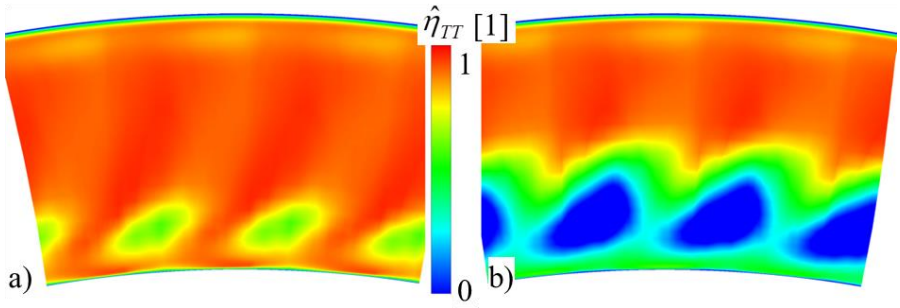

Fig. 4. Distribution of the normalized efficiency in axial section behind the rotor blades; radial clearance: a) c_{rad} = 0.1 mm, b) c_{rad} = 1.5 mm

Presented results demonstrate significant impact of the hub-seal leakage flow on the efficiency drop of the axial turbine stage. We can see that in case of higher mass flow rate through the hub-seal the seal leakage flow is able to send down the efficiency in lower half of the blade span.

Acknowledgements

This work has been supported by the project TH02020086 of the Technology Agency of the Czech Republic.

References

[1] Straka, P., Numerical study of shaft-seal parameters for various geometry configuration and operating regimes, EPJ Web of Conferences 180, 02100 (2018).
[2] Straka, P., Pelant, J., Numerical simulation of flow through a simplified model of the shaft-seal, Proceeding Conference Engineering Mechanics 2018, Svratka, 2018, pp. 821-824.
[3] Straka, P., Software for calculation of turbulent unsteady flow using the nonlinear turbulence model, Report VZLÚ R-6381, 2016. (in Czech)

COMPUTATIONAL MECHANICS 2018
34th conference with international participation
Srní
October 31 - November 2, 2018

Simulation of supersonic flow through the tip-section turbine blade cascade with a strong shock-wave/boundary-layer interaction

P. Straka [a], J. Příhoda [b], M. Luxa [b]

[a] VZLU Czech Aerospace Centre, Plc, Beranových 130, 199 05 Praha, Czech Republic
[b] Czech Academy of Sciences, Institute of Thermomechanics, Dolejškova 5, 182 00 Praha, Czech Republic

The numerical simulation of compressible flow including the laminar/turbulent transition through the turbine blade cascade with strong shock-wave/boundary-layer interactions presents a great challenge. The flow field structure depends to a large degree on the character of the boundary layer during the interaction. In case of the laminar boundary layer, the flow separation usually will come out connected with the transition in the separated flow. Therefore, the Favre-averaged Navier-Stokes equations should be completed not only by the turbulence model, but by adequate models of the laminar/turbulent transition and turbulent heat transfer as well. The numerical simulation was carried out by means of the EARSM turbulence model according to Hellsten [1] completed by the transition model with the algebraic equation for the intermittency coefficient proposed by Straka and Příhoda [5] and implemented into the in-house computational programme (see Straka and Příhoda [6]). The transition model considers two parts of the intermittency coefficient γ in the boundary layer γ_i and in the free stream γ_e. The intermittency in the boundary layer is expressed by the relation

$$\gamma_i = 1 - \exp\left[-\hat{n}\sigma\left(Re_x - Re_{xt}\right)^2\right]$$

where the transition onset is given by the Reynolds number Re_{xt} expressed by the momentum Reynolds number $Re_{\theta t}$ and the transition length by the spot generation rate $\hat{n}$ and spot propagation rate σ. Empirical correlations for $Re_{\theta t}$ and $\hat{n}\sigma$ are given by means of the pressure-gradient parameter and the free-stream turbulence for attached and separated flows as well. Using the vorticity Reynolds number instead of the momentum Reynolds number, the transition model is based on local parameter only and so it can be used for modelling of transitional flows in complex geometries like turbomachinery applications.

The numerical simulation of transonic flow through the tip-section turbine blade cascade was focused on the adequate simulation of the shock-wave/boundary-layer interaction. The flow field at the high inlet Mach number is influenced mainly by the interaction of inner branch of exit shock wave with boundary layer on the suction side of neighbouring blade. Numerical simulations were carried out for nominal conditions given by the inlet Mach number $M_1 = 1.68$ and the isentropic outlet Mach number $M_{2isSC} = 2.05$ corresponding to the pressure in the settling chamber. The isentropic outlet Mach number in the traversing plane is $M_{2is} = 1.97$ and the isentropic outlet Reynolds number $Re_{2is} = 1.98 \cdot 10^6$. The inlet free-stream turbulence was considered $Tu = 1.5$ % in the distance about one spacing upstream the blade cascade according to experimental data. Numerical results were compared with results of optical and pressure measurements, see Luxa et al. [4], [3].

Due to supersonic inlet and outlet flow conditions the computational domain was extended upstream and downstream to suppress reflections of parasitic shock waves. The outlet boundary condition is prescribed usually from experimental data in the traversing plane behind the cascade. The outlet boundary condition given the outlet isentropic Mach number was optimised according to angle of the exit shock wave and the blade chord.

The interferometric picture obtained for nominal regime is shown in Fig. 1. The interaction of the inner branch of the exit shock wave with the boundary layer on the suction side is connected with the separation on the laminar boundary layer. The detail of Mach number isolines showing the interaction of the inner branch of the exit shock wave with the boundary layer on the suction side of the blade is presented in Fig. 2. The best agreement was achieved for the isoentropic Mach number M_{2is} = 1.78 at the traversing plane behind the blade cascade. The field of Mach isolines well corresponds with the interferometric picture.

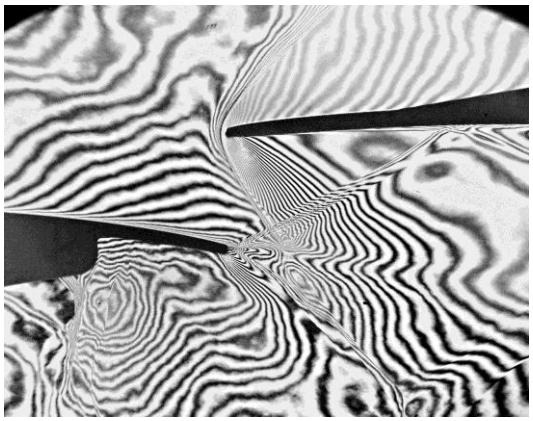

Fig. 1. Interferometric picture for M_{2is} = 1.97

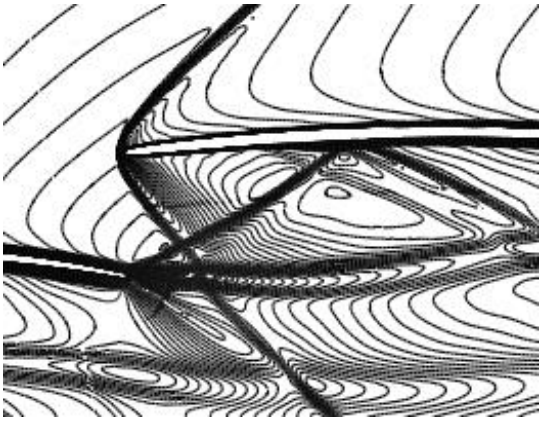

Fig. 2. Detail of Mach number isolines

Numerical simulations of the supersonic flow have shown the significant effect of the prescription of the outlet boundary condition. Simulations carried out for the standard computational domain with the output behind the blade cascade and/or for the computational domain corresponding to the experimental arrangement have shown that numerical results obtained on the basis of the numerical optimization correspond quite well to experimental data (see Louda et al. [2]). The agreement of predicted flow fields and main parameters including energy losses is acceptable.

Acknowledgements

The work was supported by the Technology Agency of the Czech Republic under the grant TH02020057. Institutional support RVO 61388998 is also gratefully acknowledged.

References

[1] Hellsten, A., New two-equation turbulence model for aerodynamics applications, Ph.D. thesis, University of Technology, Helsinki, 2004.

[2] Louda, P., Straka, P., Příhoda, J., Simulation of transonic flows through a turbine blade cascade with various prescription of outlet boundary conditions, EPJ Web of Conferences 180, 02056, 2018.

[3] Luxa, M., et al., Investigation of the compressible flow through the tip-section turbine blade cascade with supersonic inlet, Journal of Thermal Science 25 (2016) 138-144.

[4] Luxa, M., et al., Aerodynamic investigation of tip section for titanium blade 54", Proceedings of the 11th European Conference on Turbomachinery Fluid Dynamics and Thermodynamics, Madrid, 2015, pp. 1-13.

[5] Straka, P., Příhoda, J., Application of the algebraic bypass-transition model for internal and external flows, Proceedings of the International Conference Experimental Fluid Mechanics, Liberec, 2010, pp. 636-641.

[6] Straka, P., Příhoda, J., Numerical simulation of compressible transitional flow through high-loaded turbine blade cascade, Proceedings of the Conference Topical Problems of Fluid Mechanics, Praha, 2014, pp. 131-134.

COMPUTATIONAL MECHANICS 2018
34th conference with international participation
Srní
October 31 - November 2, 2018

Finite element method application for fluid structure interactions: Mathematical background and implementation

P. Sváček[a]

[a] *Faculty of Mechanical Engineering, Department of Technical Mathematics, Czech Technical University in Prague, Karlovo nám. 13, 121 35 Praha 2, Czech Republic*

In this paper the mathematical modelling of fluid-structure interaction problems is addressed particularly with the interest paid to the biomechanics of human voice. The attention is paid to the precise approximation of the fluid flow, particularly in the glottal part, with the aid of the numerical approximation of the Navier–Stokes equations. This problem is even more complicated in the context of the voice creation process, e.g., by the glottal gap closing or by the presence of the contact problem. In this case one need to take into account not only a significant mesh deformation but also the influence of the prescribed artificial inlet/outlet boundary conditions.

We shall focus particularly on several implementation aspects of the finite element method used for the solution of the fluid-structure interaction (FSI) problem. The practical realization of the finite element method shall be discussed based on the variational formulation of the underlying problems. The FSI problem consists of the solution of the fluid flow, the structure deformation and the mesh displacement problems. For the fluid flow the moving mesh should be taken into account which leeds to the Navier-Stokes system of equations on the computational domain Ω_t^f written in the ALE form

$$\rho \frac{D^{\mathcal{A}} \boldsymbol{v}}{Dt} + \rho((\boldsymbol{v} - \boldsymbol{w}_D) \cdot \nabla)\boldsymbol{v} = \operatorname{div} \boldsymbol{\tau}^f, \qquad \nabla \cdot \boldsymbol{v} = 0, \tag{1}$$

where $\boldsymbol{v}$ is the fluid velocity vector, ρ is the constant fluid density, and $\boldsymbol{\tau}^f$ is the fluid stress tensor given by $\boldsymbol{\tau}^f = -p\mathbb{I} + 2\mu\mathbb{D}(\boldsymbol{v})$. Here, p is the pressure, $\mu > 0$ is the constant fluid viscosity and $\mathbb{D}(\boldsymbol{v}) = \frac{1}{2}(\nabla \boldsymbol{v} + (\nabla \boldsymbol{v})^T)$. This system of equations is equipped with initial and boundary conditions. The deformation of the domain is result of the mutual interaction with a structural model. For the structure deformation as well as the mesh deformation, e.g., the linear elastic model can be used.

In order to describe the details of the application of the finite element method for solution of (stationary) boundary value problems, we shall use a context of an abstract variational formulation of finding $u \in \mathcal{V}$ such that

$$a(u, v) = L(v) \qquad \text{for all } v \in \mathcal{V}, \tag{2}$$

where $\mathcal{V}$ is a Banach space and $a(u, v)$, $L(v)$ are in general forms on $\mathcal{V}$. This formulation represents a weak formulation of the above mentioned specific boundary value problems and contains the information about the solved equations as well as the applied boundary conditions. The problem (2) can be formally discretized by introducing a finite dimensional finite element

space $\mathcal{V}_h$ constructed over a triangulation of the computational domain. The application of the finite element method then reads: Find the approximation solution u_h such that

$$a(u_h, v_h) = L(v_h) \qquad \text{for all } v_h. \tag{3}$$

In the case when a is bi-linear and L is linear, this system represents a system of linear equations.

Such an approach is used in various books or textbooks about the finite element method to support the theoretical analysis of the finite element method, see, e.g., [1]. In this paper it is shown that such an approach is suitable also for the implementation purposes, see also [3, 4]. The program is written in object oriented C language, see [2].

For the implementation purposes, it is usually used that the forms a and L in (2) are given by integrals which together with the use of the finite element space $\mathcal{V}_h$ defined over an triangulation $\mathcal{T}_h$ gives

$$a(U, V) = \sum_{K \in \mathcal{T}_h} \int_K \omega_a(x, U, V)dx + \sum_{S \in \mathcal{S}_h} \gamma_a(x, U, V)dS \tag{4}$$

and

$$L(V) = \sum_{K \in \mathcal{T}_h} \int_K \omega_L(x, V)dx + \sum_{S \in \mathcal{S}_h} \gamma_L(x, V)dS, \tag{5}$$

where $\mathcal{S}_h$ denotes the set of all boundary edges of elements adjacent to the boundary Γ, ω_a, ω_L are expressions (or better operator) in u, v linearly dependent on v.

Using this the Galerkin formulation can be defined in the program by definition of methods of the object scalar problem

```
typedef struct {
    void   (*getBndrCnd)(bpoint *P, short *isfixed, double *val);
    double (*aformdx)(point *P, scalar *u, scalar *v);
    double (*Lformdx)(point *P, scalar *v);
    double (*aformdS)(bpoint *P, scalar *u, scalar *v);
    double (*LformdS)(bpoint *P, scalar *v);
} scalarproblem;
```

where `aformdx`, `aformdS` corresponds to terms ω_a, γ_a, and `Lformdx`, `LformdS` corresponds to terms ω_L, γ_L. The `scalarproblem` is then used for the finite element object `fespace` based on the mesh (triangulation) `gmesh`. This corresponds well to the mathematical construction of the finite element space over a triangulation τ_h.

Acknowledgment

This work was supported by the *Czech Science Foundation* under the *Grant No. 16 - 01246S*.

References

[1] Ciarlet, P.G., The finite element methods for elliptic problems, North-Holland Publishing, 1979.

[2] Schreiner, A., Object-oriented programming with ANSI-C, e-book available from URL <www.cs.rit.edu/ ats/books/ooc.pdf>, 2011.

[3] Fenics project, URL <http://www.fenicsproject.org>.

[4] Hermes (higher-order finite element system), URL <http://hpfem.org/hermes>.

COMPUTATIONAL MECHANICS 2018
34th conference with international participation
Srní
October 31 - November 2, 2018

The numerical simulation of human phonation

J. Valášek[a], P. Sváček[a], J. Horáček[b]

[a] Faculty of Mechanical Engineering, Czech Technical University in Prague, Karlovo nám. 13, 121 35 Praha 2, Czech Republic
[b] Institute of Thermomechanics, Czech Academy of Sciences, Dolejškova 5, 182 00 Praha 8, Czech Republic

The human phonation is highly interesting phenomenon, where numerical simulations play an important role due to the practical inaccessibility of the vocal folds. This phenomenon is described by three physical fields – the deformation of elastic body, the complex fluid flow and the acoustics together with mutual couplings. The description and results of fluid-structure interaction (FSI) is here taken from [3] over and this paper focuses on the acoustic part of problem described by the acoustic analogies.

Acoustic domain. Fig. 1 presents a two-dimensional acoustic problem domain. The computational domain, where FSI problem was solved and where acoustic sources are computed, lays between $0 < x < L_{\mathrm{FSI}}$. It is connected with the propagation region (model of vocal tract), far field region and damping PML block. The model of vocal tract is inspired by the MRI data for vowel [u:] from [2].

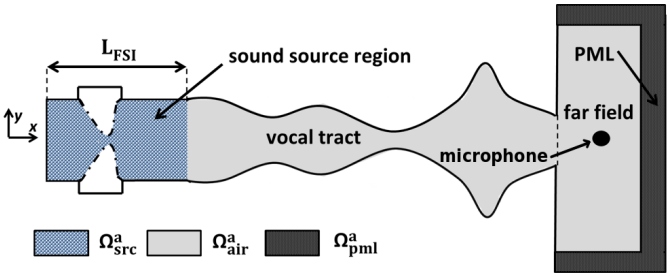

Fig. 1. Scheme of acoustic domain, all walls of acoustic domain are considered as acoustic hard

Lighthill analogy. The propagation of sound described by pressure fluctuation $p' = p - p_0$ is given by inhomogeneous wave equation in the form

$$\frac{1}{c_0^2}\frac{\partial^2 p'}{\partial t^2} - \frac{\partial^2 p'}{\partial x_i \partial x_i} = \frac{\partial^2 L_{ij}}{\partial x_i \partial x_j}, \tag{1}$$

where p_0 and ρ_0 mean stagnant pressure and density, respectively. The sound sources on the right hand side are described by the Lighthill tensor $\mathbf{L} = (L_{ij})$

$$L_{ij} = \rho^f v_i v_j + ((p - p_0) - c_0^2(\rho^f - \rho_0^f))\delta_{ij} - \tau_{ij}^f \approx \rho^f v_i v_j, \tag{2}$$

where following approximation of the Lighthill tensor valid for high Reynold number was used.

Perturbed Convective Wave Equation (PCWE) analogy. This analogy is based on general splitting of fluid flow quantities into mean, fluctuating (non-acoustic) and acoustic (i.e. compressible) parts, e.g., $p = \overline{p} + p_{ic} + p_a$. Supposing irrotational acoustic field leads to the equation

$$\frac{1}{c_0^2}\frac{D^2\psi^a}{Dt^2} - \Delta\psi^a = -\frac{1}{\rho_0^f c_0^2}\frac{Dp_{ic}}{Dt}, \tag{3}$$

where the acoustic potential ψ^a related to the acoustic particle velocity $\mathbf{v}^a = -\nabla\psi^a$ and pressure $p^a = \rho_0^f \frac{D\psi^a}{Dt}$ is sought. Symbol $\frac{D}{Dt}$ denotes the substantial derivative, i.e., $\frac{D}{Dt} = \frac{\partial}{\partial t} + \overline{\mathbf{v}} \cdot \nabla$. For further details see [1].

Numerical model. The acoustic analogies (1) and (3) were discretized in space by the finite element method and in time by the Newmark method. For implementation details see [3].

Sound sources. The computed sound sources in the form of right hand terms in Eq. (1) or (3) were analyzed by Fourier transform. The results show that main sound sources of frequency 232 Hz is located inside the glottis. The sources of higher frequency like, e.g., at 2486 Hz are mostly distributed in the channel behind the glottis, see Fig. 2.

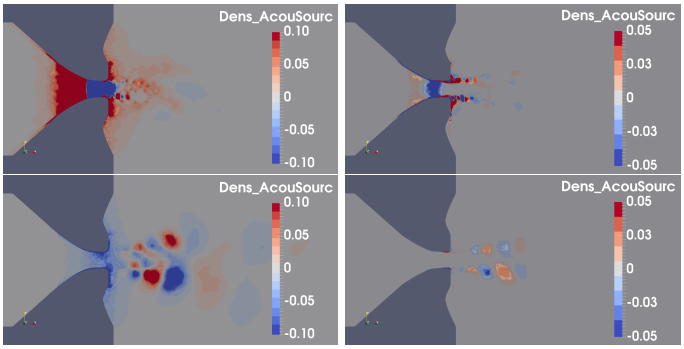

Fig. 2. The computed normalized sound source densities at 232 Hz (upper panel) and 2486 Hz (lower panel). Left are results for PCWE analogy, right for the Lighthill analogy, respectively.

Sound propagation. The computed sound sources are used as input for time solution of chosen acoustic analogy. The frequency spectra of the acoustic pressure monitored at the microphone position outside the mouth is shown in Fig. 3. The resulting peaks in frequency domain exhibit qualitatively good correspondence with the frequencies of first three formants 389 Hz, 987 Hz and 2299 Hz measured for the vowel [u:] in [2], marked in Fig. 3 by black lines.

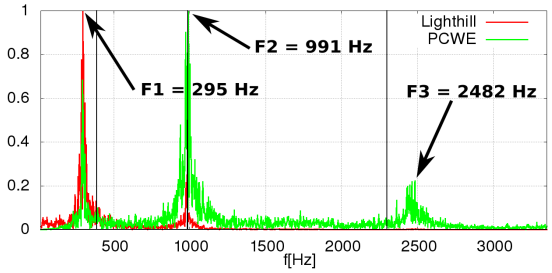

Fig. 3. The Fourier transform of acoustic pressure obtained by Lighthill and PCWE analogy

Acknowledgements

Authors are grateful for support provided by *Grant No. GA2016-01246S* of Czech Science Foundation and by *Grant No. SGS16/206/OHK2/3T/12* of the CTU in Prague.

References

[1] Hüppe, A., Kaltenbacher, M., Spectral finite elements for computational aeroacoustics using acoustic perturbation equations, Journal of Computational Acoustics 20 (2) (2012) 1240005, doi: 10.1142/S0218396X1240005X.

[2] Story, B.H., Titze, I.R., Hoffman, E.A., Vocal tract area functions from magnetic resonance imaging, Journal of the Acoustical Society of America 100 (1) (1996) 537-554.

[3] Valášek, J., Kaltenbacher, M., Sváček, P., On the application of acoustic analogies in the numerical simulation of human phonation process, Flow, Turbulence and Combustion (2018) 1-15, doi: 10.1007/s10494-018-9900-z.

COMPUTATIONAL MECHANICS 2018
34th conference with international participation
Srní
October 31 - November 2, 2018

Control of vibration suppression and motion control by piezo actuators

J. Volech [a], Z. Šika [a], K. Kraus [a], P. Beneš [a]

[a] *Faculty of Mechanical Engineering, Czech Technical University in Prague, Technická 4, 166 07 Prague 6, Czech Republic*

Piezoelectric materials are increasingly used in industry in various applications such as stabilization, micro-positioning, shakers etc. Two main disadvantages are high demand on the input voltages and relatively small range of motion. There are presented two type of piezoelectric elements implementation with respect to individual, above mention, problems and their solution. Firstly, usage piezo elements in smart materials. The price of piezo elements is still decreasing and it is not a problem to create material with heavily distributed grid of piezo patches Fig. 1 a). This material after applying voltage can modify his properties or can serve as vibration suppression element.

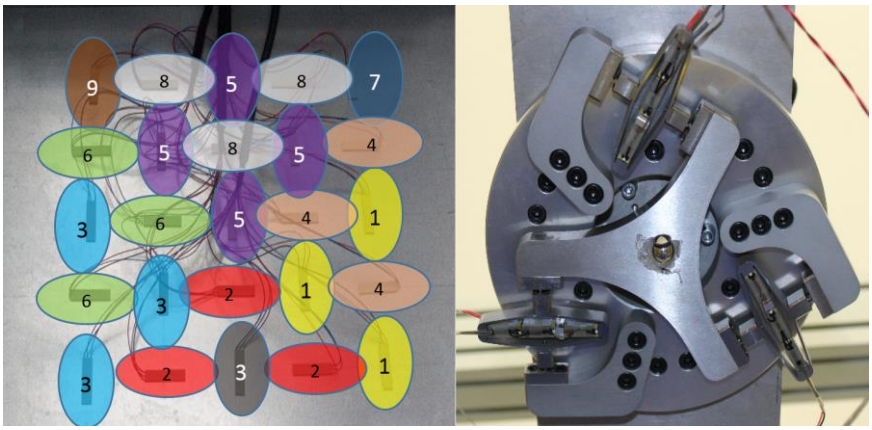

a) Heavily distributed grid of piezo patches b) Piezo platform for tracking task

Fig. 1. Examples of the use of piezoelectric elements

Such a heavily distributed grid is very demanding on control strategy and supply voltage. Normally there need to be one amplifier for one piezo patch. Therefore, several groups of the piezo patches is merged to 'clusters' see Fig. 1 a). Three concepts of clusters were proposed. Each cluster is powered with a single amplifier and single control voltage. From these clusters the optimal set of the piezo patches is tested to reduce the demands on the control strategy and control input voltage. Selection is based on the Henkel singular values [1] of the system, which represent a measure of energy for each mode

$$\gamma_i = \sqrt{\lambda_i(W_c W_o)} = \sqrt{\lambda_i(W_{cb} W_{ob})}, \quad i = 1,..,N, \tag{1}$$

and controllability parameter. When our target is to suppress primary the first four modes of the system then with selected cluster (Fig. 1 a)) can be achieved the similar results as with fully distributed control with minimal loss of energy (on average approximately 4%) for each mode with only 9 amplifiers instead of 25.

The second problem of piezo elements are their limited movement or stroke. An example of a solution to this problem is given on the example of a piezo platform perform the tracking task Fig. 1 b). Piezo elements are used as the micro positioning of the multilevel cable mechanism along the trajectory [2]. The control strategy is, because implementation obstacles, reduced to control just two degrees of freedom (x and y) with originally designed three Amplified Piezo Actuators (APA). For this reason, the redundant degree of freedom (rotation of the piezo driven platform) is used to minimize the individual APA stroke. The minimization function is based on the planar mathematical model of the platform which is delivered in the standard state space form. with inputs and outputs state as folowed

$$\boldsymbol{Y} = [x\ y]^T, \boldsymbol{u} = [u_1\ u_2\ u_3]^T. \tag{2}$$

Modeled system has not direct feedthrough. This mean, that the $\boldsymbol{D}$ matrix of the system is neglected and the static behaviour is considered $\dot{\boldsymbol{X}}$=0, then the system can be revriten as

$$\boldsymbol{Y} = \underbrace{-\boldsymbol{C}\boldsymbol{A}^{-1}\boldsymbol{B}}_{\boldsymbol{P}}\boldsymbol{u}. \tag{3}$$

Transformation matrix $\boldsymbol{P}$ has dimension 2x3. This system has two equations for three unknowns, therefore it has infinitely many solutions. But there are restrictions on the APA's stroke. They have maximum operating voltage 150 V. Based on this, one input voltage is set as variable parameter in the known range $\boldsymbol{u_3} = \langle 0\colon 1\colon 150\rangle$. Then the two vectors for inputs voltages $\mathbf{u_1}$ and $\mathbf{u_2}$ can be obtained in the specific position depending on the voltage $\mathbf{u_3}$

$$\begin{bmatrix}\boldsymbol{u_1}\\ \boldsymbol{u_2}\end{bmatrix} = \boldsymbol{P}(1\colon 2,1\colon 2)^{\boldsymbol{T}}\boldsymbol{Y} - \boldsymbol{P}(1\colon 2,3)\begin{bmatrix}\boldsymbol{u_3}\\ \boldsymbol{u_3}\end{bmatrix}. \tag{4}$$

In form of the matrix with the given structure $\boldsymbol{F} = [\boldsymbol{u_1}\ \boldsymbol{u_2}\ \boldsymbol{u_3}]^T$ can be find maximum of absolute value in the term of the maximum use of APA

$$[V, I] = min(max(abs(\boldsymbol{F}))), \tag{5}$$

where V is the value and I is the index of the position in the vector. Then the I represents the index of the optimal set of the input voltages in vector $\boldsymbol{F}$ to reach the desired position $\boldsymbol{Y}$ constrained by the operating voltage for APA 3. And the optimal voltage is selected as

$$u_{1optimal} = \boldsymbol{F}(1, I), u_{2optimal} = \boldsymbol{F}(2, I), u_{3optimal} = \boldsymbol{F}(3, I), \tag{6}$$

which achive the same results with only 80% of originaly APA's strokes.

Two main problems of usage piezoelectric material has been studied and an example was given to each problem. Solution on the first problem in the given example of heavily distributed grid of piezoelectric patches (high demand on input voltage) has been proposed as composing multiple piezo elements into one control unit. And second problem (restriction of the piezo element stroke) has been resolved by adding one piezo element which compensates for the movements of others. Both examples give promising results that will continue to be investigated and tested on real experiments.

Acknowledgements

The work has been supported by the Czech Science Foundation Project Mechatronic structures with heavily distributed actuators and sensors, 16-21961S and the grant SGS16/208/OHK2/3T/12 Mechatronics and adaptronics 2016 of CTU in Prague.

References

[1] Preumont, C.A., Mechatronics, dynamics of electromechanical and piezoelectric systems, Springer, 2006.
[2] Šika, Z., Beneš, P., Valášek, M., Volech, J., Kraus, K., "Cable driven spherical mechanism quadrosphere enhanced by 3 DOF piezo-actuated platform, Proceedings of the 8th ECCOMAS Thematic Conference on MULTIBODY DYNAMICS, 2017, pp. 551-557.

COMPUTATIONAL MECHANICS 2018
34th conference with international participation
Srní
October 31 - November 2, 2018

Treatment of gait disorder in a child with mild cerebral palsy

B. Yousefghahari [a,c], A. Vahidi-Shams [b], A. Guran [b]

[a] *Babol Medical University, Iran*
[b] *Institute of Structronics, Canada*
[c] *Behar Rheumatology Clinic, Babol, Iran*

In this paper we present a procedure to correct the gait disorder in a 4 year old girl with mild CP and spastic double monoplegia. Time series for movement of the patient were produced in the gait lab of Wigmore clinic in Yerevan (Armenia) and the orthoses were designed based on numerical computation to optimise the movement of the patients.

Diagnosis: A comprehensive physical examination of the patient and observation of the gait were done by a team of paediatric orthopaedic surgeons, a paediatric rehabilitation physician, a rheumatologist, and a biomechanician. The cause of disorder in locomotion was diagnosed upper motor neuro disorder and CP. Distal movement of the patient is not possible and the treatment should be done by using orthosis device, by physiotherapy and stretching, (Fig. 1a), and by Tracking Gait Carpet (TGC) (Fig. 1b, 1c.)

Fig. 1. (a) Physical examination, (b) gait on tracking gait carpet (TGC) bare feet (c) with assistive devices

Gait analysis and design of orthosis devices: Analysis was done with a system consisted of 8 cameras and a force plate, 15 sensors were placed on patient's body, Stroboscopic photos during a gait with bare feet and with asistive devices from start, after 5 second and after 10 second, were taken (Fig. 2). Based on analysis of numerical results the Lower-limb orthoses designed, manufactured and used (Fig. 3).

Conclusions: The cause of locomotion disorder was diagnosed as spastic double monoplegia with mild CP. A system of orthosis together with 8 physiotherapy exercises and walking on a Tracking Gait Carpet (TGC) was used to treat locomotion disorder in a 4 year old girl suffering from mild CP. Walking disorder was corrected significantly.

The disorder in movement of hands disappeared after the patient gained stability and equilibrium of the gait.

Fig. 2. Stroboscopic photos during a gait with orthoses and shoes

Fig. 3. Photos taken during various stages of design and manufacturing of the orthoses

Acknowledgements

We would like to thank Dr. Laura Movsisyan from rehabilitee centre in the city of Gosh (The Republic of Armenia) And Drs. Davit Sekoyan and Garen Koloyan from Wigmore clinic in Yerevan republic of Armenia for their collaboration this research project was conducted in "STEP" Motion Research Laboratory, Wigmore Clinic, the Republic of Armenia.

References

[1] Burtner, P.A., Qualls, C., Woollacott, M.H., Muscle activation characteristics of stance balance control in children with spastic cerebral palsy, Gait & Posture 8 (3) (1998) 163-174.

[2] Sawacha, L.Z., Paolini, G., Ingrosso, S., Nativo, R., Benedetti, M.G., Protocol for gait analysis in children Alberto, Gait & Posture 26 (4) (2007) 560-571.

COMPUTATIONAL MECHANICS 2018
34th conference with international participation
Srní
October 31 - November 2, 2018

Application of the harmonic balance method for investigation of dynamic parameters of the rotors mounted on linear/nonlinear coupling elements

F. Zaoral [a], P. Ferfecki [a,b]

[a] IT4Innovations National Supercomputing Center, VSB – TU of Ostrava, 17. listopadu 15, 708 33 Ostrava – Poruba, Czech Republic
[b] Faculty of Mechanical Engineering, VSB – TU of Ostrava, 17. listopadu 15, 708 33 Ostrava – Poruba, Czech Republic

In modelling of rotating systems, the connection of the rotor to the stator part is often performed by means of coupling elements that behave nonlinearly, such as hydrodynamic and magnetic bearings, squeeze film dampers [2], etc. The Harmonic Balance Method (HBM) represents a tool for investigating the steady-state response of nonlinear rotating systems, which is periodic or even quasiperiodic in time [3].

Computational models are designed for rotating systems [1] such as rotors and assume that individual parts are flexible bodies such as the shaft and the discs. The motion equation of the undamped rotating system including the stator part, expressed in the fixed space is

$$\mathbf{M}\ddot{\mathbf{q}}(t) + \omega_0 \mathbf{G}\dot{\mathbf{q}}(t) + \mathbf{K}\mathbf{q}(t) = \mathbf{f}(\mathbf{q}, \dot{\mathbf{q}}, t), \tag{1}$$

where **M**, **G**, and **K** are global matrices of the mass, the gyroscopic effects, and the stiffness of the system, respectively, **f** is generally a nonlinear vector which includes the loading and coupling forces, **q** is the global vector of the nodal displacements, ω is the angular velocity of rotation of the rotor and t is the time. The symbol $(\cdot)$ denotes a derivative with respect to time.

The computational model created this way can have many degrees of freedom n because the rotating system is discretized by solid finite elements (FE). HBM assumes that the steady-state response can be approximated by a finite number of members N of the Fourier series. When using HBM, the total number of primary unknowns (which are elements of vectors of the absolute, cosine and sine coefficients of the Fourier series) is equal to $(2N+1)\cdot n$, which can dramatically increase the demands on computing power. Therefore, a software library is being developed at the IT4Innovations National Supercomputing Center, which will enable problems of this type to be solved efficiently using high performance computing (HPC) resources.

A library for computational modelling of rotating systems is being developed in the MATLAB programming environment. Within this library, program packages are being created for: (i) stationary analysis, (ii) modal analysis, and (iii) calculation of transient and steady-state response of forced vibration. In this library, selected coupling elements between rotating and stationary parts can be realized with linear or nonlinear models of coupling.

The computational algorithms from the newly developed program library are tested on rotor systems. The first test rotor system (Fig. 1) consists of an elastic shaft and one elastic disc. The second test rotor system (Fig. 2) is comprised of an elastic shaft and two elastic discs. The first disc is located at the bearing span and the second one is located on an overhanging end of the shaft. Both test rotor systems are mounted on two radial hydrodynamic bearings and one axial roller bearing. The coupling areas are shown in Fig. 1

and Fig. 2 marked in green colour. The stator part is assumed to be represented by an absolutely rigid body. The rotor material was considered homogeneous, isotropic, and linearly elastic. The rotors are excited by centrifugal forces due to unbalance of the discs.

In the computational models, the shaft and the rotor discs are discretized by solid hexahedral isoparametric FEs with a linear basis function. Bearings are included in the computational models by means of force coupling and by stiffness and damping coefficients.

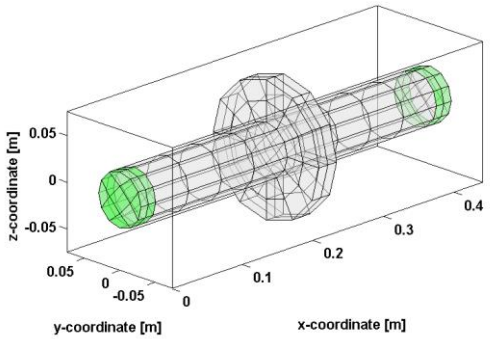

Fig. 1. Geometry of the first test problem

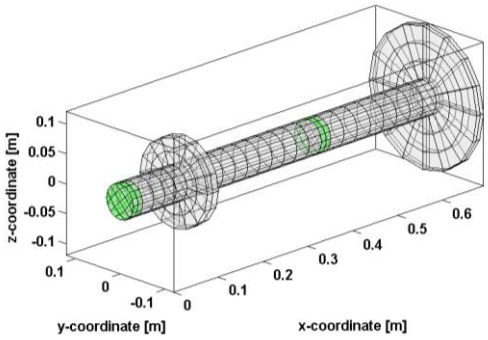

Fig. 2. Geometry of the second test problem

In Figs. 3-5, the results from the modal analysis software package are presented. Computations were performed for the first test problem, the rotor rotating with an angular velocity of 95 rad/s and with no coupling elements present. In Fig. 3, the first non-zero mode shape is plotted, and it corresponds to the bending deformation of the shaft (with two nodal lines) which lies in the xz plane. The third and fifth nonzero mode shapes are shown in Fig. 4 and Fig. 5, respectively. In the third shape, there is a bending deformation of the shaft (now with three nodal lines) and the fifth shape is a torsional deformation of the shaft.

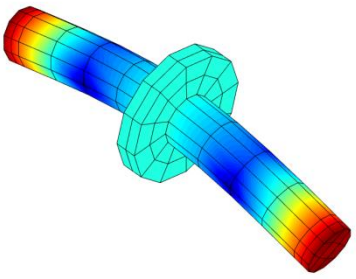

Fig. 3. First mode shape - 1415 Hz

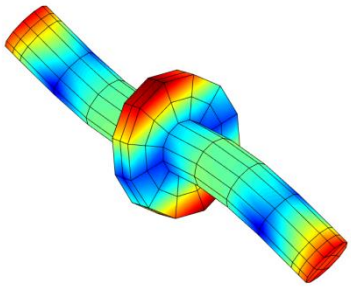

Fig. 4. Third mode shape - 3615 Hz

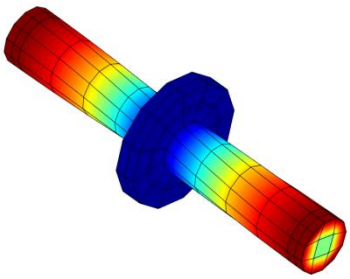

Fig. 5. Fifth mode shape - 3796 Hz

The newly developed library is intended for both stationary and nonstationary analyses. Special attention is given to the effective use of HBM using the IT4Innovations HPC resources. The simulation results obtained are verified with commercially available FE program systems.

Acknowledgements

This research work has been supported by the Ministry of Education, Youth and Sports from the National Programme of Sustainability (NPU II) project „IT4Innovations excellence in science - LQ1602“.

References

[1] Byrtus, M., Hajžman, M., Zeman, V., Dynamics of rotating systems, University of West Bohemia, Czech Republic, 2010. (in Czech)
[2] Hori, Y., Hydrodynamic lubrication, Springer, Japan, 2006.
[3] Petrov, E.P., Ewins, D.J., Analytical formulation of friction interface elements for analysis of nonlinear multi-harmonic vibrations of bladed disks, Journal of Turbomachinery 125 (2) (2003) 364-371.

COMPUTATIONAL MECHANICS 2018
34th conference with international participation
Srní
October 31 - November 2, 2018

FE analysis of the T-profile for airplane door

T. Zámečníková [a], Z. Padovec [a], R. Sedláček [a], J. Křena [b]

[a] *Department of Mechanics, Biomechanics and Mechatronics, Faculty of Mechanical Engineering, Czech Technical University in Prague, Technická 4, 166 07 Praha 6, Czech Republic*
[b] *Latecoere Czech Republic s.r.o., Beranových 65, 199 02, Praha 9, Czech Republic*

This paper deals with the replacement of the titanium profile in the airplane door with the composite one. The aim of the project is the FEM analysis of the titanium T-profile integrated in airplane door and to design a composite part which will be lighter and stiffer. It is obvious that the design will change the shape of the cross-section of the T-profile. The connecting dimensions have to remain the same. So, several ways were chosen to examine the stiffness of the titanium and composite T-profile.

First the titanium T-profile was analyzed in the FEM model. The profile was loaded by single unit forces in the directions of the axes of the coordinate system that was connected with the T-profile the same way in all analyzed cases. Than the two different composite versions of the profile were designed.

The models of the titanium and CFRP profiles have the same composition. The T-profile with the fixed coordinate system was placed on the flat composite plate which was the same for all three cases. This plate presents the attachment in the real position of the profiles. The profiles were fixed by screws, so this connection was modeled by the tie interaction. Than the models with the clamped T-profiles were realized to get the comparison of the profiles stiffness and to see the effects of the flat composite plate on the profiles deformation. The comparison of the deformation could be seen in the Fig.1.

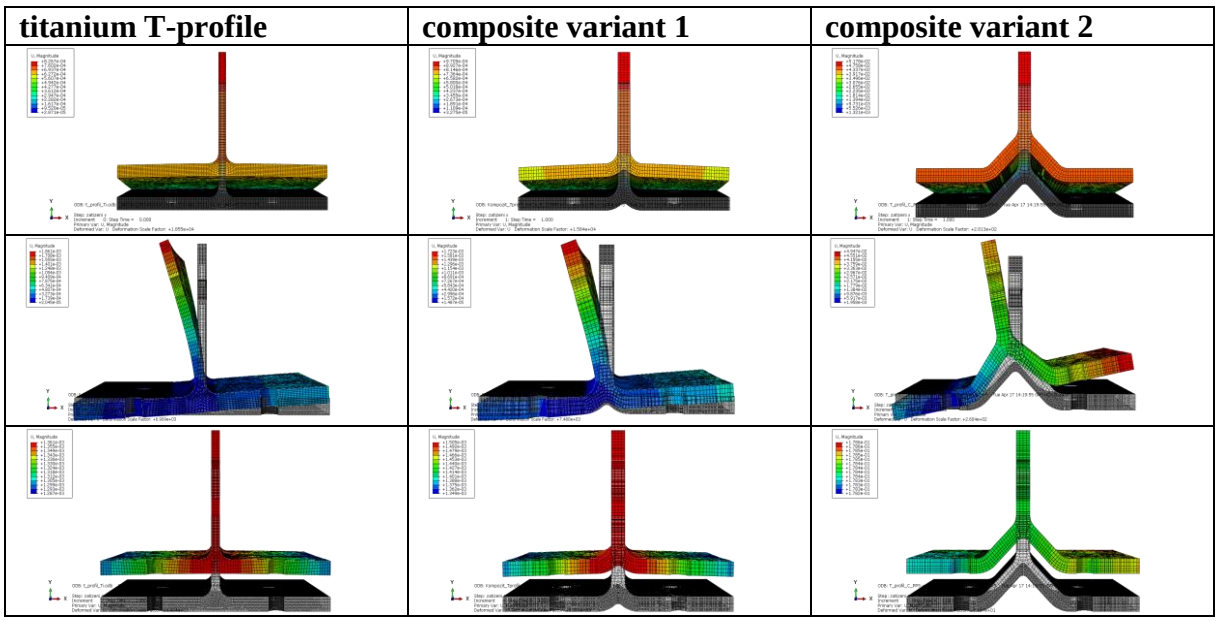

Fig. 1. The versions of the T-profile and their loading

The material constants were calculated as orthotropic homogeneous material using rule of mixtures with respect to fiber undulation (5H satin weave). The effective constants from this previous calculation are used as inputs to the FEM model. The CFRP T-profiles were modeled as volume model and the effective material constants were used. This way of modeling represents the whole volume of the model, but it allows the parametric inputs of the materials constants for orthotropic material. This is a simplification of the FEM modelling of a composite material parts.

The models were done with respect to the composite layup of the T-profiles. So, the profile was divided to some parts representing the layup composition with the same characteristic. Then the material constants with their own coordinate system for each separate part of the T-profile were assigned. The elements C3D8R were used for meshing in Abaqus [1].

The results for all three cases of T-profiles can be seen below in Fig. 2 and Fig. 3. There is a big decrease in the displacement in all directions especially for the second version of the composite T-profile. Both composite versions are stiffer than the titanium one. The maximal displacement can be seen in all cases in the direction of the *y* axis, but it is known that this direction is not so important in the real loading of the T-profiles. The most important for the real load is the decrease of the displacement of the second composite version in the direction of the *z* axis.

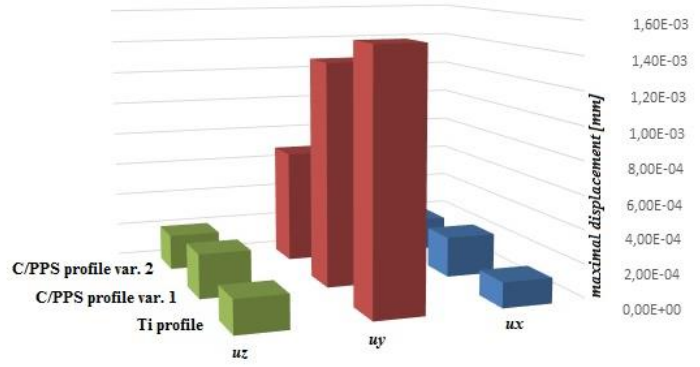

Fig. 2. Comparison of displacements for all cases of T-profiles fitting on the flat composite plate

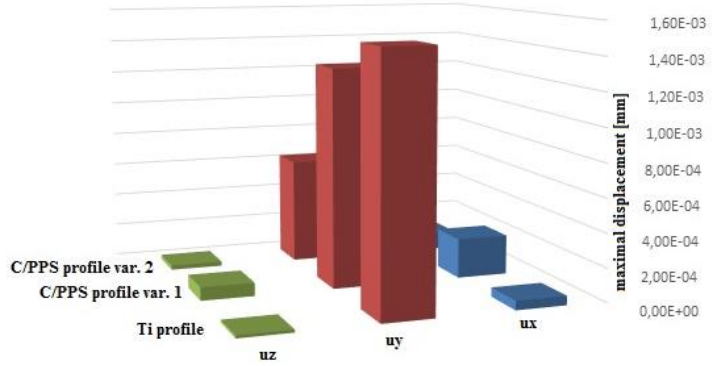

Fig. 3. Comparison of for all cases of clamped T-profiles

Acknowledgements

The work has been supported by the grant project MPO FV30033 and by the research project SGS18/175/OHK2/3T/12.

References

[1] Smith, M., ABAQUS/Standard User's Manual, Version 6.14. Providence, RI: Simulia, 2014.

COMPUTATIONAL MECHANICS 2018
34th conference with international participation
Srní
October 31 - November 2, 2018

Modeling of mechanical properties of macroporous hydrogel

J. Zavřel [a], T. Vampola [a], M. Dušková-Smrčková [b]

[a] Faculty of Mechanical Engineering,Czech Technical University in Prague, Technická 4, 166 07 Prague 6, Czech Republic
[b] Institute of Macromolecular Chemistry, Czech Academy of Sciences, Heyrovského nám. 2, 162 06 Prague 6, Czech Republic

Macroporous hydrogels with controlled morphology are widely used in biomedical fields, as drug delivery, tissue engineering, analytical and technical separations or responsive constructs. Porosity can be achieved by several methods. In the preparation of physical experiments it is made by salt crystals which are extracted from the hydrogel after polymerization. The salt crystals have different sizes and shapes. The pore sizes and their distribution affects the final mechanical properties. Such polymer structure is designed by simulations. The simulated structure is than transfered into ANSYS environment and its mechanical properties are examined and compared with experiments.

Modelling of the structure: The first step is to prepare the hydrogel structure model. It is based on the real mechanism of its formation. The porosity is achieved by salt crystals which are later extracted. In our case of modelling there are randomly distributed cubes (crystals) subtracted from the initial volume. The milestone is to reach the first through path in the initial volume. Upon further adding of the crystals, the saturation point can be reached. It corresponds to the case when the hydrogel is saturated with crystals and at is not possible to add additional crystals. Such state can be described by volume fraction of connected paths (paths going through the volume) and all paths (including all pats and crystal holes) to the whole volume (Fig. 1). It is described by the experimentally detected value Φ_{exp} and simulated value Φ_{teor}. Behaviour of different materials when using different sizes of salt grains has the same trend.

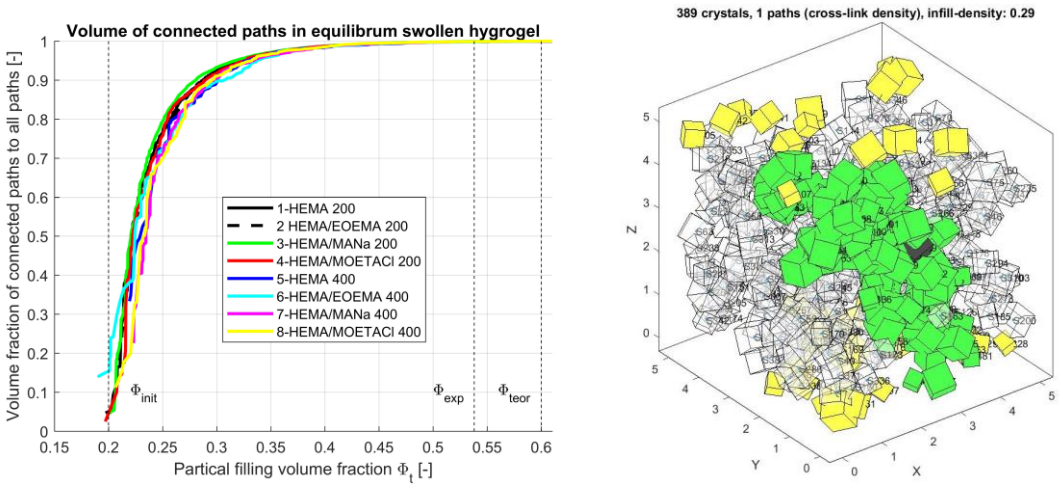

Fig. 1. Partical filling volume fraction of different materials and crystal sizes (left). An example of simulation model creation (right)

Computation of mechanical properties: The previous structure is transferred into the ANSYS environment. The export script is generated. Crystals generated in the previous step are also subtracted from the initial volume and then it is meshed. It is also the inverted structure from the Fig 1 – on the right. The boundary conditions and forces are applied. The stresses and deformation fields were analysed.

Experimental results: Oscillatory shear measurements of swollen gels (Fig. 2) were performed using the rheometer Bohlin Gemini HR Nano (Malvern Instruments, UK) equipped with a Peltier temperature table and a solvent stainless steel dish. All tests were performed using 25 mm diameter stainless steel parallel plate geometry with disc-like samples of a diameter 25 mm and swollen thickness in the range from 1 to 4 mm. During the measurement, the samples were immersed in water or aqueous solution of sodium phosphate buffer (PBS). The distance between the measuring plates – gap size – for each sample was adjusted to a value at which the sliding of samples was avoided and full contact between plates and sample was achieved [1].

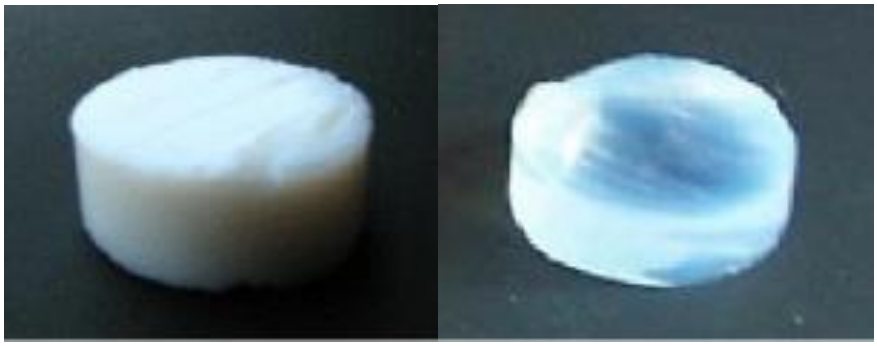

Fig. 2. Swollen macroporous gels – macroscopic appearance of tested sample

Precise sample placement between the upper and lower measuring plates is a crucial condition as the resulting apparent moduli values are very sensitive either to the plate slippage or to normal force acting on the sample excess. The amplitude sweep tests were performed first in the stress-control mode to find the linear viscoelastic range of the stress-strain response and the stress value for subsequent frequency sweep measurement was chosen within that linear range. The measurements were carried out in the range of frequencies from 0.01 Hz to 100 Hz at 25 °C. The apparent storage and loss moduli of the gels were obtained.

Acknowledgements

The research is supported by the Grant Agency of the Czech Republic by project No GA17-08531S – "Computational design of hydrogel cell scaffolds".

References

[1] Karpushkin, E., Dušková-Smrčková, M., Remmler, T., Lapčíková, M., Dušek, K. Rheological properties of homogeneous and heterogeneous poly(2-hydroxyethyl methacrylate) hydrogels, Polymer International 61 (2) (2012) 328–336.

COMPUTATIONAL MECHANICS 2018
34th conference with international participation
Srní
October 31 - November 2, 2018

Nonlinear vibration of the nuclear reactor with clearances in core barrel couplings

V. Zeman[a], Z. Hlaváč[a]

[a] *NTIS – New Technologies for the Information Society, Faculty of Applied Sciences, University of West Bohemia, Univerzitní 8, 301 00 Plzeň, Czech Republic*

The original mathematical model of the VVER-type reactor excited by coolant pressure pulsations [2] was derived as the linear clearance-free model in couplings. Assembly clearances Δ_i in the key-groove (K-G) couplings between the lower part of core barrel (CB3) and the reactor pressure vessel (PV) (Fig. 1) produce nonlinear vibration of reactor components. Friction-vibration interactions in the above mentioned couplings cause the fretting wear on their contact surfaces [1]. The aim of this contribution is an investigation of the VVER 1000 type reactor nonlinear vibration respecting the assembling side clearances and friction in eight K-G couplings uniformly deployed to circumference between CB3 and PV. Relative tangential displacements $u_i\,(i = 1,\ldots,8)$ of the K-G contact surfaces from the general starting position generate the normal contact forces

$$N_i(u_i) = k[(u_i + \Delta_i + s_i)H(-u_i - \Delta_i - s_i) + (u_i - \Delta_i + s_i)H(u_i - \Delta_i + s_i)]\,, \qquad (1)$$

where k is the stiffness in tangential direction of one key connected with PV by means of the cantilever. Small shifts s_i of the grooves with respect to keys in direction of displacements u_i from the ideal central position of CB3 was detailed investigated in a context of the K-G coupling fretting wear on the simplified reactor model in [3]. Heaviside function H in (1) is zero when the contact is interrupted. The slide of K-G contact surfaces in contact phases (when $H = 1$) causes radial $T_{i,r}$ and axial $T_{i,ax}$ components of friction forces

$$T_{i,r} = f(c_i)N_i(u_i)\frac{c_{i,r}}{c_i}\,,\ T_{i,ax} = f(c_i)N_i(u_i)\frac{c_{i,ax}}{c_i}\,,\ i = 1,\ldots,8\,, \qquad (2)$$

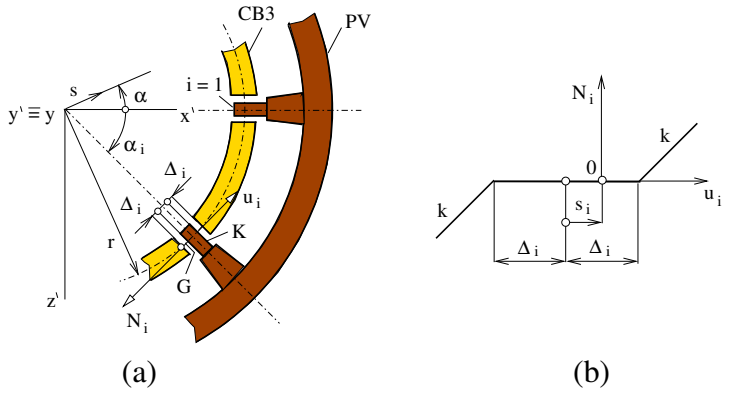

Fig. 1. Key-groove layout in contact plane between lower part of core barrel (CB3) and reactor pressure vessel (PV) (a) and stiffness characteristic of one coupling (b)

where friction coefficient f depends on relative slip velocity c_i, $c_{i,r}$ and $c_{i,ax}$ are its components in radial and axial directions. All contact forces $N_i(u_i)$, $T_{i,r}$, $T_{i,ax}$, $i = 1, \ldots, 8$ transmitted by K-G couplings are expressed by means of the vectors of generalized coordinates $\boldsymbol{q}(t)$ and speeds $\dot{\boldsymbol{q}}(t)$ in the new global reactor model

$$\boldsymbol{M}\ddot{\boldsymbol{q}}(t) + \boldsymbol{B}\dot{\boldsymbol{q}}(t) + (\boldsymbol{K} - \boldsymbol{K}_C)\boldsymbol{q}(t) = \sum_{j=1}^{4}\sum_{k=1}^{3} F_{PV}^{(k)}\boldsymbol{f}_j \cos(k\omega_j t + \delta_j) + \boldsymbol{f}(\boldsymbol{q}, \dot{\boldsymbol{q}})\,. \qquad (3)$$

The vector of elastic forces $\boldsymbol{K}_C\boldsymbol{q}(t)$ in all clearance-free and smooth K-G couplings included in vector $\boldsymbol{K}\boldsymbol{q}(t)$ of the original reactor model [2] is replaced by nonlinear force vector $\boldsymbol{f}(\boldsymbol{q}, \dot{\boldsymbol{q}})$. The reactor dynamic response excited by coolant pressure pulsations generated by four main circulation pumps (the first member on right-hand side) is investigated by a numerical integration of the nonlinear motion equations (3) in time domain.

For illustration, Fig. 2 shows the time behaviour of the normal contact force N_3 and relative velocity c_3 calculated for same clearances $\Delta_i = 25\,[\mu\mathrm{m}]$ in all eight K-G couplings, the central starting position CB3 ($s = 0$, $\alpha = 0$) and the Coulomb friction with friction coefficient $f = 1$. The presented method is applied to sensitivity analyses focused on variation in the friction characteristic and clearances in K-G couplings lead on as possible to reduce the contact forces and fretting wear.

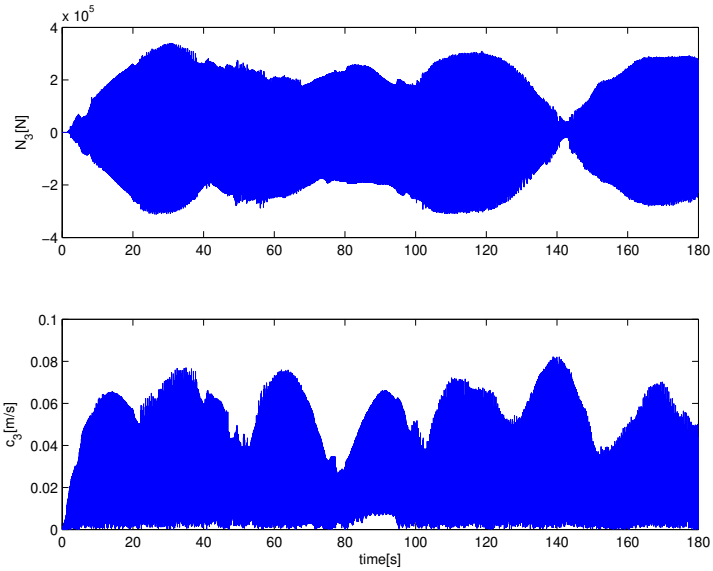

Fig. 2. Time behaviour of normal contact force N_3 and relative velocity c_3 in coupling 3

Acknowledgement

This work was supported by the project LO1506 of the Ministry of Education, Youth and Sports of the Czech Republic.

References

[1] Pečínka, L., Svoboda, J., Zeman, V., LTO problems of the WWER440/213 reactor core barrel, Proceedings of the international conference Obespečenije bezopasnosti AES s VVER, Podolsk, Rossija, 2017.

[2] Zeman, V., Hlaváč, Z., Dynamic response of VVER1000 type reactor excited by pressure pulsations, Engineering Mechanics 15 (6) (2008) 435-446.

[3] Zeman, V., Hlaváč, Z., Friction forces and fretting wear in reactor core barrel couplings, Proceedings of the 23rd international conference Engineering Mechanics 2017, Svratka, 2017, pp. 1118-1121.

COMPUTATIONAL MECHANICS 2018
34th conference with international participation
Srní
October 31 - November 2, 2018

Geometrical model of muscle attachment sites in hand

T. Zítka[a], L. Havelková[a], R. Tupý[c]

[a] *Man-Machine Interaction department, New Technologies – Research Center, University of West Bohemia, Univerzitní 8, 306 14 Plzeň, Czech Republic*

[c] *Department of Imaging Methods, Medical School and Teaching Hospital Pilsen, Charles University in Prague, Pilsen, Czech Republic*

In biomechanical modeling acquiring appropriate data is a difficult task. In our study, we attempt to overcome this by using data from MRI. We obtained MRI scans of hand in which muscle attachment sites are identifiable. These allow us to create triangular meshes that accurately model muscle origin and insertion surfaces. In AnyBody Modeling System individual muscles are replaced with user defined number of action lines or virtual muscle elements. These elements need to be placed within muscle volume in a way that respects anatomy of the muscle. This breaks into two tasks: placing required number of endpoints onto attachment surfaces and then pairing these endpoints in order to specify individual elements.

For the first task we use modified k-means algorithm. Given a finite set of points $\omega \subset \mathbb{R}^N$, $N \in \mathbb{N}$ and number $k \in \mathbb{N}$, original k-means method [4] iteratively tries to approximate solution to k-partition problem. That is to partition set ω into k classes $\omega_1, \dots \omega_k$ each corresponding with point $c_i \in \mathbb{R}^N$, $i = 1 \dots k$ called centroid, in such way that

$$\sum_{i=0}^{k} \sum_{x \in \omega_i} \|c_i - x\|^2$$

is minimal. In our setting we used set of centers of gravity of the triangles in the mesh as a set ω. We modified the basic k-means method in two ways. First we ensure that each centroid is always a point from ω by placing it in the closest point in ω after each iteration. Second we assigned each point $x \in \omega$ a weight $w(x)$ equal to the surface volume of the corresponding triangle. The generalized algorithm iteratively minimizes expression [1]

$$\sum_{i=0}^{k} \sum_{x \in \omega_i} w(x)\|c_i - x\|^2.$$

This ensures that the partition does not depend on density of points of the mesh and surface of the muscle attachment is divided between muscle elements so that the variation of surface volumes assigned to elements is minimal, see Fig. 1.

Muscle elements' endpoints are calculated separately for origin and insertion. In order to place the muscle elements we need to connect corresponding endpoints so that lines of action not only do not intersect but also are not entangled. Our approach is based on Euclidean matching problem in two dimensions. It can be proven that the minimality of total pairing distance ensures that no two line segments connecting paired points intersect. This result transfers to three dimensions, however it is too weak. It does not guarantee that action lines do not run

across each other. Fortunately minimal matching still provides good results in which virtual muscle elements are not tangled with each other.

The minimal pairing is obtained by Hungarian algorithm [3] which finds minimal matching in weighted bipartite graph. In our case we are concerned with complete bipartite graph on two sets of centroids on origin and insertion surfaces. Euclidean distances are taken as weights of the edges. This graph is complete, hence it contains perfect matching and minimal matching always exists [3]. The resulting minimal matching with pairs connected by lines can be seen in Fig. 2. We used implementation found in [2].

Our study provides novel approach to acquiring data used in biomechanical models along with dataset of hand muscle data. It also provides a tool for generating these data, relieving researchers of some tedious labor and possibly allowing for greater reproducibility of research.

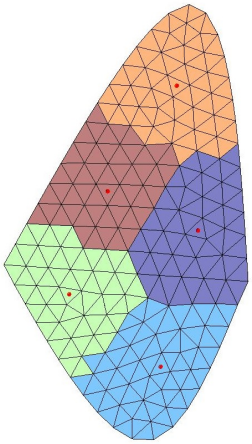

Fig. 1. Opponens pollicis insertion with five muscle elements endpoints and surfaces assigned to them colored

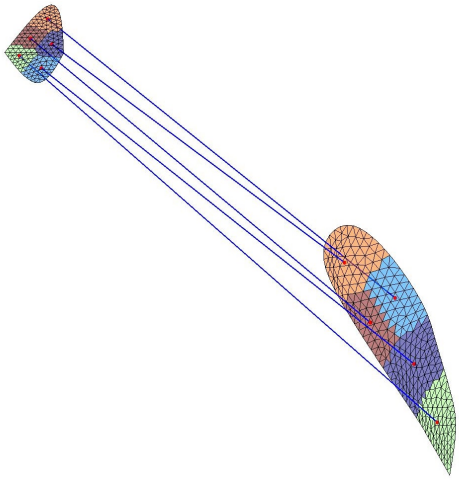

Fig. 2. Opponens pollicis connectivity with five muscle elements

Acknowledgments

This work was supported by the project n. 182 Obstetrics 2.0 – Virtual models for the prevention of injuries during childbirth realised within the frame of the Program INTERREG V-A: Cross-border cooperation between the Czech Republic and the Federal State of Germany Bavaria, Aim European Cross-border cooperation 2014-2020. The realisation is supported by financial means of the European Regional Development Fund (85 % of the costs) and the state budget of the Czech Republic (5 %). The next thanks belong to internal grant of UWB: SGS-2016-059.

References

[1] Bock, H.-H., Origins and extensions of the k-means algorithm in cluster analysis, Electronic Journal for History of Probability and Statistics 4 (2) (2008) 1-18.

[2] Cao, Y., Hungarian algorithm for linear assignment problems (V2.3). [online] https://www.mathworks.com/matlabcentral/fileexchange/20652-hungarian-algorithm-for-linear-assignment-problems-v2-3, 2011.

[3] Frank, A., On Kuhn's Hungarian method – A tribute from Hungary, Egervary Research Group, Pazmany P. setany 1/C, H1117, Budapest, 2004.

[4] MacQueen, J., Some methods for classification and analysis of multivariate observations, Proceedings of the Fifth Berkeley Symposium on Mathematical Statistics and Probability (1967) 281-297.

COMPUTATIONAL MECHANICS 2018
34th conference with international participation
Srní
October 31 - November 2, 2018

Wang tiles and metal foam micro-structure image synthesis

L. Zrůbek[a], M. Doškář[a], A. Kučerová[a], M. Meneses-Guzmán[b], F. Rodríguez-Méndez[c], B. Chiné[c]

[a] *Department of Mechanics, Faculty of Civil Engineering, CTU in Prague, Thákurova 7, 166 29 Prague 6, Czech Republic*
[b] *School of Industrial Production Engineering, Costa Rica Institute of Technology, Cartago, Costa Rica*
[c] *School of Materials Science and Engineering, Costa Rica Institute of Technology, Cartago, Costa Rica*

Our latest work is focused on image synthesis of metal foam micro-structures using the Wang tiles and Automatic tile design.

The Wang tiles method [5] is comparable to the classic game domino or the jigsaw puzzle but the used pieces are modelled visually as squares with specific information on each of the four edges (e.g. colours, patterns, etc.). Tiles are gathered in sets (Fig. 1c) and by means of one set and particular tiling algorithm the planar domain is covered.

The main advantage of Wang tiles method compared to periodic unit cell methods is the ability to preserve stochastic layout of original micro-structure. This is primarily achieved by using algorithm presented in [2] which specifies a simple rule that for placing tile in the *NW* corner position (Fig. 1b), there must be at least two valid tiles to place, from which one is chosen randomly. The algorithm can be modified by allowing to repeat the choice *n*-times to avoid occurrence of groups of same tiles in tiling.

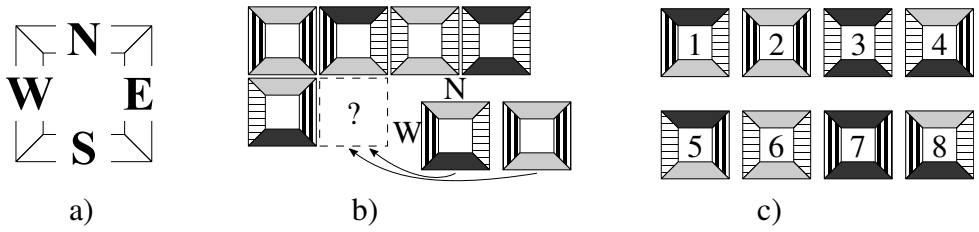

Fig. 1. a) Tile edge labels, b) North-West (NW) corner position, c) Wang tiles set consisting from eight tiles with two different codes on vertical and horizontal edges – W8/2-2

Method used for creating tiles is called Automatic tiles design [2]. From the original micro-structure is taken same number of samples as number of edge codes. For each tile the respective samples are arranged in to rhombus shape with specific overlap ω and stitched together by means of image quilting algorithm [4]. The resulting tile is then cut out from centre. As an extra step, the central area of obtained tiles can be patched to suppress the influence of repeating tile edges (and relevant tile quarters) on inducing artefacts [3].

The modelled material is particular aluminium foam produced in Laboratorio Macchine Utensili e Sistemi di Produzione (MUSP), at Politecnico di Milano in Italy [1] from the precursor composed of $AlSi_{10}$ alloy mixed with a $0.80\,\mathrm{wt}\%$ of titanium hydrate (TiH_2). The precursors are placed in steel mould and heated in convection oven until the H_2 is released into molten alloy. The created foam has irregular porosity and density through the volume (Fig. 2a).

The image synthesis process and quality of obtained results are affected by many different factors. Therefore we subject it to analysis with these settings: the tile size $h = 1000$ and 2000 px, quilting overlap $\omega = \frac{h}{10}, \frac{2h}{10}, \frac{4h}{10}, \frac{8h}{10}$ and h, classic or modified tiling algorithm, raw or patched tiles and finally tile sets W8/2-2, W16/2-2 and W18/3-3.

Through the analysis we observed that the best results (Fig. 2b) are obtained with patched tiles, modified tiling algorithm and bigger tiles as they contain more micro-structural information. The larger overlap ω is also preferable choice because it provides more space to search the best path for quilting. Finally the larger sets of tiles brings more variety in the synthesised images.

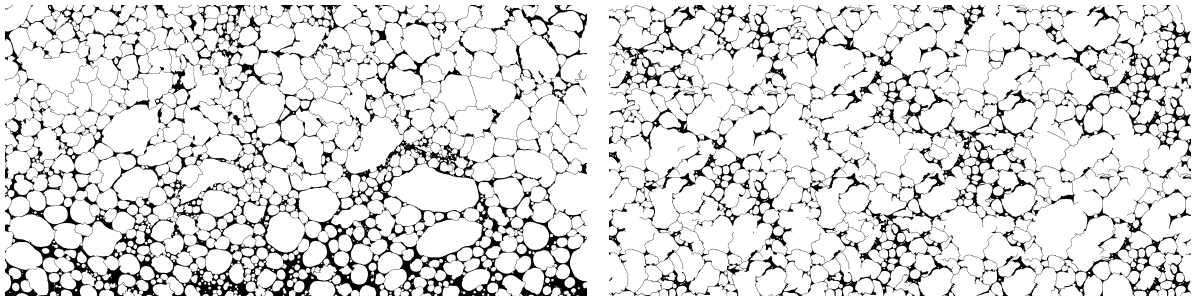

a) b)

Fig. 2. Foam micro-structures: a) original scan [1], b) synthesised sample

In spite of quite satisfactory results, the above presented approach has some major limitations. The main one rest in gradual porosity and density of original micro-structure because the Wang tiles are not capable to replicate such property. Further, the foams are very challenging for the image quilting algorithm which unfortunately leads, in many cases, to visibly damaged cells. And last, the quality of results is not easily measurable.

Acknowledgements

The authors gratefully acknowledge the financial support from the Grant Agency of the CTU in Prague, the grant No. SGS18/036/OHK1/1T/11 (L. Zrůbek, M. Doškář and A. Kučerová). Authors would also like to thank for the support from Vicerrectoría de Investigación y Extensión, project No. 1351022 (M. Meneses-Guzmán, F. Rodríguez-Méndez and B. Chiné).

References

[1] Chiné, B., Meneses-Guzmán, M., Rodríguez-Méndez, F., Characterization of aluminium foams produced via a powder metallurgy route, Proceedings of the 1st Iberic Conference on Theoretical and Experimental Mechanics and Materials / 11th National Congress on Experimental Mechanics INEGI/FEUP (2017), Porto, Portugal, 2018. [accepted for publication]

[2] Cohen, M.F., Shade, J., Hiller, S., Deussen, O., Wang tiles for image and texture generation, ACM Transactions on Graphics 22 (3) (2003) 287-294, doi: 10.1145/882262.882265.

[3] Doškář, M., Novák, J., Zeman, J., Aperiodic compression and reconstruction of real-world material systems based on Wang tiles, Physical Review E 90 (2014) 062118, doi: 10.1103/PhysRevE.90.062118.

[4] Efros, A.A., Freeman, W.T., Image quilting for texture synthesis and transfer, Proceedings of the 28th Annual Conference on Computer Graphics and Interactive Techniques, SIGGRAPH 01, New York, USA, 2001, pp. 341-346, doi: 10.1145/383259.383296.

[5] Wang, H., Proving theorems by pattern recognition–II, Bell System Technical Journal 40 (1) (1961) 1-41, doi: 10.1002/j.1538-7305.1961.tb03975.x.